

**Interface Morphology and Fracture Behavior of Friction Stir Welded
Dissimilar Metal T-lap Joints between AA7075 and AA5083**

(アルミニウム合金 7075 と 5083 からなる摩擦攪拌異種金属
T ラップ接合体の界面形態と破壊挙動)

by

DUONG DINH HAO

A Dissertation Submitted to the Graduate School of Engineering
in Partial Fulfillment of the Requirements for the Degree of

Doctoral Engineering

in

Materials Science

at the



Nagaoka University of Technology

June 2020

Interface Morphology and Fracture Behavior of Friction Stir Welded Dissimilar Metal T-lap Joints between AA7075 and AA5083

(アルミニウム合金 7075 と 5083 からなる摩擦攪拌異種金属 T ラップ接合体の界面形態と破壊挙動)

Abstract

For last three decades, Friction Stir Welding (FSW), one of the solid-state joining processes, has been widely applied in aerospace, shipbuilding, automotive, and railway industries. The FSW technology can be applied for the alloys those are difficult to be welded by normal fusion welding process, and it enables to produce dissimilar metals joints. These aspects might attract the large number of publications that has investigated welding parameters, welding defects, microstructure, residual stress, *etc.* with main purpose is to improve the mechanical properties of the FSWed joints. The weldability of the FSWed T-lap joints was investigated in literature. In spite of these, few publications have been achieved success in the improvement of the strength of the joints. The formation of some undesirable defects such as tunnel, oxide line, kissing bond, *etc.* might be responsible for these problems. Among these defects, the kissing bonds were too difficult to be improved by applying only traditional single-pass, especially at the retreating side (RS) in the FSW process. These results might be more pronounced in the failure under cyclic loadings. However, there is very limited knowledge from this aspect.

The aim of this work is to improve interface morphology and analyze the fracture behavior of the FSWed T-lap joints, those make platform for the improvement of the mechanical properties of the joints. For this purpose, a dissimilar metals T-lap joint between AA7075 and AA5083 was fabricated. The first attention was put on the fundamental formations of welding interface between the skin and stringer parts. The effect of welding parameters on the interface morphology and the strength of the joints was explored. Based on obtained results, a new method was proposed to upgrade the interface morphology of the joints. Here, the attention was put on the influences of reversed metal flow and tool offset on the interface morphology. The failure behavior of the improved T-lap joints was also investigated under cyclic loading with focusing on the role of the kissing bonds (KBs) orientation. In addition, such a new concept that the interface is modeled by an equivalent crack has been proposed to make the analysis of

the fracture behavior of the FSWed T-lap joints. Finite Element Analysis (FEA) is also applied to more quantitatively understand this failure. The prediction of crack direction under stringer-directional loading test was also presented in this work.

The experimental results showed that the formations of interface with some defects, e.g. hook, kissing bond, and bonding line defects were found under various welding conditions. Here, increasing the welding rate or decreasing the probe length might reduce the hook defect size which played the significant role in the mechanical properties of the joints; however, these changes might lead to the formation of the bonding line defects. The kissing bond defects were produced at the two corner fillets under all the welding conditions. This means that they were independent of the welding parameters. The gap between tool probe and die may be reason for the formation of the kissing bond defects. The defects seem to be too hard to be minimized by applying only single-pass FSW. The welding rate of 100 mm/min and the probe length of 3.7 mm were chosen as the available welding regimes to make platform for the improvement of the dissimilar FSWed T-lap joints.

The quality of the interface morphology was significantly improved due to the application of the double-pass FSW induced by tool offset and reversed metal flow. By this new method, the defect size and the effective bonded width were improved without the insignificant change in welding temperature and hardness profile. Noting that, the best interface morphology of the joints was obtained by offsetting the tool probe toward advancing side (AS) with the distance of 0.8 mm. Particularly, the joint efficiency was reached approximately 90% in comparison with the strength of AA5083 base metal under the optimized condition. The above results were suitably interpreted by the tool position and asymmetric metal flow during the double-pass FSW process. It is also found that the gap distance between probe and die kept a key role in the interface formation.

The failure behavior of the optimized dissimilar T-lap joints was largely investigated under cyclic loading. The experimental results showed that the fatigue life of the joints was lower than that of the base alloys in both the skin and stringer loading tests. In the skin loading tests, the fatigue crack predominantly initiated at the weld toe. The visible result showed that the KB-closing at the interfaces during testing process might lead to the stress concentration at two weld toes. Regarding the stringer loading tests, however, the fatigue crack initiations was dominantly found in the interface of the

KBs, and then propagated obliquely to the skin AA5083 under mix-mode failure. Here, the KB interfaces were comfortably delaminated to form two crack shapes that might play an important role in the failure behavior of the T-lap joints.

In order to understand the present experimental results in systematically, a simplified fracture mechanics model was proposed via introducing a new parameter; “geometrical resistance factor of defects (GRFD)”. Here, the AA7075/AA5083 interface is represented by an equivalent defect or crack which is subjected to the corresponding equivalent stress intensity factor (SIF), and the increase in defect size is expressed by decrease in the GRFD, resulting in reduction in the allowable stress. The advantage of the double-pass FSW process could be rationalized by the GRFD parameter, which was also supported by the FEA. These works suggested that the optimization of the FSW can be achieved by minimizing the defect size, by increasing the GRFD, and by increasing the interface strength those can be attained by the change in the welding conditions via the control of metal flow in the FSW process.

This page has been intentionally left blank

DEDICATIONS

To my parents

DUONG V. HOANG & HUYNH T. HIEP

To my wife

VO T. NGOC YEN

To my children

DUONG GIA BINH

DUONG VU NHAT MINH

This page has been intentionally left blank

Acknowledgements

First of all, I would like to express my deep gratitude to my supervisor, Professor Okazaki Masakazu, who not only offered me the opportunity to learn and research at a reputable university but also guided me with his wisdom, fatherly support, and patience. I would like to thank to my supervisor, Professor Miyashita Yukio, who greatly supported me in last time of researching process. I sincerely express my hearties gratitude to Professor Tran Hung Tra (Nha Trang Universiy) for his vital supports, and valuable discussion during my research. I would also like to thank my doctoral committee; Prof. Sato (Tohoku University), Prof. Miyashita, Prof. Nanko, Prof. Nagasawa, and Prof. Homma for their reviews and recommences to help me to improve this dissertation.

Furthermore, I would like to thank my gratitude to Dr. Mr. Yamagishi (now of Niigata Institute of Technology) for his advices and technical assistances. I am also grateful to Mr. Thuyen (Nha Trang University) for his helping in FSW process. I would also like to recognize my colleagues, former and current members of Okazaki Lab., especially my tutor Mr. Fukushima and fellow PhD candidates; Mr. Rajivgandhi, Mr. Balavenkatesh, Mr. Hayashi, Mr. Yonakuni, and Mr. Tai. I am also grateful to the machine shop technicians who hugely supported me in the fabrication of the specimens during last time. I would like to acknowledge all staff of Nagaoka University of Technology for their helping in during time I research here.

Success of this dissertation has great contributions from my family; especially my parent, my wife, my daughter, and my son who always believe and encourage me in during last time. So, I would like to express me deep gratitude to their supports.

This study program was supported by the Japanese Government Scholarship, Ministry of Education, Culture, Sports, Science, and Technology (MEXT).

This page has been intentionally left blank

Contents

| | |
|--|-------------|
| Abstract | i |
| Dedications | v |
| Acknowledgements | vii |
| Contents | ix |
| List of Figures | xiii |
| List of Tables | xxi |
| Chapter 1 Introduction | 1 |
| 1.1 Advanced Aluminium Alloys and Challenges in Fusion Welding | 2 |
| 1.1.1 Advanced aluminum alloys | 2 |
| 1.1.2 Challenges in fusion welding technology | 2 |
| 1.2 Potential Friction Stir Welding Technology in Manufacturing Process | 3 |
| 1.2.1 Background about Friction Stir Welding (FSW)..... | 3 |
| 1.2.2 Friction Stir Welding of dissimilar metal joints | 5 |
| 1.2.3 Application of T-joints and its weldability by FSW technology..... | 5 |
| 1.2.3.1 Application of T-joint configuration | 5 |
| 1.2.3.2 Weldability of FSWed T-joints in literature..... | 6 |
| 1.3 Classification and Role of Defects in Mechanical Properties of FSWed Joints..... | 9 |
| 1.3.1 Classification of weld defects in FSW process | 9 |
| 1.3.2 Effects of defects on mechanical properties of FSWed joints | 10 |
| 1.4 Objectives of this Dissertation..... | 11 |
| 1.5 Dissertation Outline..... | 11 |
| 1.6 Chapter References | 13 |
| Chapter 2 Fundamental Formation of Interface Morphology and Mechanical Properties of Dissimilar Metal T-lap Joints between AA7075 and AA5083 by Single-pass Friction Stir Welding | 25 |
| 2.1 Introduction..... | 26 |
| 2.2 Effect of Welding Speed..... | 26 |
| 2.2.1 Experimental procedure | 26 |
| 2.2.2 Results and discussion | 29 |
| 2.2.2.1 Cross-section of T-lap joints..... | 29 |

| | | |
|---------|---|----|
| 2.2.2.2 | Role of welding speed on defect formation..... | 35 |
| 2.2.2.3 | Mechanical properties of T-lap joints..... | 36 |
| 2.3 | Effect of Probe Length | 43 |
| 2.3.1 | Experimental procedures..... | 43 |
| 2.3.2 | Results and discussion | 44 |
| 2.3.2.1 | Cross-section of T-lap joints..... | 44 |
| 2.3.2.2 | Role of probe length on defect formation..... | 45 |
| 2.3.2.3 | Mechanical properties of T-lap joints..... | 49 |
| 2.4 | Interface Morphology Affected by Welding Parameters | 55 |
| 2.4.1 | Quantification of defects affected by welding speed..... | 55 |
| 2.4.2 | Quantification of defects affected by probe length..... | 57 |
| 2.5 | Chapter Summary..... | 59 |
| 2.6 | Chapter References | 60 |

Chapter 3 Improvement of Interface Morphology and Mechanical Properties of Dissimilar Metal T-lap Joints between AA7075 and AA5083 by Double-pass Friction Stir Welding.....63

| | | |
|---------|---|----|
| 3.1 | Introduction..... | 64 |
| 3.2 | Experimental Procedure | 65 |
| 3.2.1 | Fabrication of FSWed T-lap joints | 65 |
| 3.2.2 | Process analysis | 66 |
| 3.3 | Experimental Results..... | 67 |
| 3.3.1 | Temperature during FSW process | 67 |
| 3.3.2 | Effects of reversed material flow and tool offset on microstructure of interface..... | 68 |
| 3.3.2.1 | Effect of reversed metal flow..... | 68 |
| 3.3.2.2 | Effect of tool offset..... | 70 |
| 3.3.3 | Mechanical properties of FSWed T-lap joints..... | 73 |
| 3.3.3.1 | Microhardness profile..... | 73 |
| 3.3.3.2 | Tensile test | 74 |
| 3.3.4 | Interface morphology affected by double-pass FSW and tool offset.... | 77 |
| 3.3.4.1 | Quantification of defects affected by double-pass FSW | 77 |
| 3.3.4.2 | Quantification of defects affected by tool offset..... | 78 |
| 3.4 | Discussion..... | 80 |
| 3.4.1 | Role of kissing bond defects on failure behavior of FSWed T-lap joints..... | 80 |
| 3.4.2 | Formation of kissing bond defects in during FSWed T-lap joints.... | 83 |

| | | |
|--|---|------------|
| 3.5 | Chapter Summary..... | 86 |
| 3.6 | Chapter References | 87 |
| Chapter 4 Fatigue Failure Behavior of Friction Stir Welded Dissimilar Metal | | |
| T-lap Joints between AA7075 and AA5083..... | | 89 |
| 4.1 | Introduction..... | 90 |
| 4.2 | Experimental Procedure | 91 |
| 4.2.1 | Fabrication of T-lap joints by applying double-pass FSW | 91 |
| 4.2.2 | Process analysis | 92 |
| 4.3 | Results and Discussion..... | 92 |
| 4.3.1 | Microstructure of a double-pass FSWed T-lap joints..... | 92 |
| 4.3.2 | Hardness distribution and tensile strength | 94 |
| 4.3.3 | Fatigue failure behavior of FSWed T-lap joints..... | 95 |
| 4.3.3.1 | Fatigue S-N curves | 95 |
| 4.3.3.2 | Fatigue crack initiation under skin fatigue test..... | 98 |
| 4.3.3.3 | Fatigue crack initiation under stringer fatigue test..... | 100 |
| 4.3.3.4 | Fracture morphology | 102 |
| 4.4 | Chapter Summary..... | 105 |
| 4.5 | Chapter References | 106 |
| Chapter 5 Numerical Model on Effect of Interface Morphology on Fracture | | |
| Behavior of FSWed T-lap Joints | | 109 |
| 5.1 | Introduction..... | 110 |
| 5.2 | Fracture Mechanic Concepts | 110 |
| 5.2.1 | Stress intensity factor (SIF) | 110 |
| 5.2.2 | A simplified model to describe the interface, or defect morphology... .. | 111 |
| 5.2.2.1 | Kinked edge crack in a semi-infinity plane | 111 |
| 5.2.2.2 | Single inclined edge crack plate loaded in tension..... | 112 |
| 5.2.2.3 | Double inclined edge crack plate loaded in tension | 113 |
| 5.2.3 | Stress components around a crack tip | 113 |
| 5.2.4 | Crack propagation direction criteria in mixed mode failure..... | 114 |
| 5.2.4.1 | Maximum tangential stress (MTS) criterion..... | 114 |
| 5.2.4.2 | Strain energy density (SED) criterion..... | 115 |
| 5.3 | Semi-Quantitative Discussion on Effect of Interface Morphology on Fracture Behavior of FSWed T-lap Joints..... | 116 |
| 5.3.1 | Effect of interface morphology in single-pass FSW..... | 116 |

| | | |
|---|--|------------|
| 5.3.2 | Effect of interface morphology in double-pass FSW | 119 |
| 5.4 | Finite Element Analysis (FEA)..... | 122 |
| 5.4.1 | Model and material description | 122 |
| 5.4.2 | FEA results | 124 |
| 5.4.3 | Prediction of crack growth angle under stringer test | 127 |
| 5.5 | Brief Summary..... | 128 |
| 5.6 | Chapter Summary..... | 129 |
| 5.7 | Chapter References | 130 |
| Chapter 6 Conclusions and Future Work..... | | 133 |
| 6.1 | Conclusions..... | 134 |
| 6.2 | Future Work..... | 136 |

List of Figures

| | |
|---|----|
| Figure 1-1 Schematic diagram of the FSW process | 4 |
| Figure 1-2 (a) Hull structure of ship [126] and (b) plate panel in ship structure [127]..... | 6 |
| Figure 1-3 Common FSWed T-Joint configurations: (a) T-butt joint, (b) T-lap joint, and (c) T-fillet joint..... | 7 |
| Figure 1-4 Large structural panels in transportation [132] | 7 |
| Figure 1-5 Comparison about joint efficiency between loading along skin and stringer in literature..... | 8 |
| Figure 1-6 Cross-sections of FSWed T-lap joints in literature [133,143]..... | 8 |
| Figure 1-7 Geometry of (a) zigzag line [146] and (b) hook defects in the joints [156]..... | 9 |
| Figure 1-8 Classification of defects in FSWed T-lap joints in this work | 10 |
| Figure 2-1 (a) Schematic view of T-lap joints and (b) detail geometry of welding tool | 28 |
| Figure 2-2 Global evaluation of T-lap joints by (a) skin and (b) stringer tensile tests | 28 |
| Figure 2-3 (a) Evaluation of local interface bonding strength, (b) miniature specimens were extracted from the sites [A] through [E], and (c) test system for loading process | 28 |
| Figure 2-4 Macrostructures on the cross-section of specimens produced by welding speed of (a) 50 mm/min and (b) 200 mm/min | 29 |
| Figure 2-5 Interface morphology of T-lap joints affected by various welding speeds..... | 30 |
| Figure 2-6 (a) Hook defect produced by welding speed of 50 mm/min and (b) oxide layer along hook defects | 31 |
| Figure 2-7 Illustration of formation of hook and kissing bond defects in T-lap joints at welding speed of 50 mm/min..... | 32 |

| | |
|--|----|
| Figure 2-8 Distribution of oxygen along KBs measuring at (a) RS and (b) AS (as marked in Figures 2-5(e-1,2), respectively) | 33 |
| Figure 2-9 (b-d) Bonding line defects along bonding interface compared to (a,e) KBs at welding speed of 100 mm/min..... | 34 |
| Figure 2-10 (a) SEM image and (b) EDS spectrum with inserting oxygen mapping around the bonding line defects..... | 34 |
| Figure 2-11 Bonding line defects produced under various welding conditions measured at center bonding interface..... | 34 |
| Figure 2-12 Influence of welding speed on the formation of each type of defect in T-lap joints | 35 |
| Figure 2-13 Effects of welding speed on hardness maps of (a) skin and (b) stringer plates | 36 |
| Figure 2-14 Local bonding strengths along interface with inserting fracture locations at welding speed of 50 mm/min..... | 37 |
| Figure 2-15 Effect of welding parameters on the bonding strength of interface measured at center | 38 |
| Figure 2-16 Mechanical properties of the full size joint by the skin test. (a) Stress-strain curves and (b) maximum ultimate tensile strength and rupture strain | 39 |
| Figure 2-17 Mechanical properties of the full size joint by the stringer test. (a) Load-displacement curves and (b) maximum load and displacement at maximum load..... | 40 |
| Figure 2-18 Failure behavior of specimens under skin tensile test in T-lap joints. (a-c) fracture location and (d-i) corresponding fractographies..... | 42 |
| Figure 2-19 (a) Fracture location and (b-e) fractography of FT4 at welding rate of 50 mm/min | 42 |
| Figure 2-20 (a) Fracture location and (b-o) fractography of FT5 at welding rate of 100 mm/min..... | 42 |
| Figure 2-21 (a) Schematic diagrams of FSWed T-lap joints and (b) tool probe geometry..... | 43 |

| | |
|---|----|
| Figure 2-22 Representative images of macrostructure of cross-section of T-lap joints produced by (a) Probe 1, (b) Probe 2, (c) Probe 3, and (d) Probe 4..... | 45 |
| Figure 2-23 Microstructure of cross-section of T-lap joints produced by Probe 4: (a) cross-section, (b) geometry of hook defects and KBs at RS, (c) bonding interface at center, (d) geometry of KBs at AS, and (e) bonding line defects at center marked in Figure 2-22(a) | 45 |
| Figure 2-24 Effect of probe lengths on size of defect and bonding interface | 47 |
| Figure 2-25 Schematic for determining probe penetration into workpieces..... | 47 |
| Figure 2-26 Effect of probe lengths on probe penetration | 48 |
| Figure 2-27 Schematic illustration of material flow produced by (a) probe length of 3.0 and (b) probe 3.7 in FSW process..... | 48 |
| Figure 2-28 Mechanical properties of skin tensile test: (a) Stress-strain curves and (b) maximum tensile strength and rupture strain..... | 50 |
| Figure 2-29 Fracture location of specimens produced by various probe lengths under skin tensile test..... | 50 |
| Figure 2-30 Two types of fracture: (a) Cracked “Lazy S”, (b) cracked at hook defects, (c-e) microstructure at KBs, hook defects and “Lazy S”, and (f,g) fracture surface of FT1 and FT2, respectively | 51 |
| Figure 2-31 Effect of probe lengths on effective skin thickness | 51 |
| Figure 2-32 (a) Load-displacement curves and (b) maximum load and displacement at rupture under stringer tensile test | 53 |
| Figure 2-33 Fracture location of specimens produced by various probe lengths under stringer tensile test..... | 54 |
| Figure 2-34 (a) Location of miniature specimen extracted from original samples and (b) effect of probe lengths on bonding strength of interface | 54 |
| Figure 2-35 (a-d) Specimens before testing, (e-h) microstructure along interface, and (i-m) fracture location of specimens produced by various probe lengths | 54 |
| Figure 2-36 (a-c) Macro- and (d-f) micro-morphology of fracture surface of specimens produced by various probe lengths | 55 |

| | |
|--|----|
| Figure 2-37 Define some parameters of quantification of defects | 56 |
| Figure 2-38 Effect of the welding speeds on quantification of defects at (a) the RS, (b) the AS, and (c) effective ligament ratio, t/T | 57 |
| Figure 2-39 Effect of the probe length on quantification of defects at (a) the RS, (b) AS, and (c) effective ligament ratio, t/T | 58 |
| Figure 3-1 (a) Schematic view of FSWed T-lap joints and (b) dimension of welding tool..... | 66 |
| Figure 3-2 (a) Schematic diagrams of tool offset and reversed metal flow and the positions of welding tool at offsetting (b) -0.8 mm, (c) 0.0 mm, and (d) 0.8 mm..... | 66 |
| Figure 3-3 Evaluation of T-lap joints: (a) skin and (b) stringer tensile tests | 67 |
| Figure 3-4 (a) Temperature history at the AS and RS of first- and second-pass welding at tool offset of 0.0 mm and (b) peak temperature under various distances of tool offset | 68 |
| Figure 3-5 Macrostructure of welding interface produced by (a) single- and (b) double-pass FSWs at offsetting 0.0 mm | 69 |
| Figure 3-6 Microstructures of KBs and bonding interface produced by (a,b) single- and (c,d) double-pass FSWs at offsetting 0.0 mm | 69 |
| Figure 3-7 Effect of reversed material flow on (a) curve lengths of KBs and (b) effective bonded width produced by single- and double-pass FSWs | 70 |
| Figure 3-8 (a-d) Macro- and (e,f) micro-structures of welding interface produced under various distances of tool offsets..... | 71 |
| Figure 3-9 Effect of tool offset on the curve length of KBs and effective bonded width..... | 72 |
| Figure 3-10 (a) Effect of various welding conditions on hardness profile along skin parts | 73 |
| Figure 3-10 (b) Effect of various welding conditions on hardness profile along stringer parts..... | 74 |
| Figure 3-11 Strength of the joints under the skin tensile test: (a) nominal stress- strain curves and (b) maximum nominal stress and rupture strain | 75 |

| | |
|--|----|
| Figure 3-12 Strength of the joints under the stringer tensile test: (a) load-displacement curves and (b) maximum load and displacement at rupture | 76 |
| Figure 3-13 Local bonding strength distributed along interface produced by offsetting 0.8 mm..... | 77 |
| Figure 3-14 Fracture location of miniature specimens along interface produced by offsetting 0.8 mm..... | 77 |
| Figure 3-15 (a) Define some parameters of quantification of interface and effect of double-pass on these parameters at (b) AS and (c) RS..... | 78 |
| Figure 3-16 (a) Define some parameters of quantification of interface and effect of tool offset on these parameters of interface at (b) RS1/AS2 and (c) AS1/RS2..... | 79 |
| Figure 3-17 Strain maps of specimens produced by (a) offset -0.8 and (b) 0.8 mm from DIC measurement under skin tensile test | 81 |
| Figure 3-18 Effect of distances of tool offset on the effective skin thickness t , effective bonded width W , and effective ligament ratio t/T | 81 |
| Figure 3-19 Relationship between load-displacement curve and fracture location of stringer tensile test..... | 82 |
| Figure 3-20 Quantitative comparison in some values of kissing bond size measured based on fracture surface and oxide layer | 82 |
| Figure 3-21 Fracture morphology of specimen produced by offset -0.8 mm | 83 |
| Figure 3-22 Schematic illustration of material flow in single-pass FSW process..... | 84 |
| Figure 3-23 Schematic illustration of KB formation in the double-pass FSW by the tool offsets of (a) -0.8 and (b) 0.8 mm | 84 |
| Figure 3-24 Schematic illustration of probe penetration into corner fillets at the various distances of tool offset..... | 85 |
| Figure 3-25 Relationship between the representative KBs distance and the gap distance..... | 85 |
| Figure 4-1 (a) Schematic diagrams of tool offset, (b) location of welding tool in reversed metal flow and (c) welding tool geometry (AS1, RS1 and AS2, RS2: advancing side and retreating side of first-pass and second-pass in double-pass welding, respectively) | 91 |

| | |
|---|-----|
| Figure 4-2 Specimen geometry and evaluation of T-lap joints under (a) skin and (b) stringer fatigue tests..... | 92 |
| Figure 4-3 Representative image of microstructure at cross-section..... | 93 |
| Figure 4-4 (a) Curve length and (b) angle of KBs at the RS1/AS2 and AS1/RS2 | 94 |
| Figure 4-5 Hardness profile along cross-section of skin plate | 95 |
| Figure 4-6 S-N curves of the T-lap joints under skin and stringer fatigue tests..... | 97 |
| Figure 4-7 (a) Maximum tensile strength and fatigue strength under skin and stringer tests..... | 97 |
| Figure 4-7 (b) Relationship between tensile and fatigue strength presented by value of coefficient m | 98 |
| Figure 4-8 Representative images of specimens cracked at (a) KB-RS2 and (b) WT-AS2 | 99 |
| Figure 4-9 (a) Schematic diagrams for determining EST and (b) the value of EST at various locations | 100 |
| Figure 4-10 Images of specimens failed under stringer fatigue loading at (a) $\Delta\sigma = 18.3$ MPa, (b) $\Delta\sigma = 16.1$ MPa, and (c) $\Delta\sigma = 14.6$ MPa..... | 101 |
| Figure 4-11 Effect of stress on KB-opening | 102 |
| Figure 4-12 Fracture morphology of specimen cracked at KB-RS2 under skin fatigue test | 103 |
| Figure 4-13 Fracture morphology of specimen cracked at weld toe under skin fatigue test | 103 |
| Figure 4-14 Fracture morphology of specimen S16 cracked at KB-RS2 under stringer fatigue test..... | 104 |
| Figure 5-1 Three types of failure modes in fracture mechanics | 111 |
| Figure 5-2 Kinked edge crack in a semi-infinity plane under uniform tension, a simplified model of the skin test..... | 112 |
| Figure 5-3 Single inclined edge crack plate loaded in tension, a simplified model of the stringer test | 112 |

| | |
|--|-----|
| Figure 5-4 Double inclined edge cracks plate loaded in tension, a simplified model of the stringer test | 113 |
| Figure 5-5 Stress components in (a) Cartesian co-ordinate and (b) polar co-ordinate systems..... | 114 |
| Figure 5-6 Comparison crack size between RS and AS affected by (a) welding speed and (b) probe length | 116 |
| Figure 5-7 Effect of (a) welding speed and (b) probe length on GRFD under skin test..... | 118 |
| Figure 5-8 Effect of welding speed on GRFD under stringer test..... | 118 |
| Figure 5-9 Comparison crack size between AS1/RS2 and RS1/AS2 affected by tool offset..... | 120 |
| Figure 5-10 Effect of various welding conditions on (a) cross-section, (b) crack length, and (c) simple mechanical model in fracture of FSWed T-lap joints | 120 |
| Figure 5-11 Normalized SIFs, F in three mechanical modes..... | 121 |
| Figure 5-12 Effect of tool offset on GRFD under skin test..... | 121 |
| Figure 5-13 Effect of tool offset on GRFD under stringer test | 122 |
| Figure 5-14 Model of specimen for FEA..... | 123 |
| Figure 5-15 Image of meshing model of specimen S12 | 123 |
| Figure 5-16 (a,b) Von-Mises equivalent stress distribution and (c,d) normal stress (X axis) around two crack tips at RS1/AS2 and AS1/RS2 | 125 |
| Figure 5-17 Effect of crack tip angle at AS1/RS2 on the SIFs | 126 |
| Figure 5-18 (a) Crack tip angle at AS1/RS2 measured on specimens and (b) effect of crack tip angle on the fatigue life of T-lap joints | 126 |
| Figure 5-19 Comparison in crack initiation angle between prediction and experiment..... | 128 |

This page has been intentionally left blank

List of Tables

| | |
|---|-----|
| Table 1-1 Previous researches on FSWed T-lap joints | 8 |
| Table 2-1 Chemical compositions (wt%) of AA5083 and AA7075..... | 27 |
| Table 2-2 Mechanical properties of AA5083 and AA7075 | 28 |
| Table 2-3 Summary influence of defects on failure of T-lap joints | 43 |
| Table 2-4 Main dimensions of various probes | 44 |
| Table 3-1 Welding tool geometry and investigated location | 66 |
| Table 4-1 Tensile strength of T-lap joints..... | 95 |
| Table 4-2 Fatigue experiment data of skin and stringer fatigue tests..... | 96 |
| Table 5-1 Mechanical properties of AA5083 and AA7075 for FEA model..... | 123 |
| Table 5-2 Stress intensity factor at two crack tips..... | 125 |
| Table 5-3 Stress intensity factor and crack initiation angle at AS1/RS2 | 127 |

This page has been intentionally left blank

Chapter 1

Introduction

A brief introduction to challenge in fabricating T-joint configuration by traditional fusion welding is presented in this chapter. The basic knowledge and advantages of Friction Stir Welding (FSW) technology are exhibited. The limitation of the weldability of the FSWed T-joints in literature is highlighted. Based on literature inspections, the role of some defects on the mechanical properties of the FSWed joints is indicated. Finally, the objectives and dissertation outline of this work are indicated.

1.1 Advanced Aluminum Alloys and Challenges in Fusion Welding

1.1.1 Advanced aluminium alloys

Aluminum alloys are one of the light metals that are widely applied in the structural components such as the shipbuilding, automotive, railway, and aerospace industries [1]. The high strength to weight ratio, good hot formability, and good corrosion resistance are considered as the best properties of them [2-7]. Two advanced aluminum alloys that contained the highest strength and the best corrosion resistance are AA7075 and AA5083, respectively.

AA7075 is one of the heat treatable aluminum alloys that respond to strengthening by heat treatment. The major elements of AA7075 include zinc, magnesium, and copper. The precipitation of Mg_2Zn and Al_2CuMg phases derives a high strength [8]. Due to the high strength, it has specially high reaction to natural age hardening that makes it a great selection for a number of aircraft structure, military vehicles, bridges, *etc* [5,6,9]. Moreover, this alloy is sensitive to welding temperature [10]. So, welding of this alloy can reduce the strength of the joints. The enhancement in the strength properties in these alloys depends on age-hardening phenomena [6,7]. One of the other limitations of this alloy is difficulty to apply fusion welding technology because it is extremely sensitive to solidification cracking [11].

In contrast, AA5083 is one of the non-heat treatable aluminum alloys that respond to strengthening by cold working or strain hardening. It exhibits the best property of corrosion resistance to salt-water and the marine atmosphere, moderate mechanical properties and a high fatigue fracture resistance [12]. Dissimilar to AA7075, this alloy can weld well by traditional fusion welding without hot cracking phenomenon. Due to the good properties, it is used for the production of welded components for shipbuilding and railway vehicles, structure panels and platforms for boats and trains, storage tanks, pressure vessels, *etc*. [5,7,12].

1.1.2 Challenges in fusion welding technology

Fusion welding technology is well known as one of the common methods to join metal. It is widely applied in welding techniques for many various materials. Some methods are known as arc welding, gas welding, radiant energy welding, and resistance welding, *etc*. In these methods, the materials are heated to a melting temperature before

they are diffused each other [13]. It is true that these techniques are generally difficult to apply for the light metal alloys. For example, the joint of titanium alloys produced conventional welding method frequently occur porosity, hot cracking, distortion, and high residual stress [14-17]. A similar result was also found in the joints of magnesium alloys [18-22]. These undesirable defects were almost formed in the fusion welding of aluminum alloys and were investigated by many researchers [22-31]. Specially, the solidification cracking of aluminum alloys of 7xxx and 2xxx series are more susceptible than that of other series [24,32-34]. This result might be related to high solidification temperature, coefficient of thermal expansion, shrinkage stresses, and tendency to form low-melting constituents [24]. Consequently, the mechanical properties of the joints might be drastically reduced by these defects [35-37].

In addition, one of the greatest challenges in fusion welding lies at dissimilar joints that have been applying widely in many manufacturing fields. Here the best characteristics of dissimilar materials are optimized for various purposes [38]. However, the success of dissimilar joints can be affected strongly by the differences in melting temperature, the thermal conductivity, and the electrochemical potential of the different materials. As a result, a brittle intermetallic compounds may be formed along interface, resulting in reducing the strength of the joints [39]. In spite of that, the difficulties associated with conventional welding can be improved by the solid-state joining process that has been broadly applied in near decades.

1.2 Potential Friction Stir Welding Technology in Manufacturing Process

1.2.1 Background about Friction Stir Welding (FSW)

Friction Stir Welding (FSW) that was invented by The Welding Institute (TWI) in 1991 is one of the solid-state welding technologies [40]. This technique uses frictional heat induced by rotating tool to weld materials. It means that the welding temperature during FSW process is lower than the melting temperature of base materials [41-44]. The schematic diagram of the FSW process is shown in Figure 1-1. Here, a non-consumable welding tool involves probe and shoulder, those are specially designed, is applied to insert into workpieces [41]. Due to the rotational welding tool, the frictional heating was generated to soften the metal. Thereby, the material can move around tool probe to mix and bond each other under the solid-state [41,45-51]. In order to create

reasonable heat input, controlling the welding parameters in terms of welding speed, rotational speed, tool geometry, *etc.* played important role during the FSW process. So, the influences of these parameters on heat input [52-57], microstructure, and the mechanical properties [58-69] of the joints were noticed in the former researches.

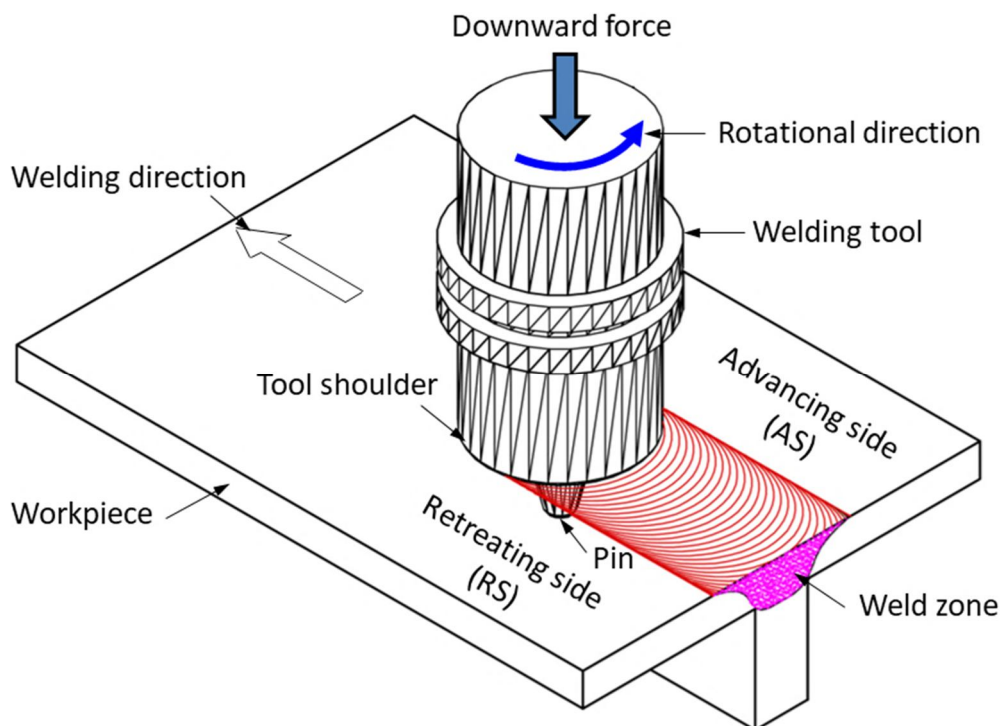


Figure 1-1 Schematic diagram of the FSW process.

The FSW has been considered as one of the advanced technologies in the near decades [41]. Unlike the conventional welding methods, the FSW do not use filler metal, cover gas or flux that may cause environmental pollution [41,42]. Thereby, the FSW is considered as green technology and environmental friendliness [41,70]. Due to low welding temperature, furthermore, the joints were obtained with a low distortion [70,71], low residual stress [72-74], and fine microstructure [37,75-81]. Consequently, the joint efficiencies might be reached larger than 90% compared to the base strengths that were applied for different materials such as aluminum [82-85], magnesium [86-89], copper [90-92], steel [93,94], and titanium alloys [95-98]. Based on these findings, the FSW technology has been commercially employed in a large amount of various industries such as automotive, shipbuilding [99-101], high-speed train manufacturing [99,101], aerospace [102], and railway [101,103].

1.2.2 Friction Stir Welding of dissimilar metal joints

In recent years, the structural weight and material saving are one of the great interesting of manufacturers, especially in aerospace industry [104,105]. The applications of lightweight alloys and dissimilar metal joints are considered as two of the solutions to approach these goals. However, it is not easy to attain a good dissimilar metal joint by utilizing traditional fusion welding technique [106]. Because of significant difference in material properties and welding temperature may produce the interfaces with brittle intermetallic compound characteristics that reduce the strength of joints [107-110]. Unlike the traditional fusion welding, the low welding temperature and special mechanism formation of the FSW may produce sound dissimilar metal joints between aluminum alloys and some other metals such as titanium alloys [111-113], copper alloys [114,115], or steels [116,117].

The FSW of dissimilar aluminum alloys was early investigated in literature [118-121]. Recently, the combination of a non-heat treatable aluminum alloy 5083 (known as an excellent corrosion resistance) and a heat treatable aluminum alloy 7075 (known as a high strength and light density) was noted. These results showed that the high efficiency of a defect-free but-joint might be obtained about 87-100% in comparison with the base strength [66,122,123]. This means that the application of the FSW technology can substitute the conventional method as fusion welding and rivet to join these alloys. In spite of this, the success of the FSWed lap-joints of two alloys has not been verified in literature.

1.2.3 Application of T-joints and its weldability by FSW technology

1.2.3.1 Application of T-joint configuration

The T-joints composed stringer and skin plates is one of the common junctions in the structures of railway tankers, aircraft wing-box and ship panel [42,124]. Particularly, in order to decrease the weight of structure, the structural panel plate that was widely used in hull structure of ship was combined between longitudinal bars (stringer) and shell plate (skin) as shown in Figure 1-2 [125-127]. It is well known that the maximum stress in the stringer is much higher than that in the skin under bending load. In addition, the skin covers outside and contacts directly to the seawater environment. So, the stringer is often designed as strong web while the skin is a light plate. A reasonable combination of dissimilar joint with high durability for stringer and good corrosion

resistance for skin may be suitable for these kinds of structures. It is well known that non-heat treatable aluminum alloy 5083-H116 possesses an excellent corrosion resistance and commonly applied in shipbuilding. Meanwhile heat treatable aluminum alloy 7075-T651 possesses a highest strength and light density but it is difficult to apply fusion welding [5]. The success in combination between these alloys is platform for producing plate panel structure employed in shipbuilding industry.

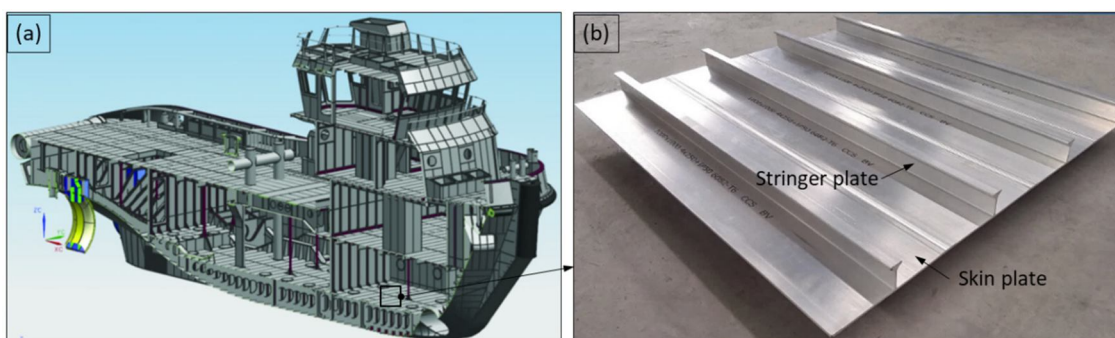


Figure 1-2 (a) Hull structure of ship [126] and (b) plate panel in ship structure [127].

1.2.3.2 Weldability of FSWed T-joints in literature

The application of fusion welding technologies to fabricate the T-joints was investigated in some earlier researches [37,128,129]. In spite of these, the strength of the joints was low due to the undesirable occurrence of porosity, coarse microstructure grain, and lack of wetting. Moreover, this technology is too difficult to employ for aluminum alloys of 7xxx and 2xxx series [23,32-34].

The weldability of the similar and dissimilar FSWed T-joints has been early investigated in literature [130,131]. Recently, there are three common methods used to fabricate the FSWed T-joints, i.e. T-butt joint, T-lap joint, and T-fillet joint, as seen in Figure 1-3. Among these methods, the T-lap joint is considered as the fastest and simplest methods [41]. In addition, the application of this method is more convenient for producing large structural panels in transportation (Figure 1-4) [132].

From above overviews, it seems that the most special attentions from the former researchers have been focused on the FSWed T-lap joints [133-142]. However, the strength of the joints in these researches was not satisfactory. To improve the T-lap joint efficiency, the influences of some FSW parameters such as welding and rotational speeds [133-135,137], and welding tool [136,137] as well as the metal flow [138,139] have been explored. In spite of these changes, the T-lap joint efficiency has still been

low, especially in stringer loading test, as presented in Table 1-1 and Figure 1-5. This result is due to the undesirable formation of some defects in the T-lap joints. As shown in Figure 1-6, the frequent presences of tunnel, oxide line, and kissing bond defects (KBs) might degrade the strength of the joints. The formation of the KBs at two corner fillets, especially at retreating side (RS) seems to be too difficult to eliminate in comparison with other defects. Some authors applied the T-fillet joints that penetrated tool probe into two corner fillets to eliminate this kind of defects [140-142]. Despite this method is a suitable solution, it is too difficult to employ widely in manufacturing process because of complex welding tool and clamping fixture. Recently, Feistauer and co-worker applied the second FSW pass that was the same direction of rotational tool but the opposite welding direction with first welding pass to minimize the KBs [143]. Consequently, the KBs size was impressively decreased and significantly improved the strength of the T-lap joints. From these works, it is clearly that the welding interface might be kept a key role in the strength of the FSWed T-lap joints. In spite of this, the formation of welding interface in terms of the KBs and bonding characteristics in both single- and double-pass welding has not been understood in these works.

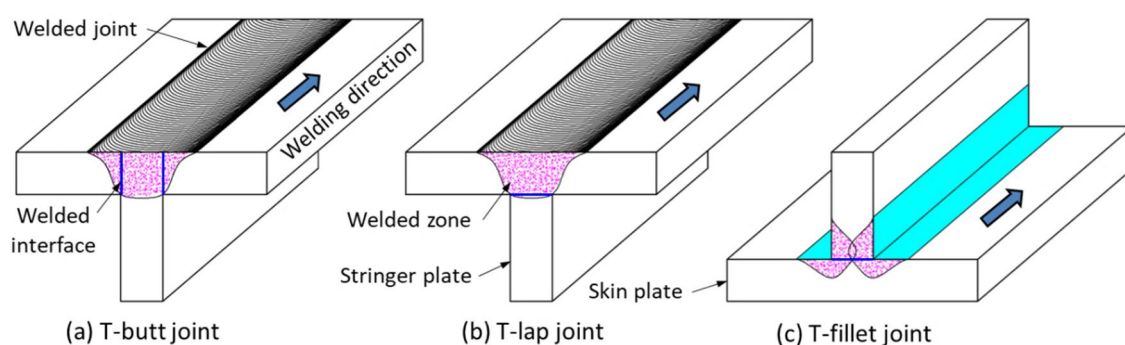


Figure 1-3 Common FSWed T-joint configurations: (a) T-butt joint, (b) T-lap joint, and (c) T-fillet joint.



Figure 1-4 Large structural panels in transportation [132].

Table 1-1 Previous researches on FSWed T-lap joints.

| Skin | | Stringer | | Joint efficiency | | References |
|-----------|-----------|-----------|-----------|--------------------|------------------------|------------|
| Materials | Thickness | Materials | Thickness | Loading along skin | Loading along stringer | |
| AA2024 | 2.3 mm | AA7075 | 2.8 mm | N/A | 72% | [130] |
| AA2198 | 3.0 mm | AA6056 | 6.0 mm | 63% | 61% | [131] |
| AA6061 | 3.0 mm | AA6061 | 3.0 mm | 75% | 55% | [133] |
| AA6013 | 2.5 mm | AA6013 | 2.5 mm | 68% | 53% | [134] |
| AA6082 | 3.0 mm | AA6082 | 3.0 mm | 56% | N/A | [135] |
| AA5083 | 3.0 mm | AA5083 | 3.0 mm | 87% | N/A | [137] |
| AA6082 | 3.0 mm | AA6082 | 3.0 mm | 50% | N/A | [137] |
| AA5083 | 6.0 mm | AA5083 | 6.0 mm | 88% | 53% | [143] |

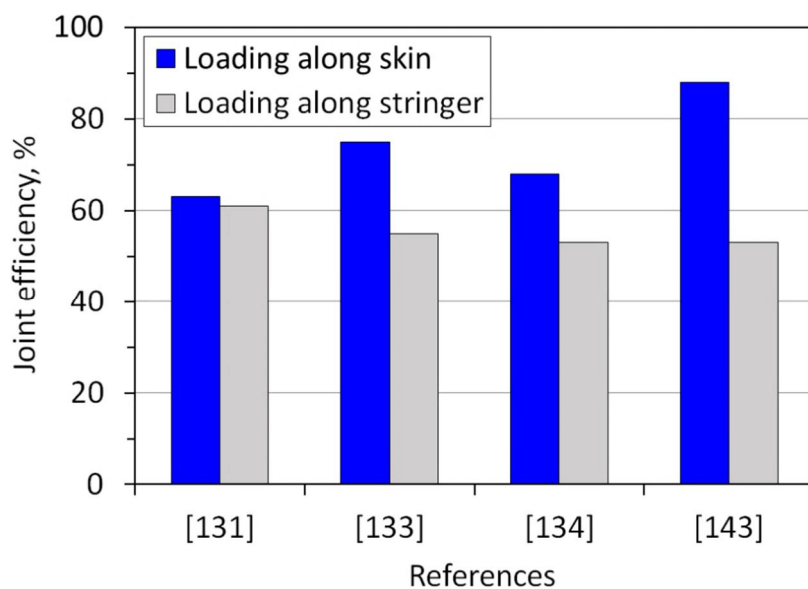


Figure 1-5 Comparison about joint efficiency between loading along skin and stringer in literature.

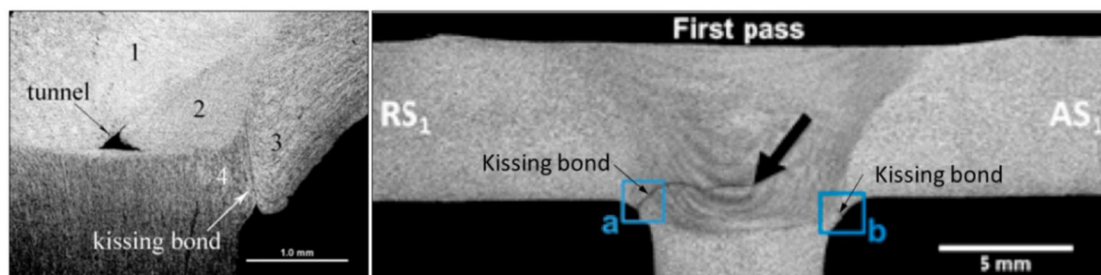


Figure 1-6 Cross-sections of FSWed T-lap joints in literature [133,143].

1.3 Classification and Role of Defects in Mechanical Properties of FSWed Joints

1.3.1 Classification of weld defects in FSW process

Despite the FSW technology has many advantages in producing the good joint; it does not always make defect free joints [144]. The selection of optimal welding parameters to obtain a defect free and high strength of the joints is a challenge in the FSW process. This means that some internal defects fluently appear inside the joints. The appearance of natural oxide film on the surfaces of materials can lead to the formation of a discontinuous, wavy line after welding those often refer to as the weld defects [145]. However, the classification of these defects is not clearly established and unified in the literature [145]. For example, it has been mentioned to as zigzag line [146-148] (Figure 1-7(a)), joint line remnant (JLR) [145,149,150], lazy S [151,152], or kissing bond (KB) [153-155]. Moreover, some defects formed in the FSW lap-joint have been referred to as hook [156] (Figure 1-7(b)), kissing bond [143] (Figure 1-6), or cold lap defects [157].

In this research, welding interface with some dark lines was found along interface. Dark line seems to be remnant of initial interface, but its fragmentation degree might be not same. This result might lead to difference in the bonding strength of interface. With the aim for improving interface morphology, the classification and notation of defects will be carried out based on the fragmentation degree of initial interface that seems to be relationship to the location of interface, as illustrated in Figure 1-8. Here, the interface locates outside stirred zone is referred to as kissing bond defects that were also mentioned in literature [133,134,137]. The interface locates inside the SZ with hook geometry is referred to as a hook defects that are often observed in the FSWed lap-joint [156,157]. The other interface located inside the SZ with oxide film is referred to as bonding line defects. A cavity is also found in the SZ at advancing side (AS) is denoted as tunnel defects. These defects will be discussed in the next chapter.

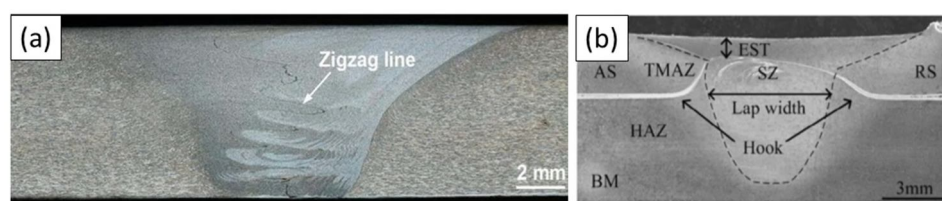


Figure 1-7 Geometry of (a) zigzag line [146] and (b) hook defects in the joints [156].

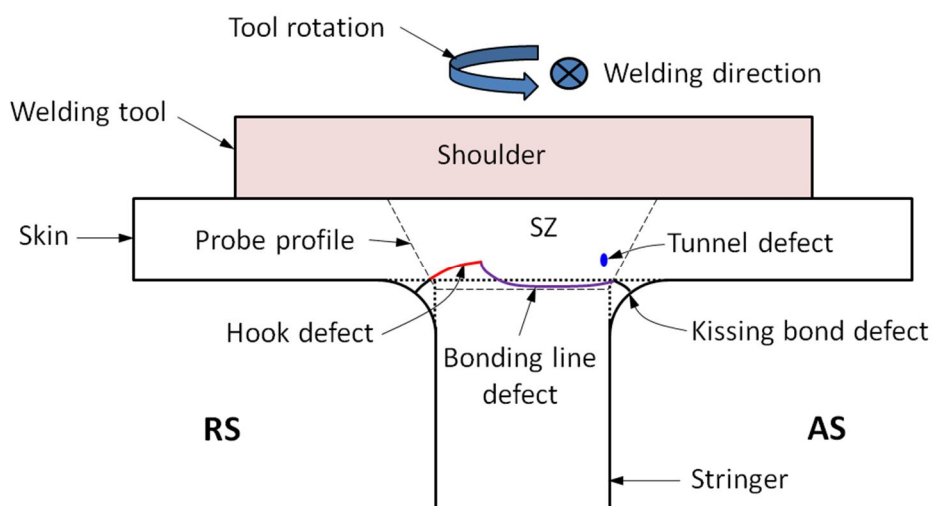


Figure 1-8 Classification of defects in FSWed T-lap joints in this work.

1.3.2 Effects of defects on mechanical properties of FSWed joints

The low strength of the FSWed joints had a big contribution of some internal defects those were formed inside the joints. These defects might decrease up to 50% of joint efficiency [133,134,143]. So, the effect of the weld defects on the failure behavior of the FSWed joints have been one of the attractive issues with respect to researchers [145,150,153-157]. Several papers showed that the crack path might appear along the KBs in some welding regimes [154,155]. The fatigue life of joints contained the KBs was 21-43 times smaller than that of the joints without the KBs [155]. However, Kadlec et al. [153] found that a big size of the KBs was insignificant influence on the strength of the joints compared to flawless.

The significant effect of defects on the strength of the FSWed T-lap joints was found in literature [133-139,143]. The low strength of the joint had the big contribution of tunnel, kissing bond or bonding line defects [133,134,137,143]. Especially in applying load along stringer part, most of the defects affected the strength of the joints, resulting in reduction in joint efficiency, compared to applying load along skin part (Table 1-1). So, minimizing or eliminating the defects is one of the vital problems in fabricating the FSWed T-lap joints to advance the mechanical properties.

1.4 Objectives of this Dissertation

The main goal of this work is to investigate the interface morphology and fracture behavior of the FSWed dissimilar metal T-lap joints of aluminum alloys, those make platform for the improvement of the mechanical properties of the joints. In order to approach these goals, the primary work is to fabricate the FSWed T-lap joints between AA7075-T651 (denoted as AA7075) and AA5083-H116 (denoted as AA5083) to reveal the fundamental formation of welding interface between skin and stringer parts. The initial attention was put on how to produce a good interface by controlling the FSW parameters to minimize or eliminate the defects formed along interface. The reduction in the strength of the joints by these defects was discussed. Based on these findings, an advanced method was suggested to improve the interface morphology and the mechanical properties of the T-lap joints. Thereafter, the fracture behavior of the optimized joints was largely explored under cyclic loading in both skin and stringer tests. In order to clarify the present experimental results in systematically, a simplified fracture mechanics model was also proposed via introducing a new parameter; “geometrical resistance factor of defects (GRFD)”. The role of interface morphology in terms of the size and orientation of the defects in the fracture behavior of the joints was addressed. A prediction of crack direction under stringer fatigue test was presented.

1.5 Dissertation Outline

The interface morphology and the fracture behavior of the FSWed T-lap dissimilar metal joints between AA7075 and AA5083 have been investigated in this work. Dissertation is arranged in six chapters as following:

Chapter 1: The challenge of the traditional fusion welding technologies is highlighted. A background about FSW technique and its weldability in dissimilar joints and T-lap joints is summarized. The effect of defects on the mechanical properties of the FSWed joints is given.

Chapter 2: Dissimilar metal T-lap joint between two aluminum alloys AA7075 and AA5083 is fabricated by traditional single-pass FSW. The fundamental formation of welding interface between skin and stringer parts affected by welding parameters in terms of welding speed and tool geometry is investigated in this chapter. The effect of some undesirable defects formed along interface on the strength of the joints is

addressed. Based on these findings, the some available parameters are selected to make platform for the improvement of the dissimilar FSWed T-lap joints.

Chapter 3: The improvement of the interface morphology and mechanical properties of the dissimilar T-lap joints between AA7075 and AA5083 is carried out by applying double-pass FSW. The special attention is put on the effects of reversed metal flow and tool offset on the formation of the interface morphology in terms of the kissing bond defects and effective bonded width. The performance of the joints is evaluated by both skin and stringer tensile tests. The local deformation of the joints is shown by applying a digital image correlation (DIC) system that is connected to the tensile test machine. The formation mechanism of welding interface in this new method is obviously discussed in this chapter.

Chapter 4: The fracture behavior of the dissimilar FSWed T-lap joints between AA7075 and AA5083 that is optimized in Chapter 3 is investigated under cyclic loading in both skin and stringer tests. The fatigue life and fatigue crack initiation of the joints are indicated. The fracture morphology of the specimens under the skin and stringer tests was observed by means of scanning electron microscopy (SEM). The effect of kissing bonds in terms of the orientation and bonding strength on the fatigue life and fatigue crack initiation of the joint are addressed.

Chapter 5: The effect of interface geometry on fracture behavior of the FSWed T-lap joints under skin and stringer tests is explored in this chapter. In order to consider the unified treatment for the present experimental results, a simplified fracture mechanics model is proposed via introducing a new parameter; “geometrical resistance factor of defects (GRFD)”. Here, the AA7075/AA5083 interface is presented by an equivalent defect or crack which is subjected to the corresponding equivalent stress intensity factor (SIF). The roles of the interface geometries in terms of the size and orientation of the defects on the GRFD parameter are addressed. The Finite Element Analysis (FEA) is applied to elucidate the failure behavior of the T-lap joints. In addition, the crack direction under mixed mode failure is predicted by the Maximum Tangential Stress (MTS) criterion.

Chapter 6: Conclusions derived from this work and suggestions for future work are exhibited to end of this dissertation.

1.6 Chapter References

- [1] Monteiro, W. A., *Light Metal Alloys Applications*, In Tech, (2014).
- [2] Zhang, X., Chen, Y., and Hu, J., Recent advances in the development of aerospace materials, *Progress in Aerospace Sciences*, Vol.97, (2018), pp.22-34.
- [3] Heinz, A., Haszler, A., Keidel, C., Moldenhauer, S., Benedictus, R., and Miller, W., Recent development in aluminium alloys for aerospace applications, *Materials Science and Engineering: A*, Vol.280(1), (2000), pp.102-107.
- [4] Barnes, A.J., Raman, H., Lowerson, A., and Edwards, D., Recent Application of Superformed 5083 Aluminum Alloy in the Aerospace Industry, *Materials Science Forum*, Vol.735, (2012), pp.361-371.
- [5] Davis, J.R., *Aluminum and aluminum alloys*, ASM International, pp.351-416, (2001).
- [6] Shah, P.H, Vishvesh Badheka, An experimental investigation of temperature distribution and joint properties of Al 7075 T651 friction stir welded aluminium alloys, *Procedia Technology*, Vol.23, (2016), pp.543-550.
- [7] ASM Handbook, *Properties of Wrought Aluminum and Aluminum Alloys ASM Handbook*, Vol.2: Properties and Selection: Nonferrous Alloys and Special-Purpose Materials, (1990), pp.62-122.
- [8] Rajakumar, S., Muralidharan, C., Balasubramanian, V., Influence of friction stir welding process and tool parameters on strength properties of AA7075-T6 aluminium alloy joints, *Materials & Design*, Vol.32, (2011), pp.535-49.
- [9] Scott MacKenzie, D., Heat treating aluminum for aerospace applications, *Heat Treat. Prog*, Vol.5, (2005), pp.37-43.
- [10] Cole, E.G., Fehrenbacher, A., Duffie, N.A., Zinn, M.R., Pfefferkorn, F.E., & Ferrier, N.J., Weld temperature effects during friction stir welding of dissimilar aluminum alloys 6061-T6 and 7075-T6, *The International Journal of Advanced Manufacturing Technology*, Vol.71(1-4), (2013), pp.643-652.
- [11] Gene Mathers, *The welding of aluminium and its alloys*, Woodhead Publishing Ltd., (2002).
- [12] Damjan Klobar, Ladislav Kosec, Adam Pietras, Anton Smolej, Friction stir welding of aluminium alloy 5083, *Materials and technology*, Vol.46, (2012) pp.483-488.
- [13] Mandal, N.R., *Fusion Welding Methods*. In: *Ship Construction and Welding*, Springer Series on Naval Architecture, Marine Engineering, Shipbuilding and Shipping, Vol.2, (2017).
- [14] Christoph, L., Manfred, P. *Titanium and Titanium Alloys-Fundamentals and Application*, 1st ed., Wiley-VCH, Weinheim, Germany, (2003).
- [15] Yi, H.-J., Lee, Y.-J., and Lee, K.-O., TIG Dressing Effects on Weld Pores and Pore Cracking of Titanium Weldments, *Metals*, Vol.6(10), (2016), pp.243.
- [16] Huang, J.L., Warnken, N., Gebelin, J.-C., Strangwood, M., and Reed, R.C., On the mechanism of porosity formation during welding of titanium alloys, *Acta Materialia*, Vol.60(6-7), (2012), pp.3215-3225.

- [17] Blackburn, J.E., Allen, C.M., Hilton, P.A., Li, L., Hoque, M.I., and Khan, A.H., Modulated Nd: YAG laser welding of Ti-6Al-4V, *Science and Technology of Welding and Joining*, Vol.15(5), (2010), pp.433-439.
- [18] Chen, M., Xu, J., Xin, L., Zhao, Z., Wu, F., Ma, S., and Zhang, Y., Effect of keyhole characteristics on porosity formation during pulsed laser-GTA hybrid welding of AZ31B magnesium alloy, *Optics and Lasers in Engineering*, Vol.93, (2017), pp.139-145.
- [19] Yu, Z., Yan, H., Yin, X., Li, Y., and Yan, G., Liquefaction cracking in laser beam welded joint of ZK60 magnesium alloy, *Transactions of Nonferrous Metals Society of China*, Vol.22(12), (2012), pp.2891-2897.
- [20] Sun, D.X., Sun, D.Q., Gu, X.Y., and Xuan, Z.Z., Hot Cracking of Metal Inert Gas Arc Welded Magnesium Alloy AZ91D, *ISIJ International*, Vol.49(2), (2009), pp.270-274.
- [21] Liu, K., and Kou, S., Susceptibility of magnesium alloys to solidification cracking, *Science and Technology of Welding and Joining*, (2019), pp.1-7.
- [22] Kou, S., Firouzdor, V., and Haygood, I.W., Hot Cracking in Welds of Aluminum and Magnesium Alloys, *Hot Cracking Phenomena in Welds III*, (2011), pp.3-23.
- [23] Kou, S., Firouzdor, V., and Haygood, I.W., Hot Cracking in Welds of Aluminum and Magnesium Alloys, *Hot Cracking Phenomena in Welds III*, (2011), pp.3-23.
- [24] Madhusudhan Reddy, G., and Gokhale, A.A., Welding Aspects of Aluminum-Lithium Alloys, *Aluminum-Lithium Alloys*, (2014), pp.259-302.
- [25] Matsuda, F., Assessment of solidification cracking test for aluminum alloy welds, *Transactions of JWRI (Japanese Welding Research Institute)*, Vol.11(1), (1982), pp.67-77.
- [26] Liu, R., Dong, Z., and Pan, Y., Solidification crack susceptibility of aluminum alloy weld metals, *Transactions of Nonferrous Metals Society of China*, Vol.16(1), (2006), pp.110-116.
- [27] Cheng, C.M., Chou, C.P., Lee, I.K., and Lin, H.Y., Hot cracking of welds on heat treatable aluminium alloys, *Science and Technology of Welding and Joining*, Vol.10(3), (2005), pp.344-352.
- [28] Katayama, S., *Handbook of Laser Welding Technologies*, A volume in Woodhead Publishing Series in Electronic and Optical Materials, (2013).
- [29] Mathers, G., Introduction to the welding of aluminium, *The Welding of Aluminium and Its Alloys*, (2002), pp.1-9.
- [30] Ibrahim, M.F.A., Bakar, S.R.S., Jalar, A., Othman, N.K., Sharif, J., Daud, A.R., and Rashdi, N.M., Effect of Porosity on Tensile Behaviour of Welded AA6061-T6 Aluminium Alloy, *Applied Mechanics and Materials*, Vol.66-68, (2011), pp.534-539.
- [31] Seto, N., Katayama, S., and Matsunawa, A., Porosity Formation Mechanism and Suppression Procedure in Laser Welding of Aluminum Alloy, *Quarterly Journal Of The Japan Welding Society*, Vol.18(2), (2000), pp.243-255.
- [32] Holzer, M., Hofmann, K., Mann, V., Hugger, F., Roth, S., and Schmidt, M., Change of Hot Cracking Susceptibility in Welding of High Strength Aluminum Alloy AA 7075, *Physics Procedia*, Vol.83, (2016), pp.463-471.

- [33] Ghaini, F. M., Sheikhi, M., Torkamany, M.J., and Sabbaghzadeh, J., The relation between liquation and solidification cracks in pulsed laser welding of 2024 aluminium alloy, *Materials Science and Engineering: A*, Vol.519(1-2), (2009), pp.167-171.
- [34] Kim, H.T., and Nam, S.W., Solidification cracking susceptibility of high strength aluminum alloy weldment. *Scripta Materialia*, Vol.34(7), (1996), pp.1139-1145.
- [35] Zhang, Y., Lu, F., Cui, H., Cai, Y., Guo, S., and Tang, X., Investigation on the effects of parameters on hot cracking and tensile shear strength of overlap joint in laser welding dissimilar Al alloys, *The International Journal of Advanced Manufacturing Technology*, Vol.86(9-12), (2016), pp.2895-2904.
- [36] Brandt, U., Lawrence, F.V., and Sonsino, C.M., Fatigue crack initiation and growth in AlMg4.5Mn butt weldments, *Fatigue Fracture of Engineering Materials and Structures*, Vol. 24(2), (2001), pp.117-126.
- [37] Costa, J.D.M., Jesus, J.S., Loureiro, A., Ferreira, J.A.M., and Borrego, L.P., Fatigue life improvement of Mig welded aluminium T-joints by friction stir processing, *International Journal of Fatigue*, Vol.61, (2014), pp.244-254.
- [38] Kah, P., Shrestha, M., and Martikainen, J., Trends in Joining Dissimilar Metals by Welding, *Applied Mechanics and Materials*, Vol.440, (2013), pp.269-276.
- [39] Mvola, B., Kah, P., and Martikainen, J., Welding of dissimilar non-ferrous metals by GMAW processes, *International Journal of Mechanical and Materials Engineering*, Vol. 9(1), (2014).
- [40] Thomas, W.M., Nicholas, E.D., Needham, J.C., Murch, M.G., Temple-Smith, P. and Dawes, C.J., Friction-stir butt welding, International Patent Application PCT/GB92/02203 and GB Patent Application 9125978.8, UK Patent Office, London, December 6, (1991).
- [41] Mishra, R.S. and Ma, Z.Y., Friction stir welding and processing, *Materials Science and Engineering R*, Vol.50, (2005), pp.1-78.
- [42] Bharat Raj Singh, *A Handbook on Friction Stir Welding*, LAP Lambert Academic Publishing, (2012).
- [43] Tokisue, H. ed, "Friction stir welding", Nikkan Kogyo Publisher (2005) (in Japanese).
- [44] Khan, N.Z., Siddiquee, A.N., Khan, Z.A., *Friction Stir Welding: Dissimilar Aluminium Alloys*, Publisher: CRC Press, (2017).
- [45] Djurdjanovic, M.B., Mijajlovic, M.M., Milcic, D.S., Stamenkovic, D.S., Heat Generation During Friction Stir Welding Process, *Tribology in Industry*, Vol.31(1-2), (2009), pp. 8-14.
- [46] Chao, Y.J., Qi, X., and Tang, W., Heat Transfer in Friction Stir Welding-Experimental and Numerical Studies, *Journal of Manufacturing Science and Engineering*, Vol.125(1), (2003), pp.138.
- [47] Padhy, G.K., Wu, C.S., and Gao, S., Friction stir based welding and processing technologies-processes, parameters, microstructures and applications: A review, *Journal of Materials Science & Technology*, Vol.34(1), (2018), pp.1-38.
- [48] Ma, Z.Y., *Friction Stir Processing Technology: A Review*, *Metallurgical and Materials Transactions A*, Vol.39(3), (2008), pp.642-658.

- [49] Gite, R.A., Loharkar, P.K., and Shimpi, R., Friction stir welding parameters and application: A review, *Materials Today: Proceedings*, (2019).
- [50] Guerra, M., Schmidt, C., McClure, J., Murr, L., and Nunes, A., Flow patterns during friction stir welding, *Materials Characterization*, Vol.49(2), (2002), pp.95-101.
- [51] Donatus, U., Thompson, G.E., Zhou, X., Wang, J. and Beamish, K., Flow patterns in friction stir welds of AA5083 and AA6082 alloys, *Materials and Design*, Vol.83, (2015), pp.203-213.
- [52] Yi, D., Onuma, T., Mironov, S., Sato, Y.S., and Kokawa, H., Evaluation of heat input during friction stir welding of aluminium alloys, *Science and Technology of Welding and Joining*, Vol.22(1), (2016), pp.41-46.
- [53] Sato, Y.S., Onuma, T., Ikeda, K., and Kokawa, H., Experimental verification of heat input during friction stir welding of Al alloy 5083, *Science and Technology of Welding and Joining*, Vol.21(4), (2016), pp.325-330.
- [54] Aota, K., Okamura, H., Ezumi, M., Takai, H., Heat input and mechanical properties in friction stir welding, *Proceeding 3rd, International FSW Symposium, Kobe, Japan*, (2001).
- [55] Schmidt, H., Hattel, J., and Wert, J., An analytical model for the heat generation in friction stir welding, *Modelling and Simulation in Materials Science and Engineering*, Vol.12(1), (2003), pp.143-157.
- [56] Statsenko, V., Sukhorada, A., and Bernvskaya, M., Research of Heat Input in Friction Stir Welding, *Materials Science Forum*, Vol.945, (2019), pp.634-638.
- [57] Kumar, R., Singh, K., and Pandey, S., Process forces and heat input as function of process parameters in AA5083 friction stir welds, *Transactions of Nonferrous Metals Society of China*, Vol.22(2), (2012), pp.288-298.
- [58] Cavaliere, P., Squillace, A., and Panella, F., Effect of welding parameters on mechanical and microstructural properties of AA6082 joints produced by friction stir welding, *Journal of Materials Processing Technology*, Vol.200(1-3), (2008), pp.364-372.
- [59] Kulekci, M.K., Şik, A., and Kaluç, E., Effects of tool rotation and pin diameter on fatigue properties of friction stir welded lap joints, *The International Journal of Advanced Manufacturing Technology*, Vol.36, (2008), pp.877-882.
- [60] Salih, O. S., Neate, N., Ou, H., and Sun, W., Influence of process parameters on the microstructural evolution and mechanical characterizations of friction stir welded Al-Mg-Si alloy, *Journal of Materials Processing Technology*, Vol.275, (2020).
- [61] Caetano, G. de Q., Silva, C.C., Motta, M.F., Miranda, H.C., Farias, J.P., Bergmann, L.A., and F. dos Santos, J., Influence of rotation speed and axial force on the friction stir welding of AISI 410S ferritic stainless steel, *Journal of Materials Processing Technology*, Vol.262, (2018), pp.430-436.
- [62] Sharma, C., Dwivedi, D.K., and Kumar, P., Effect of welding parameters on microstructure and mechanical properties of friction stir welded joints of AA7039 aluminum alloy, *Materials & Design*, Vol.36, (2012), pp.379-390.
- [63] Cavaliere, P., De Santis, A., Panella, F., and Squillace, A., Effect of welding

- parameters on mechanical and microstructural properties of dissimilar AA6082-AA2024 joints produced by friction stir welding, *Materials & Design*, Vol.30(3), (2009), pp.609-616.
- [64] Abrahams, R., Mikhail, J., and Fasihi, P., Effect of friction stir process parameters on the mechanical properties of 5005-H34 and 7075-T651 Aluminium alloys, *Materials Science and Engineering: A*, Vol.751, (2019), pp.363-373.
- [65] Raturi, M., Garg, A., and Bhattacharya, A., Joint strength and failure studies of dissimilar AA6061-AA7075 friction stir welds: Effects of tool pin, process parameters and preheating, *Engineering Failure Analysis*, Vol.96, (2019), pp.570-588.
- [66] Kalemba-Rec, I., Kopyściński, M., Miara, D., and Krasnowski, K., Effect of process parameters on mechanical properties of friction stir welded dissimilar 7075-T651 and 5083-H111 aluminum alloys, *The International Journal of Advanced Manufacturing Technology*, Vol.97(5-8), (2018), pp.2767-2779.
- [67] Badarinarayan, H., Shi, Y., Li, X., Okamoto, K., Effect of tool geometry on hook formation and static strength of friction stir spot welded aluminum 5754-O sheets, *International Journal of Machine Tools and Manufacture*, Vol.49, (2009), pp.814-823.
- [68] Amini, S., Amiri, M.R. and Barani, A., Investigation of the effect of tool geometry on friction stir welding of 5083-O aluminum alloy, *The International Journal of Advanced Manufacturing Technology*, Vol.76, (2015), pp.255-261.
- [69] Kumar, K., Kailas, S.V., and Srivatsan, T.S., Influence of Tool Geometry in Friction Stir Welding, *Materials and Manufacturing Processes*, Vol. 23(2), (2008), pp.188-194.
- [70] Threadgill, P.L., Leonard, A.J., Shercliff, H.R., and Withers, P.J., Friction stir welding of aluminium alloys, *International Materials Reviews*, Vol.54(2), (2009), pp.49-93.
- [71] Defalco, J., Friction stir welding vs. fusion welding, *Welding Journal*, Vol. 85(3), 2006, pp.42-44.
- [72] Tra, T.H., Okazaki, M., and Suzuki, K., Fatigue crack propagation behavior in friction stir welding of AA6063-T5: Roles of residual stress and microstructure, *International Journal of Fatigue*, (2012), Vol.43, pp.23-29.
- [73] Zhang, C., and Shirzadi, A.A., Measurement of residual stresses in dissimilar friction stir-welded aluminium and copper plates using the contour method, *Science and Technology of Welding and Joining*, Vol.23(5), (2017), pp.394-399.
- [74] He, W., Liu, J., Hu, W., Wang, G., and Chen, W., Controlling residual stress and distortion of friction stir welding joint by external stationary shoulder, *High Temperature Materials and Processes*, Vol.38, (2019), pp.662-671.
- [75] Muñoz, A.C., Rückert, G., Huneau, B., Sauvage, X., and Marya, S., Comparison of TIG welded and friction stir welded Al-4.5Mg-0.26Sc alloy, *Journal of Materials Processing Technology*, Vol.197(1-3), (2008), pp.337-343.
- [76] Singh, G., Kang, A.S., Singh, K., and Singh, J., Experimental comparison of friction stir welding process and TIG welding process for 6082-T6 Aluminium alloy, *Materials Today: Proceedings*, Vol.4(2), (2017), pp.3590-3600.

- [77] Kumar, L., Yazar, K.U., and Pramanik, S., Effect of fusion and friction stir welding techniques on the microstructure, crystallographic texture and mechanical properties of mild steel, *Materials Science and Engineering: A*, Vol.754, (2019), pp.400-410.
- [78] Khanna, N., Chaudhary, B., Airao, J., Dak, G., and Badheka, V.J., Experimental Comparison of TIG and Friction Stir Welding Process for AA6063-T6 Aluminum Alloy, *Innovations in Infrastructure*, (2018), pp.619-628.
- [79] Borrego, L.P., Costa, J.D., Jesus, J.S., Loureiro, A.R., and Ferreira, J.M., Fatigue life improvement by friction stir processing of 5083 aluminium alloy MIG butt welds, *Theoretical and Applied Fracture Mechanics*, Vol.70, (2014), pp.68-74.
- [80] Fuller, C.B., and Mahoney, M.W., The effect of friction stir processing on 5083-H321/5356 Al arc welds: Microstructural and mechanical analysis, *Metallurgical and Materials Transactions A*, Vol.37(12), (2006), pp.3605-3615.
- [81] Da Silva, J., Costa, J.M., Loureiro, A., and Ferreira, J.M., Fatigue behavior of AA6082-T6 MIG welded butt joints improved by friction stir processing, *Materials & Design*, Vol.51, (2013), pp.315-322.
- [82] Leitao, C., Leal, R.M., Rodrigues, D.M., Loureiro, A., and Vilaça, P., Mechanical behaviour of similar and dissimilar AA5182-H111 and AA6016-T4 thin friction stir welds, *Materials & Design*, Vol.30(1), (2009), pp.101-108.
- [83] Fujii, H., Cui, L., Maeda, M., and Nogi, K., Effect of tool shape on mechanical properties and microstructure of friction stir welded aluminum alloys, *Materials Science and Engineering: A*, Vol.419(1-2), (2006), pp.25-31.
- [84] Svensson, L.-E., Karlsson, L., Larsson, H., Karlsson, B., Fazzini, M., and Karlsson, J., Microstructure and mechanical properties of friction stir welded aluminium alloys with special reference to AA 5083 and AA 6082, *Science and Technology of Welding and Joining*, Vol.5(5), (2000), pp.285-296.
- [85] Hirata, T., Oguri, T., Hagino, H., Tanaka, T., Chung, S.W., Takigawa, Y., and Higashi, K., Influence of friction stir welding parameters on grain size and formability in 5083 aluminum alloy, *Materials Science and Engineering: A*, Vol.456(1-2), (2007), pp.344-349.
- [86] Park, H.S.C., Sato, Y.S., Kokawa, H., Effect of micro-texture on fracture location in friction stir weld of Mg alloy AZ61 during tensile test, *Scripta Materialia*, Vol.49(2), (2003), pp.161-166.
- [87] Lee, W.-B., Kim, J.-W., Yeon, Y.-M., and Jung, S.-B., The Joint Characteristics of Friction Stir Welded AZ91D Magnesium Alloy, *Materials Transactions*, Vol.44(5), (2003), pp.917-923.
- [88] Xie, G.M., Ma, Z.Y., Geng, L., and Chen, R.S., Microstructural evolution and mechanical properties of friction stir welded Mg-Zn-Y-Zr alloy, *Materials Science and Engineering: A*, Vol.471(1-2), (2007), pp.63-68.
- [89] Park, S.H.C., Sato, Y.S., and Kokawa, H., Microstructural evolution and its effect on Hall-Petch relationship in friction stir welding of thixomolded Mg alloy AZ91D, *Journal of Materials Science*, Vol.38(21), (2003), pp.4379-4383.
- [90] Xie, G.M., Ma, Z.Y., and Geng, L., Development of a fine-grained microstructure and the properties of a nugget zone in friction stir welded pure copper, *Scripta Materialia*, Vol.57(2), (2007), pp.73-76.

- [91] Fuller, M.D., Swaminathan, S., Zhilyaev, A.P., and McNelley, T.R., Microstructural transformations and mechanical properties of cast NiAl bronze: Effects of fusion welding and friction stir processing, *Materials Science and Engineering: A*, Vol.463(1-2), (2007), pp.128-137.
- [92] Çam, G., Serindağ, H.T., Çakan, A., Mistikoglu, S., and Yavuz, H., The effect of weld parameters on friction stir welding of brass plates, *Materialwissenschaft Und Werkstofftechnik*, Vol.39(6), (2008), pp.394-399.
- [93] Reynolds, A.P., Tang, W., Posada, M., and Deloach, J., Friction stir welding of DH36 steel, *Science and Technology of Welding and Joining*, Vol.8(6), (2003), pp.455-460.
- [94] Reynolds, A., Tang, W., Gnaupel-Herold, T., and Prask, H., Structure, properties, and residual stress of 304L stainless steel friction stir welds, *Scripta Materialia*, Vol.48(9), (2003), pp.1289-1294.
- [95] Fujii, H., Sun, Y., Kato, H., and Nakata, K., Investigation of welding parameter dependent microstructure and mechanical properties in friction stir welded pure Ti joints, *Materials Science and Engineering: A*, Vol.527(15), (2010), pp.3386-3391.
- [96] Ramulu, M., Edwards, P.D., Sanders, D.G., Reynolds, A.P., and Trapp, T., Tensile properties of friction stir welded and friction stir welded-superplastically formed Ti-6Al-4V butt joints, *Materials & Design*, Vol.31(6), (2010), pp.3056-3061.
- [97] Zhang, Y., Sato, Y.S., Kokawa, H., Park, S.H.C., and Hirano, S., Microstructural characteristics and mechanical properties of Ti-6Al-4V friction stir welds, *Materials Science and Engineering: A*, Vol.485(1-2), (2008), pp.448-455.
- [98] Zhou, L., Liu, H.J., and Liu, Q.W., Effect of rotation speed on microstructure and mechanical properties of Ti-6Al-4V friction stir welded joints, *Materials & Design (1980-2015)*, Vol.31(5), (2010), pp.2631-2636.
- [99] Thomas, W., and Nicholas, E., Friction stir welding for the transportation industries, *Materials & Design*, Vol.18(4-6), (1997), pp.269-273.
- [100] Dawes, C.J. and Thomas, W.M., Friction Stir Process Welds Aluminum Alloys, *Welding Journal*, Vol.75, (1996), pp.41-45.
- [101] Kallee, S.W., Davenport, J., and Nicholas, E.D., Railway Manufacturers implement friction Stir Welding, *Welding Journal*, Vol.81, (2002), pp.47-50.
- [102] Ding, J., Carter, R., Lawless, K., Nunes, A., Russel, C., Suits, M., and Schneider, J., Friction Stir Welding Flies High at NASA, *Welding Journal*, Vol.85, (2006), pp.54-59.
- [103] Çam, G., and Mistikoglu, S., Recent Developments in Friction Stir Welding of Al-alloys, *Journal of Materials Engineering and Performance*, Vol.23(6), (2014), pp.1936-1953.
- [104] Suhuddin, U., Fischer, V., Kroeff, F., and dos Santos, J.F., Microstructure and mechanical properties of friction spot welds of dissimilar AA5754 Al and AZ31 Mg alloys, *Materials Science and Engineering: A*, Vol.590, (2014), pp.384-389.
- [105] Watanabe, T., Takayama, H., and Yanagisawa, A., Joining of aluminum alloy to steel by friction stir welding, *Journal of Materials Processing Technology*,

- Vol.178(1-3), (2006), pp.342-349.
- [106] Choi, J.-W., Liu, H., Ushioda, K., and Fujii, H., Dissimilar friction stir welding of immiscible titanium and magnesium, *Materialia*, Vol.7, (2019), 100389.
- [107] Tomashchuk, I., Sallamand, P., Belyavina, N., and Pilloz, M., Evolution of microstructures and mechanical properties during dissimilar electron beam welding of titanium alloy to stainless steel via copper interlayer, *Materials Science and Engineering: A*, Vol.585, (2013), pp.114-122.
- [108] Gao, M., Wang, Z.M., Yan, J., and Zeng, X.Y., Dissimilar Ti/Mg alloy butt welding by fibre laser with Mg filler wire – preliminary study. *Science and Technology of Welding and Joining*, Vol.16(6), (2011), pp.488-496.
- [109] Atieh, A.M., and Khan, T.I., Effect of process parameters on semi-solid TLP bonding of Ti–6Al–4V to Mg–AZ31, *Journal of Materials Science*, Vol.48(19), (2013), pp.6737-6745.
- [110] Baqer, Y.M., Ramesh, S., Yusof, F., and Manladan, S.M., Challenges and advances in laser welding of dissimilar light alloys: Al/Mg, Al/Ti, and Mg/Ti alloys, *The International Journal of Advanced Manufacturing Technology*, Vol.95(9-12), (2018), pp.4353-4369.
- [111] Chen, Y.C., and Nakata, K., Microstructural characterization and mechanical properties in friction stir welding of aluminum and titanium dissimilar alloys, *Materials & Design*, Vol.30(3), (2009), pp.469-474.
- [112] Aonuma, M., and Nakata, K., Effect of calcium on intermetallic compound layer at interface of calcium added magnesium–aluminum alloy and titanium joint by friction stir welding, *Materials Science and Engineering: B*, Vol.173(1-3), (2010), pp.135-138.
- [113] Dressler, U., Biallas, G., and Alfaro Mercado, U., Friction stir welding of titanium alloy TiAl6V4 to aluminium alloy AA2024-T3, *Materials Science and Engineering: A*, Vol.526(1-2), (2009), pp.113-117.
- [114] Galvão, I., Verdera, D., Gesto, D., Loureiro, A., and Rodrigues, D.M., Influence of aluminium alloy type on dissimilar friction stir lap welding of aluminium to copper, *Journal of Materials Processing Technology*, Vol.213(11), (2013), pp.1920-1928.
- [115] Shankar, S., Vilaça, P., Dash, P., Chattopadhyaya, S., and Hloch, S., Joint strength evaluation of friction stir welded Al-Cu dissimilar alloys, *Measurement*, Vol.146, (2019), pp.892-902.
- [116] Pourali, M., Abdollah-zadeh, A., Saeid, T., and Kargar, F., Influence of welding parameters on intermetallic compounds formation in dissimilar steel/aluminum friction stir welds, *Journal of Alloys and Compounds*, Vol.715, (2017), pp.1-8.
- [117] Coelho, R.S., Kostka, A., dos Santos, J.F., and Kaysser-Pyzalla, A., Friction-stir dissimilar welding of aluminium alloy to high strength steels: Mechanical properties and their relation to microstructure, *Materials Science and Engineering: A*, Vol.556, (2012), pp.175-183.
- [118] Miles, M.P., Nelson, T.W., and Melton, D.W., Formability of friction-stir-welded dissimilar-aluminum-alloy sheets, *Metallurgical and Materials Transactions A*, Vol.36(12), (2005), pp.3335-3342.

- [119] Shigematsu, I., Kwon, Y.-J., Suzuki, K., Imai, T., and Saito, N., Joining of 5083 and 6061 aluminum alloys by friction stir welding, *Journal of Materials Science Letters*, Vol.22(5), (2003), pp.353-356.
- [120] Ouyang, J.H., and Kovacevic, R., Material flow and microstructure in the friction stir butt welds of the same and dissimilar aluminum alloys, *Journal of Materials Engineering and Performance*, Vol.11(1), (2002), pp.51-63.
- [121] Soundararajan, V., Yarrapareddy, E., and Kovacevic, R., Investigation of the Friction Stir Lap Welding of Aluminum Alloys AA 5182 and AA 6022, *Journal of Materials Engineering and Performance*, Vol.16(4), (2007), pp.477-484.
- [122] Ahmed, M.M.Z., Sabbah Ataya, El-Sayed Seleman, M.M., Ammar, H.R. and Ahmed E., Friction stir welding of similar and dissimilar AA7075 and AA5083, *Journal of Materials Processing Technology*, Vol.242, (2017), pp.77-91.
- [123] Kalembe-Rec, I., Hamilton, C., Kopyściański, M., Miara, D., and Krasnowski, K., Microstructure and mechanical properties of friction stir welded 5083 and 7075 aluminum alloys, *Journal of Materials Engineering and Performance*, Vol.26, No.3 (2017), pp.1032-1043.
- [124] Chintapalli, S., Elsayed, M.S.A., Sedaghati, R. and Abdo, M., The development of a preliminary structural design optimization method of an aircraft wing-box skin-stringer panels, *Aerospace Science and Technology*, Vol.14, No.3 (2010), pp.188-198.
- [125] Deng, D., and Murakawa, H., FEM prediction of buckling distortion induced by welding in thin plate panel structures, *Computational Materials Science*, Vol.43(4), (2008), pp.591-607.
- [126] <https://www.plm.automation.siemens.com/global/ko/industries/marine/commercial-shipbuilding/ship-structures-design.html>
- [127] <http://marine-grade-aluminum.com/marine-grade-aluminum-plate-sheet/marine-grade-ribbed-aluminum-plate-sheet.html>
- [128] Darko Frank, Heikki Remes, Jani Romanoff, Fatigue assessment of laser stake-welded T-joints. *International Journal of Fatigue*, Vol.33(2), (2011), pp.102-114.
- [129] Jesus, J.S., Costa, J.M., and Loureiro, A., J.M., Ferreira, Fatigue strength improvement of GMAW T-welds in AA 5083 by friction-stir processing, *International Journal of Fatigue*, Vol.97, 2017, pp.124-134.
- [130] Acerra, F., Buffa, G., Fratini, L. and Troiano, G., On the FSW of AA2024-T4 and AA7075-T6 T-joints: an industrial case study, *International Journal of Advanced Manufacturing Technology*, Vol.48, (2010), pp.1149-1157.
- [131] Fratini, L., Micari, F., Squillace, A. and Giorleo, G., Experimental characterization of FSW T-joints of light alloys, *Key Engineering Materials*, Vol.344, (2007), pp.751-758.
- [132] <https://www.shapesbyhydro.com/en/manufacturing/know-the-differences-between-friction-welding-techniques/>
- [133] Cui, L., Yang, X., Zhou, G., Xu, X. and Shen, Z., Characteristics of defects and tensile behaviors on friction stir welded AA6061-T4 T-joints, *Materials Science and Engineering A*, Vol.543, (2012), pp.58-68.
- [134] Zhao, Y., Zhou, L., Wang, Q., Yan, K. and Zou, J., Defects and tensile properties

- of 6013 aluminum alloy T-joints by friction stir welding, *Materials and Design*, Vol.57, (2014), pp.146-155.
- [135] Silva, A.C.F., Braga, D.F.O., Figueiredo, M.A.V. de, and Moreira, P.M.G.P., Friction stir welded T-joints optimization, *Materials & Design*, Vol.55, (2014), pp.120-127.
- [136] Manuel, N., Silva, C., da Costa, J.M.D., and Loureiro, A., Friction stir welding of T-joints in dissimilar materials: Influence of tool geometry and materials properties, *Materials Research Express*, Vol.6(10), (2019), 106528.
- [137] Jesus, J.S., Costa, J.M., Loureiro, A., and Ferreira, J.M., Assessment of friction stir welding aluminium T-joints, *Journal of Materials Processing Technology*, Vol.255, (2018), pp.387-399.
- [138] Buffa, G., Fratini, L., Micari, F. and Shivpuri, R., Material Flow in FSW of T-joints: Experimental and Numerical Analysis, *International Journal of Material Forming*, Vol.1(1), (2008), pp.1283-1286.
- [139] Fratini, L., Buffa, G., Micari, F. and Shivpuri, R., On the material flow in FSW of T-joints: Influence of geometrical and technological parameters, *International Journal of Advanced Manufacturing Technology*, Vol.44(5-6), (2009), pp.570-578.
- [140] Suna, T., Roy, M. J., Strong, D., Simpson, C., and Withers, P. J., Prangnell, P. B., Weld zone and residual stress development in AA7050 stationary shoulder friction stir T-joint weld, *Journal of Materials Processing Technology*, Vol.263, (2019), pp.256-265.
- [141] Martin, J.P., Stanhope, C. and Gascoyne, S., Novel techniques for corner joints using friction stir welding, In book: *Friction Stir Welding and Processing VI* (2011), pp.177-186.
- [142] Li, D., Yang, X., Cui, L., He, F., and Zhang, X., Fatigue property of stationary shoulder friction stir welded additive and non-additive T joints, *Science and Technology of Welding and Joining*, Vol.20(8), (2015), pp.650-654.
- [143] Feistauer, E.E., Bergmann, L.A., and dos Santos, J.F., Effect of reverse material flow on the microstructure and performance of friction stir welded T-joints of an Al-Mg alloy, *Materials Science and Engineering A*, Vol.731, (2018), pp.454-464.
- [144] Al-Moussawi, M., and Smith, A.J., Defects in Friction Stir Welding of Steel, *Metallography, Microstructure, and Analysis*, Vol.7(2), (2018), pp.194-202.
- [145] Le Jolu, T., Morgeneyer, T.F., Denquin, A., and Gourgues-Lorenzon, A.F., Fatigue lifetime and tearing resistance of AA2198 Al-Cu-Li alloy friction stir welds: Effect of defects, *International Journal of Fatigue*, Vol.70, (2015), pp.463-472.
- [146] Zhang, H., Luo, S., and Xu, W., Influence of Welding Speed on Zigzag Line Feature and Tensile Property of a Friction-Stir-Welded Al-Zn-Mg Aluminum Alloy, *Journal of Materials Engineering and Performance*, Vol.28, (2019), pp.1790-1800.
- [147] Sato, Y.S., Yamashita, F., Sugiura, Y., Park, S.H.C., and Kokawa, H., FIB-assisted TEM study of an oxide array in the root of a friction stir welded aluminium alloy, *Scripta Materialia*, Vol.50(3), (2004), pp.365-369.

- [148] Okamura, H., Aota, K., Sakamoto, M., Ezumi, M., and Ikeuchi, K., Behavior of Oxide during Friction Stir Welding of Aluminum Alloy and Its Influence on Mechanical Properties, *Quarterly Journal of The Japan Welding Society*, Vol.19(3), (2001), pp.446-456.
- [149] Dialami, N., Cervera, M., Chiumenti, M., and Segatori, A., Prediction of joint line remnant defect in Friction Stir Welding, *International Journal of Mechanical Sciences*, Vol.151, (2019), pp.61-69.
- [150] Jolu, T.L., Morgeneyer, T.F., and Gourgues-Lorenzon, A.F., Effect of joint line remnant on fatigue lifetime of friction stir welded Al–Cu–Li alloy, *Science and Technology of Welding and Joining*, Vol.15(8), (2010), pp.694-698.
- [151] Chen, H.-B., Yan, K., Lin, T., Chen, S.-B., Jiang, C.-Y., & Zhao, Y., The investigation of typical welding defects for 5456 aluminum alloy friction stir welds, *Materials Science and Engineering: A*, Vol.433(1-2), (2006), pp.64-69.
- [152] Klages, Holli K., The "Lazy S" feature in Friction Stir Welding of AA2099 Aluminum-Lithium alloy, *Theses and Dissertations*, Monterey, California, Naval Postgraduate School, (2007).
- [153] Kadlec, M., Růžek, R., and Nováková, L., Mechanical behaviour of AA 7475 friction stir welds with the kissing bond defect, *International Journal of Fatigue*, Vol.74, (2015), pp.7-19.
- [154] Zhou, N., Song, D., Qi, W., Li, X., Zou, J., and Attallah, M.M., Influence of the kissing bond on the mechanical properties and fracture behaviour of AA5083-H112 friction stir welds, *Materials Science and Engineering: A*, Vol.719, (2018), pp.12-20.
- [155] Zhou, C., Yang, X., and Luan, G., Effect of kissing bond on fatigue behavior of friction stir welds on Al 5083 alloy, *Journal of Materials Science*, Vol.41(10), (2006), pp.2771-2777.
- [156] Yue, Y., Li, Z., Ji, S., Huang, Y., and Zhou, Z., Effect of Reverse-threaded Pin on Mechanical Properties of Friction Stir Lap Welded Alclad 2024 Aluminum Alloy, *Journal of Materials Science & Technology*, Vol.32(7), (2016), pp.671-675.
- [157] Moraes, J.F.C., Rodriguez, R.I., Jordon, J.B., Su, X., Effect of overlap orientation on fatigue behavior in friction stir linear welds of magnesium alloy sheets, *International Journal of Fatigue*, Vol.100, (2017), pp.1-11.

This page has been intentionally left blank

Chapter 2

Fundamental Formation of Interface Morphology and Mechanical Properties of Dissimilar Metal T-lap Joints between AA7075 and AA5083 by Single-pass Friction Stir Welding

The main aim of this chapter is to investigate dissimilar metal T-lap joints between AA7075 and AA5083 by employing traditional single-pass Friction Stir Welding (FSW). The fundamental formation of welding interface between skin and stringer parts affected by welding speed and probe length is explored. Here, the special attention is concentrated on the formation of some undesirable defects along interface. The influences of these defects on the mechanical properties of the joints are evaluated. The quantifications of defects of interface affected by welding parameters are shown. Some available welding parameters are proposed to make platform for the improvement of the dissimilar FSWed T-lap joints in the next chapter.

2.1 Introduction

The welding and rotational speeds are two of the important FSW parameters that significantly affected heat input during the welding process [1,2]. They are key factors to advance the strength of the FSWed joints which has been successfully reached in literature [3-7]. In addition, the strength of the joints is strongly induced by the geometry of welding tool [8-10]. Especially in the FSWed lap joints, the optimal probe length was considered as one of the important aspects for improving lap interface due to the change in the metal flow [11-13].

The weldability of the FSWed T-lap joints has been investigated in the literature from different aspects such as welding parameters [14-17], welding tool [18,19], and material flows [20,21]. The major aim of these works was to upgrade the strength of the joints. However, most of the efficiency of the T-lap joints was significantly low, especially in loading along stringer part. This result might be due to the undesirable formation of some defects along interface such as hook, bonding line, and kissing bond defects those were affected by the asymmetric material flows during the FSW process [14,15,18]. It is clear that a good interface without defects can bring about a high performance of the T-lap joints. So, understanding formation mechanism and role of these types of defects on the FSWed T-lap joints is key factor in the improvement of the strength of the joints.

The first goal of this work is to understand clearly the FSWed T-lap dissimilar metal joints between AA7075 and AA5083. The special focus is concentrated on the formation of welding interface in terms of undesirable defects. In addition, the role of them in the mechanical properties of dissimilar T-lap joints is explored. The effect of welding parameters on the quantification of defects of the interface is also considered. Therefrom, the available welding condition is selected to make platform for minimizing or eliminating these defects from the joints.

2.2 Effect of Welding Speed

2.2.1 Experimental procedure

In order to produce advanced panel structure with main T-joint configuration that was presented in previous Chapter, two dissimilar metals were used in this work; aluminum alloys of 7075-T651 (denoted as AA7075) for the stringer and 5083-H116

(denoted as 5083) for the skin plate with the dimensions of 300×50×8.2 mm and 300×150×3.0 mm, respectively. The chemical compositions and mechanical properties of them are shown in Table 2-1 and Table 2-2, respectively. The T-lap joint configuration is illustrated in Figure 2-1(a). Before welding process, the contact surface was polished by abrasive SiC paper to limit the effect of oxide layers on joint quality.

The welding speed was arranged from 50 to 200 mm/min and the rotational speed was kept constant at 400 rpm. A simple conical probe was designed detail, as illustrated in Figure 2-1(b). The probe axis alignment was kept at a constant with the tilt angle of 2.0° to the vertical direction. The tool shoulder penetrated into the surface of skin plate with the depth of 0.2 mm that was determined before the FSW process. All of samples in this work were no post-weld and analyzed after welding process about one month.

The specimen for the investigation of microstructures was cut perpendicular to welding direction. Then, all of them were ground and polished by water abrasive SiC paper and alumina, respectively to achieve mirror surfaces before etching with Kroll's reagent (2%HF, 6%HNO₃(30%), 92% water) for 10s. Optical microscope, scanning electron microscope (SEM), and Energy Dispersive X-Ray Spectroscopy (EDS) were employed to clarify the formation of some defects in the joints.

Two types of tests were carried out to assess the strength of the T-lap joints; one is the tensile test along the skin part (denoted as “skin tensile test”, Figure 2-2(a)) and the other is along the stringer part (denoted as “stringer tensile test”, Figure 2-2(b)). According to that, the skin specimen was prepared via ASTM E08 standards [22] where a part of stringer is still remaining by the length of 8.0 mm (Figure 2-2(a)). A jig made of steel material was used to support for the stringer tensile test (Figure 2-2(b)). The local bonding strength along the interface was evaluated by some miniature specimens those were extracted from the different locations of the joints, as demonstrated in Figure 2-3(a). Specimen geometry and loading process are displayed in Figures 2-3(b) and 2-3(c), respectively. All of these tests were executed under a speed of 1.0 mm/min at room temperature.

Table 2-1 Chemical compositions (wt%) of AA5083 and AA7075.

| Compositions | Si | Fe | Cu | Mn | Mg | Cr | Zn | Ti | Al |
|--------------|-----|-----|---------|---------|---------|-----------|------|------|------|
| AA5083 | 0.4 | 0.4 | 0.1 | 0.4-1.0 | 4.0-4.9 | 0.05-0.25 | 0.25 | 0.15 | Bal. |
| AA7075 | 0.5 | 0.7 | 1.2-2.0 | 0.3 | 2.1-2.9 | 0.18-0.40 | 6.1 | 0.2 | Bal. |

Table 2-2 Mechanical properties of AA5083 and AA7075.

| Mechanical properties | Yield strength (MPa) | Ultimate tensile strength (MPa) | Shear strength (MPa) | Vicker hardness (HV) |
|-----------------------|----------------------|---------------------------------|----------------------|----------------------|
| AA5083 | 260 | 320 | 180 | 95 |
| AA7075 | 520 | 570 | 320 | 180 |

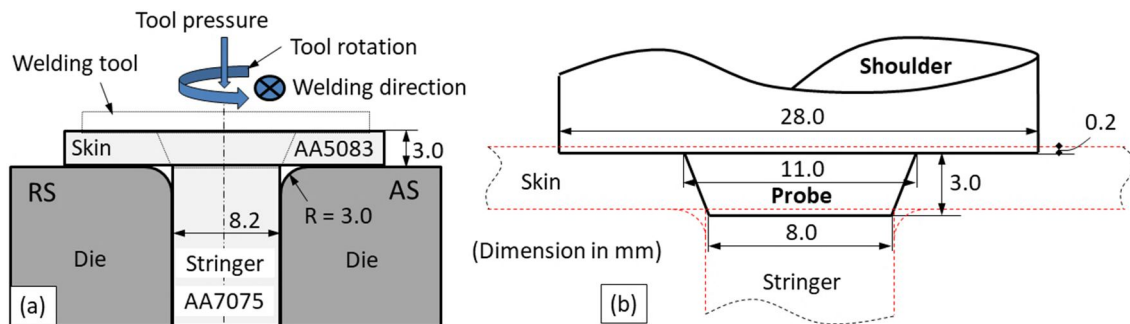


Figure 2-1 (a) Schematic view of T-lap joints and (b) detail geometry of welding tool.

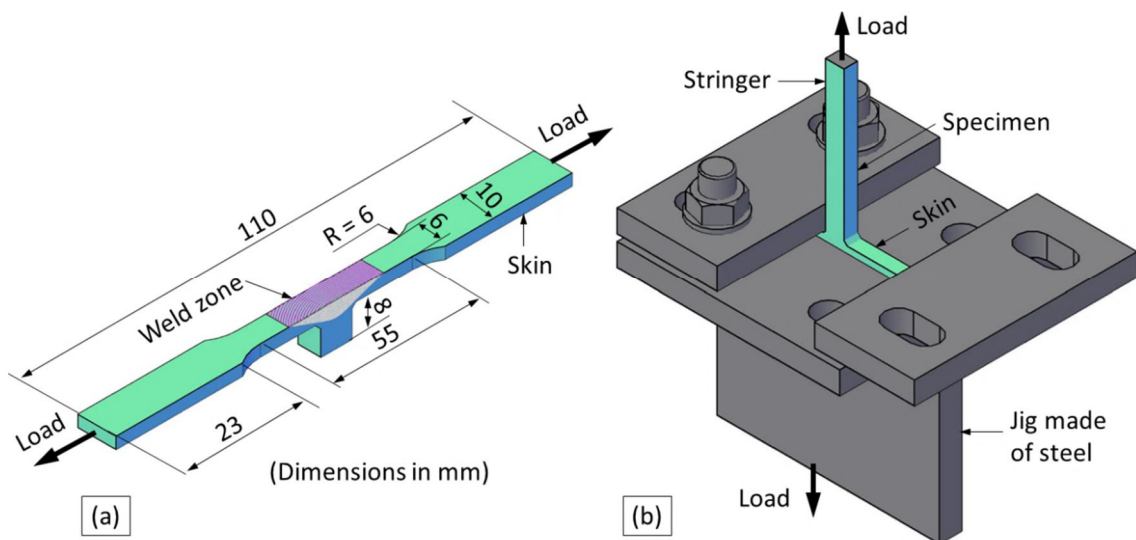


Figure 2-2 Global evaluation of T-lap joints by (a) skin and (b) stringer tensile tests.

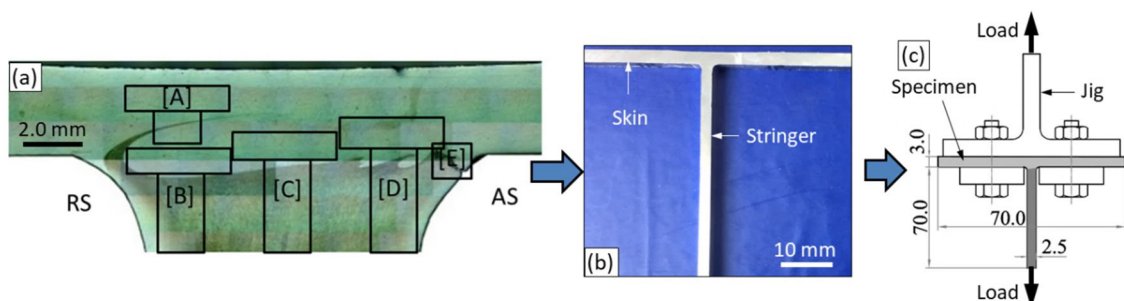


Figure 2-3 (a) Evaluation of local interface bonding strength, (b) miniature specimens were extracted from the sites [A] through [E], and (c) test system for loading process.

2.2.2 Results and discussion

2.2.2.1 Cross-section of T-lap joints

Figures 2-4(a) and 2-4(b) show the macrostructures on the cross-sections of the specimens produced by the welding speed of 50 and 200 mm/min, respectively. Here, interface morphology was strongly affected by some typical kinds of defects those were found depending on the welding conditions: kissing bond (KB), hook, and bonding line defects. These defects seem to be remnant of initial interface that were fragmented during FSW process with not same degree. This result might lead to difference in the bonding strength of interface. This result might be related to the location of interface, as presented in Figure 2-4. Hereinafter, the characteristics and formation mechanisms of these defects are given as following;

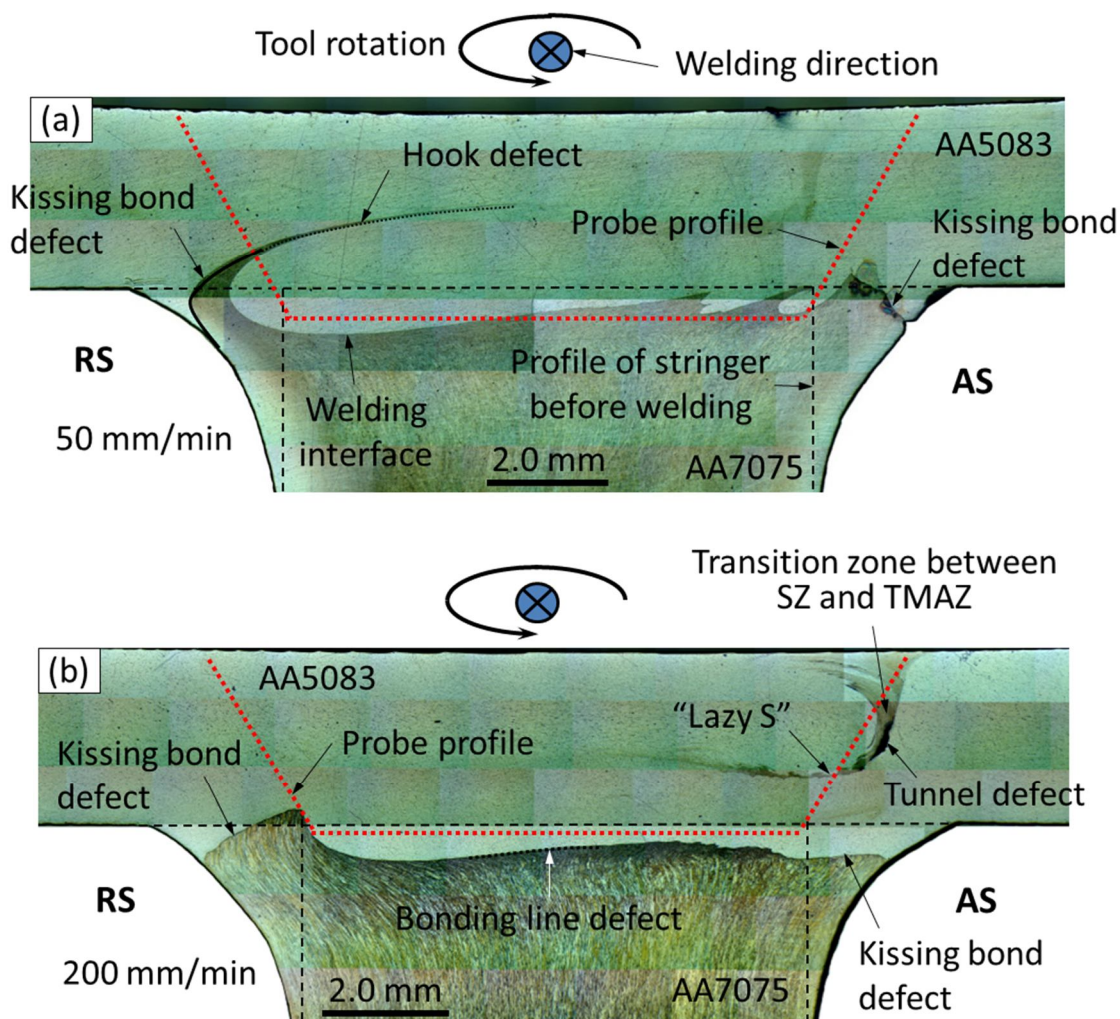


Figure 2-4 Macrostructures on the cross-section of specimens produced by welding speed of (a) 50 mm/min and (b) 200 mm/min.

(a) **Tunnel defect:** A representative tunnel defect at the welding rate of 200 mm/min is shown Figure 2-4(b). The formation of this type of defects was originated by non-filling materials during the FSW process. They were pronounced in advancing side (AS), and located at the transition zone between stirred zone (SZ) and thermo-mechanically affected zone (TMAZ). It is worthy to note from Figures 2-5(a-c), the tunnel defects might be eliminated at the low welding speeds (from 50 to 100 mm/min) but appeared at the higher welding speeds of 150 and 200 mm/min (Figures 2-5(d,e)). These results might be related to the low flow of plasticized metal that was affected by heat input during the FSW process [15,18,23,24].

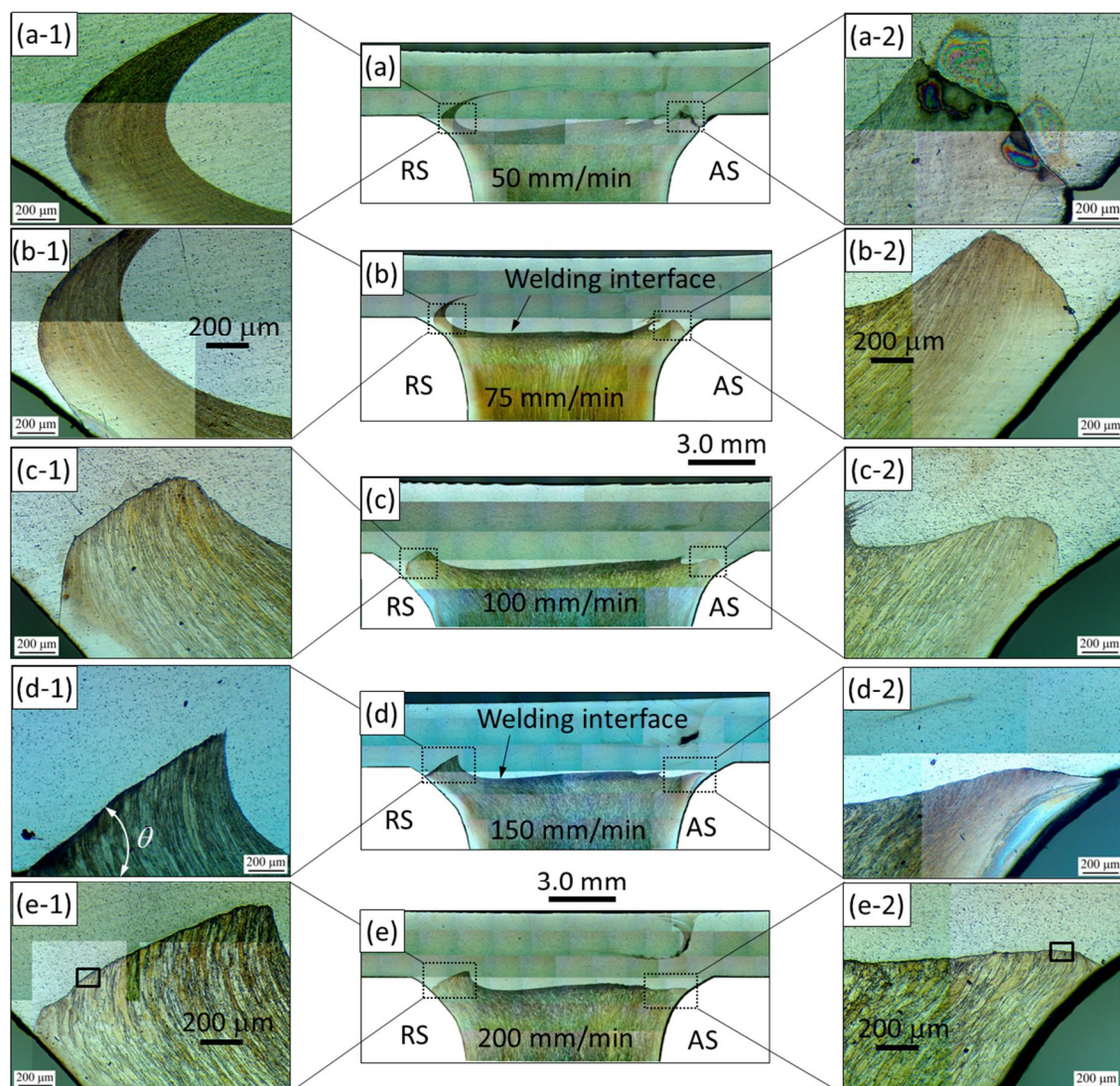


Figure 2-5 Interface morphology of T-lap joints affected by various welding speeds.

(b) Hook defect: The hook defect seems to be a feature in the FSWed lap-joints observed as a joint line uplifted. Here, it predominantly initiated in the retreating side (RS) and had tendency towards the weld center of the joints under low welding speed (Figure 2-6(a)). As shown in Figures 2-5(a,b), the hook defect was formed at 50 and 75 mm/min, respectively. It is worth to note that a small dark line was observed along the hook defects as oxide layer (Figure 2-6(c)). This type of defects in the FSWed T-lap joints might be minimized by growing the welding speed. In fact, it was disappeared at the high welding speed of 150 and 200 mm/min, as seen Figure 2-5(c-e). A sound weld without the tunnel and hook defects was achieved at 100 mm/min (Figure 2-5(c)).

The formation mechanism of the hook defects can be induced by metal flow, as indicated in Figure 2-7. Here, the noteworthy conjunction of two metal flows that was observed as a “Lazy S” was produced by shoulder-driven material and probe-driven material. While the shoulder-driven metal flow was induced by the rotation of tool shoulder, the probe-driven material depended on the stirred efficiency of probe. This phenomenon was also observed by some researchers [25,26]. As shown in Figure 2-7, the initial interface is pushed upward by the vertical material flow which is induced by tool probe at the low welding speed. The move of shoulder-driven material flow unwittingly lugs interface into the welded center at the same time. Consequently, the hook defects remarkably increased both the height and length.

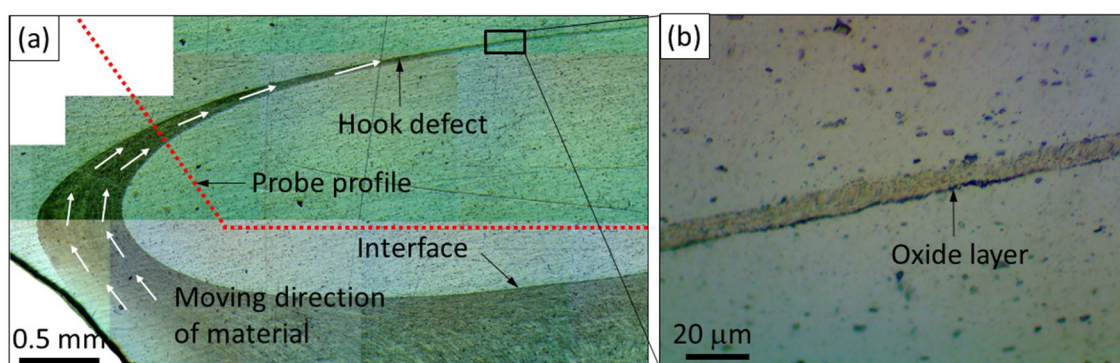


Figure 2-6 (a) Hook defect produced by welding speed of 50 mm/min and (b) oxide layer along hook defects.

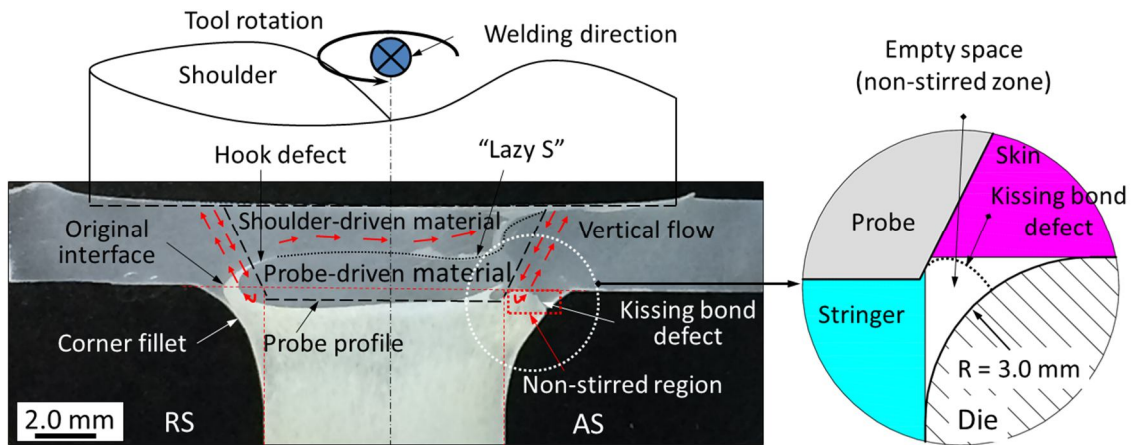


Figure 2-7 Illustration of formation of hook and kissing bond defects in T-lap joints at welding speed of 50 mm/min.

(c) **Kissing bond defect:** Unlike other defects, the kissing bond defects (KBs) were found at two corner fillets at both the RS and AS sides under all of the welding regimes. As presented in literature, it is a typical type of defects with little or no metallic bonding [27,28]. This type of defects often occurs outside the stirred zone where the materials are in close touch although they have not formed a chemical or mechanical bond. Figure 2-5 displays the geometries of the KBs which were asymmetric through centerline under all welding conditions. Here, the geometry of the KBs in terms of direction angle (θ) and size at the RS and AS was significantly different by the change in the welding speed (Figure 2-5(a-1) through Figure 2-5(e-1) and Figure 2-5(a-2) through Figure 2-5(e-2), respectively). These features may be driven by the asymmetric material flows during the FSW process.

A large dark line was detected along the KBs and examined by means of Energy Dispersive X-Ray Spectroscopy (EDS). It was found that a large amount of oxygen concentrated along the KBs at both the RS and AS (Figure 2-8). This result means that oxide layer might be hardly extruded in this work, as case by some researchers [24,27-29]. The lack of stirred action during the welding process might be reason for this defect formation. In fact, the positions at corner fillets beyond tool probe (Figure 2-7) did not get stirring action, resulting in the KBs formation.

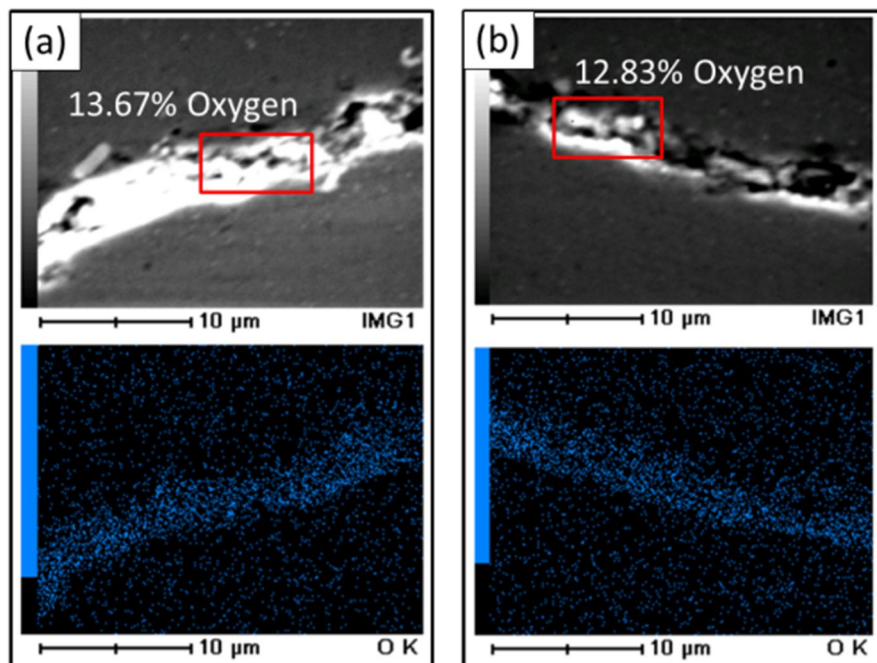


Figure 2-8 Distribution of oxygen along KBs measuring at (a) RS and (b) AS (as marked in Figures 2-5(e-1,2), respectively).

(d) Bonding line defect: Unlike the KBs, the bonding line defects were formed along the welding interface in the stirred zone (Figure 2-4), where experienced severely plastic deformation during the welding process. The low stirred efficiency of probe might be reason for this defect formation. Note that the oxide layer along the bonding line defects (Figures 2-9(b-d)) seems to be discontinuous and thinner than that along the KBs (Figures 2-9(a,e)), as compared between Figures 2-8 and 2-10. Furthermore, the formation of oxide layer along bonding interface was heterogeneous and depended strongly on the welding speeds. As shown in Figure 2-11, the bonding line defects appeared more common at the high welding speed that generated low heat input. This reason might lead to the low efficiency in breaking the oxide layer on the surfaces of the interface. This result might affect the erratic distribution of the local bonding strength along interface, and will be documented in the next section. A background of the formation of the bonding line defects might be closely related to heat input between the two joining materials, induced by stirring action of welding tool [18]. This may be significant under such a condition that the horizontal oxide layer in original interface is not easy to be removed from the FSWed T-lap joints.

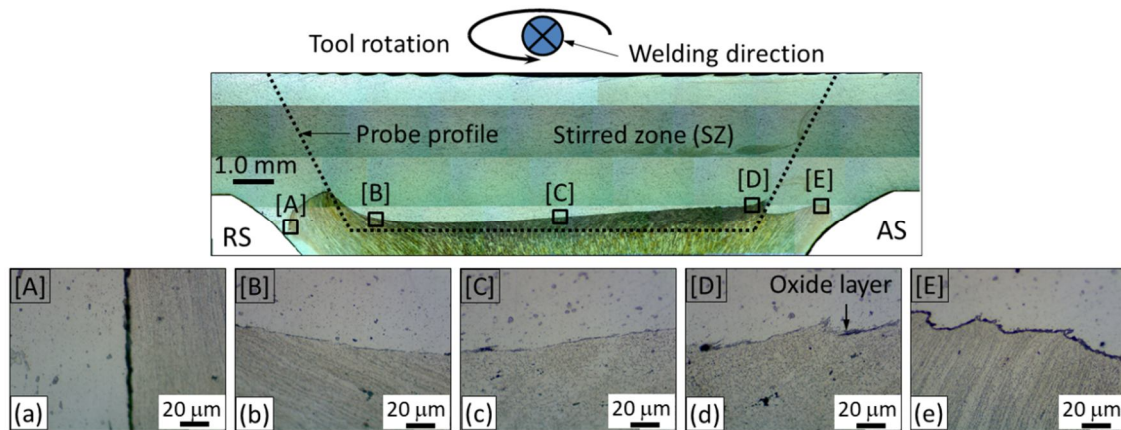


Figure 2-9 (b-d) Bonding line defects along bonding interface compared to (a,e) KBs at welding speed of 100 mm/min.

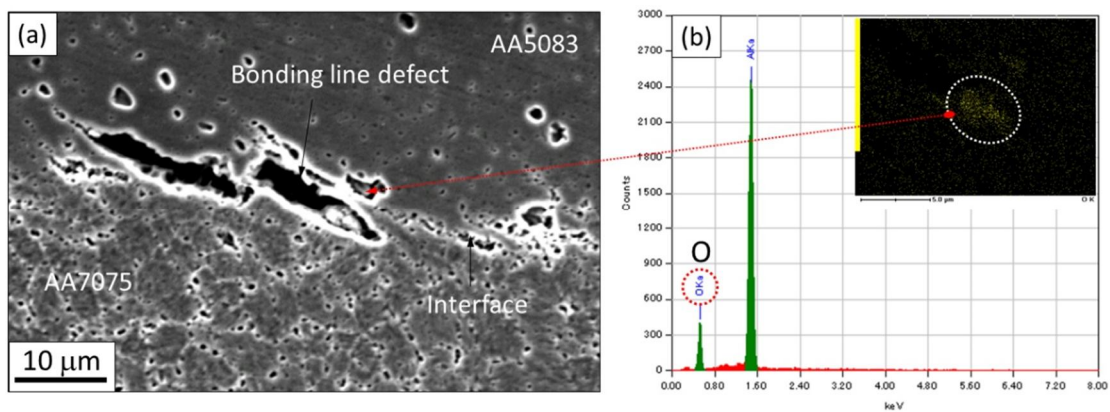


Figure 2-10 (a) SEM image and (b) EDS spectrum with inserting oxygen mapping around the bonding line defects.

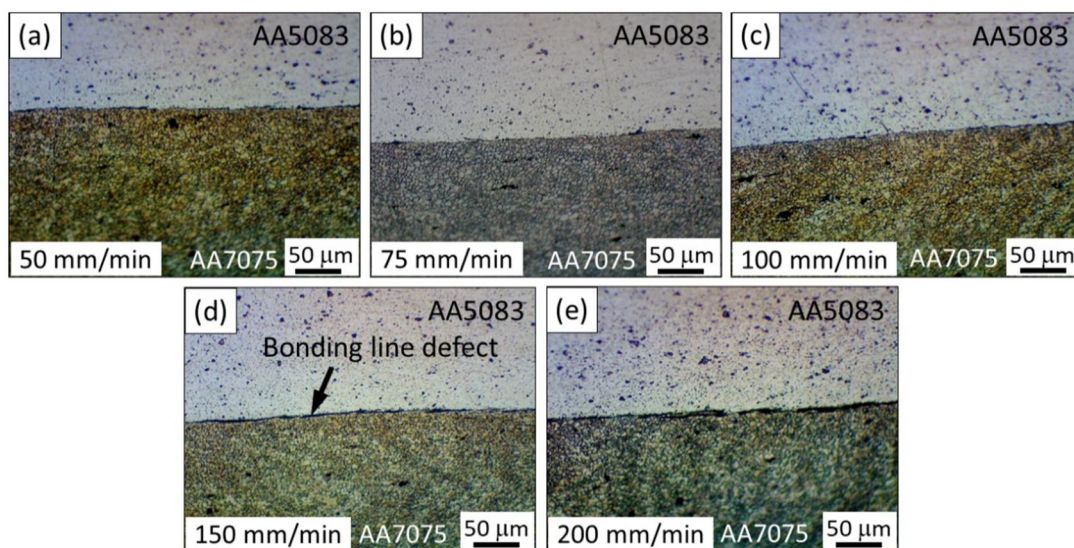


Figure 2-11 Bonding line defects produced under various welding conditions measured at center bonding interface.

2.2.2.2 Role of welding speed on defect formation

The effect of welding speed on the formation of four types of defects in T-lap joints is quantitatively summarized in Figure 2-12. Here, the defect sizes were directly measured based on oxide film on the cross-section of the specimens by means of the optical microscope. In addition, the difference in the bonding strength of defect interfaces would lead to the dissimilar fracture surface. The size of defects can be determined based on these differences by means of the SEM. The results showed that the welding speed significantly impacted the defect formations. The tunnel and bonding line defects were drastically changed by controlling welding speed. According to that, these types of defects might be minimized by decreasing the welding speed. In contrast, increasing the welding rate is useful to reduce hook defects size. However, the KBs which formed under all welding conditions were insensitive to welding speed. It seems that the specimen produced at the welding rate of 100 mm/min showed the best interface with small defect size. The presence of the hook and the KB defects can decrease the effective bonded width that affected the strength of the T-lap joints.

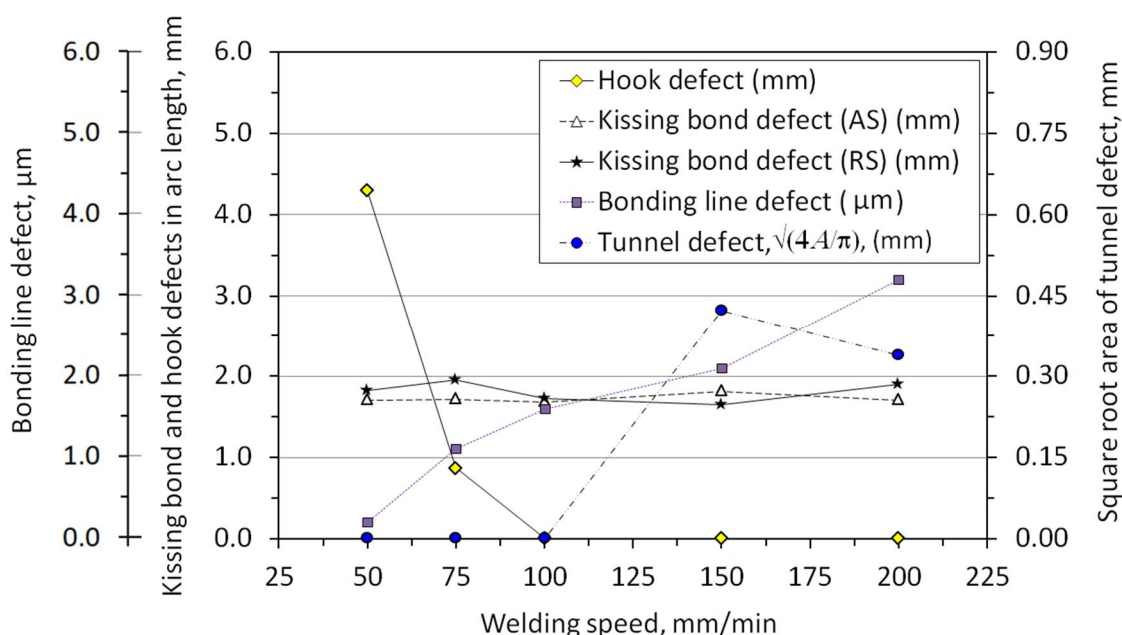


Figure 2-12 Influence of welding speed on the formation of each type of defect in T-lap joints.

2.2.2.3 Mechanical properties of T-lap joints

(a) Hardness distribution: The influence of the welding speed on the hardness profile of the T-lap joints along skin plate are shown in Figure 2-13(a). It is found that there is insignificant difference in hardness value under various welding conditions. Note from the experimental data in Figure 2-13, the soft zone with lower hardness was formed around the jointed area. The width of soft zone tended to be narrowed down with increasing welding speed. This result might be affected by heat input that depended on the welding parameters. The longitudinal hardness profile along the stringer is depicted in Figure 2-13(b). The lowest hardness value of 95 HV was found on the AA7075 side at area apart from 10.0 mm the upper surface of the skin plate. The type of heat affected zone (HAZ) was more pronounced with decreasing the welding rate, or specific heat input.

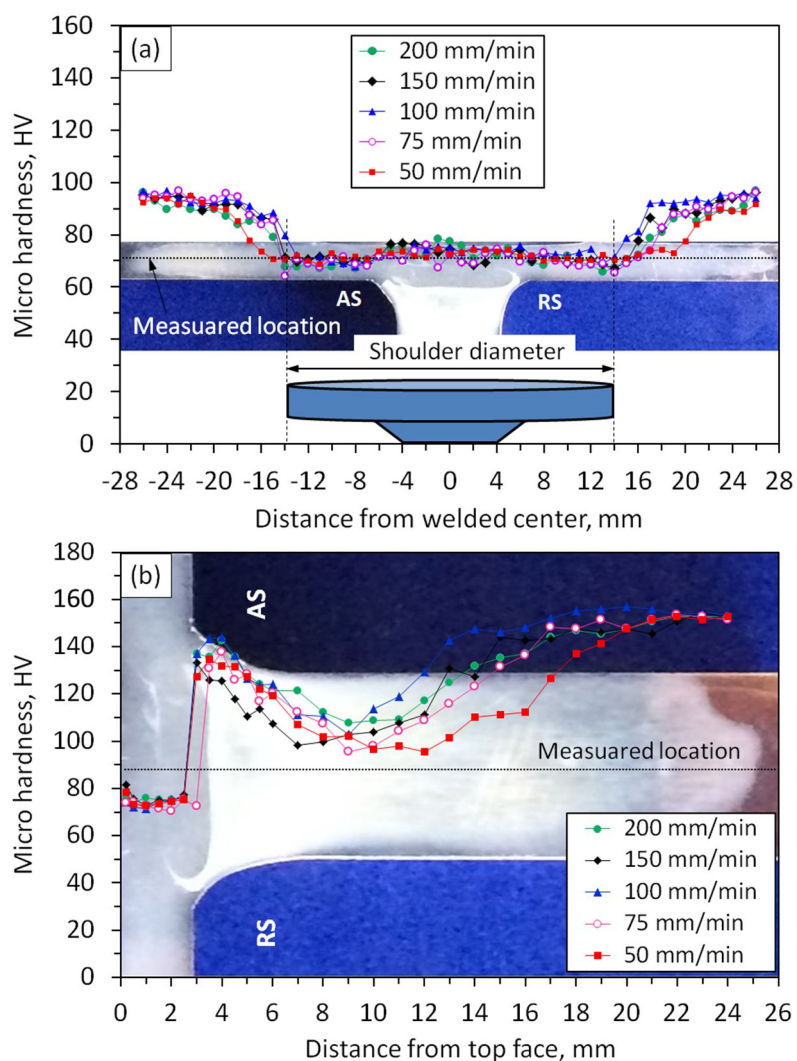


Figure 2-13 Effect of welding speed on hardness maps of (a) skin and (b) stringer plates.

(b) Local bonding strength: The local bonding strength along the interface of the T-lap joints by the welding rate of 50 mm/min is measured in Figure 2-14, where the testing process is demonstrated in Figure 2-3. It is clear that the maximum tensile strength was heterogeneous. The strength at position [E] with the presence of the KBs was nearly zero. The bonding strength at hook position (as denoted [A]) was higher than that at the KBs site. However, it was much lower than the strength of [B], [C], and [D] sites those were the bonding interface. These results showed that the effects of the KBs and hook defects on the bonding strength was the most harmful. Furthermore, the local bonding strength at the RS (denoted [B]) was more dominant than that at other sites, which location fracture was took place at the HAZ with the lowest value hardness, as seen in Figure 2-13(b). The asymmetry of metal flow during the FSW process might bring about this result. The influence of welding parameters on the local bonding strength along the interface extracted from the site [C] is presented in Figure 2-15. It is found that the welding condition which could minimize the bonding line defects reached the highest tensile strength (compare Figure 2-15 with Figure 2-11); it was taken by the welding speed of 50 mm/min.

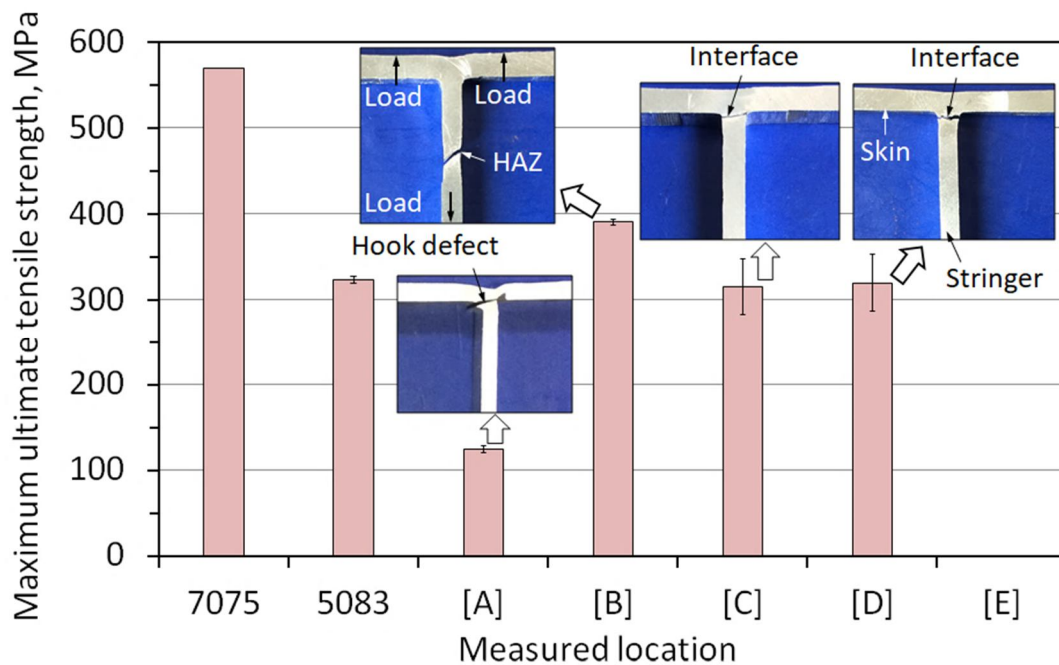


Figure 2-14 Local bonding strengths along interface with inserting fracture locations at welding speed of 50 mm/min.

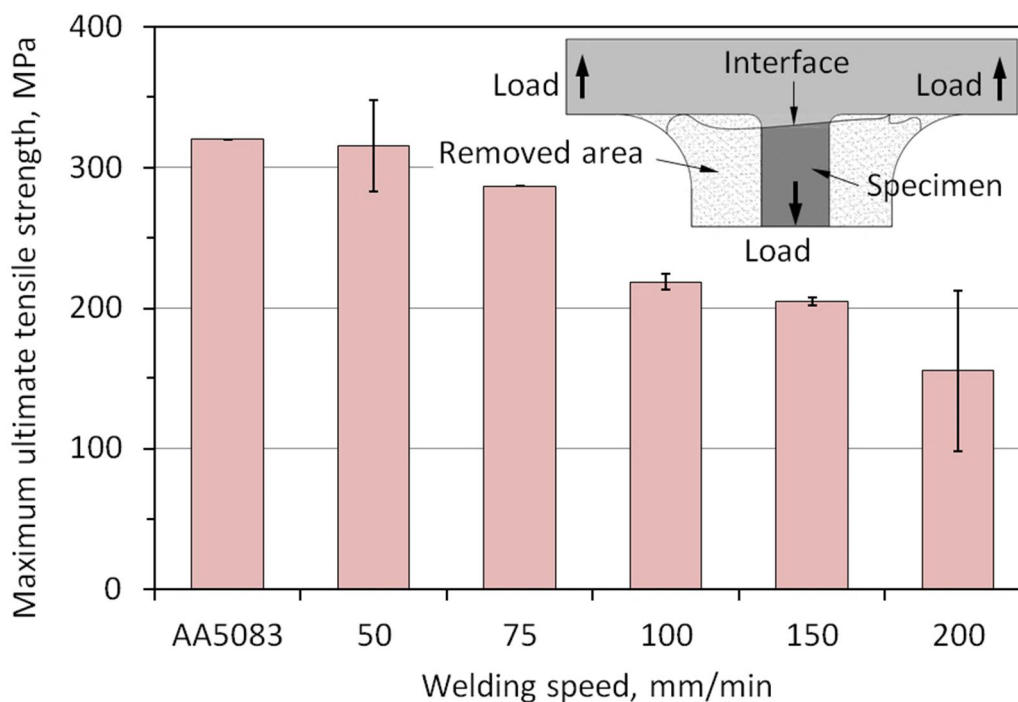


Figure 2-15 Effect of welding parameters on the bonding strength of interface measured at center.

(c) Tensile strength of global T-lap joint: Figure 2-16(a) displays the comparison of the different stress-strain curves of the global T-lap joints under the skin tensile test with various welding conditions. It is worthy to note that most of these curves overlapped each other in elastic deformation regime. However, they are significant differences after the yield strength. As presented in Figure 2-16(b), the ultimate tensile strength was raised with increasing the welding speeds from 50 to 100 mm/min, and then deeply reduced at 200 mm/min. The highest tensile strength and rupture strain of the specimen under the skin test was approximate 290 MPa and 12%, respectively, which was attained at 100 mm/min. According to that, the joint efficiency was about 90% compared to the strength of AA5083 base alloy. These results might relate to the defect formation during the FSW process. Similarly to the stress-strain curve in the skin tensile test, the load-displacement curves under the stringer test were also significantly affected by welding rate (Figure 2-17). Noting that there was an optimum welding rate by which the maximum stringer strength was attained; it was by 100 mm/min.

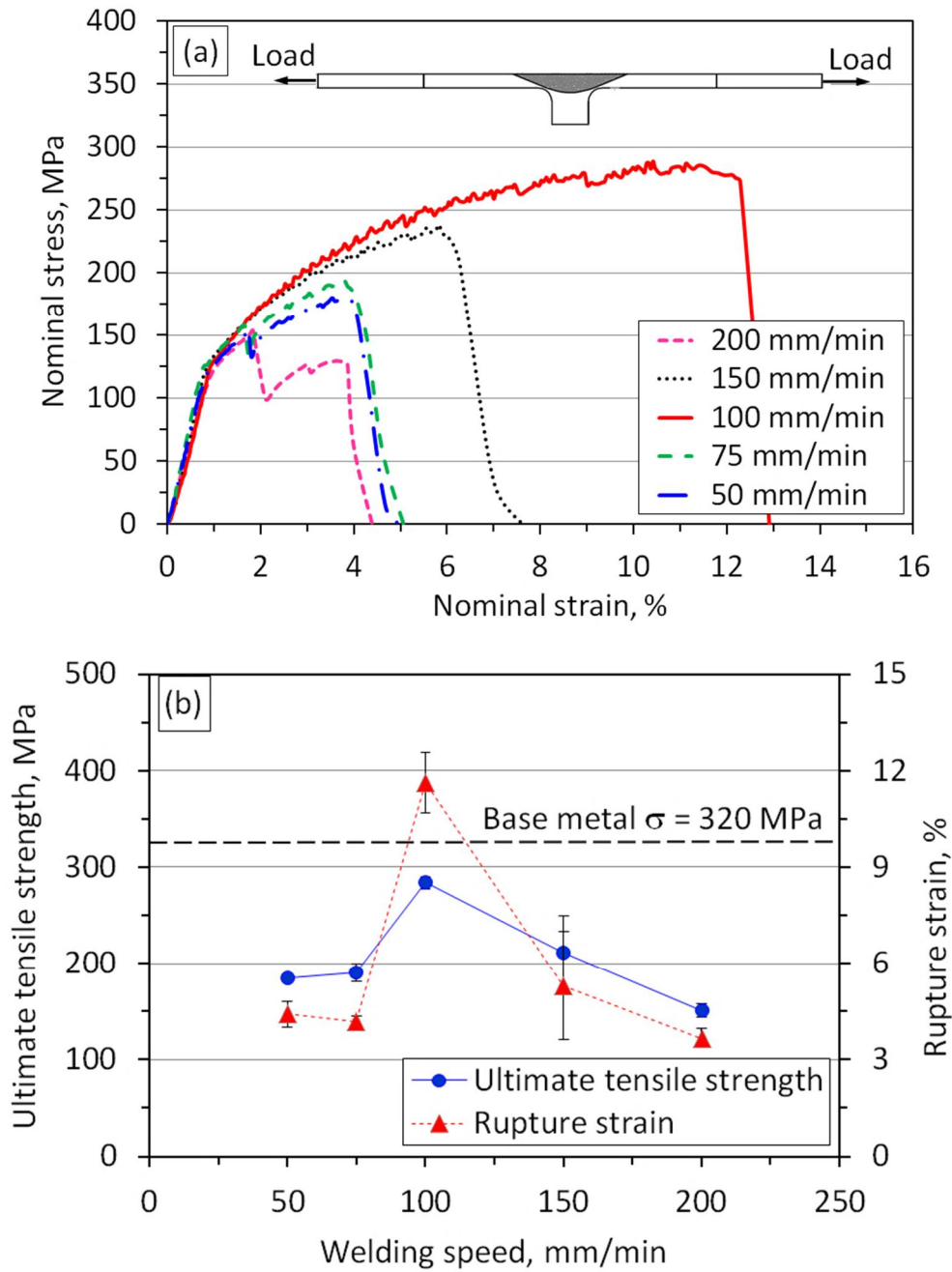


Figure 2-16 Mechanical properties of the full size joint by the skin test. (a) Stress-strain curves and (b) maximum ultimate tensile strength and rupture strain.

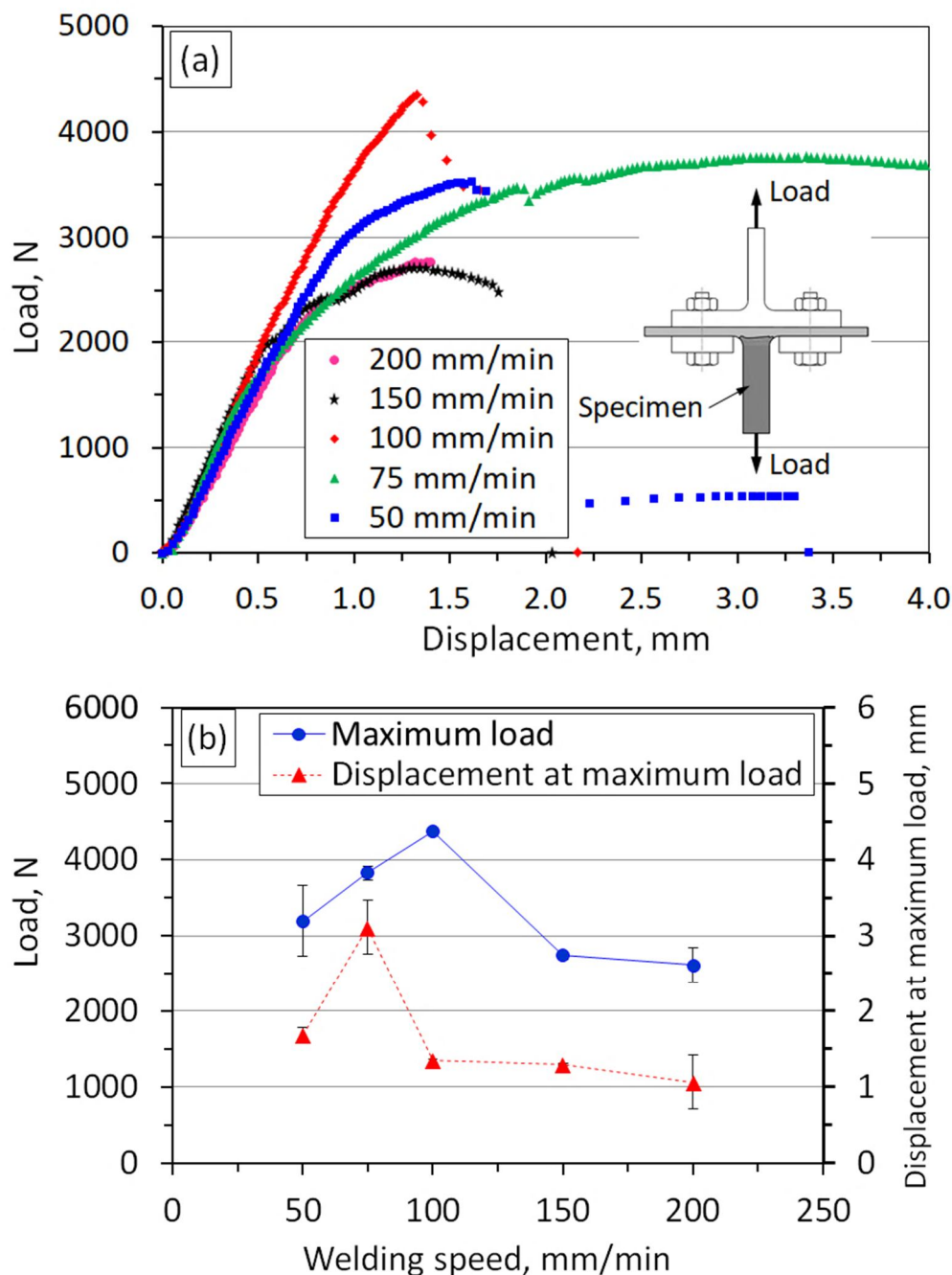


Figure 2-17 Mechanical properties of the full size joint by the stringer test. (a) Load-displacement curves and (b) maximum load and displacement at maximum load.

(d) Role of defects on mechanical properties of T-lap joints: the fracture location and fractography of the specimens under the skin tensile test is presents in Figure 2-18. Three typical modes of failure were observed; those were denoted by FT1, FT2, and FT3, respectively. In the FT1 mode, the fracture took place at the hook defects region that was pronounced in the joints at the low welding rates of 50 and 75 mm/min

associating with smooth fracture surface (Figures 2-18(d,g)). The joints failed by this mode showed the low strength (Figure 2-16(b)). In the FT2 mode, on the other hand, the fracture was nucleated around the HAZ area (Figure 2-18(b)) where the hardness value is the lowest, as shown in Figure 2-13(a). Consequently, the highest strength was found with fracture surface associated with the ductile dimples mode (Figures 2-18(e,h)). This type of mode was realized at the welding rate of 100 mm/min. The role of the tunnel defects was clear in the FT3 mode; these were significant under the high welding speed (Figures 2-18(c,f,i)). It is worthy to note that in all cases the bonding line defects seems to have insignificant effect on the skin tensile test.

Regarding the stringer tensile test, two main modes; denoted by FT4 and FT5, were observed as shown in Figures 2-19(a) and 2-20(a), respectively. The mode FT4 that was found in the welding rates of 50 and 75 mm/min was stimulated not only by the hook defects but also by the KBs. These defects degraded the strength and increased displacement of the joints, as shown in Figure 2-17. Based on local bonding strength along interface shown in Figure 2-14, this failure can be initiated at the KBs in both the AS and RS sides in which the bonding strength was the lowest, and then propagated along the hook defects before rupture. From the microscopic aspect shown in Figures 2-19(b-e), the fracture morphologies were heterogeneous with some of them revealed ductile fracture, the others did brittle fracture. Meanwhile, the bonding line defects were considered as main reason for the failure of FT5 mode that cracked along interface (Figure 2-20(a)). This kind of failure was found at the higher welding speeds. Figures 2-20(c-o) show the difference in fracture surface at various positions, as marked in Figure 2-20(b). Some trench-likes with a large number of oxygen were more dominant at the AS compared to the RS. This might lead to the lower bonding strength at the AS in comparison with the RS, as indicated in Figure 2-14. A large number of dimple on the fracture surface indicated ductile failure in this mode.

Based on these observations, the role of each type of defects in the mechanical properties of the T-lap joints is summarized in Table 2-3. Since the welding speed of 100 mm/min took the highest strength, the selection of the welding condition which can minimize the hook defects size must be the most effective.

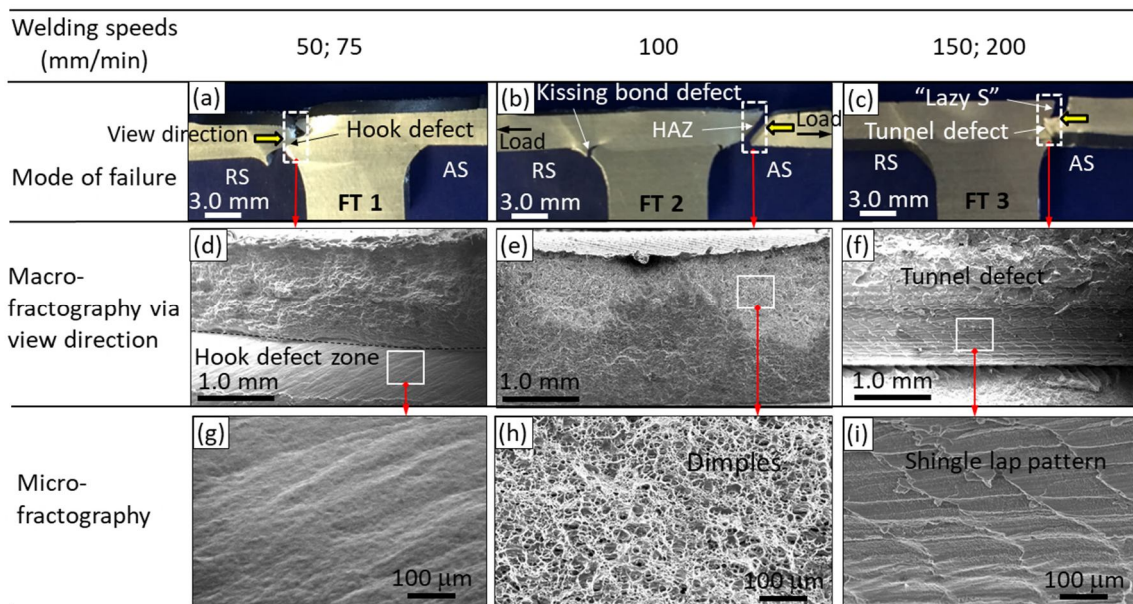


Figure 2-18 Failure behavior of specimens under skin tensile test in T-lap joints. (a-c) fracture location and (d-i) corresponding fractographies.

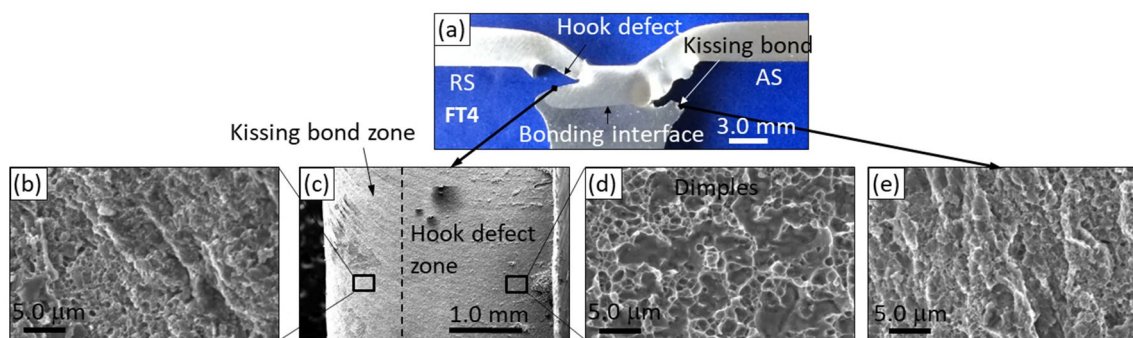


Figure 2-19 (a) Fracture location and (b-e) fractography of FT4 at welding rate of 50 mm/min.

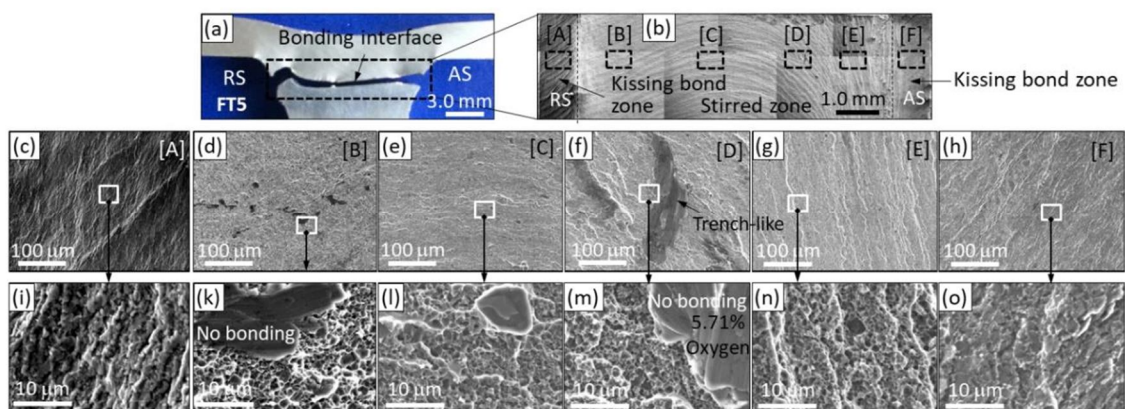


Figure 2-20 (a) Fracture location and (b-o) fractography of FT5 at welding rate of 100 mm/min.

Table 2-3 Summary influence of defects on failure of T-lap joints.

| Type of test | Skin tensile test | | | Stringer tensile test | |
|---------------------|-------------------|----------------|-----|-----------------------|-----|
| Modes of failure | FT1 | FT2 | FT3 | FT4 | FT5 |
| Tunnel defect | ⊗ | ⊗ | ○ | ⊗ | ⊗ |
| Hook defect | ○ | ⊗ | ⊗ | ○ | ⊗ |
| Kissing bond defect | △ | ⊗ | ⊗ | △ | △ |
| Bonding line defect | ⊗ | ⊗ | ⊗ | ⊗ | ○ |
| | ⊗ No effect | ○ Major effect | | △ Minor effect | |

2.3 Effects of Probe Length

2.3.1 Experimental procedures

In this section, the dissimilar T-lap joints were still produced by applying single-pass FSW induced by four various probe lengths. Note that, in order to limit the formation of hook defects at the RS found in previous section, the geometry of welding tool and die was designed again, as presented at Figure 2-21(a). Here, four welding tools were same non-thread cylinder probe but different probe length. The probe geometries and detail dimensions are illustrated in Figure 2-21(b) and Table 2-4, respectively. The probe axis alignment was set at a constant with the tilt angle of 2.0° . The shoulder penetration into the surface of skin plate was set up at the depth of 0.2 mm during the FSW process. Based on previous work, the skin and stringer plates were welded at a welding rate of 100 mm/min and rotational speed of 400 rpm. The performance of the T-lap joints was also carried out with two types of tests as presented in first section (Figure 2-2).

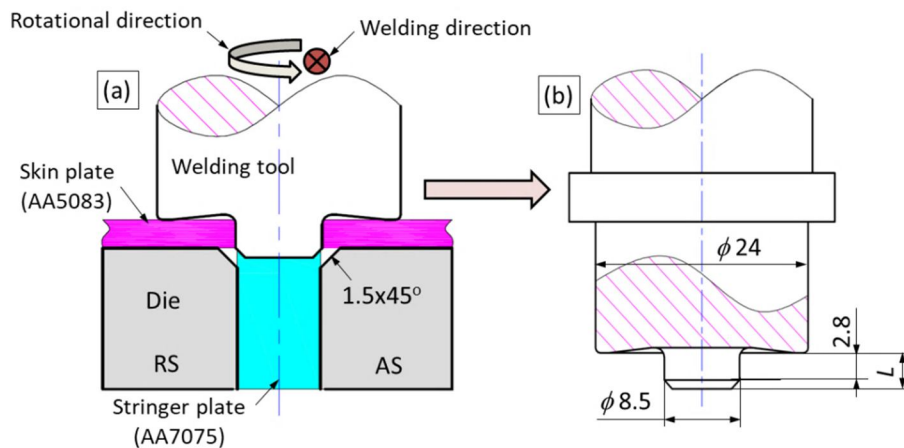


Figure 2-21 (a) Schematic diagrams of FSWed T-lap joints and (b) tool probe geometry.

Table 2-4 Main dimensions of various probes.

| Dimension of probe | Probe 1 | Probe 2 | Probe 3 | Probe 4 |
|------------------------|---------|---------|---------|---------|
| Probe length, L (mm) | 3.0 | 3.2 | 3.4 | 3.7 |
| Shoulder diameter (mm) | | 24.0 | | |
| Probe diameter (mm) | | 8.5 | | |

2.3.2 Results and discussion

2.3.2.1 Cross-section of T-lap joints

The representative macrostructure on the cross-section of the T-lap joints produced by the various probe lengths is displayed in Figure 2-22. Here, the images of welding interface defined as boundary between two materials formed after the FSW process were observed. There were three typical types of defects along welding interface were detected: hook, kissing bond (KBs), and bonding line defects. It seems that the size and geometry of these defects significantly depended on the various probe lengths.

The microstructure of cross-section produced by Probe 4 is shown in Figure 2-23. The locations of welding zone and the defects were indicated in Figure 2-23(a). Here, the KBs were formed in two corner fillets (Figure 2-23(d)). In other words, they were outside stirred zone (SZ). In contrast, the hook defects were a joint line uplifting originated from the RS to SZ (Figure 2-23(b)). These types of defects were identified due to the continuous dark line of oxide layer along interface. Meanwhile, the bonding line defects were observed at the SZ along interface that was produced by shorter probe length. The discontinuous dark line of oxide layer was the characteristic of this defect, as shown in Figure 2-23(e). A perfect interface without oxide layer produced by longer probe was referred to as “bonding interface” in this work (Figure 2-23(c)).

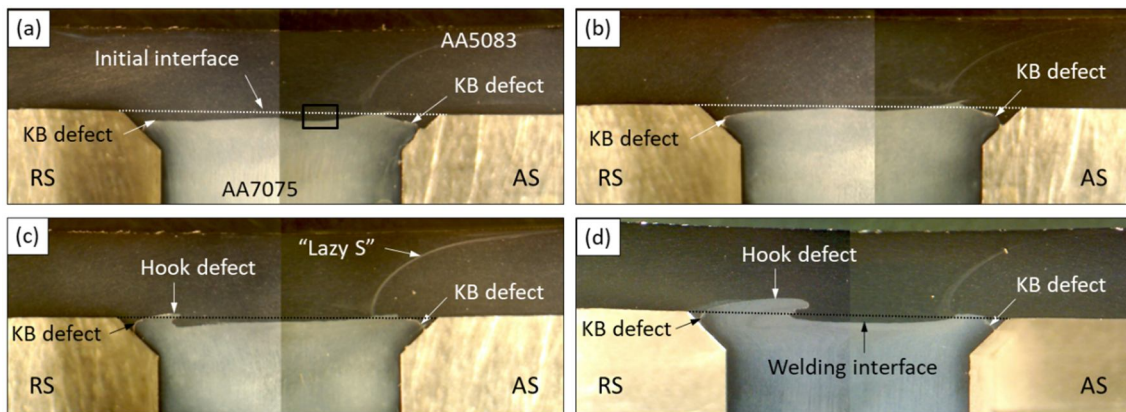


Figure 2-22 Representative images of macrostructure of cross-section of T-lap joints produced by (a) Probe 1, (b) Probe 2, (c) Probe 3, and (d) Probe 4.

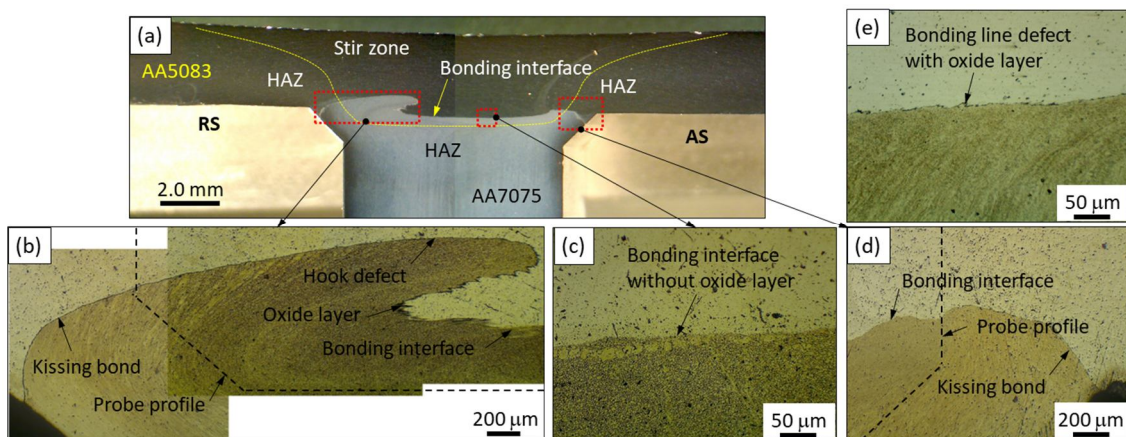


Figure 2-23 Microstructure of cross-section of T-lap joints produced by Probe 4: (a) cross-section, (b) geometry of hook defects and KBs at RS, (c) bonding interface at center, (d) geometry of KBs at AS, and (e) bonding line defects at center marked in Figure 2-22(a).

2.3.2.2 Role of probe length on defect formation

In order to evaluate quantitatively the influence of probe length on the defect formations, the sizes of them were directly measured on the specimens based on oxide layer and fracture surface, and shown in Figure 2-24. It is worthy to note that the hook and bonding line defects were significantly affected by probe length. Here, increasing the length of tool probe would lead to reduction in the size of bonding line defects but this increased the formation of hook defects, resulting in reducing the width of bonding interface. Dissimilar to hook and bonding line defects, the KBs seem to be independent of the probe length. The insignificant change in the KBs size indicated this postulation.

On other words, the FSWed interface was strongly susceptible with the change in probe length that related to the penetration of probe into the stringer plate. The probe penetration into workpieces is illustrated in Figure 2-25 and is expressed as following:

$$T = d + L\cos\alpha - (R-r)\sin\alpha \quad (1)$$

$$s = T - t \quad (2)$$

where T , t , d , L , R , r , s and α is determined in Figure 2-25. The calculated results showed that increasing probe length would lead to growth in probe penetration into the stringer, as shown in Figure 2-26. It is noted that the probe with 3.0 mm of length seems to be not enough to produce a stirring action along the stringer part. In this case, the welding interface might be formed by severe thermal deformation during the FSW process. This means that the lack of stirring action along the interface was reason for the formation of oxide layer (Figure 2-23(e)), resulting in low bonding strength. In addition, the interface was not pulled up by vertical flow, as illustrated in Figure 2-27(a). Consequently, the hook defects were not formed in this case [11,30,31].

Figure 2-27(b) illustrates the penetration of probe length of 3.7 mm into the stringer part. It is clear that using longer probe allows penetration to further exceed the initial interface between the skin and stringer parts. As a result, the stirring action strongly happened along interface during the FSW process, resulting in the formation of a sound bonding interface without oxide layer, as shown in Figure 2-23(c). This means that a high bonding strength might be reached at the interface. It is worthy to note from Figure 2-27(b), a hook defect was significantly formed at the RS. This is the result of pulling up interface caused by vertical and horizontal flows [32,33]. In all cases, the probe length was not main reason for the KBs formation. Minimizing this type of defects will be carried out in the next chapter.

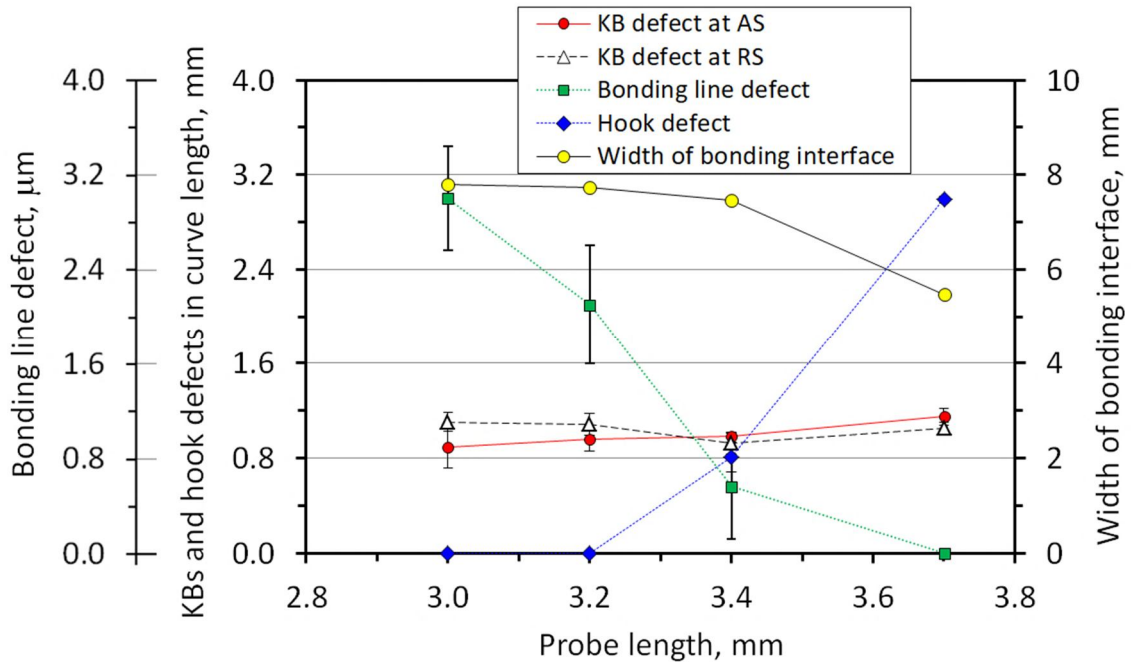


Figure 2-24 Effect of probe lengths on size of defect and bonding interface.

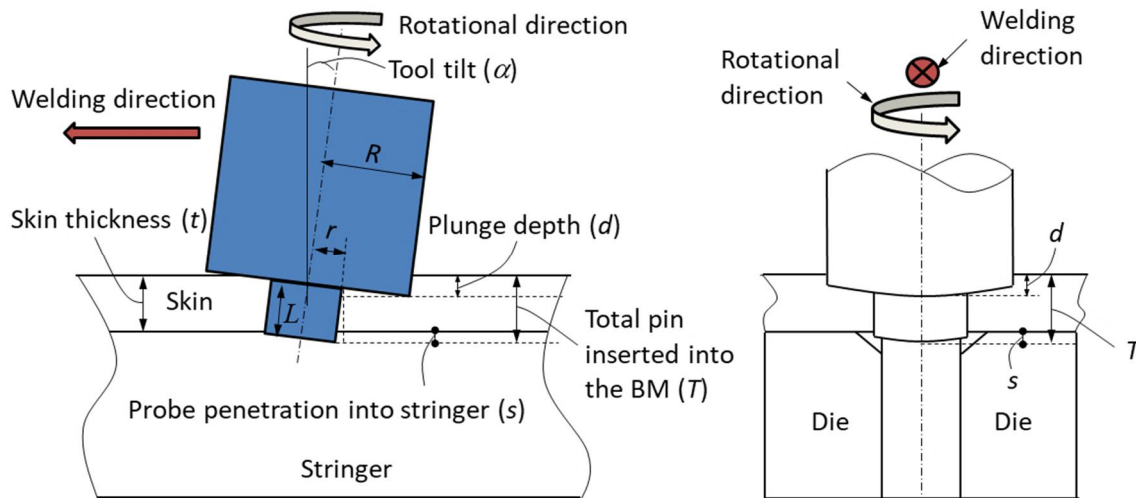


Figure 2-25 Schematic for determining probe penetration into workpieces.

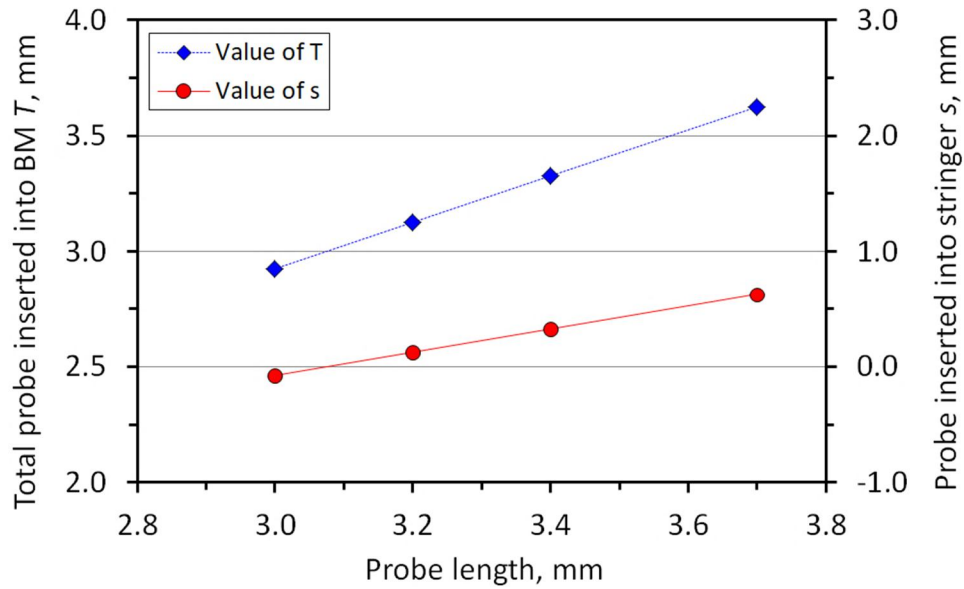


Figure 2-26 Effect of probe lengths on probe penetration.

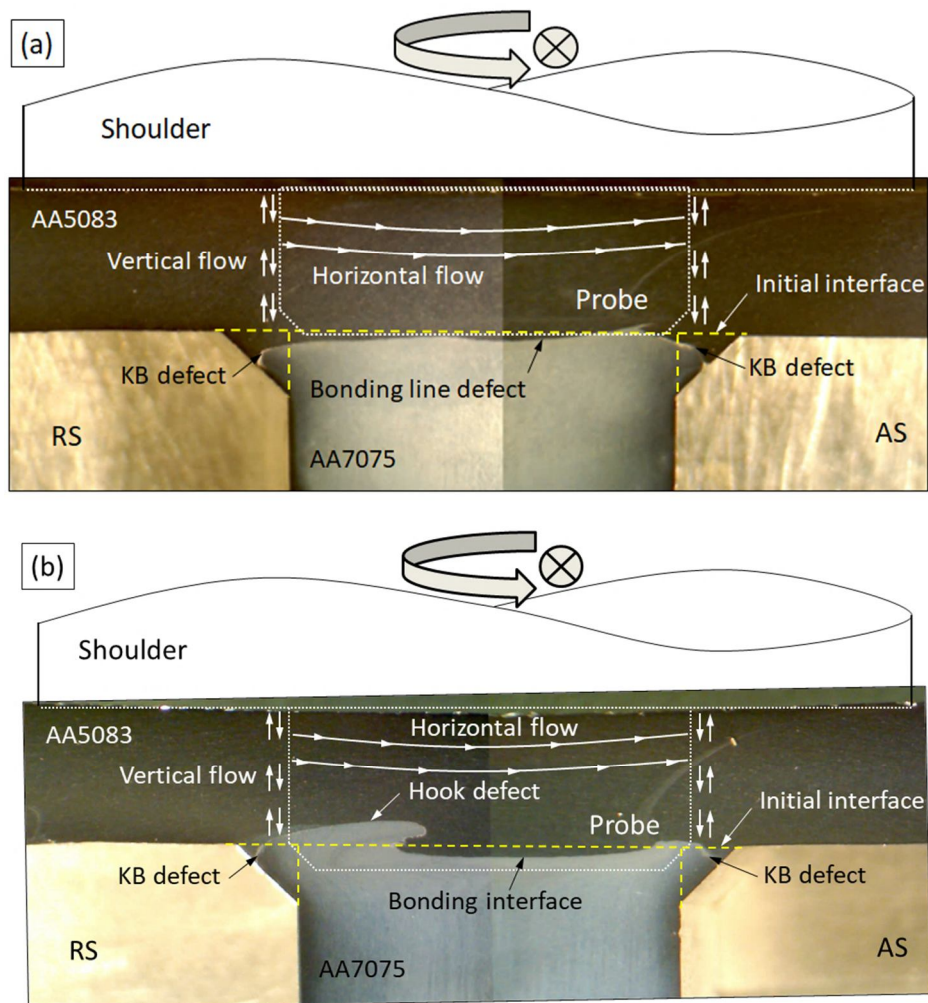


Figure 2-27 Schematic illustration of material flow produced by (a) probe length of 3.0 mm and (b) 3.7 mm in FSW process.

2.3.2.3 Mechanical properties of T-lap joints

(a) Tensile strength under skin tensile test: The representative stress-strain curves under skin tensile test are presented in Figure 2-28(a). It is worthy to note that the curves nearly overlapped each other but difference in maximum stress and rupture strain. The application of different probe lengths did not affect the yield strength of samples that was attained about 130 MPa. However, there were significant differences in the maximum tensile strength and rupture strain, as presented in Figure 2-28(b). Here, the tensile strength and rupture strain of the joints lightly raised with growing the probe lengths from 3.0 mm to 3.4 mm, and then deeply reduced at 3.7 mm. The highest value was attained approximately 290 MPa of the tensile strength and 11% of the rupture strength at the probe length of 3.4 mm. In this case, the joint efficiency was reached about 90% in comparison with the AA5083 base alloys.

Figure 2-29 shows the fracture location of the specimens. It can be seen that two typical modes of failure were detected; those were FT1 and FT2. Here, the fracture location of the specimens in FT1 originated from the KBs at the AS, then propagated and failed at the “Lazy S”, as shown more clearly in Figure 2-30(a). This type of fracture was pronounced at the short probes of 3.0 mm and 3.2 mm. The oxide layer that was found along at the “Lazy S” might be reason for degrading the strength of the joints, as shown in Figure 2-30(d). The fracture surface of this mode is displayed in Figure 2-30(f) associating with smooth facet, not much dimples could be observed in this region.

On the other hand, the fracture was nucleated from the hook defects in the FT2 mode, as shown in Figure 2-30(b). This mode was realized at the probe lengths of 3.4 mm and 3.7 mm. The highest strength in this mode was detected with fracture surface associated with the ductile dimples, as seen in Figure 2-30(g). It seems that the fracture at the hook defects in this type of mode had relationship to effective skin thickness (EST) that is defined as minimum distance from interface of defects to the top face of skin part. As presented in Figure 2-31, increasing the probe length led to reduction in the EST, especially in the RS, resulting in fracture at the hook defects. Noting that, in all cases the bonding line defects seem to do not affect the strength of the joint under the skin tensile test.

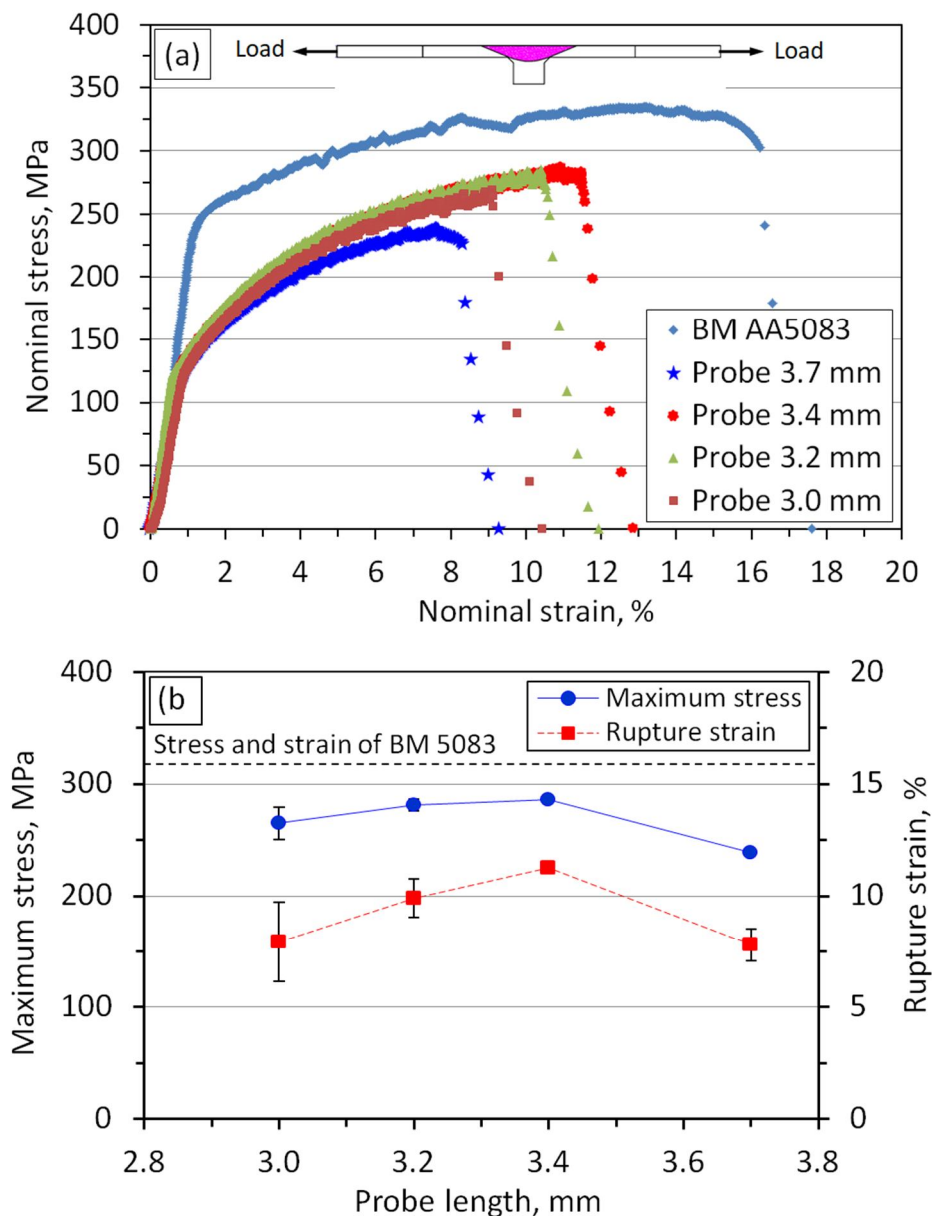


Figure 2-28 Mechanical properties of skin tensile test: (a) Stress-strain curves and (b) maximum tensile strength and rupture strain.

| Type of probe | Probe 3.0 mm | Probe 3.2 mm | Probe 3.4 mm | Probe 3.7 mm |
|-------------------|--------------|--------------|--------------|--------------|
| Type of fracture | FT1 | | FT2 | |
| Fracture location | | | | |
| 4.0 mm | | | | |

Figure 2-29 Fracture location of specimens produced by various probe lengths under skin tensile test.

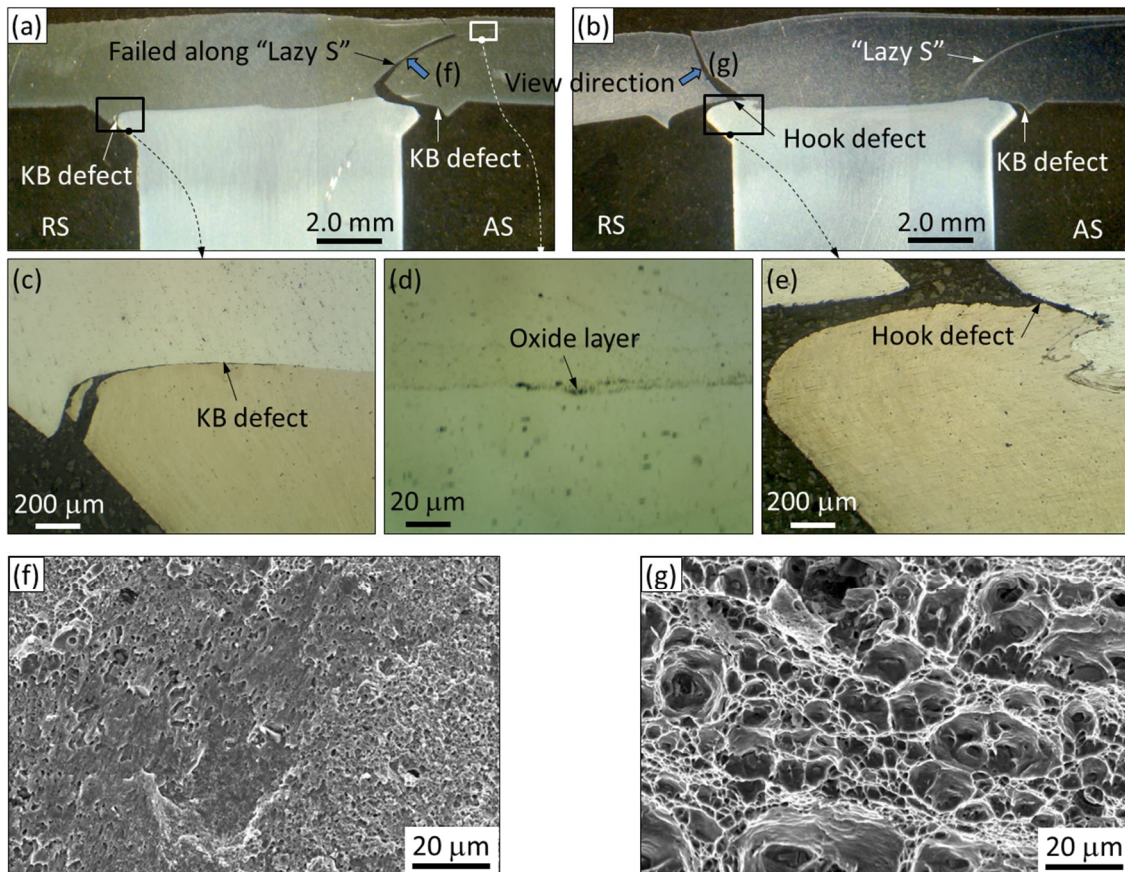


Figure 2-30 Two types of fracture: (a) Cracked “Lazy S”, (b) cracked at hook defects, (c-e) microstructure at KBs, hook defects and “Lazy S”, and (f,g) fracture surface of FT1 and FT2, respectively.

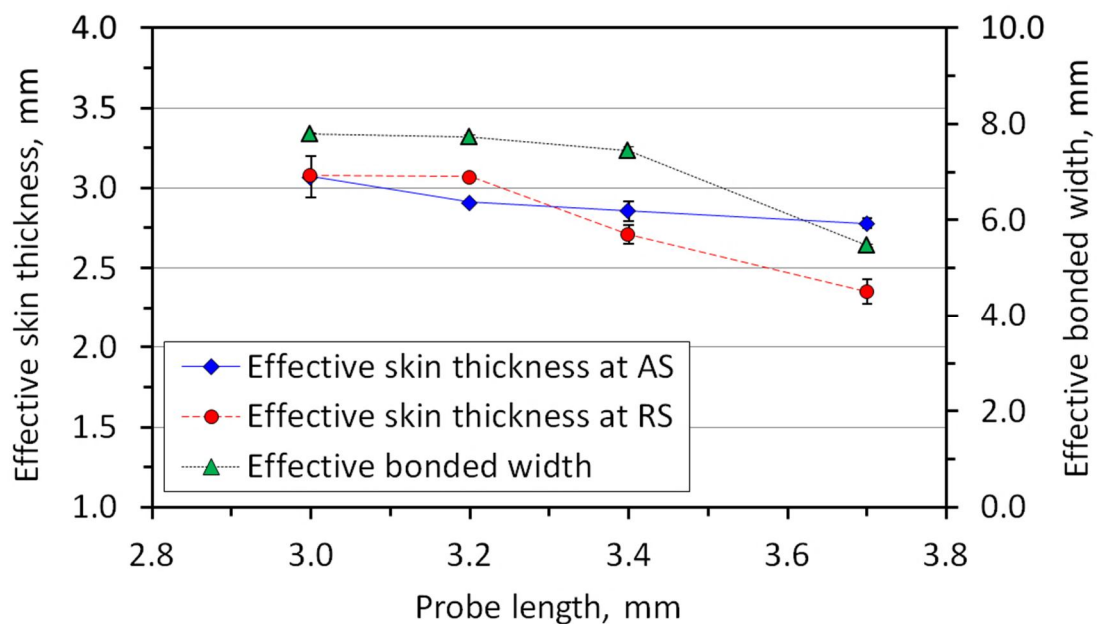


Figure 2-31 Effect of probe lengths on effective skin thickness.

(b) Tensile strength under stringer tensile test: The load-displacement curves of the specimens under the stringer tensile test are shown in Figure 2-32(a). Here, the curves of the specimens produced by the probe lengths of 3.0 and 3.2 mm were nearly similar. A same result was also obtained by applying the probe lengths of 3.4 and 3.7 mm. The quantitative evaluation of the influence of the probe length on the strength of the T-lap joints under stringer tensile test is displayed in Figure 2-32(b). It is clear that increasing the length of probe expressively improved the tensile strength of the joints. It seems that the reasonable probe length was ranged from 3.4 to 3.7 mm those were attained the high strength of the joints. However, the highest joint efficiency was low about 67% compared to the BM AA5083.

Three main failure modes were observed under the stringer tensile test, denoted by FT3, FT4, and FT5, as presented in Figure 2-33. The type of FT3 was observed in the short probe lengths of 3.0 mm and 3.2 mm. The welding joints failed by this mode brought about the low strength (Figure 2-32(b)). In contrast, the FT5 mode, that was found at the probe length of 3.7 mm, initiated from the KBs, then propagated and cracked the skin plate at the end of the hook defects. A mixed-crack of FT3 and FT5 modes was detected in FT4 produced by the probe length of 3.4 mm. Here, the crack originated at two KBs, then moved along interface and finally ruptured at the skin plate. It seems that the bonding strength of center interface was stronger than that of other sites.

The bonding line defects were considered as main reason for these failures. In order to evaluate quantitatively this postulation, the bonding strength of interface produced by various probe lengths was investigated. Here, a miniature specimen extracted from original sample was applied, as presented in Figure 2-34(a) and Figures 2-35(a-d). It is clear that using longer probe increased the bonding strength of the interface (Figure 2-34(b)). As shown in Figures 2-35(e-h), the probe length had the weighty effect on the formation of the bonding line defects. Applying the probe length of 3.7 mm eliminated oxide layer from the interface, resulting in reaching the highest bonding strength. The fracture location of miniature specimen is evidence for this result (Figures 2-35(i-m)).

From the microscopic aspect shown in Figure 2-36, the fracture morphologies were heterogeneous under the various probe lengths. Fracture surface produced by the

probe lengths of 3.0 and 3.2 mm was observed as smooth facet with some trenches that indicated a weak bonding strength (Figures 2-36(a,b,d,e)). In contrast, arc-shaped stripes [34] that were caused by probe penetration were occurred on fracture surface produced by the probe length of 3.4 mm (Figures 2-36(c,f)). The fracture morphologies with some dimples showed as ductile fracture mode.

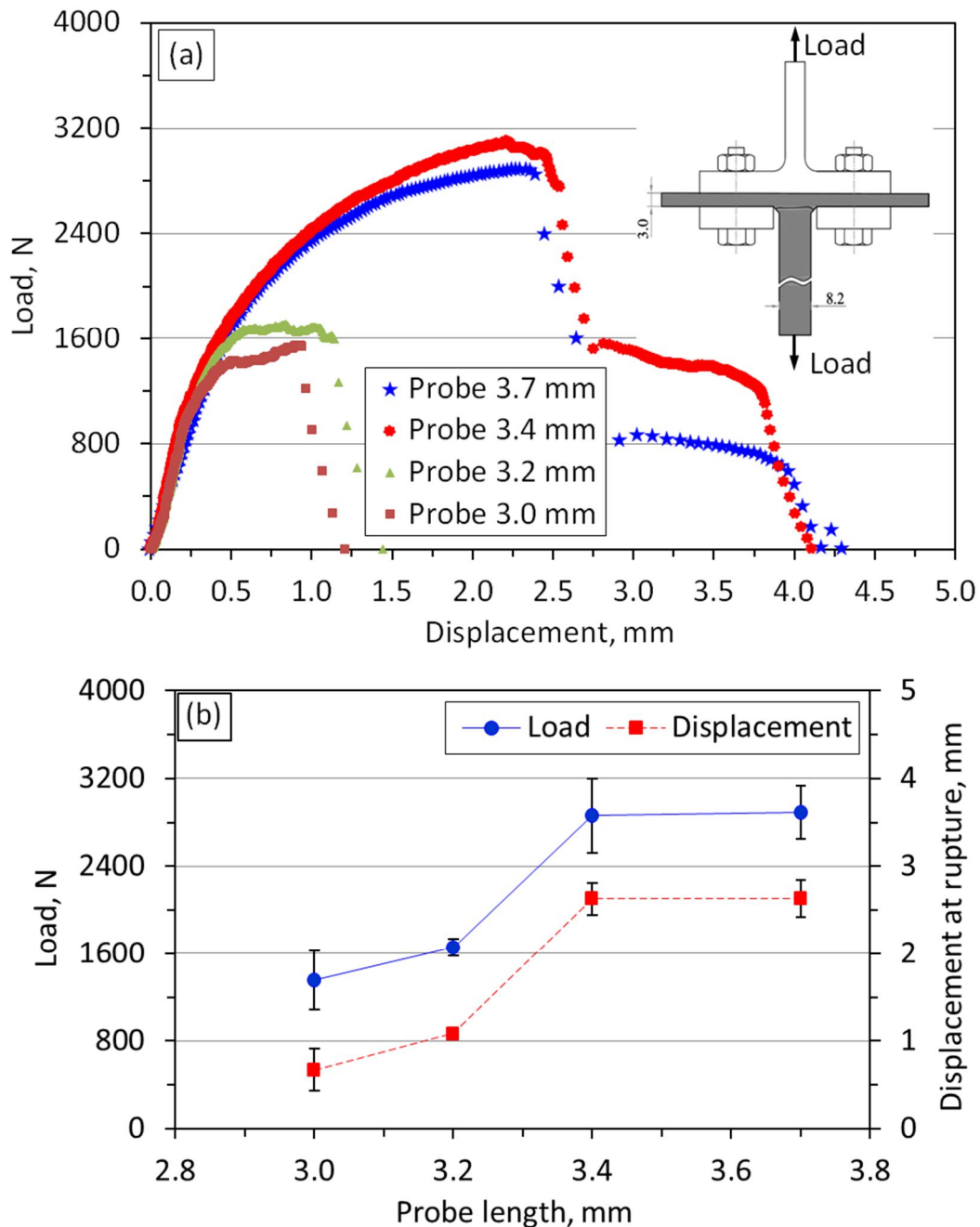


Figure 2-32 (a) Load-displacement curves and (b) maximum load and displacement at rupture under stringer tensile test.

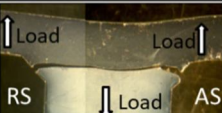
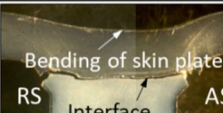
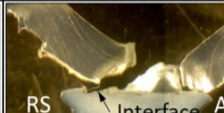
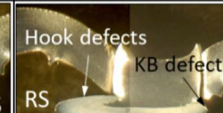
| Type of probe | Probe 3.0 mm | Probe 3.2 mm | Probe 3.4 mm | Probe 3.7 mm |
|-------------------|---|---|--|---|
| Type of fracture | FT3 | | FT4 | FT5 |
| Fracture location |  |  |  |  |

Figure 2-33 Fracture location of specimens produced by various probe lengths under stringer tensile test.

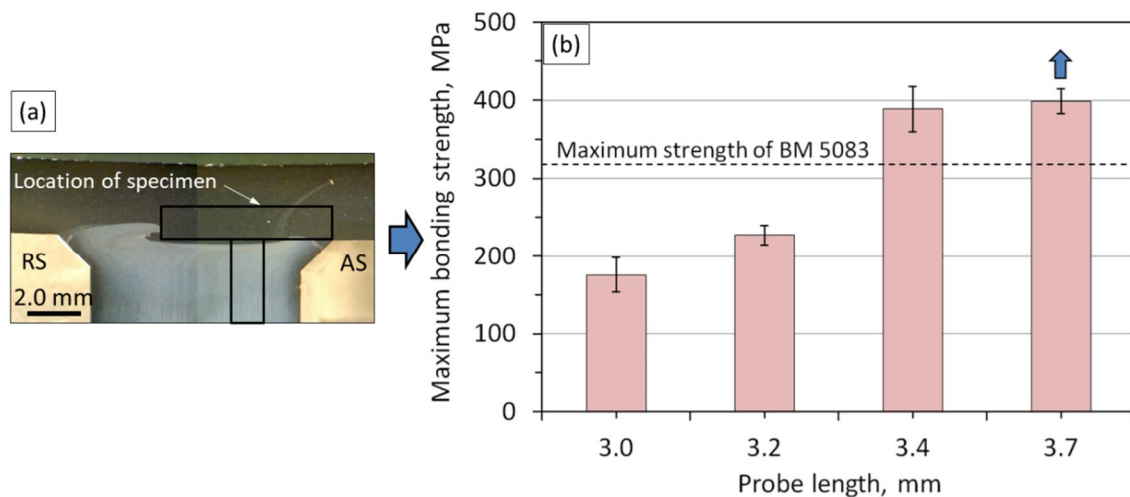


Figure 2-34 (a) Location of miniature specimen extracted from original samples and (b) effect of probe lengths on bonding strength of interface.

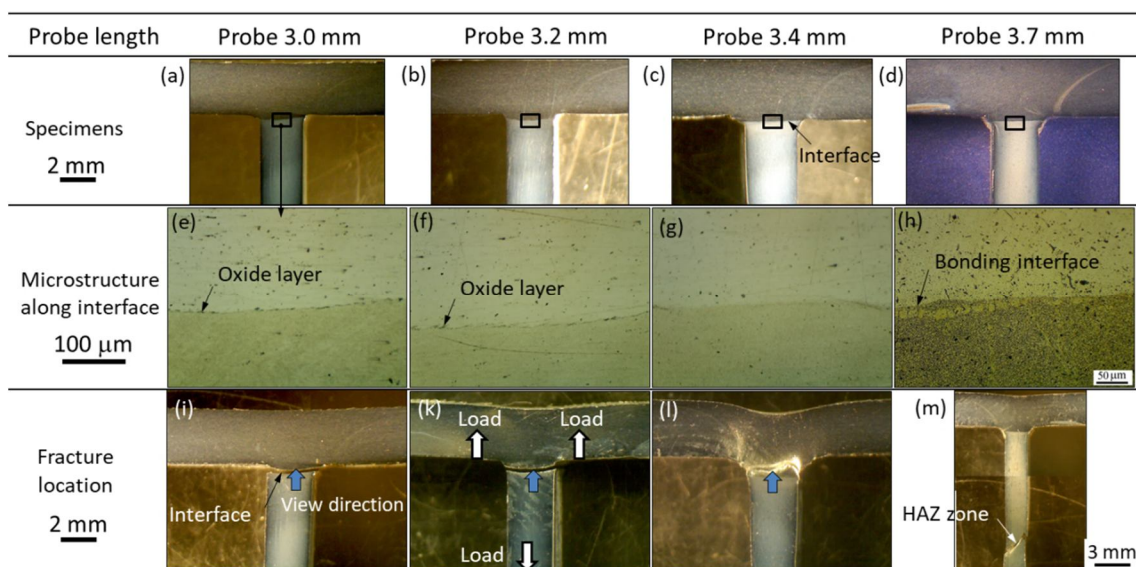


Figure 2-35 (a-d) Specimens before testing, (e-h) microstructure along interface, and (i-m) fracture location of specimens produced by various probe lengths.

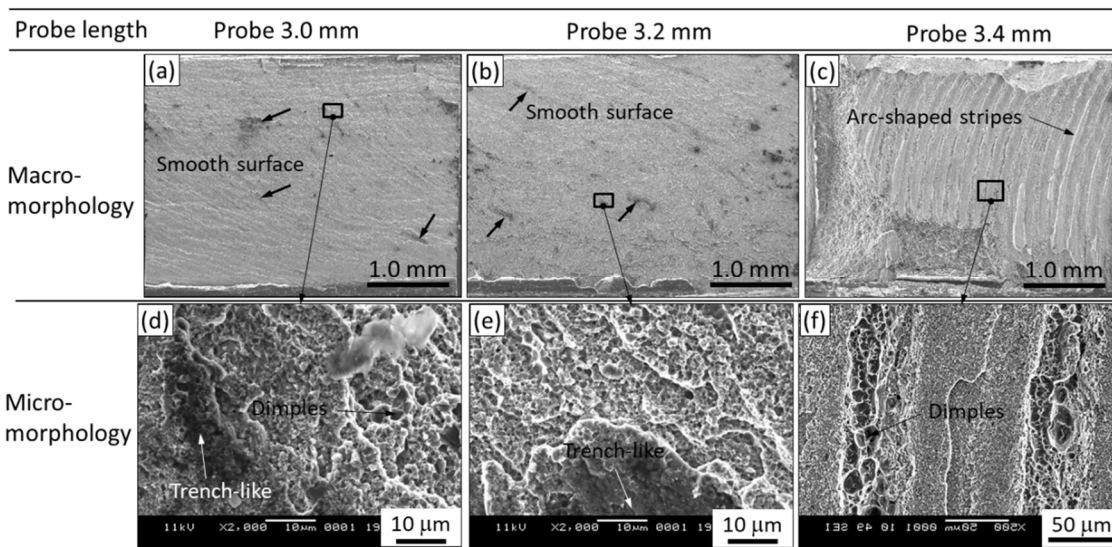


Figure 2-36 (a-c) Macro- and (d-f) micro-morphology of fracture surface of specimens produced by various probe lengths.

2.4 Interface Morphology Affected by Welding Parameters

As presented in previous sections, the interface morphology was significantly changed with increasing or decreasing welding speed as well as probe length, especially in the RS. In order to make platform for quantitative assessment about these influences on the strength of the T-lap joints, the quantification of defects at the AS and RS was investigated as following:

2.4.1 Quantification of defects affected by welding speed

The quantification of defects of the interface is defined as in Figure 2-37. The effect of the welding speed on these parameters is shown in Figure 2-38(a) at the RS and Figure 2-38(b) at the AS. It is clear that the parameters at the RS were more sensitive to the welding speeds than that at the AS, especially in the low value of the welding speed. As mentioned in previous section, the formation of the hook defects at the low welding speed led to significant reduction in the effective skin thickness (t), or effective ligament ratio (t/T) (Figure 2-38(c)), and increase in the projected length a . The effect of these parameters on the strength of the T-lap joints will be discussed in Chapter 5.

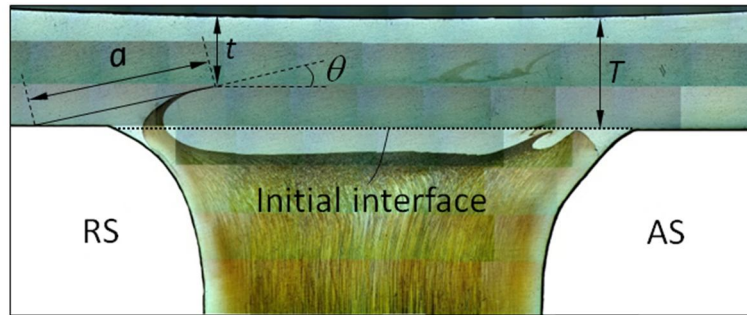
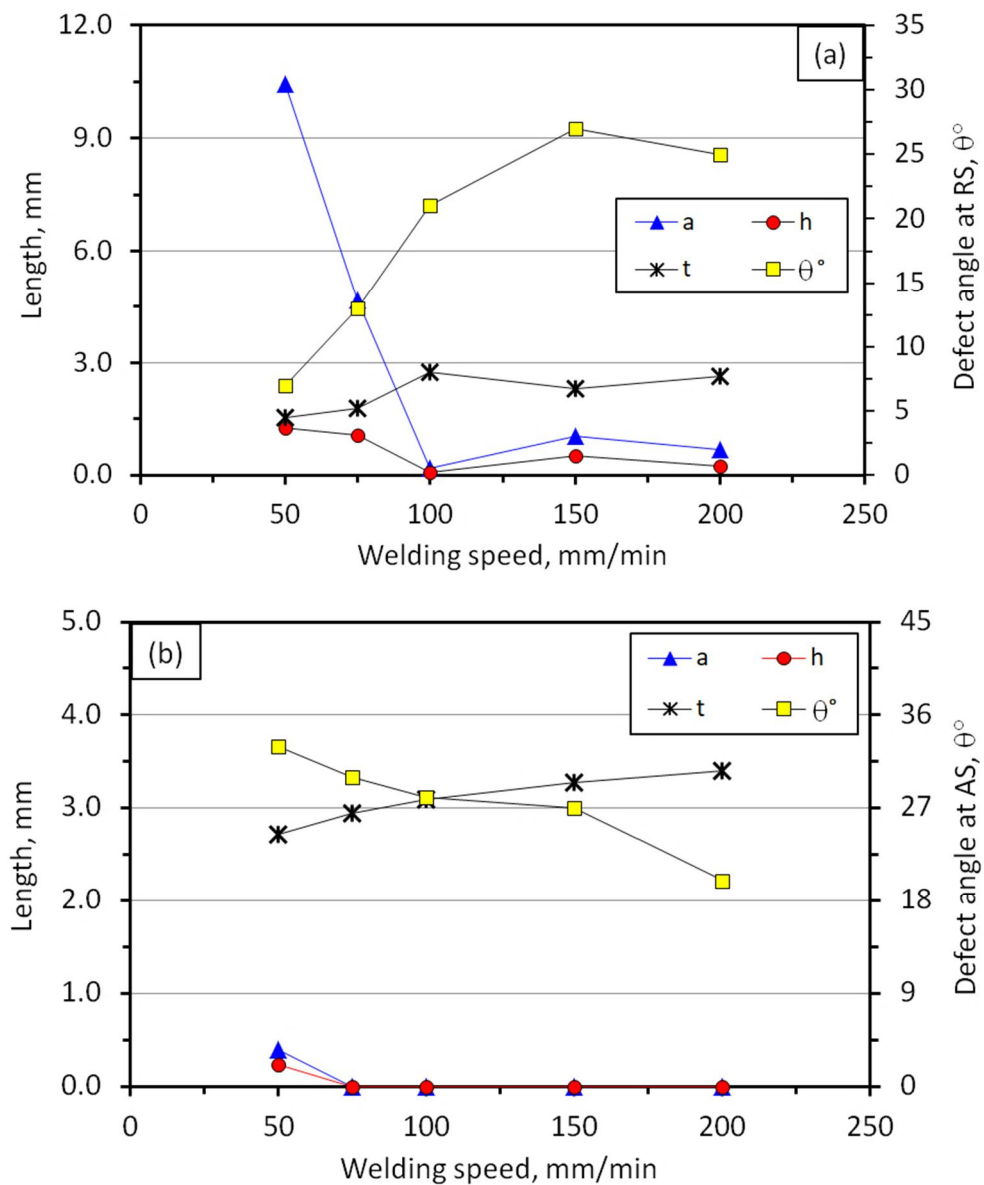


Figure 2-37 Define some parameters of quantification of defects.



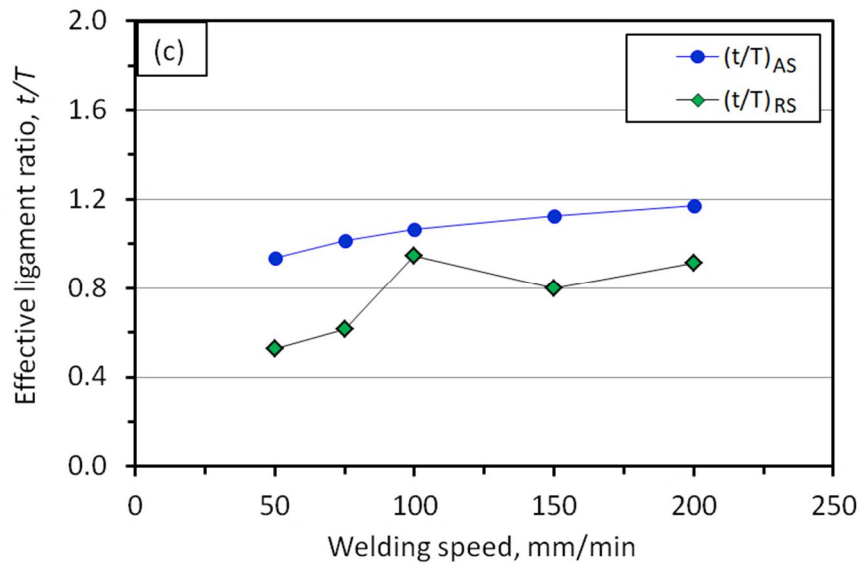


Figure 2-38 Effect of the welding speeds on quantification of defects at (a) the RS, (b) the AS, and (c) effective ligament ratio, t/T .

2.4.2 Quantification of defects affected by probe length

The effect of the probe length on the quantification of defects is shown in Figure 2-39(a) at the RS and Figure 2-39(b) at the AS. It is similar to the effect of the welding speed, the parameters at the AS seem to be insensitive to the probe length, compared to the RS. The formation of the hook defects at the RS with the long probe might be reason for this change. Here, increasing the probe length would lead to significant increase in the projected length a , bonding angle θ , and reduction in effective ligament ratio (t/T) (Figure 2-39(c)). The influence of these parameters on the strength of the T-lap joints will be discussed in Chapter 5.

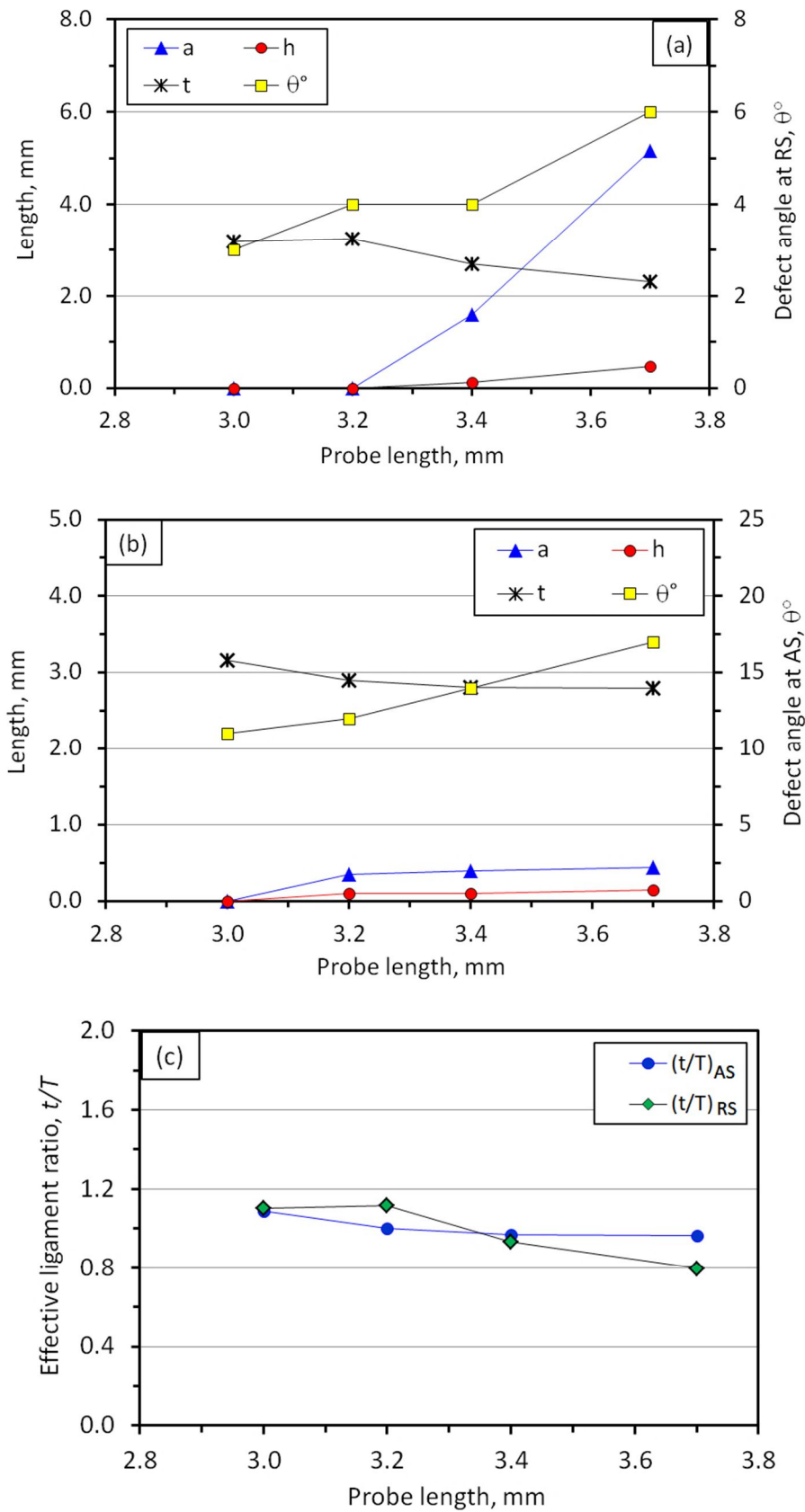


Figure 2-39 Effect of the probe lengths on quantification of defects at (a) the RS, (b) AS, and (c) effective ligament ratio, t/T .

2.5 Chapter Summary

The dissimilar metal T-lap joints between AA5083 and AA7075 were fabricated by traditional single-pass FSW. The fundamental formation of the interface morphology and the mechanical properties of the joints were investigated. The following conclusions were reached:

- (2-1) The welding speed and probe length were two of the important variables to control interface morphology that had close relation to the formation of some defects. Here, the increase in the welding speed or reduction in the probe length could contribute to decrease the hook defect size. However, these changes would lead to increase in the formation of the bonding line defects that reduced the bonding strength of the interface.
- (2-2) The kissing bond defects seem to be too hard to be eliminated by applying only traditional single-pass welding. The gap between tool probe and die may be reason for the formation of this defect.
- (2-3) The good interface morphology of the T-lap joints with small defect size was found at the welding speed of 100 mm/min. In this case, the joint efficiency under the skin tensile test might be reached about 90% compared to AA5083 base alloy. However, the strength of the joints under the stringer tensile test was not satisfactory.
- (2-4) The quantification of defects of the interface at the AS seems to be insensitive to welding parameters, compared to the RS. The formation of the hook defects at the RS can be reason for these results. The influence of these parameters on the strength of the T-lap joints will be discussed in Chapter 5.
- (2-5) It seems that the application of traditional single-pass FSW is too hard to improve the interface morphology of the T-lap joints. This issue will be dealt with by a new method in next chapter. Based on the findings in this chapter, the welding speed of 100 mm/min and the probe length of 3.7 mm were chosen as two of the basic parameters in the improvement of the interface morphology and mechanical properties of the FSWed T-lap joints that were carried out in Chapter 3.

2.6 Chapter References

- [1] Mishra, R.S. and Ma, Z.Y., Friction stir welding and processing, *Materials Science and Engineering R*, Vol.50, (2005), pp.1-78.
- [2] Threadgill, P.L, Leonard, A.J, Shercliff, H.R and Withers, P.J, Friction stir welding of aluminum alloys, *International Materials Reviews*, Vol.54, (2009), pp.49-93.
- [3] Malopheyev, S., Vysotskiy, I., Kulitskiy, V., Mironov, S., Kaibyshev, R., Optimization of processing-microstructure-properties relationship in friction-stir welded 6061-T6 aluminum alloy, *Materials Science and Engineering: A*, Vol.662, (2016), pp.136-143.
- [4] Cavaliere, P., Squillace, A., Panella, F., Effect of welding parameters on mechanical and microstructural properties of AA6082 joints produced by friction stir welding, *Journal of Materials Processing Technology*, Vol.200, (2008), pp.364-372.
- [5] Doude, H., Schneider, J., Patton, B., Stafford, S., Waters, T., Varner, C., Optimizing weld quality of a friction stir welded aluminum alloy, *Journal of Materials Processing Technology*, Vol.222, (2015), pp.188-196.
- [6] Costa, M.I., Verdera, D., Costa, J.D., Leitao, C., Rodrigues, D.M., Influence of pin geometry and process parameters on friction stir lap welding of AA5754-H22 thin sheets, *Journal of Materials Processing Technology*, Vol.225, (2015), pp.385-392.
- [7] Kulekci, M.K., Şik, A. and Kaluç, E., Effects of tool rotation and pin diameter on fatigue properties of friction stir welded lap joints, *The International Journal of Advanced Manufacturing Technology*, Vol.36, (2008), pp.877-882.
- [8] Badarinarayan, H., Shi, Y., Li, X., Okamoto, K., Effect of tool geometry on hook formation and static strength of friction stir spot welded aluminum 5754-O sheets, *International Journal of Machine Tools and Manufacture*, Vol.49, (2009), pp.814-823.
- [9] Amini, S., Amiri, M.R., and Barani, A. Investigation of the effect of tool geometry on friction stir welding of 5083-O aluminum alloy, *The International Journal of Advanced Manufacturing Technology*, Vol.76, (2015), pp.255-261.
- [10] Kumar, K., Kailas, S.V., and Srivatsan, T.S., Influence of Tool Geometry in Friction Stir Welding, *Materials and Manufacturing Processes*, Vol. 23(2), (2008), pp.188-194.
- [11] Ge, Z., Gao, S., Ji, S., and Yan, D., Effect of pin length and welding speed on lap joint quality of friction stir welded dissimilar aluminum alloys, *The International Journal of Advanced Manufacturing Technology*, Vol.98, (2018), pp.1461-1469.
- [12] Wang, M., Zhang, H., Zhang, J., Zhang, X., & Yang, L., Effect of Pin Length on Hook Size and Joint Properties in Friction Stir Lap Welding of 7B04 Aluminum Alloy, *Journal of Materials Engineering and Performance*, Vol.23(5), (2014), pp.1881-1886.
- [13] Piccini, J.M., and Svoboda, H., Effect of pin length on Friction Stir Spot Welding (FSSW) of dissimilar Aluminum-steel joints, *Procedia Materials Science*, Vol.9, (2015), pp. 504-513.

- [14] Cui, L., Yang, X., Zhou, G., Xu, X. and Shen, Z., Characteristics of defects and tensile behaviors on friction stir welded AA6061-T4 T-joints, *Materials Science and Engineering A*, Vol.543, (2012), pp.58-68.
- [15] Zhao, Y., Zhou, L., Wang, Q., Yan, K. and Zou, J., Defects and tensile properties of 6013 aluminum alloy T-joints by friction stir welding, *Materials and Design*, Vol.57, (2014), pp.146-155.
- [16] Donati, L., Tomesani, L. and Morri, A., Structural T-joint produced by means of friction stir welding (FSW) with filling material, *International Journal of Material Forming* Vol.2, (2009), pp.295-298.
- [17] Said, M.T.S.M., Hamid, D.A., Ismail, A., Zainal, S.N.N., Awang, M., Rojan, M.A., Ikram, I.M. and Makhtar, M.F., Experimental Study on Effect of Welding Parameters of Friction Stir Welding (FSW) on Aluminium AA5083 T-joint, *Information Technology Journal*, Vol.15, (2016), pp.99-107.
- [18] Jesus, J.S., Costa, J.M., Loureiro, A. and Ferreira, J.M., Assessment of friction stir welding aluminium T-joints, *Journal of Materials Processing Technology*, Vol.255, (2018), pp.387-399.
- [19] Manuel, N., Silva, C., Costa, J.M.D., and Loureiro, A., Friction stir welding of T-joints in dissimilar materials: Influence of tool geometry and materials properties. *Materials Research Express*, Vol.6, (2019), pp.106528.
- [20] Buffa, G., Fratini, L., Micari, F. and Shivpuri, R., Material Flow in FSW of T-joints: Experimental and Numerical Analysis, *International Journal of Material Forming*, Vol.1(1), (2008), pp.1283-1286.
- [21] Fratini, L., Buffa, G., Micari, F. and Shivpuri, R., On the material flow in FSW of T-joints: Influence of geometrical and technological parameters, *International Journal of Advanced Manufacturing Technology*, Vol.44(5-6), (2009), pp.570-578.
- [22] Annual Book of ASTM Standards, Test methods for tension testing of metallic materials, E08, (2004), ASTM International.
- [23] Chen, H.B., Yan, K., Lin, T., Chen, S.B., Jiang, C.Y. and Zhao, Y., The investigation of typical welding defects for 5456 aluminum alloy friction stir welds. *Materials Science and Engineering A*, Vol.433, (2006), pp.64-69.
- [24] Khan, N.Z., Khan, Z.A., Siddiquee, A.N., Al-Ahmari, M., A. and Abidi, M.H., Analysis of defects in clean fabrication process of friction stir welding, *Transactions of nonferrous metals society of china*, Vol.27(7), (2017), pp.1507-1516.
- [25] Liu, Z., Zhou, Z. and Ji, S., Improving interface morphology and shear failure load of friction stir lap welding by changing material concentrated zone location, *International journal of advanced manufacturing technology*, Vol.95, (2018), pp.4013-4022.
- [26] Meng, X., Xu, Z., Huang, Y., Xie, Y., Wang, Y., Wan, L., Lv, Z. and Cao, J., Interface characteristic and tensile property of friction stir lap welding of dissimilar aircraft 2060-T8 and 2099-T83 Al-Li alloys, *International Journal of Advanced Manufacturing Technology*, Vol.94, (2018), pp.1253-1261.
- [27] Oosterkamp, O., Oosterkamp, L.D. and Nordeide, A., 'Kissing bond' phenomena in solid-state welds of aluminum alloys, *Welding Journal*, Vol.83, (2004), pp.225-

231.

- [28] Sato, Y.S., Takauchi, H., Park, S.H.C. and Kokawa, H., Characteristics of the kissing-bond in friction stir welded Al alloy 1050, *Materials Science and Engineering A*, Vol.405, (2005), pp.333-338.
- [29] Kadlec, M., Růžek, R. and Nováková, L., Mechanical behaviour of AA 7475 friction stir welds with the kissing bond defect, *International Journal of Fatigue*, Vol.74, (2015), pp.7-19.
- [30] Chen, H., Fu, L., Liang, P., Liu, F., Defect features, texture and mechanical properties of friction stir welded lap joints of 2A97 Al-Li alloy thin sheets, *Materials Characterization*, Vol.125, (2017), pp.160-173.
- [31] Ericsson, M., Jin, L.Z., Sandström, R., Fatigue properties of friction stir overlap welds, *International Journal of Fatigue*, Vol.29(1), (2007), pp.57-68.
- [32] Silva, B.H., Zepon, G., Bolfarini, C., dos Santos, J.F., Refill friction stir spot welding of AA6082-T6 alloy: Hook defect formation and its influence on the mechanical properties and fracture behavior, *Materials Science and Engineering: A*, (2019).
- [33] Rajesh, S., and Badheka, V.J., Process parameters/material location affecting hooking in friction stir lap welding: Dissimilar aluminum alloys, *Materials and Manufacturing Processes*, Vol.33(3), (2017), pp.323-332.
- [34] Song, Y., Yang, X., Cui, L., Hou, X., Shen, Z., Xu, Y., Defect features and mechanical properties of friction stir lap welded dissimilar AA2024–AA7075 aluminum alloy sheets, *Materials & Design*, Vol.55, (2014), pp.9-18.

Chapter 3

Improvement of Interface Morphology and Mechanical Properties of Dissimilar Metal T-lap Joints between AA7075 and AA5083 by Double-pass Friction Stir Welding

From Chapter 2, it is obviously that the control of welding interface is a vital role in improving the strength of the FSWed T-lap joints. However, the application of traditional single-pass FSW with change in welding parameters seems to be unable to eliminate/or minimize absolutely the defects. The aim of this chapter is to improve the interface morphology and the strength of the dissimilar FSWed T-lap joints between AA7075 and AA5083. For this purpose, the double-pass FSW induced by reversed material flow and tool offset is applied as a new method. The effect of this method on the interface morphology and the mechanical properties of the T-lap joints is investigated in this chapter.

3.1 Introduction

The weldability of the dissimilar FSWed T-lap joints between AA7075 and AA5083 by traditional single-pass welding has been evaluated in Chapter 2. The effects of some FSW parameters on the T-lap joints characteristics have been investigated to improve the joint efficiency from the viewpoints of welding speed [1-5], tool geometry [6,7], and metal flow [8,9]. In spite of these works, the T-lap joint efficiency has still been unsatisfactory, especially in the stringer loading test. This result is due to the formation of some undesirable defects in the joints.

As presented in Chapter 2, three main types of defects were formed along interface; i.e. kissing bond, hook, and bonding line defects, those directly degraded the mechanical properties of the T-lap joints. Controlling welding parameters was unable to eliminate these defects at the same time. Although the formation mechanism of these defects was different, all of their bonding strength was low due to the occurrence of oxide layer along the interface. In order to be simple show, hereafter they will be referred to as the kissing bond defects (as denoted by KBs), as presented by Jolu et al. [10] and Feistauer et al. [11].

Some researchers applied double-pass welding as one of solutions in order to eliminate this KBs. Use of double-passes with stationary shoulder to insert the tool probe into two corner fillets of the T-lap joints seems to be effective to eliminate the KBs [12-14]. However, this method is difficult to be widely applied for the T-joints because of being complex in fabrication process. Feistauer et al. [11] tried to use the second-pass welding by keeping the similar the FSWed rotational tool direction but the reserved welding direction. Consequently, the size of the KBs was significantly reduced.

The aim of this chapter is to improve the interface morphology and the strength of the dissimilar FSWed T-lap joints between AA7075 and AA5083. For this purpose, the special attention was put on the effects of both the reversed material flow and the tool offset induced by the double-pass welding on the interface characteristics.

3.2 Experimental Procedure

3.2.1 Fabrication of FSWed T-lap joints

In this work, the skin (AA5083) and stringer (AA7075) plates were prepared in the dimensions of 300×150×3.0 mm and 300×50×8.2 mm, respectively. Based on Chapter 2, the welding tool with a cylinder probe had the shoulder diameter of 24.0 mm was chosen to fabricate the dissimilar T-lap joints (Figure 3-1(a)). The detail dimension of the welding tool is summarized in Figure 3-1(b) and Table 3-1. The probe axis alignment was kept at a constant with the tilt angle of 2.0° to the vertical direction. The tool shoulder penetrated into the surface of skin plate with the depth of 0.2 mm that was determined before the FSW process. All of samples in this work were no post-weld and analyzed after welding process about one month. Based on the Chapter 2, the welding speed and rotational speed were chosen by 100 mm/min and 400 rpm, respectively through this work.

In general, the welding temperature and material flow during FSW process are often unstable near the starting location. This can affect the quality of the joint at 0.8 mm of tool offset. In order to improve this issue, the rate of probe penetration into the base metal was applied at the low value of 5 mm/min with the dwell time of 5 s before welding. These factors might increase the stability of metal flow near the starting location.

The T-lap joints were fabricated by applying double-pass FSWed method that combined between a tool offset and reversed metal flow. Here, the tool offset which the welding tool was located at an eccentric position to the centerline of the T-joints for both the first- and second-pass FSWs is demonstrated in Figure 3-2(a). The offset interval was considered as the experimental variable in this work; those had distances from 0.0 to 1.0 mm toward both the advancing side (denoted as plus value “+”) and retreating side (denoted as minus value “-”), as illustrated in Figures 3-2(b-d). In addition, the second-pass FSW was the same welding direction but reversed tool rotation with the first-pass welding, as schematically displayed in Figure 3-2(a). So this implies, after the second-pass FSW, a new advancing side (denoted as RS1/AS2) and retreating side (denoted as AS1/RS2) were formed at retreating side (denoted as RS1) and advancing side (denoted as AS1) of the first-pass welding, respectively.

Table 3-1 Welding tool geometry and investigated location.

| Tool geometry (mm) | | | | Representative locations for investigation (mm) | | | | |
|--------------------|------------------|---------|--------------|---|--------|------------------|-----|-----|
| Ø Shoulder | Concave shoulder | Ø Probe | Probe length | Offsetting to RS | Center | Offsetting to AS | | |
| 24.0 | 5° | 8.5 | 3.7 | -0.8 | -0.4 | 0.0 | 0.4 | 0.8 |

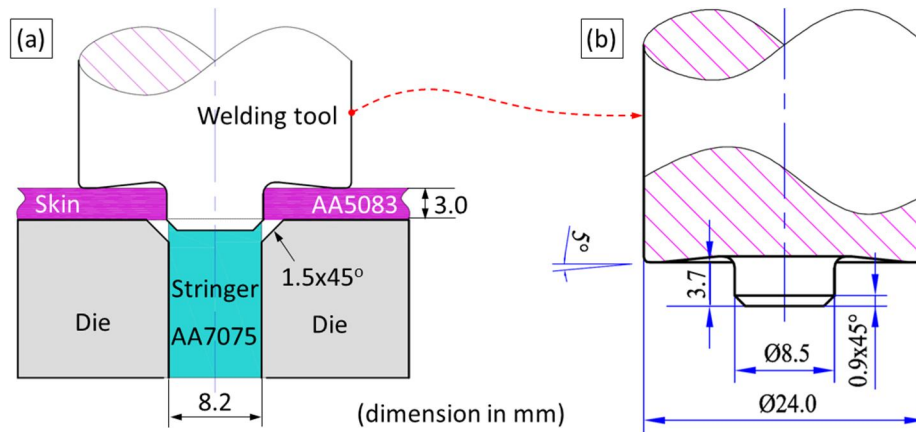


Figure 3-1 (a) Schematic view of FSWed T-lap joints and (b) dimension of welding tool.

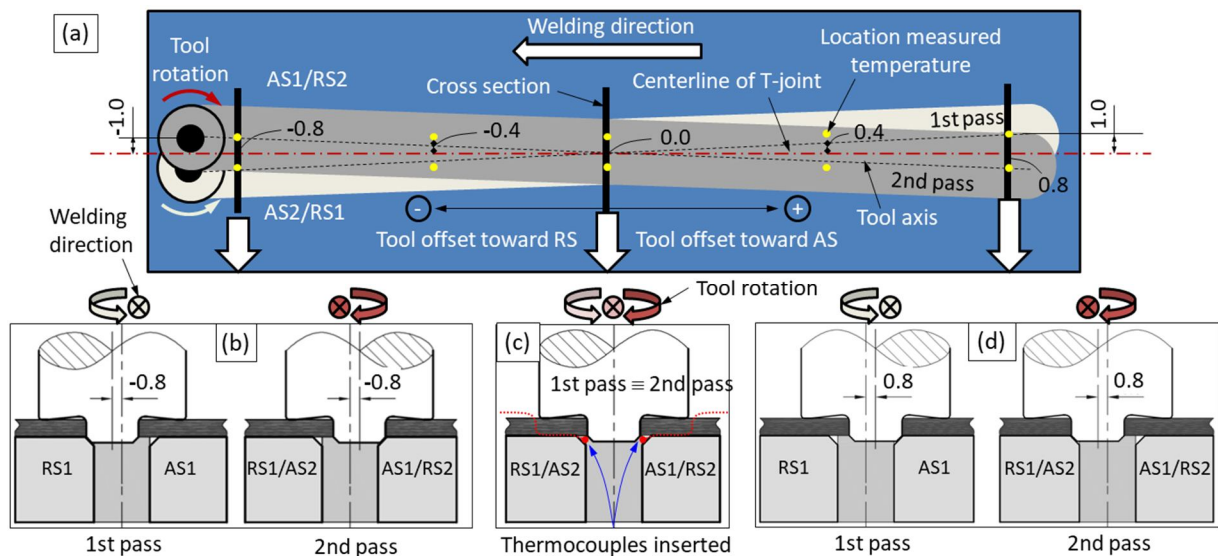


Figure 3-2 (a) Schematic diagrams of tool offset and reversed metal flow and the positions of welding tool at offsetting (b) -0.8 mm, (c) 0.0 mm, and (d) 0.8 mm.

3.2.2 Process analysis

It is well known that the temperature history provides an important knowledge to evaluate the performance of the FSW process. So, it was monitored by the K-type thermocouples inserted into two corner fillets at the multiple sites of offsetting, as indicated in Figures 3-2(a,c). The performance of the FSWed T-lap joints at each site

was evaluated from the multiple aspects in terms of the size of kissing bonds, microstructure characteristic, hardness profile, and tensile strength. A special focus was paid to the effects of the reversed metal flow and tool offset on these measurements. Here, the hardness map was measured along the centerline of the skin and stringer plates by means of micro Vickers indenter under the load of 200 gf for the hold time of 10 s. The tensile strengths were evaluated by two types of tensile tests under a strain rate of 1.0 mm/min; one is the tensile test with loading direction along the skin part, following the ASTM E8 [15] (Figure 3-3(a), denoted as “skin tensile test”), and the other is along the stringer part (Figure 3-3(b), denoted as “stringer tensile test”) with the support of a jig made of steel material. The local deformation behavior of the joints was evaluated by applying a digital image correlation system (DIC) that was connected to the tensile testing machine. The strain map was recorded during the testing process.

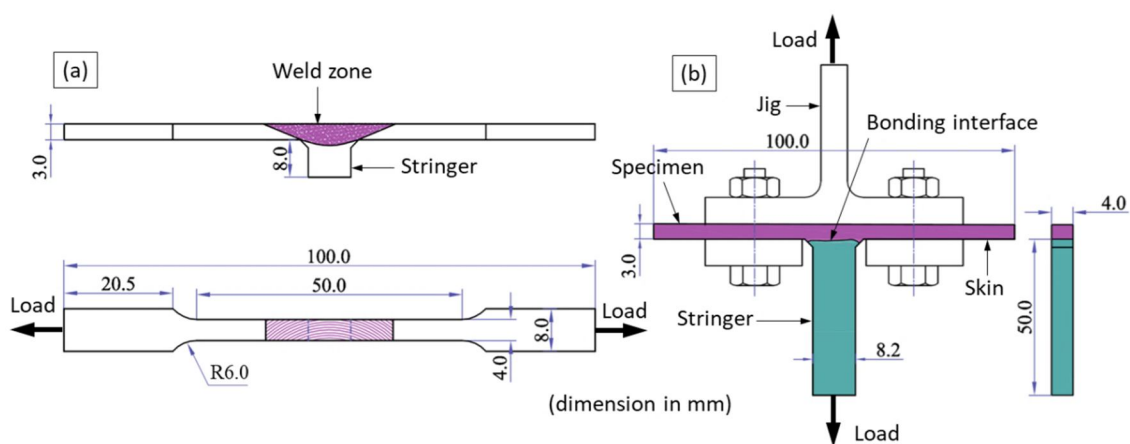


Figure 3-3 Evaluation of T-lap joints: (a) skin and (b) stringer tensile tests.

3.3 Experimental Results

3.3.1 Temperature during FSW process

Figure 3-4(a) displays the temperature history at the AS and RS for both first- and second-pass FSWs according to the Figure 3-2 method. It seems that the insignificant difference in peak temperature was found under the current welding conditions. Here, the peak value at the AS was about 450°C while that at the RS was slightly lower than that at the AS by about 20°C (Figure 3-4(b)). The disparity in peak temperature might be caused by asymmetric metal flow that created different temperature fields during the FSW process [11,16]. Based on above results, the effects of reversed or multiple metal stirring and the tool offset on the welding temperature were insignificant in this work.

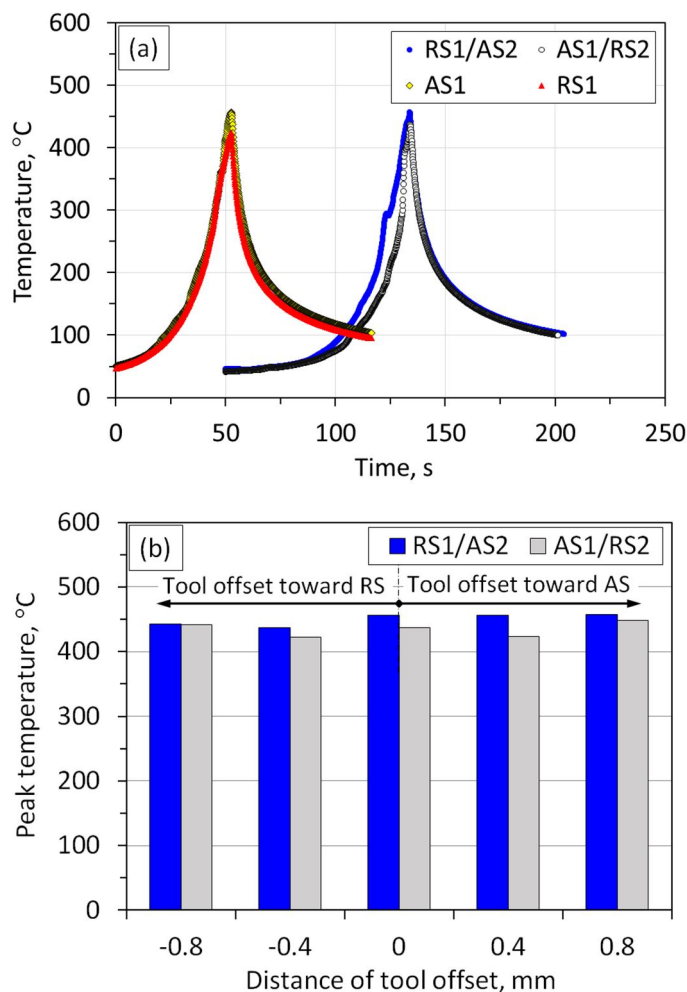


Figure 3-4 (a) Temperature history at the AS and RS of first- and second-pass welding at tool offset of 0.0 mm and (b) peak temperature under various distances of tool offset.

3.3.2 Effects of reversed metal flow and tool offset on microstructure of interface

3.3.2.1 Effect of reversed metal flow

The effect of the reversed tool rotation to the primary FSW process on the welding interface feature is shown in Figure 3-5 for the case of the tool offset of 0.0 mm. Here, the welding interface can be postulated as boundary between skin and stringer plates after the welding process. It can be seen that two types of bonding were achieved along the welding interface; i.e. an interface associating with oxide layer referred to as kissing bond defects (KBs), and other interface without oxide layer referred to as bonding interface, as shown in Figure 3-6. Note that the welding interface produced by the single-pass FSW was associated with pronounced the KBs at the RS1 (Figure 3-5(a)). The application of double-pass welding with the reversed tool rotation significantly changed the interface morphology in both the KBs and bonding interface (Figure 3-5(b)).

The sizes of the KBs and bonding interface were measured on the basis of the size of oxide layer to quantitatively evaluate welding interface. The results are summarized in Figures 3-7(a,b) in terms of the curve length of the KBs and the effective bonded width (denoted as W), respectively in the single- and double-pass FSW. It is found from Figure 3-7(a) that the application of the double-pass welding dramatically reduced the KBs size at the RS1 (corresponding to the RS1/AS2). By this way, the effective bonded width between the skin and stringer was significantly improved, as seen in Figure 3-7(b). This phenomenon may be attributed by reversing successfully metal flow, as suggested by Figure 3-5(b) and will be discussed again in the next section.

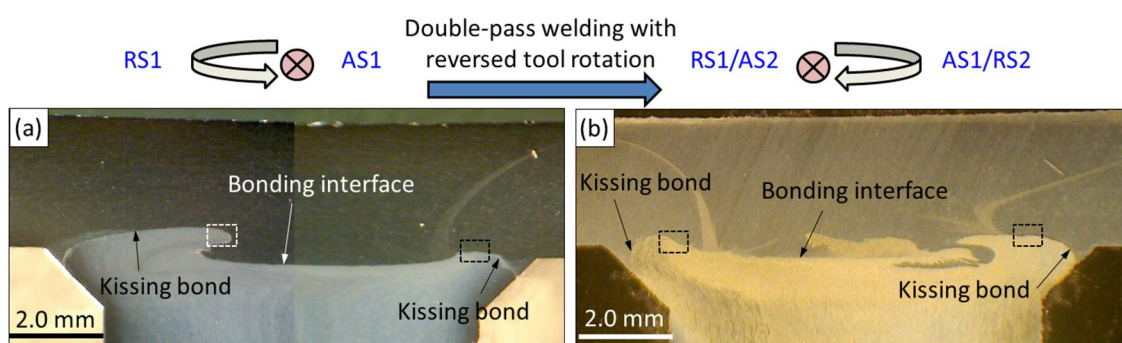


Figure 3-5 Macrostructure of welding interface produced by (a) single- and (b) double-pass FSWs at offsetting 0.0 mm.

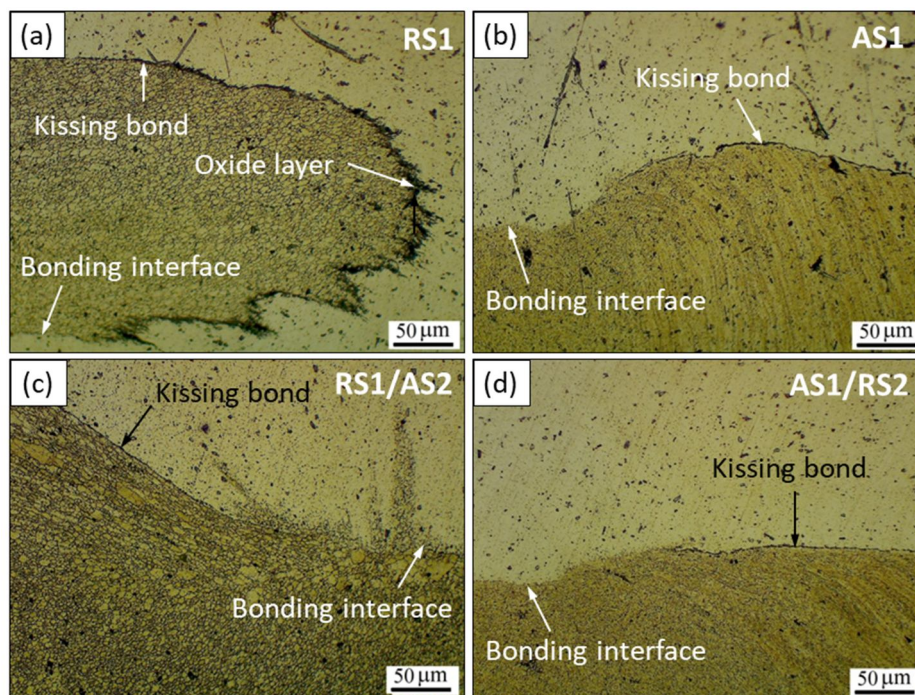


Figure 3-6 Microstructures of KBs and bonding interface produced by (a,b) single- and (c,d) double-pass FSWs at offsetting 0.0 mm.

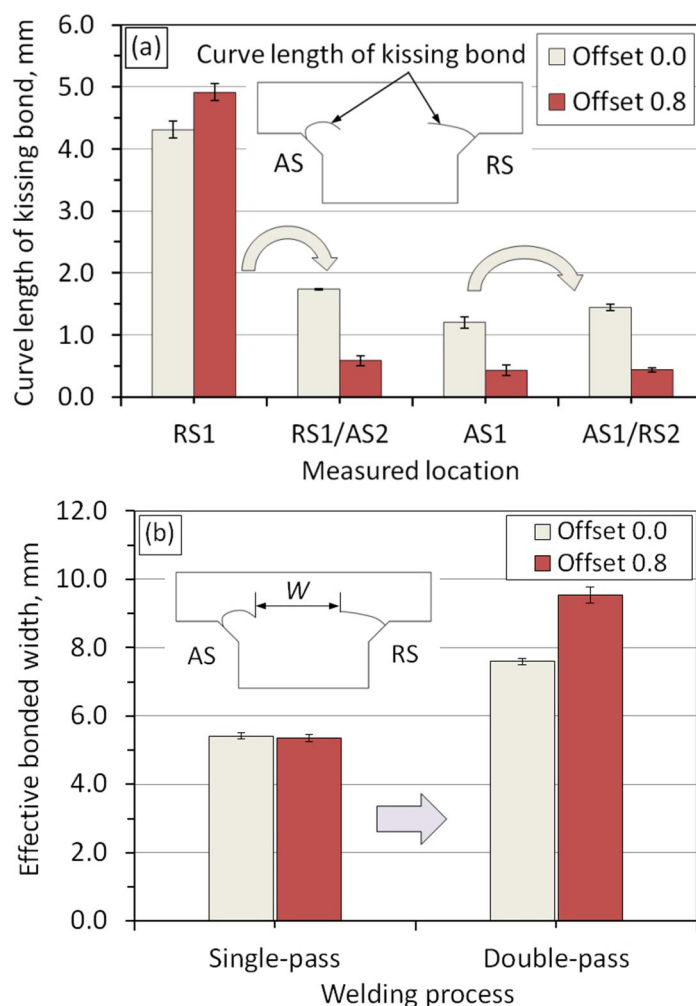


Figure 3-7 Effect of reversed material flow on (a) curve lengths of KBs and (b) effective bonded width produced by single- and double-pass FSWs.

3.3.2.2 Effect of tool offset

Despite the KBs significantly decreased due to applying reversed metal flow method, they had remained large size in two corner fillets about 1.6 mm (Figure 3-7(a)). In other words, the bonding interface was not satisfactory in this method. So, a combination between reversed metal flow and tool offset was applied to advance interface morphology. Figure 3-8 shows the representative images of macro- and micro-structures of welding interface produced by the double-pass FSW under the various direction and distances of tool offset. It is worthy to note that the morphology of welding interface was significantly changed upon these changes. Here, the geometry of the KBs tended upward from the two corner fillets, and then moved deeply into welded center by offsetting the tool probe toward the RS, as seen Figures 3-8(a,b). This phenomenon might be harmful to the strength of the FSWed T-lap joints and will be

discussed in the next section. In contrast, the KBs were significantly minimized because of offsetting tool toward the AS (Figures 3-8(c,d)), especially in offsetting 0.8 mm, as shown in Figures 3-8(d-1) and 3-8(d-2). Furthermore, the material welded interface seems to be mixed better when the tool probe was offsetted to the AS. As shown in Figure 3-8(f), the mixture of two aluminum alloys was observed along the bonding interface. This result can bring about the higher bonding strength of interface compared to that of interface without mixing two materials (Figure 3-8(e)).

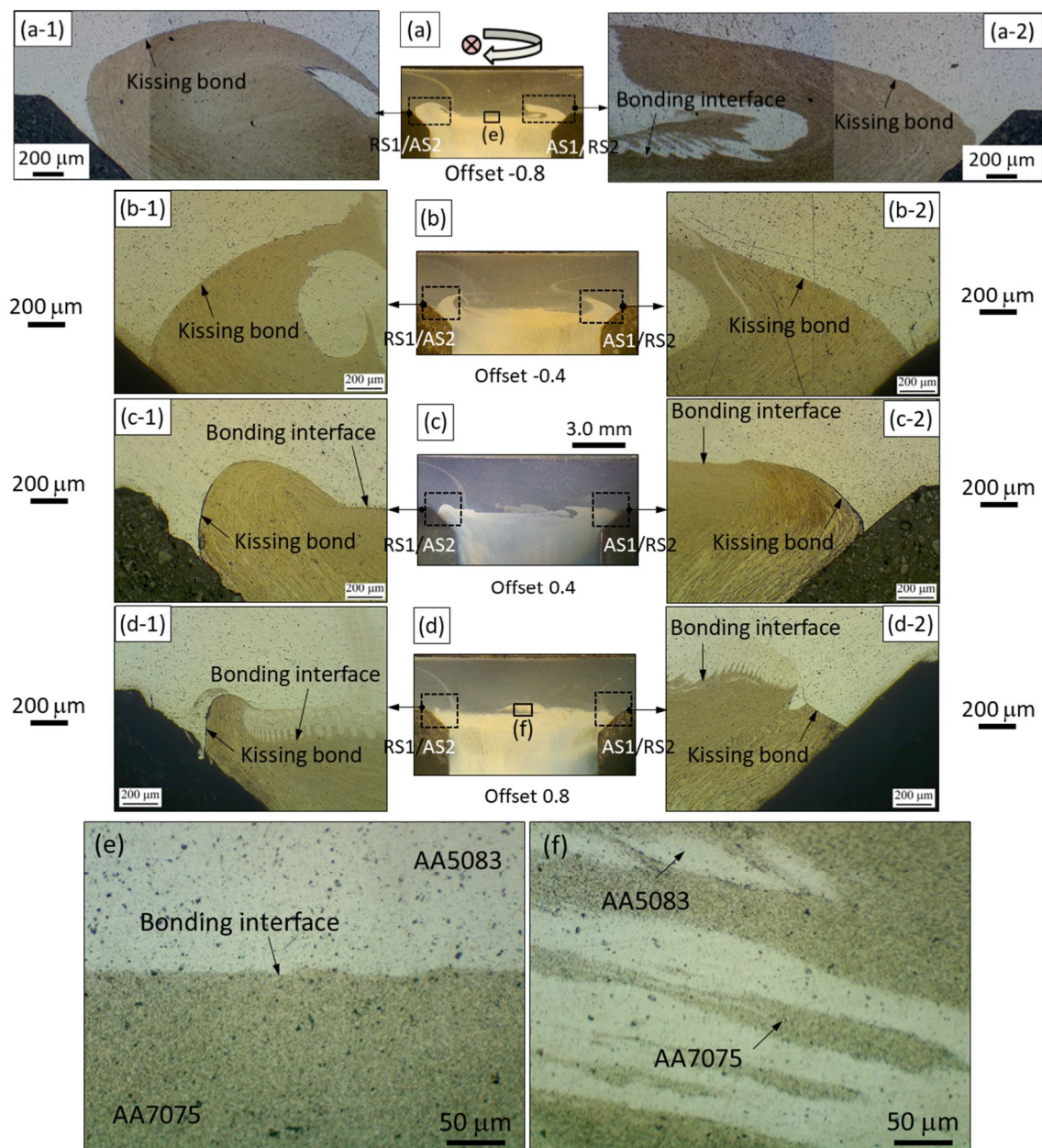


Figure 3-8 (a-d) Macro- and (e,f) micro-structures of welding interface produced under various distances of tool offsets.

The curve length of the KBs and the value of effective bonded width were directly measured on the specimens to quantitatively evaluate this method in the improvement of the welding interface characteristic, as shown in Figure 3-9. It is found that although the volume of probe penetration into two corner fillets was symmetrical through the centerline of the T-lap joints, the tendencies of both KBs and bonding interface sizes were opposite. Here, increasing the distance of tool offset toward the RS seems to increase the curve length of the KBs, whereas the KBs were impressively decreased by offsetting the tool to the AS. Another worthy finding is that the curve length of the KBs at the RS1/AS2 was longer than that at the AS1/RS2 in all cases. From above these results, it can be concluded that the welding interface was successfully improved due to applying both tool offset of 0.8 mm and reversed metal flow that created small KBs size compared to method without tool offset (Figure 3-7).

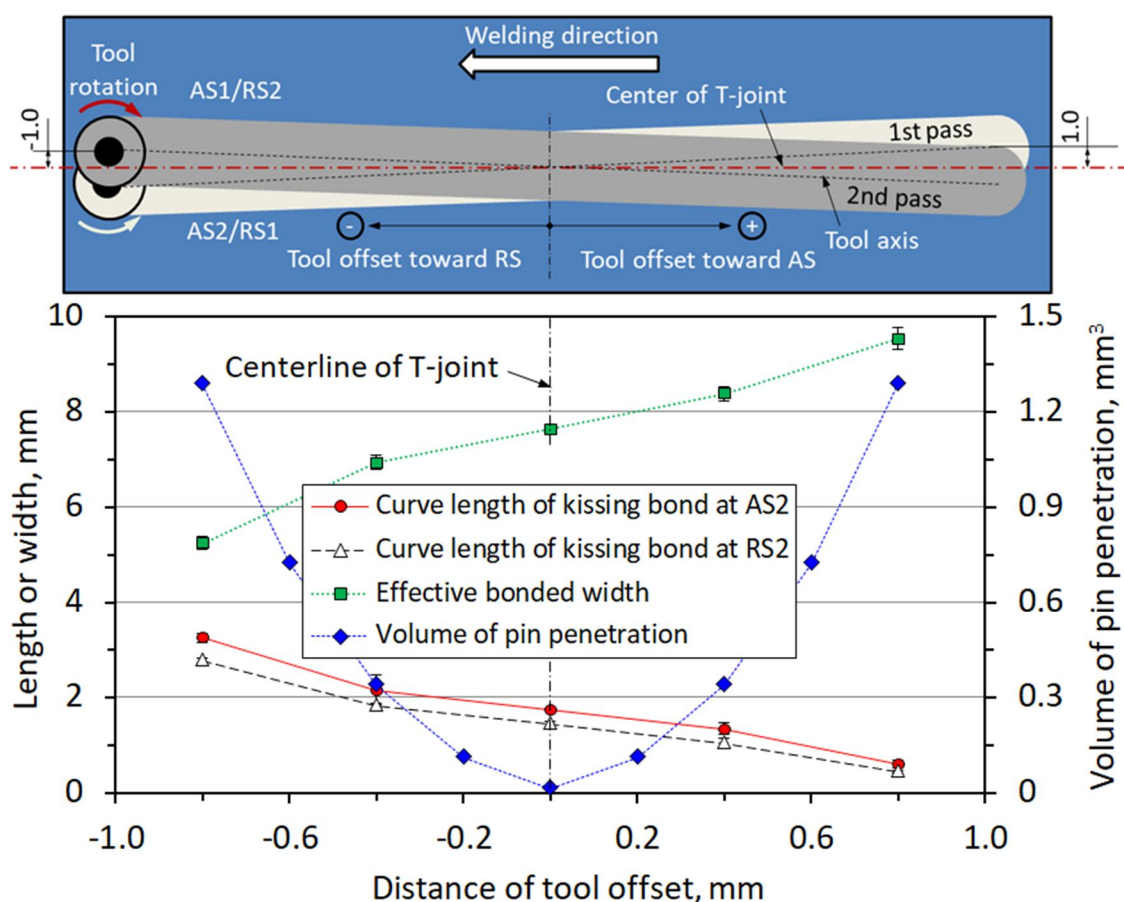


Figure 3-9 Effect of tool offset on the curve length of KBs and effective bonded width.

3.3.3 Mechanical properties of FSWed T-lap joints

3.3.3.1 Microhardness profile

The effect of the double-pass induced by reversed metal flow and the tool offset on the hardness profile along the skin and stringer plates of the FSWed T-lap joints is shown in Figures 3-10(a) and 3-10(b), respectively. It seems that the hardness distribution along skin of the RS and AS was reversed by offsetting tool (Figure 3-10(a)). This result might be concerned to the reversed welding temperature between the AS and RS, resulting from two factors. Firstly, the temperature in the AS is higher than that in the RS, as seen in Figure 3-4. Secondly, the reversed tool rotation, or reversed metal flow was applied in the double-pass regimes. It is also interesting that the microhardness map along the stringer seems to be insensitive to the welding conditions (Figure 10(b)). The hardness value inside and around welded zone was lower than that of the base alloys.

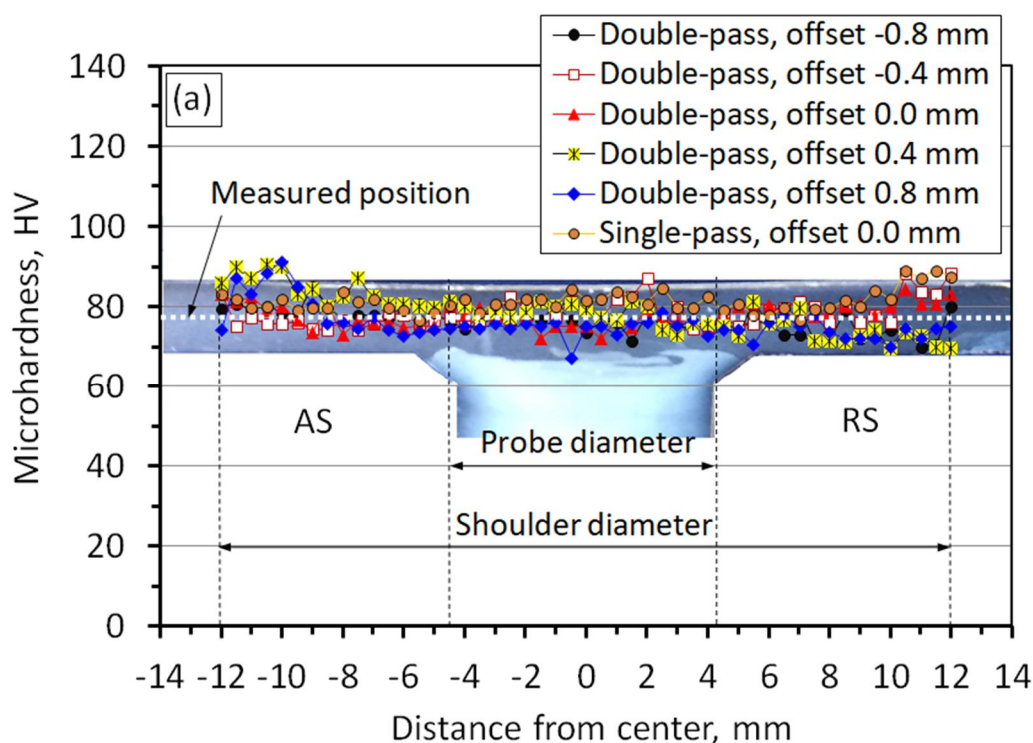


Figure 3-10 (a) Effect of various welding conditions on hardness profile along skin parts.

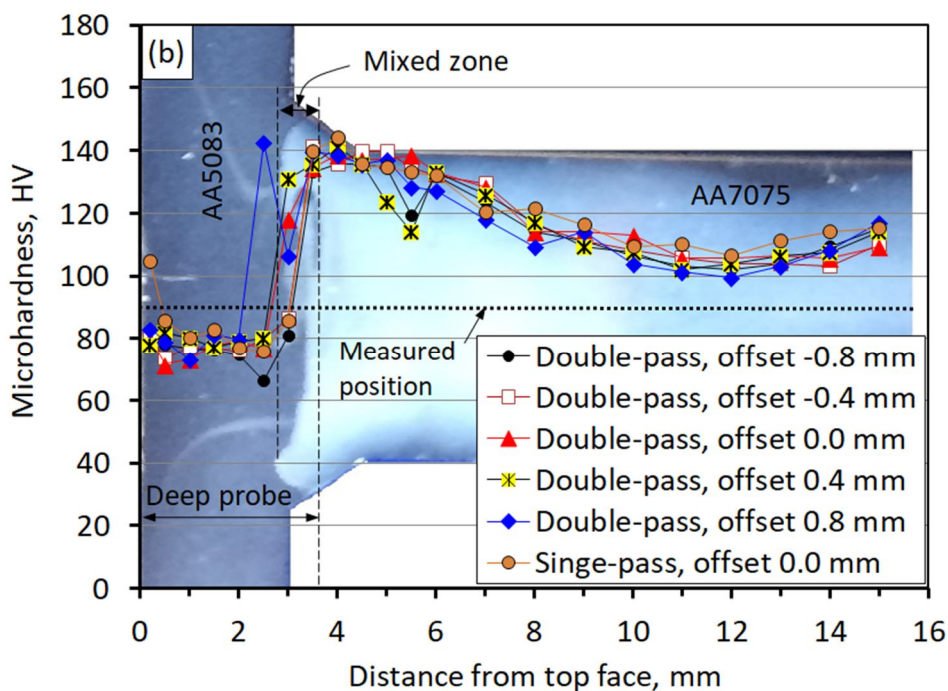


Figure 3-10 (b) Effect of various welding conditions on hardness profile along stringer parts.

3.3.3.2 Tensile test

The representative stress-strain curves of the specimens produced by various welding conditions under the skin tensile test are shown in Figure 3-11(a). It is worthy to note that the tensile strength and the rupture strain were significantly improved by employing the double-pass FSW, especially upon offsetting toward the AS (Figure 3-11(b)). According to that, the maximum stress and rupture strain of the joints were attained by about 290 MPa (90% joint efficiency) and 12%, respectively when the tool probe was set up by 0.8 mm. In contrast, this efficiency was only reached approximately 75% as offsetting toward the RS.

The representative load-displacement curves under the stringer tensile test are displayed in Figure 3-12(a). Unlike the skin tensile test, most of these curves were discontinuous associating with “pop-in” phenomenon, except the case when the tool offset was set up by 0.8 mm. Similarly to the skin tensile test, the strength of the T-lap joints under stringer tensile test was expressively improved but the displacement at rupture was reduced as employing the double-pass FSW by offsetting toward the AS, as shown in Figure 3-12(b). These results might be attributed by the formation of the KBs, and will be discussed in the next section.

Distribution of local bonding strength along interface produced by offsetting 0.8 mm is shown in Figure 3-13. Minimizing the KBs size led to the high strength of adhesive interface, that was higher than that of the base alloy AA5083. Noting that, the fracture location of mini specimen was at the heat affected zone (HAZ) of the stringer Figure 3-14 where had low hardness value (Figure 3-10(b)).

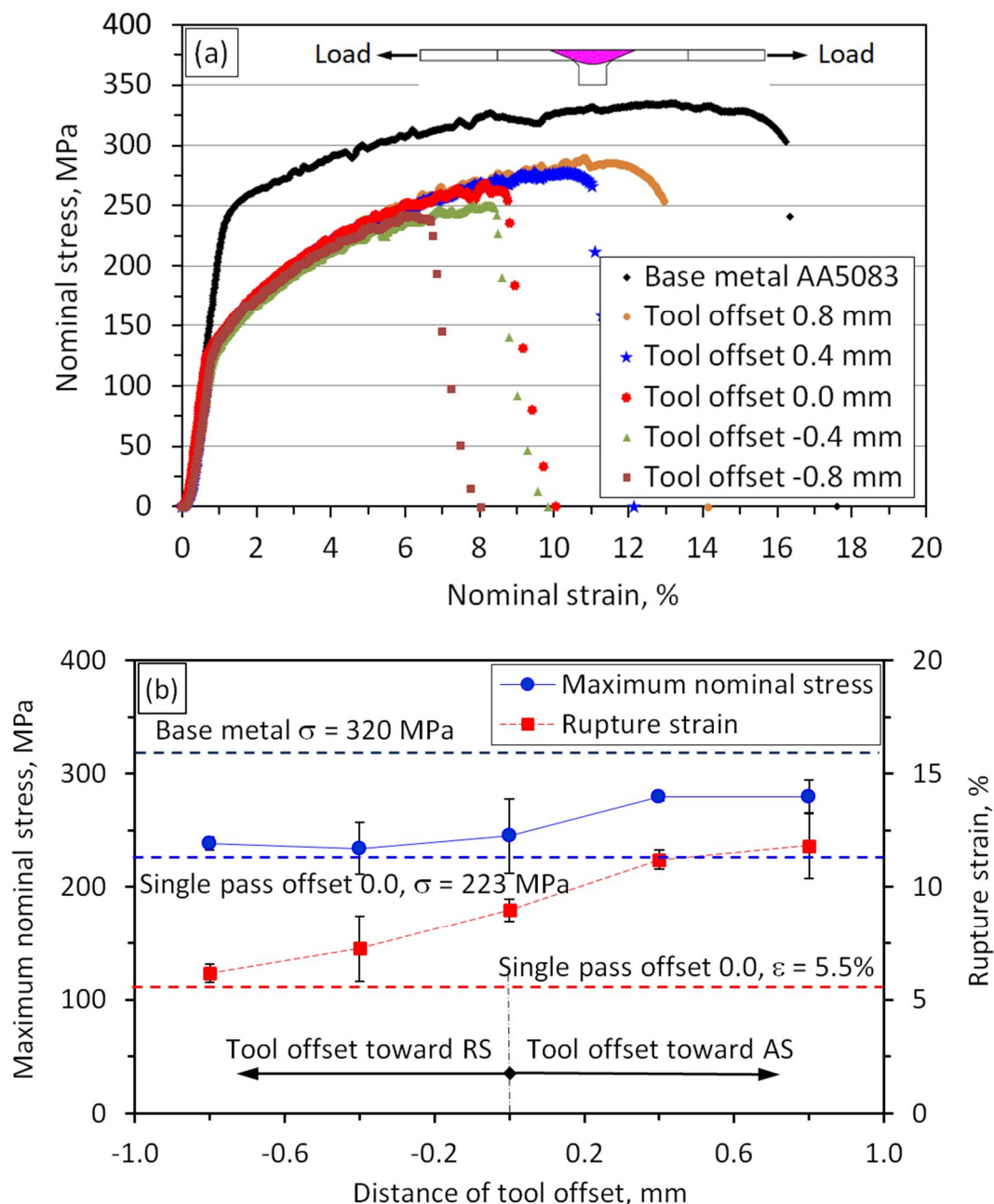


Figure 3-11 Strength of the joints under the skin tensile test: (a) nominal stress-strain curves and (b) maximum nominal stress and rupture strain.

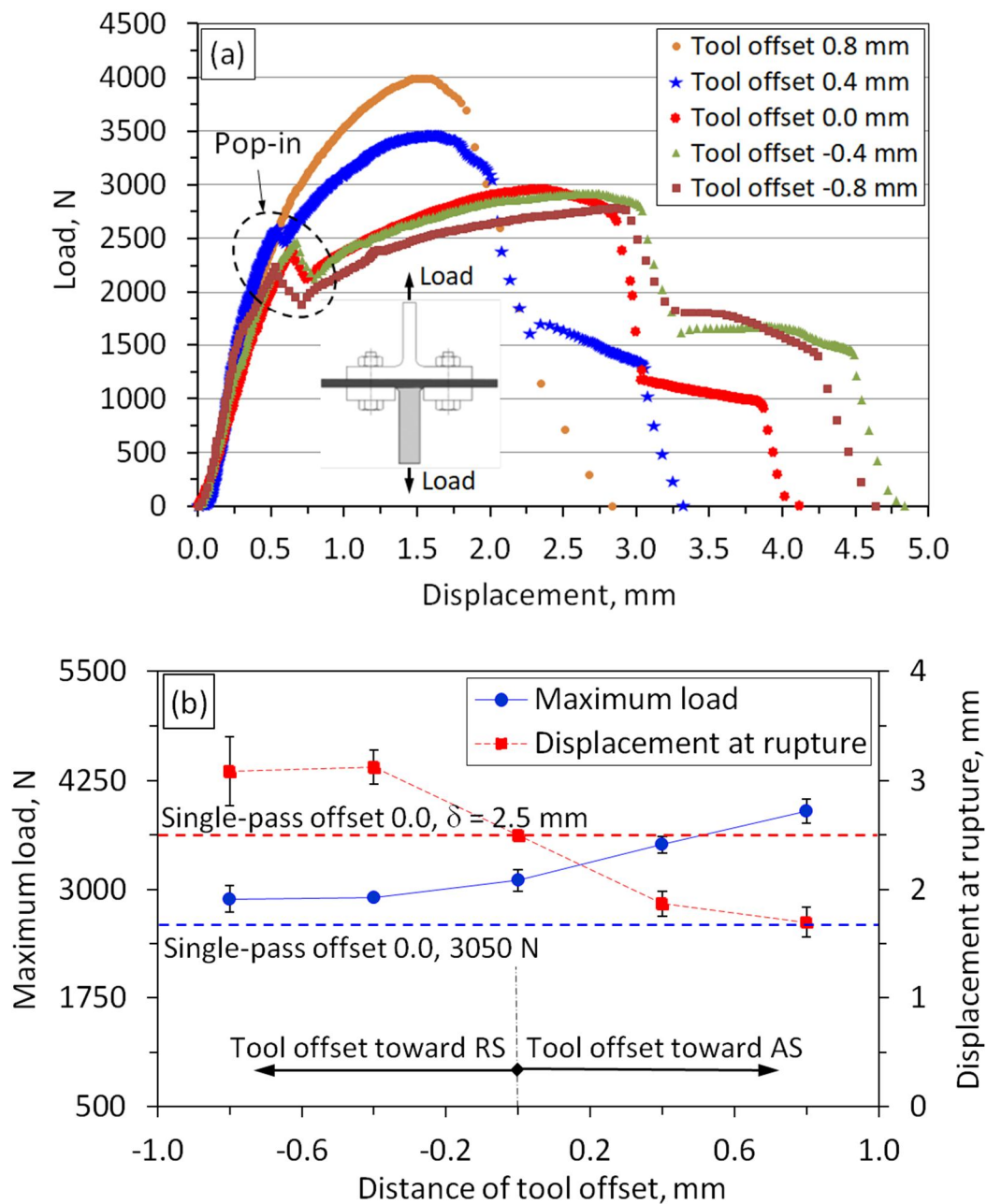


Figure 3-12 Strength of the joints under the stringer tensile test: (a) load-displacement curves and (b) maximum load and displacement at rupture.

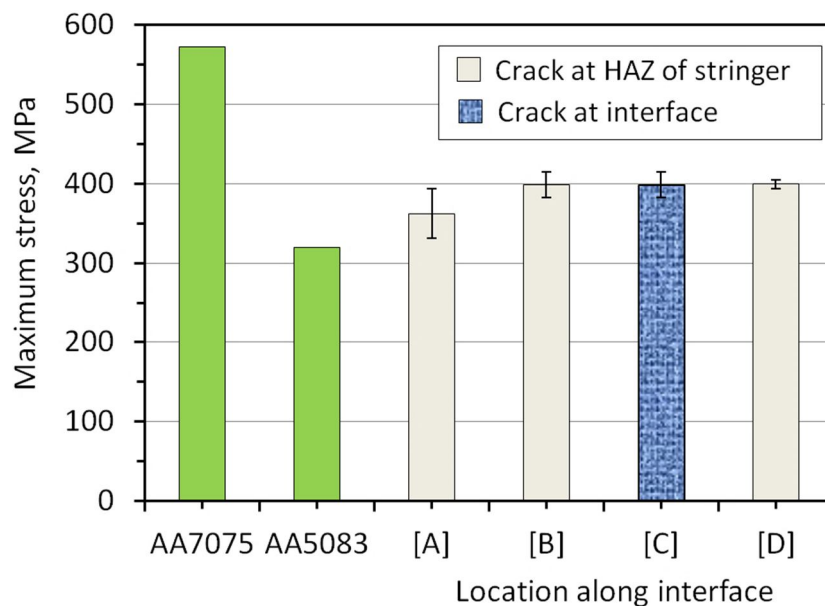


Figure 3-13 Local bonding strength distributed along interface produced by offsetting 0.8 mm.

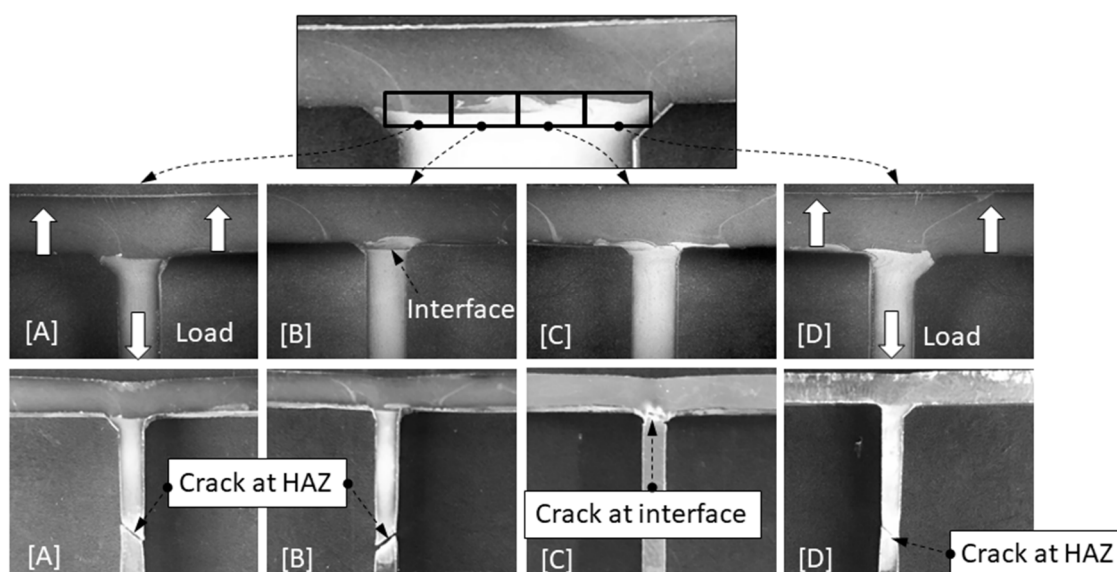


Figure 3-14 Fracture location of miniature specimens along interface produced by offsetting 0.8 mm.

3.3.4 Interface morphology affected by double-pass FSW and tool offset

3.3.4.1 Quantification of defects affected by double-pass FSW

The effect of double-pass on the quantification of defects of interface that are defined as in Figure 3-15(a) are shown in Figure 3-15(b) for the AS and Figure 3-15(c) for the RS. It seems that the change in the parameters at the AS is insignificant in

comparison with the RS. Here, the application of double-pass remarkably reduced the projected length a .

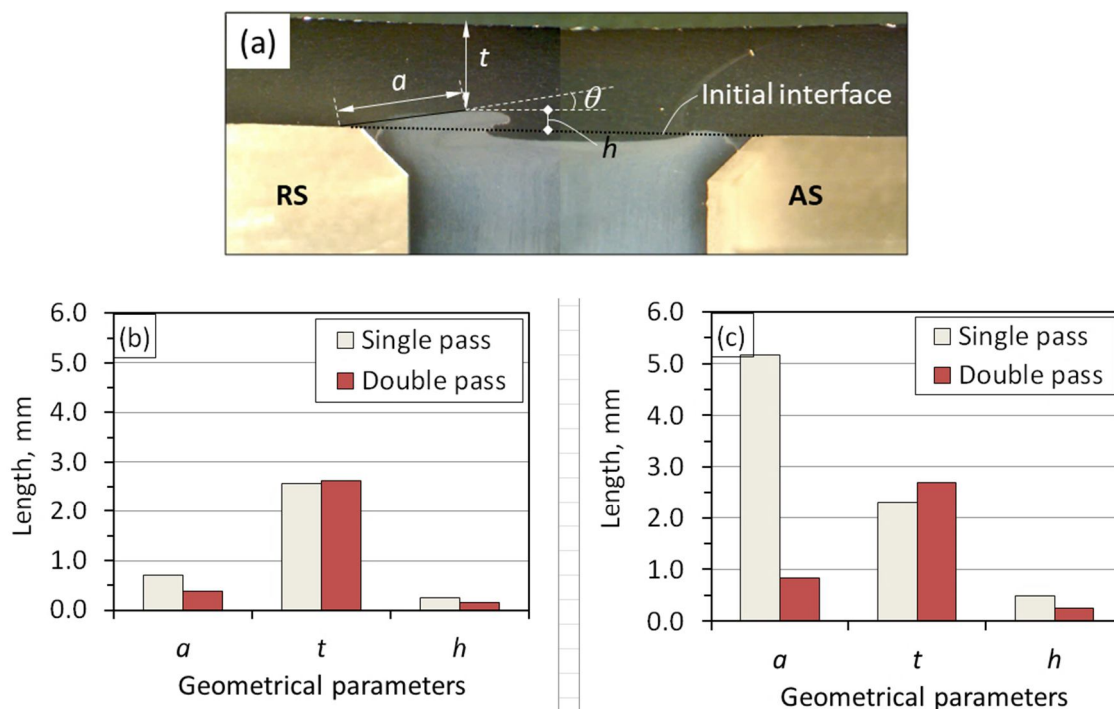


Figure 3-15 (a) Define some parameters of quantification of interface and effect of double-pass on these parameters at (b) AS and (c) RS.

3.3.4.2 Quantification of defects affected by tool offset

The effect of distance of tool offset on the quantification of defects of the interface that are defined as in Figure 3-16(a) are shown in Figure 3-16(b) for the RS1/AS2 and Figure 3-16(c) for the AS1/RS2. There is similar tendency in these parameters at the RS1/AS2 and AS1/RS2. Here, the projected length a and the height h were decreased with increasing the distance of tool offset toward the AS. In this case, the effective skin thickness t was significantly improved with the best value corresponding to offsetting 0.8 mm. The influence of these parameters on the strength of the T-lap joints will be discussed in Chapter 5.

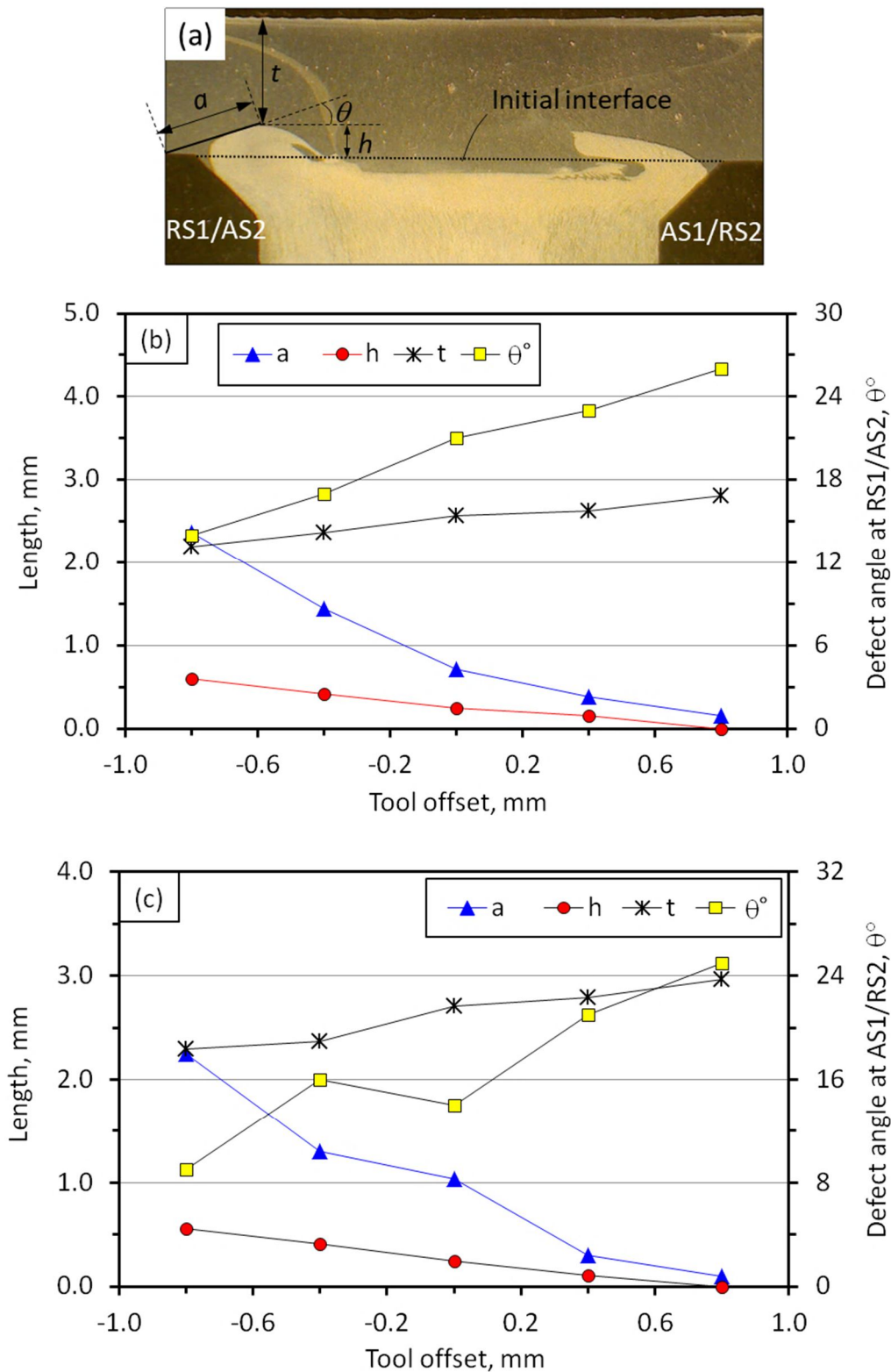


Figure 3-16 (a) Define some parameters of quantification of interface and effect of tool offset on these parameters of interface at (b) RS1/AS2 and (c) AS1/RS2.

3.4 Discussion

3.4.1 Role of kissing bond defects on failure behavior of FSWed T-lap joints

Figure 3-17 shows the DIC strain maps of specimen under skin tensile test. It seems that the distribution of strain was inhomogeneous along specimens. The strain mainly concentrated around the KBs at the AS1/RS2 (Figure 3-17(a)) and the HAZ region at the RS1/AS2 (Figure 3-17(b)) in which the final cracked took place. The existence of the KBs had big contribution to the failure of specimens produced by the tool offset of -0.8 mm. This postulation was more clearly understood in Figure 3-17(b) that the size of the KBs was minimized by offsetting the tool probe toward the AS with 0.8 mm of distance. These results are summarized in Figure 3-18, from different aspects in terms of the effective bonded width (as denoted by W), effective skin thickness (as denoted by t_{AS} and t_{RS}), and effective ligament ratio (as denoted by t/T) those are defined as illustrated in Figure 3-18. The application of tool offset towards the AS would lead to the larger values of both W , t_{AS} , t_{RS} , and t/T resulting in higher tensile properties, as shown in Figures 3-13 and 3-14. In other words, the quality of the T-lap joints strongly depends on some appropriate methods to enable to minimize the size of the KBs which had little and bonding strength [17,18].

The effect of the KBs on stringer tensile test is shown in Figure 3-19. It can be seen that the load-displacement curve of the specimen offsetted by -0.8 mm possessed the “pop-in” phenomenon, corresponding to three stages. Here, the “pop-in” phenomenon might be related to the kissing bond cracking. Then, the first load drop related to the specimen was fractured in the AS1/RS2. Finally, the second load drop related to the specimen was completely fractured in the RS1/AS2. In contrast, the load-displacement curve of the specimen offsetted by 0.8 mm was smooth without pop-in. In this case, the KBs were mostly eliminated, resulting in the higher tensile strength. The size of the KBs measured based on oxide line from the cross-section of specimen before the tensile test is compared with that was measured from the fracture surface. There is good agreement between these values, as shown in Figure 3-20. This means that the KBs size played an imperative role in the fracture behavior of the FSWed T-lap joints.

Figure 3-21 shows the representative fractography of specimen produced by the tool offset of -0.8 mm after the rupture. Two zones can be identified on the fracture

surface, i.e. KBs zone and bonding interface zone (see in Figures 3-21(a-c)). Here, the fracture surface in the KBs region displayed a smooth facet (Figure 3-21(d)) while the remaining region associated with the ductile dimples mode (Figure 3-21(e)).

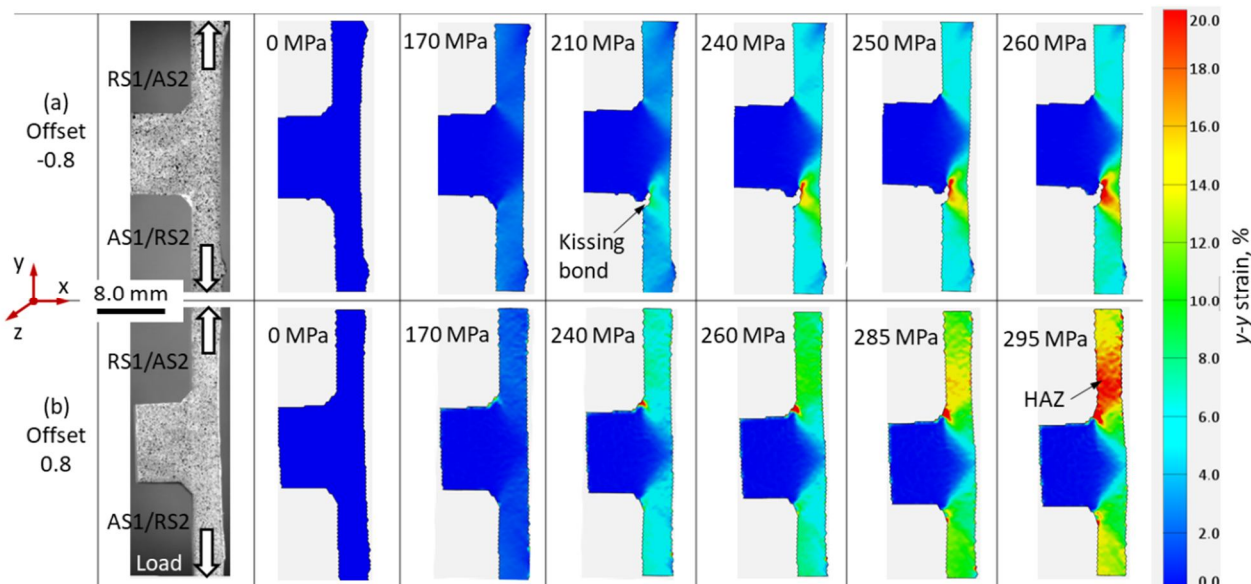


Figure 3-17 Strain maps of specimens produced by (a) offset -0.8 and (b) 0.8 mm from DIC measurement under skin tensile test.

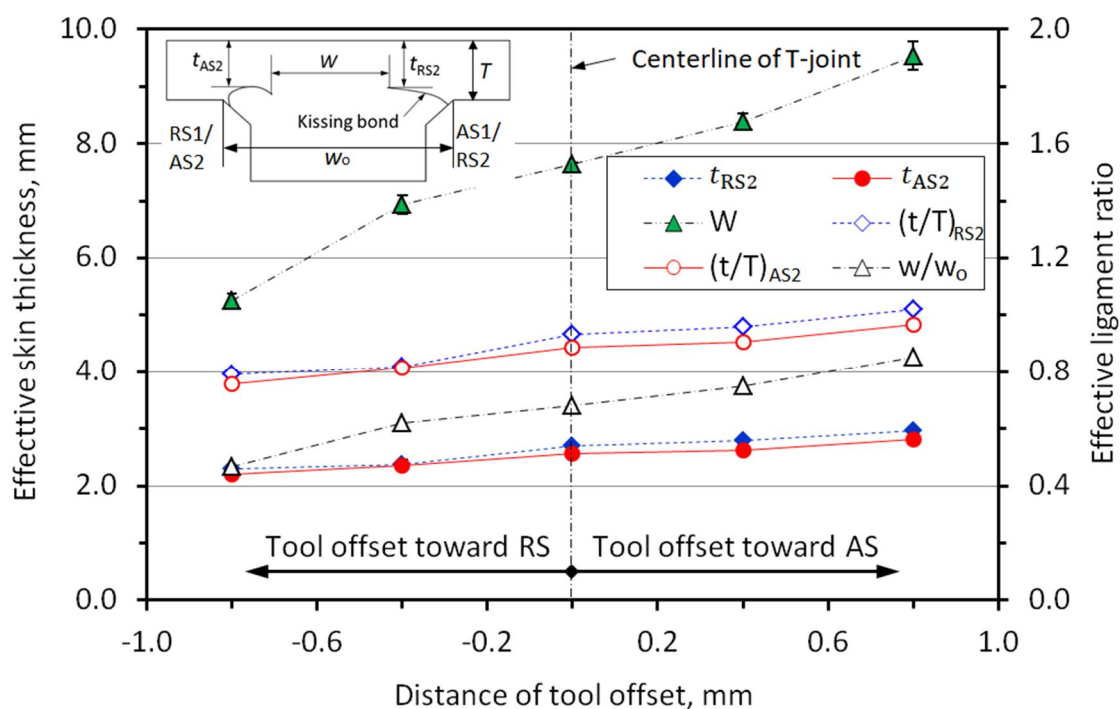


Figure 3-18 Effect of distances of tool offset on the effective skin thickness t , effective bonded width W , and effective ligament ratio t/T .

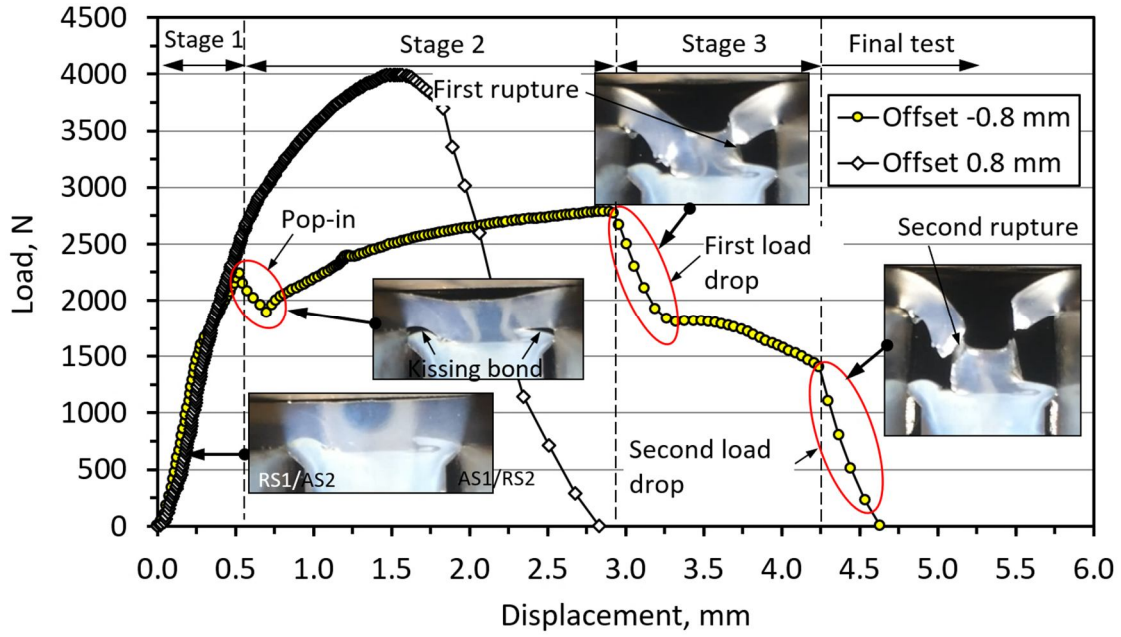


Figure 3-19 Relationship between load-displacement curve and fracture location of stringer tensile test.

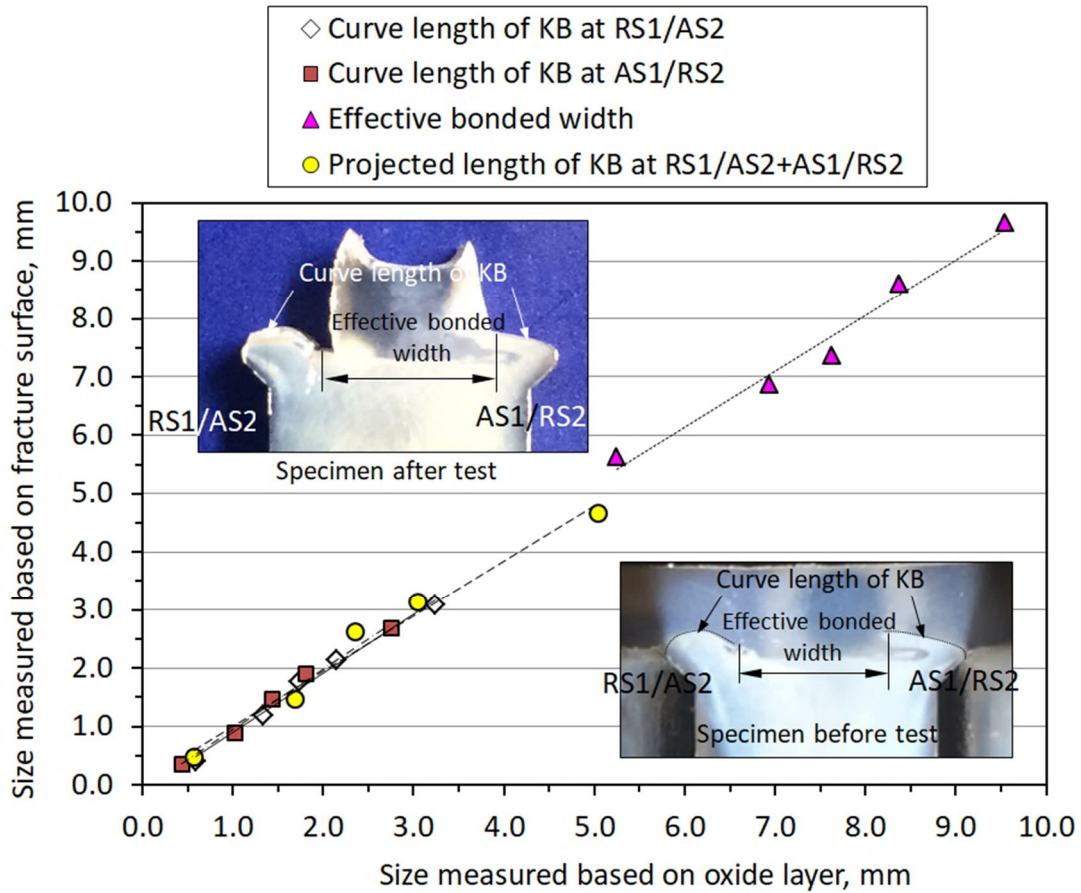


Figure 3-20 Quantitative comparison in some values of kissing bond size measured based on fracture surface and oxide layer.

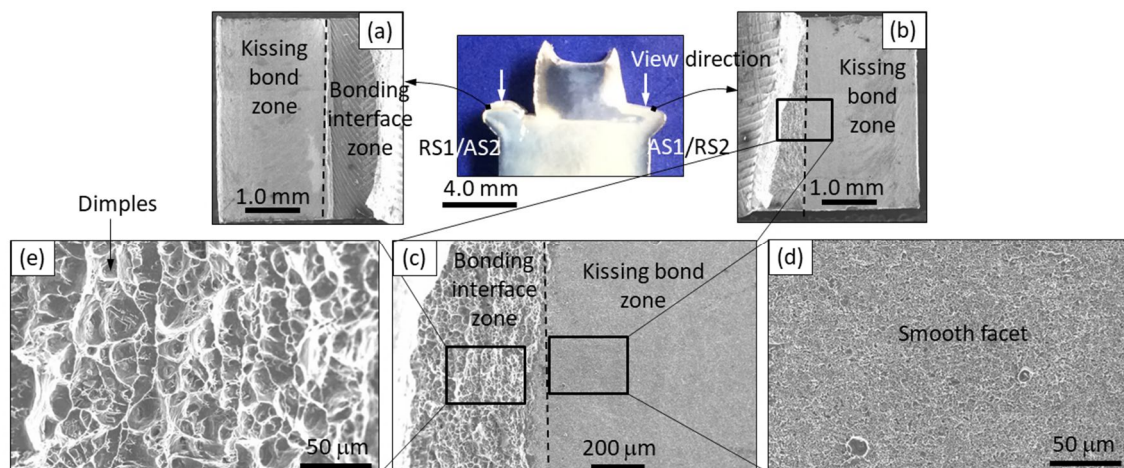


Figure 3-21 Fracture morphology of specimen produced by offset -0.8 mm.

3.4.2 Formation of kissing bond defects in during FSWed T-lap joints

Following the references [8,19], the material flow in a single FSW process can be shown in Figure 3-22. Here, the material at the front AS seems to be involved into tool probe while that at the back RS is nearly escaped from tool probe. This might lead to the mixture of material at the AS1 was more severe than that at the RS1, as reported in literature [1,9,11,20]. In addition, the KBs at the RS1 must be achieved by horizontal material flow that moved from the RS1 to the AS1, as indicated in previous chapter. In other words, a mere single-pass FSW is not good enough to minimize the KBs in the T-lap joints. A double-pass FSW accompanying with the reversed tool rotation and tool offset can compensate the above disadvantage, especially at the RS1, as postulated by Figure 3-23. It is clear that the KBs are often formed after the first-pass FSW, as observed in Figures 3-23(a1-a2,b1-b2). After the second-pass FSW, the KBs were minimized due to the difference in probe location when the appropriate tool offset was undertaken. The KBs were minimized at the RS1/AS2 by the tool offset of 0.8 mm (Figures 3-23(b3,b4)), whereas the large KBs remained at the AS1/RS2 by the inappropriate tool offset of -0.8 mm (Figures 3-23(a3,a4)).

Figure 3-24 at the same time suggests an importance of gap distance, δ when the tool probe was offsetted toward the AS and is geometrically expressed by

$$\delta = (D - x)\sin\alpha \quad \text{with } x \leq D \quad (3-1)$$

where D (mm) is a distance between the body probe and the edge of die, and x (mm) is the distance of tool offset and α is the chamfer angle of die. Figure 3-25 expresses the

relationship between the representative KBs distance, d and the gap distance, δ in this work, suggesting the usefulness of set up of moderate δ to minimize the KBs.

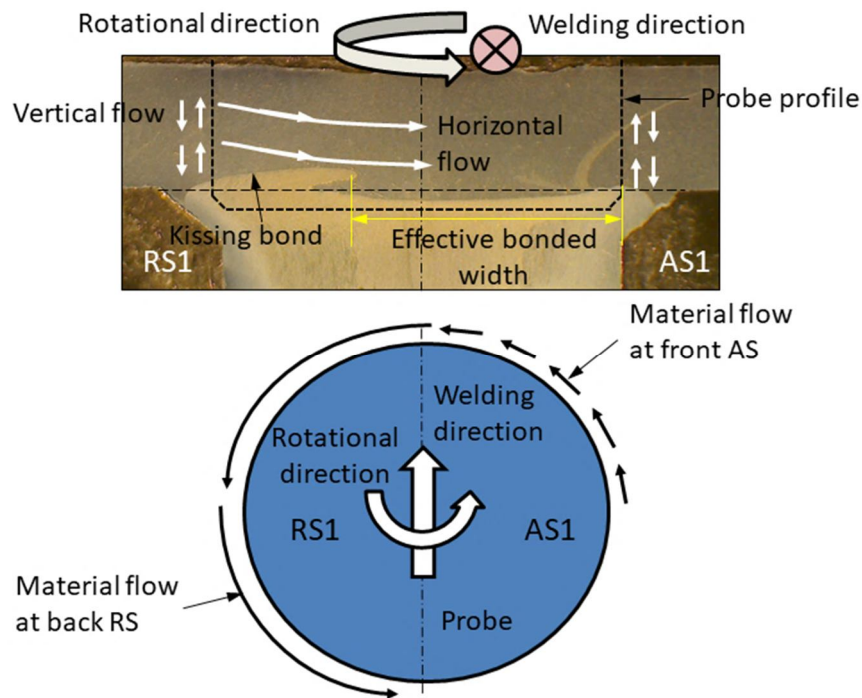


Figure 3-22 Schematic illustration of material flow in single-pass FSW process.

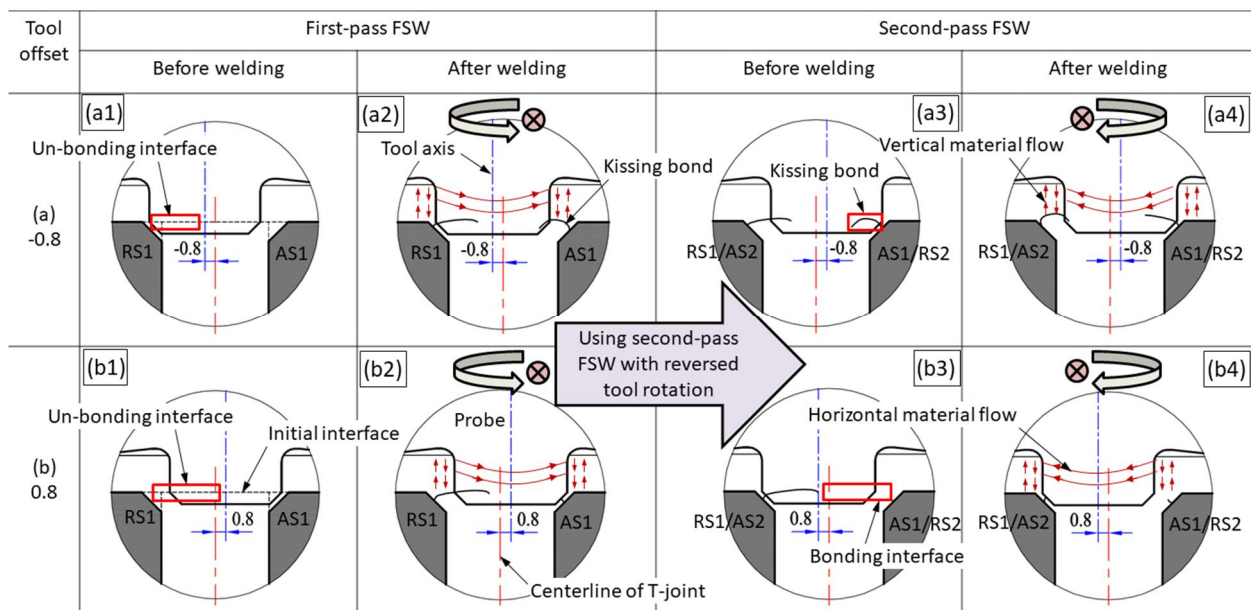


Figure 3-23 Schematic illustration of KB formation in the double-pass FSW by the tool offsets of (a) -0.8 and (b) 0.8 mm.

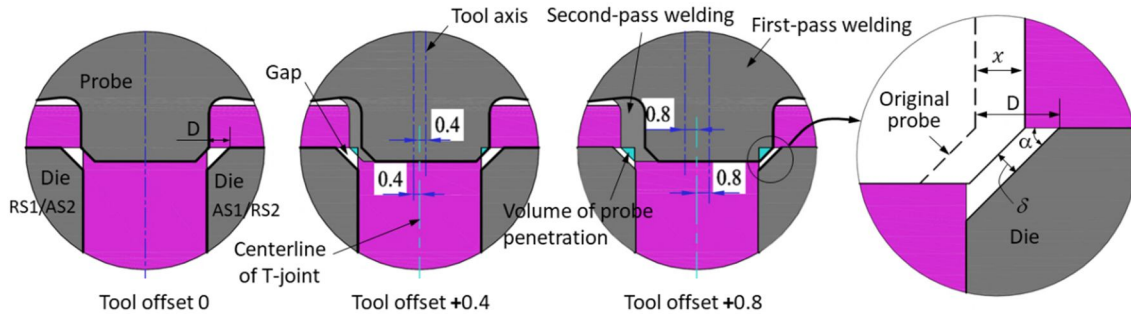


Figure 3-24 Schematic illustration of probe penetration into corner fillets at the various distances of tool offset.

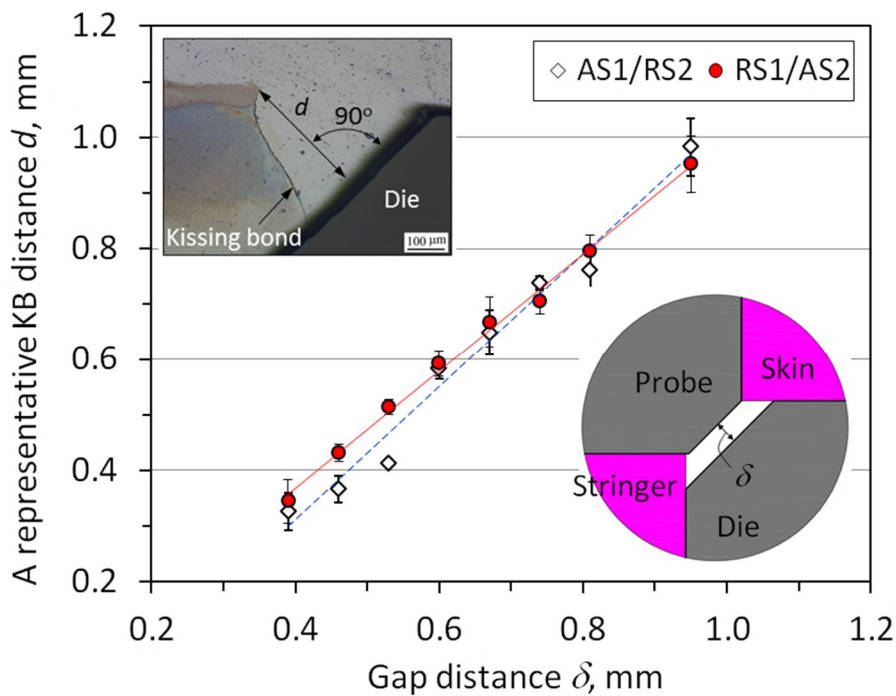


Figure 3-25 Relationship between the representative KBs distance and the gap distance.

3.5 Chapter Summary

The dissimilar FSWed T-lap joints between AA7075 and AA5083 were fabricated by the application of double-pass FSW. The effects of the tool offset and the reversed metal flow on the interface morphology and mechanical properties of the T-lap joints were examined. The following conclusions were reached:

- (3-1) Applying the double-pass FSW induced by a reversed material flow could significantly improve the quality of the welding interface; decrease in the KBs size and increase in the effective bonded width, without insignificant change in welding temperature and hardness profile.
- (3-2) The tool position and asymmetric material flow had a significant influence on the KBs formation. By combining the reversed material flow and the tool offset toward the AS, the KBs size could be significantly minimized at both the AS and the RS. Especially, the joint efficiency might be reached approximately 90% in comparison with the AA5083 base metal for both the skin and stringer tensile tests due to applying offsetting tool toward the AS with the distance of 0.8 mm.
- (3-3) The above behavior was reasonably interpreted by the metal flow during the double-pass FSW process. The gap distance played an important role in the formation of the welding interface.
- (3-4) The parameters of quantification of defects were significantly improved due to the application both reserved metal flow and tool offset. The reduction in kissing bond defects can be reason for these results. The influence of these parameters on the strength of the T-lap joints will be discussed in Chapter 5.

3.6 Chapter References

- [1] Cui, L., Yang, X., Zhou, G., Xu, X. and Shen, Z., Characteristics of defects and tensile behaviors on friction stir welded AA6061-T4 T-joints, *Materials Science and Engineering A*, Vol.543, (2012), pp.58-68.
- [2] Zhao, Y., Zhou, L., Wang, Q., Yan, K. and Zou, J., Defects and tensile properties of 6013 aluminum alloy T-joints by friction stir welding, *Materials and Design*, Vol.57, (2014), pp.146-155.
- [3] Donati, L., Tomesani, L. and Morri, A., Structural T-joint produced by means of friction stir welding (FSW) with filling material, *International Journal of Material Forming* Vol.2, (2009), pp.295-298.
- [4] Said, M.T.S.M., Hamid, D.A., Ismail, A., Zainal, S.N.N., Awang, M., Rojan, M.A., Ikram, I.M. and Makhtar, M.F., Experimental Study on Effect of Welding Parameters of Friction Stir Welding (FSW) on Aluminium AA5083 T-joint, *Information Technology Journal*, Vol.15, (2016), pp.99-107.
- [5] Hao, D.D., Okazaki, M., and Tra, H.T., Effect of welding parameters on mechanical properties of friction stir welded T-lap dissimilar metal joints between 7075 and 5083 aluminum alloys, *JSME-Mechanical Engineering Journal*, Vol.6(4), (2019), DOI: 10.1299/mej.19-00091.
- [6] Jesus, J.S., Costa, J.M., Loureiro, A. and Ferreira, J.M., Assessment of friction stir welding aluminium T-joints, *Journal of Materials Processing Technology*, Vol.255, (2018), pp.387-399.
- [7] Manuel, N., Silva, C., Costa, J.M.D., and Loureiro, A., Friction stir welding of T-joints in dissimilar materials: Influence of tool geometry and materials properties. *Materials Research Express*, Vol.6, (2019), pp.106528.
- [8] Buffa, G., Fratini, L., Micari, F. and Shivpuri, R., Material Flow in FSW of T-joints: Experimental and Numerical Analysis, *International Journal of Material Forming*, Vol.1(1), (2008), pp.1283-1286.
- [9] Fratini, L., Buffa, G., Micari, F. and Shivpuri, R., On the material flow in FSW of T-joints: Influence of geometrical and technological parameters, *International Journal of Advanced Manufacturing Technology*, Vol.44, (2009), pp.570-578.
- [10] Le Jolu, T., Morgeneyer, T.F., Denquin, A., and Gourgues-Lorenzon, A.F., Fatigue lifetime and tearing resistance of AA2198 Al-Cu-Li alloy friction stir welds: Effect of defects, *International Journal of Fatigue*, Vol.70, (2015), pp.463-472.
- [11] Feistauer, E.E., Bergmann, L.A. and dos Santos, J.F., Effect of reverse material flow on the microstructure and performance of friction stir welded T-joints of an Al-Mg alloy, *Materials Science and Engineering A*, Vol.731, (2018), pp.454-464.
- [12] Suna, T., Roy, M.J., Strong, D., Simpson, C., Withers, P.J. and Prangnell, P.B., Weld zone and residual stress development in AA7050 stationary shoulder friction stir T-joint weld, *Journal of Materials Processing Technology*, Vol.263, (2019), pp.256-265.
- [13] Martin, J.P., Stanhope, C. and Gascoyne, S., Novel techniques for corner joints using friction stir welding, In book: *Friction Stir Welding and Processing VI*

- (2011), pp.177-186.
- [14] Li, D., Yang, X., Cui, L., He, F., & Zhang, X., Fatigue property of stationary shoulder friction stir welded additive and non-additive T-joints. *Science and Technology of Welding and Joining*, Vol.20(8), (2015), pp.650-654.
- [15] Annual Book of ASTM Standards, Test methods for tension testing of metallic materials, E08, (2004), ASTM International.
- [16] Darvazi, A.R. and Iranmanesh, M., Prediction of asymmetric transient temperature and longitudinal residual stress in friction stir welding of 304L stainless steel, *Material and Design*, Vol.55, (2014), pp.812-820.
- [17] Oosterkamp, O., Oosterkamp, L.D. and Nordeide, A., 'Kissing bond' phenomena in solid-state welds of aluminum alloys, *Welding Journal*, Vol.83, (2004), pp.225-231.
- [18] Sato, Y.S., Takauchi, H., Park, S.H.C. and Kokawa, H., Characteristics of the kissing-bond in friction stir welded Al alloy 1050, *Materials Science and Engineering A*, Vol.405, (2005), pp.333-338.
- [19] Guerra, M., Schmidt, C., McClure, J.C, Murr, L.E. and Nunes, A.C, Flow patterns during friction stir welding, *Materials Characterization*, Vol.49(2), (2002), pp.95-101.
- [20] Donatus, U., Thompson, G.E., Zhou, X., Wang, J. and Beamish, K., Flow patterns in friction stir welds of AA5083 and AA6082 alloys, *Materials and Design*, Vol.83, (2015), pp.203-213.

Chapter 4

Fatigue Failure Behavior of Friction Stir Welded Dissimilar Metal T-lap Joints between AA7075 and AA5083

In this chapter, the fatigue failure behavior of the FSWed dissimilar metal T-lap joints between AA7075 and AA5083 under skin and stringer loading tests was investigated. The fatigue life and crack initiation of the joints were indicated. The fracture morphology of the specimens under the skin and stringer tests was observed by means of scanning electron microscopy (SEM). The effect of the kissing bonds in terms of the orientation and bonding strength on the fatigue life and crack initiation were addressed.

4.1 Introduction

As presented in Chapter 3, the application of double-pass welding induced by the reversed metal flow and tool offset has significantly improved the FSWed interface. According to that, the bonding interface without oxide layer was significantly improved. The size of the kissing bond defects (KBs) was impressively minimized with about 300 μm -500 μm of length curves. It means that the KBs seem to be too difficult to eliminate completely in this work. It is true that the KBs were considered as a common phenomenon in solid-state welding that is difficult to eliminate absolutely them [1,2]. In other words, the existence of the KBs in the FSW process apparent phenomenon and it almost appears in the butt-joint [3-10], lap-joint [11-15], and T-joints [16-25]. This type of defects might significantly affect the strength of the joints, especially under cyclic loading.

Despite the fatigue behavior of the FSWed joints has been largely attended on butt-joint and lap-joint [3-6,13,15], not many publications have investigated the T-lap joints [20,24], especially in applying load along the stringer part. In these researches, the influence of the KBs on the fatigue failure behavior of the joints was elucidated. According to that, the fatigue life of the joints contained the KBs was 21-43 times smaller than that of the joints without the KBs [3]. However, Kadlec et al. [4] found that a KBs size of 315 μm was the insignificant effect on the fatigue behavior. Le Jolu et al. [5] showed that the KBs orientation significantly affected the fatigue lifetime of the joints. These results indicated that the argument about the effect of the KBs on the failure behavior of the joints has not been still ended and need to be clarified. Furthermore, the fatigue life of the FSWed T-joints produced by single- [20] and multi-pass welding [24] have been evaluated. In spite of these, the effect of the KB characteristics on the failure behavior of the FSWed T-lap joints has been still knowledge gaps in the literature, especially in the stringer fatigue test.

In this chapter, the aim is to investigate the failure behavior of the dissimilar T-lap joints, that was minimized the KBs, in both skin and stringer tests under cyclic loading. The role of the KBs in terms of the orientation and bonding strength of interface in the fatigue life and fatigue crack initiation were addressed.

4.2 Experimental Procedure

4.2.1 Fabrication of T-lap joints by applying double-pass FSW

Based on success in the improvement of the bonding interface of the FSWed T-lap joints in Chapter 3, the joints were fabricated by applying double-pass welding that was combined between the tool offset and reversed metal flow. Here, two parallel welding lines were the same welding direction but reversed rotational tool, as schematically displayed in Figure 4-1(a). The tool offset of 0.8 mm toward the advancing side (AS) was applied for both pass welding, as illustrated in Figure 4-1(b). The skin and stringer plates were welded at a welding speed of 100 mm/min and the rotational speed of 400 rpm. Welding tool was a non-thread cylinder probe with the detail dimension is illustrated in Figure 4-1(c). The tool axis alignment was set at a constant with the tilt angle of 2.0° . The shoulder penetration into the surface of the skin plate was the depth of 0.2 mm during the FSW process. All of samples were no post-weld and analyzed after welding process about one month.

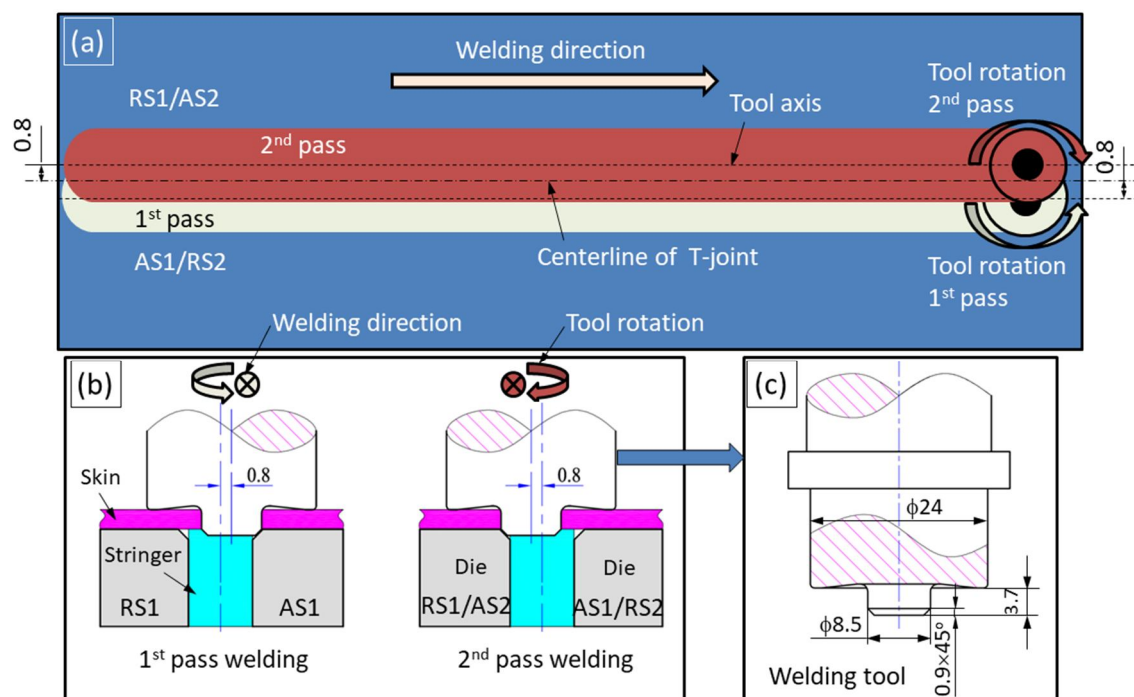


Figure 4-1 (a) Schematic diagrams of tool offset, (b) location of welding tool in reversed metal flow and (c) welding tool geometry (AS1, RS1 and AS2, RS2: advancing side and retreating side of first-pass and second-pass in double-pass welding, respectively).

4.2.2 Process analysis

In order to observe the microstructure, the specimens were prepared by cutting perpendicular to welding direction. The hardness profile was measured on the cross-section of the specimens by means of a micro Vickers indenter with 0.2 kgf loading in 10 s hold time. A hydraulic load testing machine was used to perform the tensile and fatigue tests. This performance was carried out with two types of tests to evaluate the failure behavior of the T-lap joints; One is skin-directional loading test (Figure 4-2(a), denoted by “skin fatigue test”), and the other is stringer-directional loading test (Figure 4-2(b), denoted by “stringer fatigue test”) with the support of a jig made of steel material. The geometries of skin specimens for fatigue tests were prepared via ASTM E466 standards [26], respectively. A sinusoidal waveform load was applied at the stress ratio of 0.1 and the frequency of 20 Hz. Testing process will stop if the specimen is ruptured or reached 4×10^6 cycles.

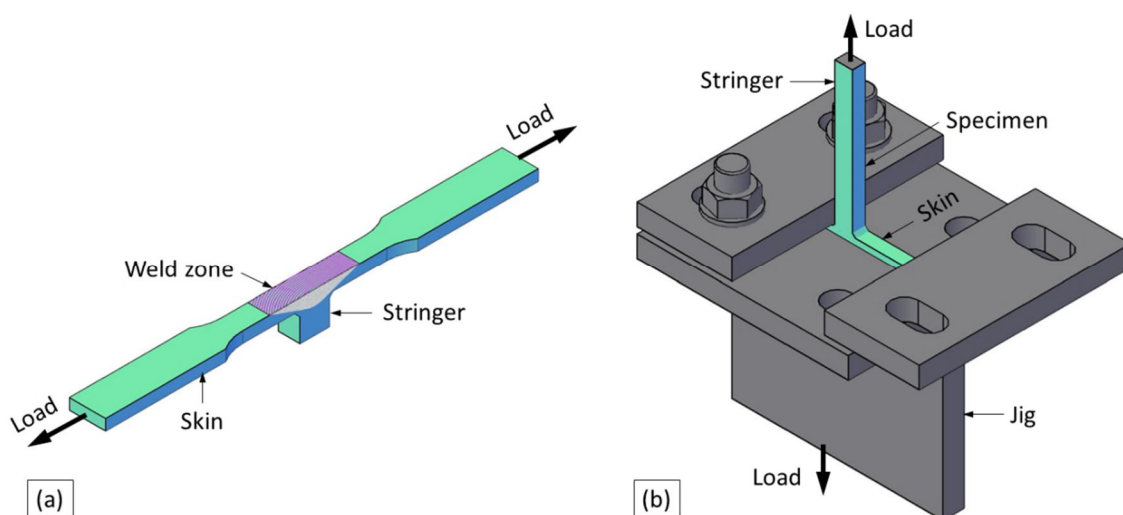


Figure 4-2 Specimen geometry and evaluation of T-lap joints under (a) skin and (b) stringer fatigue tests.

4.3 Results and Discussion

4.3.1 Microstructure of a double pass FSWed T-lap joints

Figure 4-3(a) displays the representative macrostructure on the cross-section of the joints. It is clear that the KBs at two corner fillets were significantly minimized by employing double-pass welding (Figures 4-3(b,d)). Here, they were observed as continuous dark line that was considered as oxide layer, as reported in former Chapter.

Dissimilar to the KBs, the bonding interface without oxide layer was only produced in the stirred zone (Figure 4-3(c)). The formation mechanism of the KBs and bonding interface by applying double-pass welding was detailed in Chapter 3. A quantitative evaluation about the KBs is also shown in Figure 4-4. Here, the curve length of the KBs was significantly minimized at both the RS1/AS2 and AS1/RS2 (Figure 4-4(a)), whereas the initial KBs angles were insignificantly different (Figure 4-4(b)). In addition, the KBs geometry at two corner fillets was absolutely different (as compared between Figures 4-3(b) and 4-3(d)). As presented in literature [1,2], the KBs were a typical type of the defect of solid-state welding with little or no metallic bonding. These characteristics might influence the fatigue behavior of the T-lap joints that will be considered in the next section.

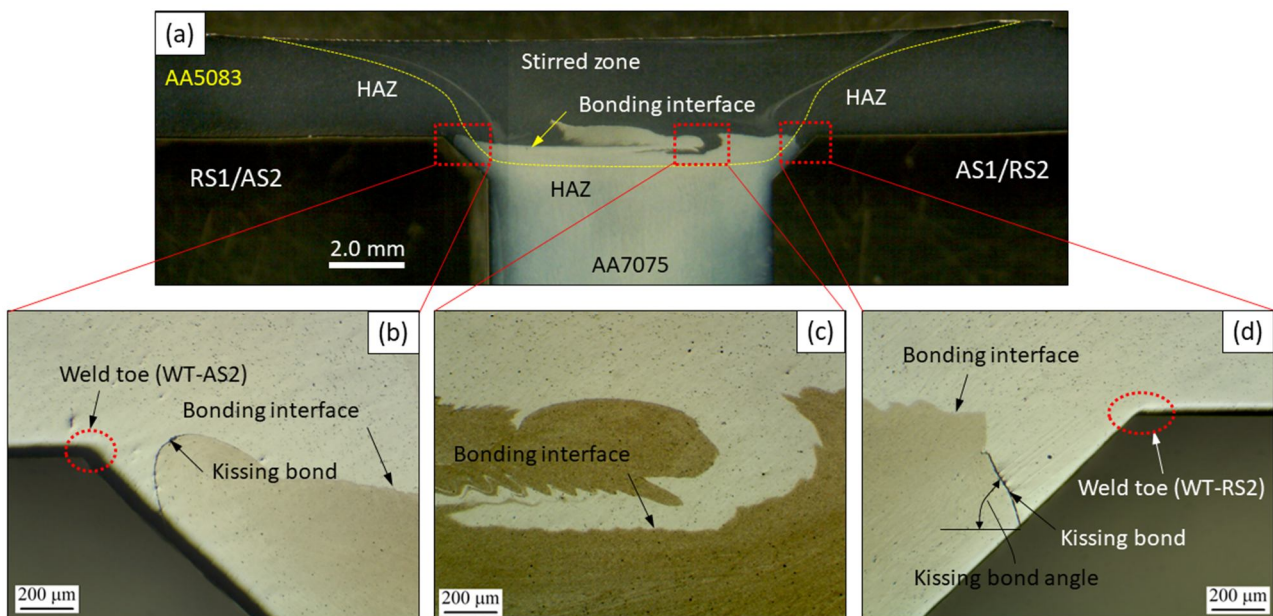


Figure 4-3 Representative image of microstructure at cross-section.

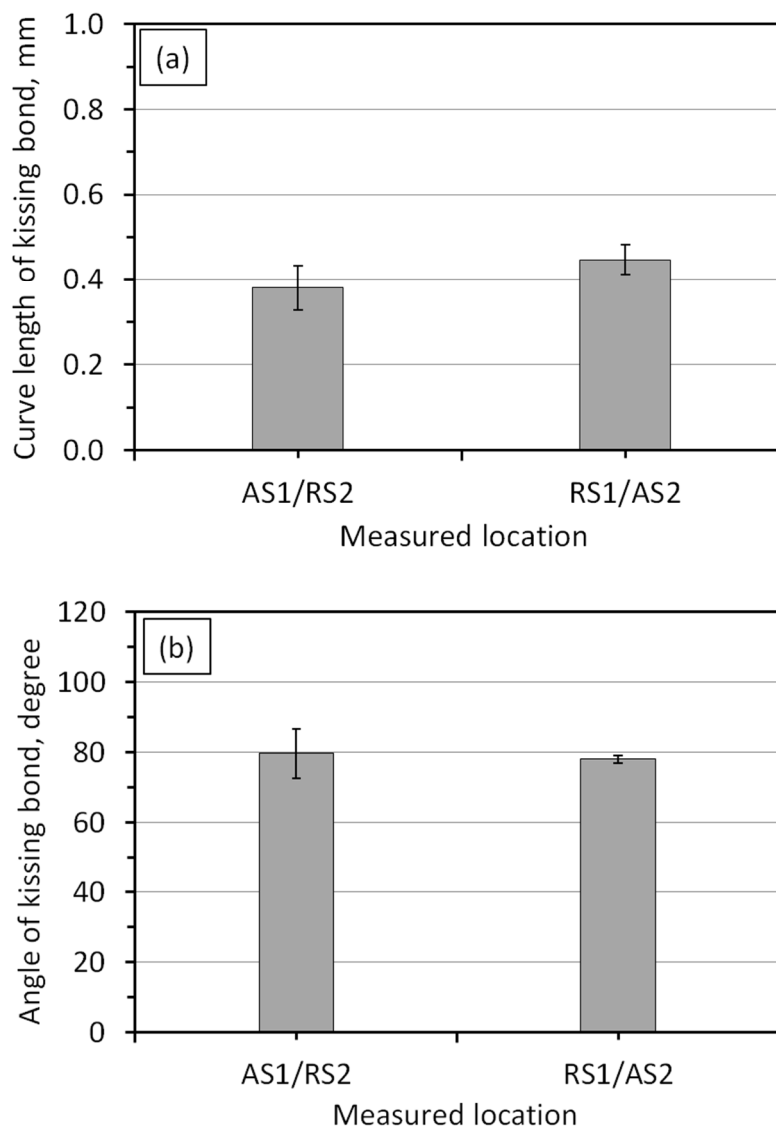


Figure 4-4 (a) Curve length and (b) angle of KBs at the RS1/AS2 and AS1/RS2.

4.3.2 Hardness distribution and tensile strength

Microhardness map measured on the cross-section of the skin is presented in Figure 4-5. There was slightly low in the hardness value at the RS1/AS2 in comparison with that at the AS1/RS2. This result might be related to different welding temperature between the RS1/AS2 and AS1/RS2 [24,25]. The hardness distribution along interface had significant fluctuation (Line 3). While the hardness value measured in the shoulder contact area of skin was attained about 70-90 HV, that in mixed region was reached from 95 to 120 HV. The highest hardness value was obtained about 150 HV in AA7075 region.

The tensile properties of the FSWed T-lap joints are shown in Table 4-1. Here, the strengths of the joints are defined as the ratio of applied load to the cross-section area of the skin/stringer. In comparison with single-pass welding that was investigated in Chapter 2, applying double-pass FSW significantly improved the strength of the T-lap joints, especially in the stringer tensile test.

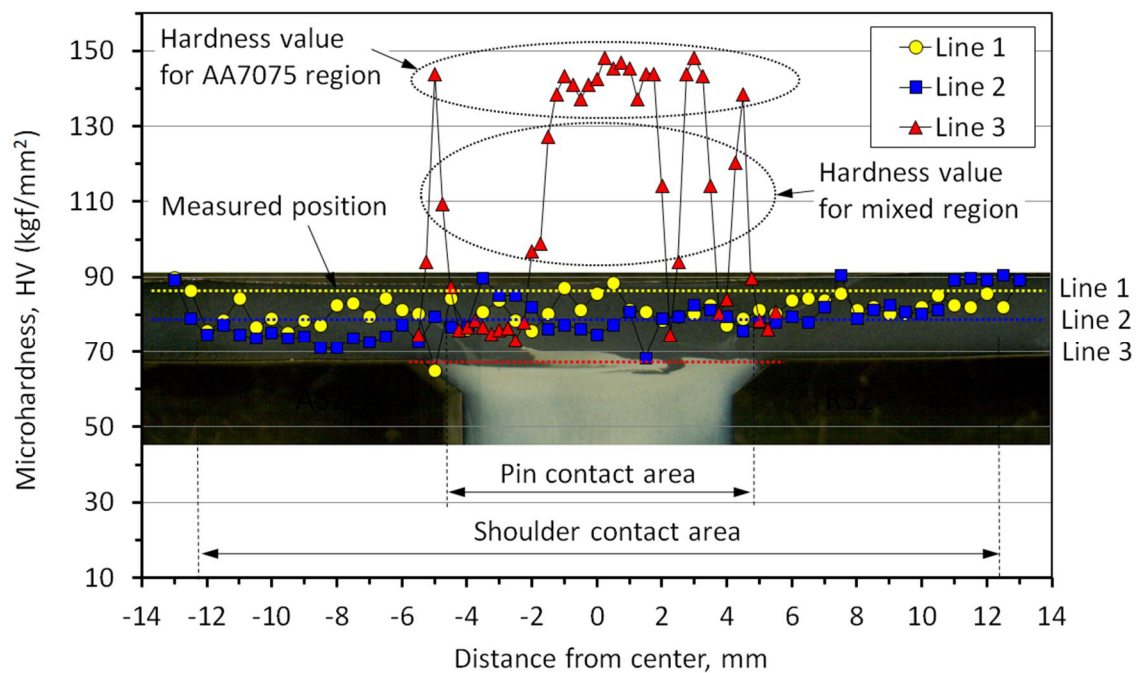


Figure 4-5 Hardness profile along cross-section of skin plate.

Table 4-1 Tensile strength of T-lap joints.

| Type of tests | Yield strength (MPa) | Ultimate tensile strength (MPa) | Strain (%) |
|-----------------------|----------------------|---------------------------------|------------|
| Skin tensile test | 128.5 | 279.6 | 11.8 |
| Stringer tensile test | --- | 118.8 | --- |

4.3.3 Fatigue failure behavior of FSWed T-lap joints

4.3.3.1 Fatigue S-N curves

The fatigue experimental data and the S-N curves of the dissimilar FSWed T-lap joints are indicated in Table 4-2 and Figure 4-6, respectively. Here, the normal stress range was used to assess the fatigue endurance of both the skin and stringer tests. In both cases, the S-N curves of the joints were lower than that of the base alloys,

especially in the stringer fatigue test. The fatigue strength of the skin and stringer tests those were not failed at 4×10^6 cycles reached at about 80 MPa and 16 MPa, respectively. Noting that, the data point of the stringer fatigue test was dispersed and unstable compared to that of the skin fatigue test. These results might be contributed by the various geometries of the KBs formed during the FSW process.

To evaluate the effect of the KBs on the fatigue strength of the T-lap joints, relationship between the ultimate tensile strength (σ_b) and fatigue strength (σ_f) is shown in Figure 4-7 that was expressed by Equation 4-1, as mentioned in literatures [27,28].

$$\sigma_f = m\sigma_b \quad (4-1)$$

where m is coefficient and is shown in Figure 4-7(b). Here, the coefficient m of the joints in both types of tests was much smaller than that of the base alloys, especially in the stringer fatigue test. This result might indicate that the low performance in the fatigue strength had significant contribution by the KBs and will be discussed in the next section.

Table 4-2 Fatigue experiment data of skin and stringer fatigue tests.

| Skin fatigue test | | | | | Stringer fatigue test | | | | |
|-------------------|-----------------------------|----------------------|-----------|-------------------|-----------------------|-----------------------------|----------------------|-----------|-------------------|
| Samples | Stress $\Delta\sigma$ (MPa) | Load ΔP (kN) | Cycles | Fracture location | Samples | Stress $\Delta\sigma$ (MPa) | Load ΔP (kN) | Cycles | Fracture location |
| S1 | 160 | 2.9 | 17,620 | KB-RS2 | S12 | 32.9 | 1.62 | 18,330 | KB-RS2 |
| S2 | 150 | 2.7 | 21,520 | KB-RS2 | S13 | 29.3 | 1.44 | 35,460 | KB-RS2 |
| S3 | 140 | 2.5 | 32,910 | WT-AS2 | S14 | 25.6 | 1.26 | 28,880 | KB-RS2 |
| S4 | 130 | 2.3 | 38,950 | WT-AS2 | S15 | 25.6 | 1.26 | 18,560 | KB-RS2 |
| S5 | 125 | 2.3 | 89,670 | WT-AS2 | S16 | 22.0 | 1.08 | 121,200 | KB-RS2 |
| S6 | 120 | 2.2 | 109,230 | WT-AS2 | S17 | 18.3 | 0.90 | 198,670 | KB-RS2 |
| S7 | 110 | 2.0 | 350,650 | WT-AS2 | S18 | 16.8 | 0.83 | 136,460 | KB-AS2 |
| S8 | 105 | 1.9 | 1,221,230 | WT-AS2 | S19 | 16.1 | 0.79 | 156,190 | KB-RS2 |
| S9 | 100 | 1.8 | 1,874,500 | WT-AS2 | S20 | 16.1 | 0.79 | 4,000,000 | No failure |
| S10 | 95 | 1.7 | 1,444,620 | WT-AS2 | S21 | 14.6 | 0.72 | 2,386,780 | WT-AS2 |
| S11 | 80 | 1.4 | 4,000,000 | No failure | S22 | 14.6 | 0.72 | 560,450 | KB-RS2 |

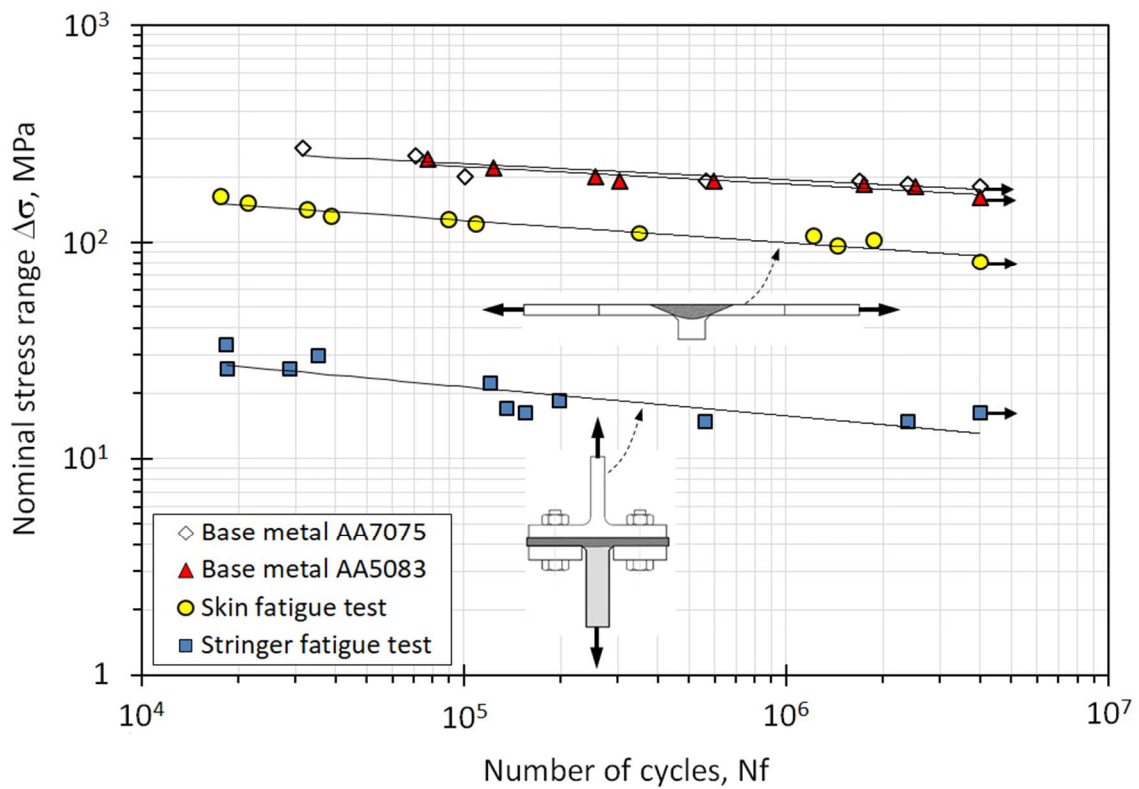


Figure 4-6 S-N curves of the T-lap joints under skin and stringer fatigue tests.

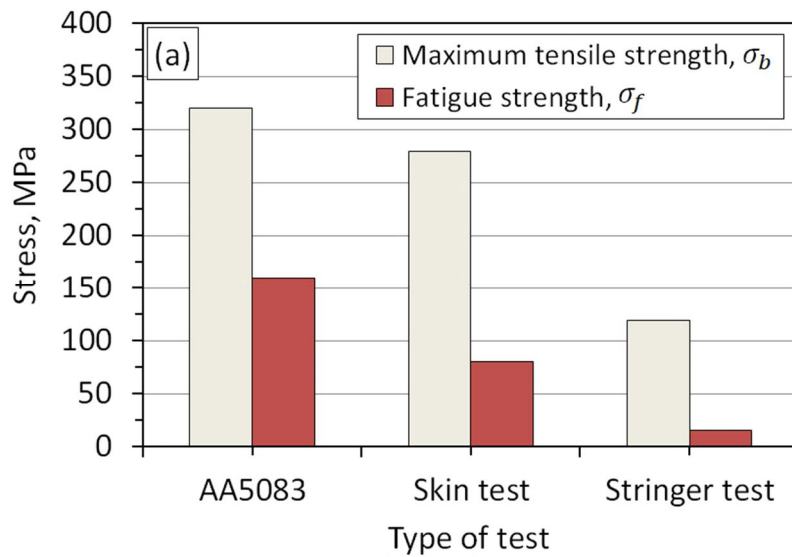


Figure 4-7 (a) Maximum tensile strength and fatigue strength under skin and stringer tests.

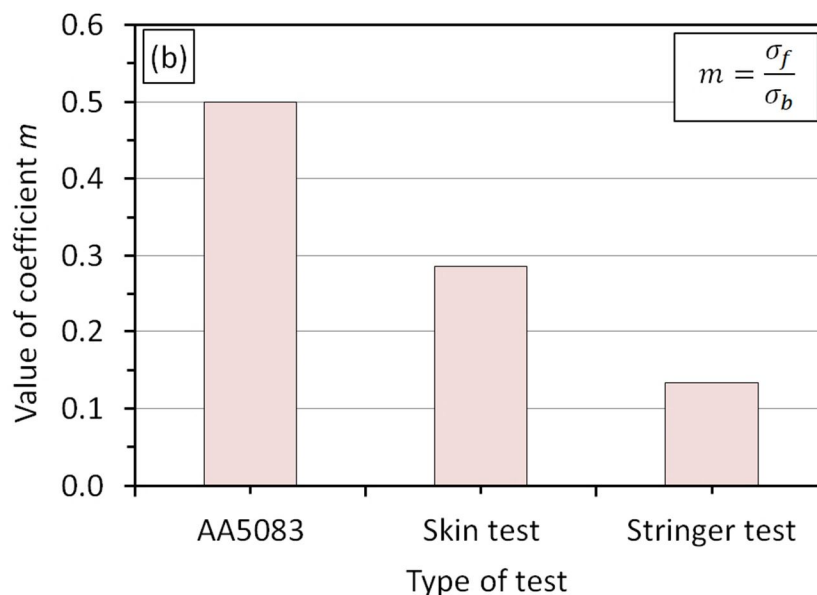


Figure 4-7 (b) Relationship between tensile and fatigue strength presented by value of coefficient m .

4.3.3.2 Fatigue crack initiation under skin fatigue test

As shown in Table 4-2, the main crack initiation was nucleation at the weld toe. Under high stress range, however, the crack initiated at the interface of the KBs at the AS1/RS2 (denoted as KB-RS2). The weld toe at the RS1/AS2 (denoted as WT-AS2) was found as main failure under lower stress range. Figure 4-8(a) shows the fatigue failure of the specimen at the KB-RS2 under the stress range of 150 MPa. It is worthy to note from Figure 4-8(a-1), the KB-AS2 seems to be closed during testing process. This means that the KB-opening at the AS1/RS2 was easier than that at the RS1/AS2. As mentioned in literature [16,23-25,29], the stirring efficiency at the AS was more severe than that at the RS, resulting in the higher bonding strength at the KB-AS2. When the KBs were opened, the higher stress concentration was at the crack tip instead of the WT-RS2. As shown in Figure 4-8(a-2), the absence of crack at the WT-RS2 might illustrate this postulation. By contrast, a small crack at the WT-AS2 was caused by the KB-closing at the RS1/AS2 (Figure 4-8(a-1)).

Figure 4-8(b) shows the representative image of the specimens cracked at the WT-AS2 under the stress range of 100 MPa. It is noted from Figures 4-8(b-1) and (b-2), the KBs at the RS1/AS2 and AS1/RS2 seems to be not opened during testing process. Consequently, the high stress concentration was at two weld toes without at the KBs. The fracture of the specimens at the WT-AS2 and a small crack at the WT-RS2 (Figure

4-8(b-2)) was an evidence for this result. As observed in Figure 4-8, the location of the KBs was under the skin plate where was outside main stress field in the skin fatigue test. So, the low stress range might be not enough to delaminate the interface of the KBs that the bonding strength was formed by the severe thermal deformation during the FSW process [25].

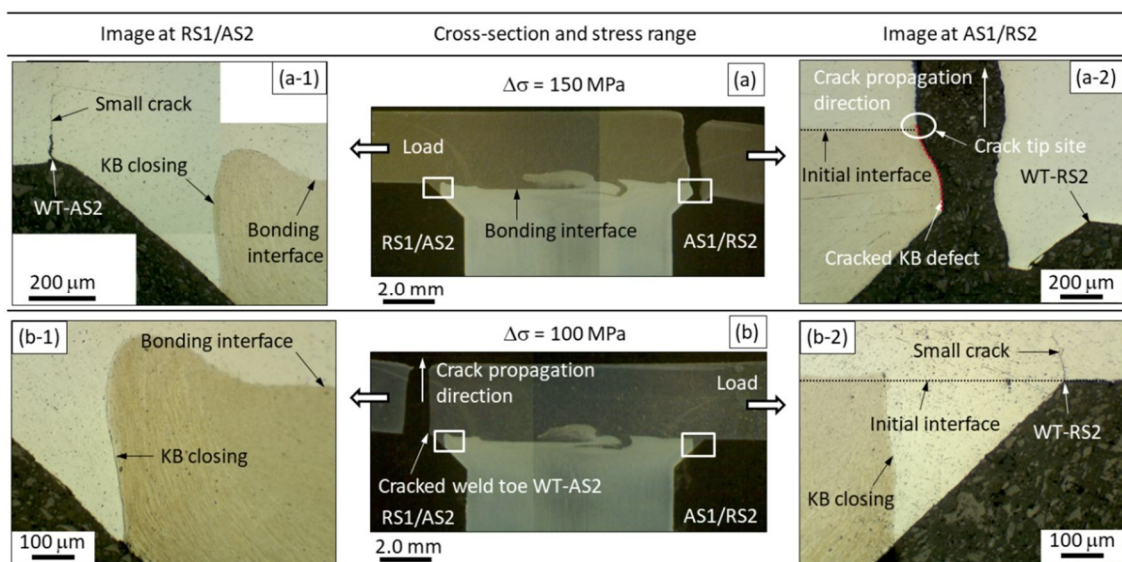


Figure 4-8 Representative images of specimens cracked at (a) KB-RS2 and (b) WT-AS2.

The effective skin thickness (denoted as EST) along the cross-section of specimens, which is defined as minimum distance from interface of defects to the top face of skin part, is displayed in Figure 4-9. According to that, the EST at the RS1/AS2 was lower than that at the AS1/RS2 (Figure 4-9(b)). As mentioned in previous Chapter, using the double-pass FSW and offsetting welding tool to the AS as well as the tilt of welding tool might be these reasons for this result. In this case, the theoretical (k_t) and fatigue stress concentration factors (k_f) at two weld toes might be determined by using Equation (4-2) [30] and Equation (4-3) [31], respectively.

$$k_t = 1.03 + 0.27\theta^{0.22} \times \left(\frac{\rho}{t}\right)^{-0.47} \times \left(\frac{s}{t}\right)^{0.18} \quad (4-2)$$

$$k_f = 1 + \frac{k_t - 1}{1 + \frac{\sqrt{a}}{\sqrt{\rho}}} \quad (4-3)$$

where θ , ρ , and s are defined in Figure 4-9(a). $\sqrt{a} = 0.61 \text{ mm}^{0.5}$ is Neuber material constant for aluminium alloys [32] at the maximum tensile strength of the joints. t is the EST was measured at the WT-AS2 (denoted as $t_{\text{WT-AS2}}$) and the WT-RS2 (denoted as

t_{WT-RS2}). The calculated results were obtained the higher value of stress concentration factors at the WT-AS2 ($k_t = 3.25$ and $k_f = 1.60$) in comparison with that at the WT-RS2 ($k_t = 3.21$ and $k_f = 1.58$). In other words, the low value of hardness and the EST at the WT-AS2 might lead to increase in the stress concentration, resulting in cracking at the WT-AS2.

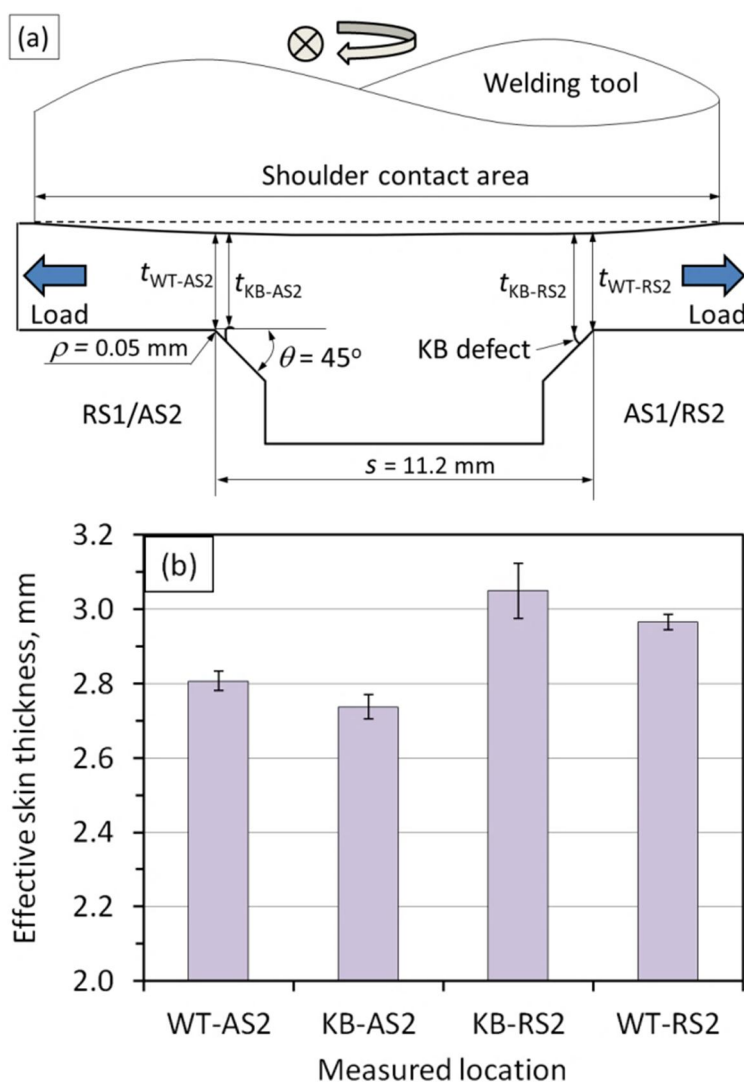


Figure 4-9 (a) Schematic diagrams for determining EST and (b) the value of EST at various locations.

4.3.3.3 Fatigue crack initiation under stringer fatigue test

In the stringer tests, the crack mainly initiated from the interface of the KBs which was found at the KB-RS2 (Table 4-2). The representative images of failed specimens are presented in Figure 4-10. In all cases, the specimens seem to be failed under mixed mode with the plane of crack was about 40°-60° to loading direction. Here, the thinner

thickness of the skin might increase the occurrence of mode II during the testing process, as concluded in literature [33,34].

Figure 4-10(a) shows the specimen was failed under the stress range of 18.3 MPa. It seems that the KBs at two corner fillets were easily opened due to combining between tensile and bending loading, as presented in Figures 4-10(a-1,2). It is worthy to note from Figures 4-10(b-1,2) that the KB-AS2 was not opened under the stress range of 16.1 MPa. Under the lower stress range of 14.6 MPa, the interfaces of the KBs were not delaminated at both RS1/AS2 and AS1/RS2, as observed in Figures 4-10(c-1,2). This means that the stress concentration and crack took place at the weld toe (Figure 4-10(c)). The KB-opening in during testing process is presented in Figure 4-11. The stress caused the KB-opening at the AS1/RS2 was lower than that at the RS1/AS2. As presented in previous section, the different bonding strength of the KBs at the RS1/AS2 and the AS1/RS2 might be main reason for this result.

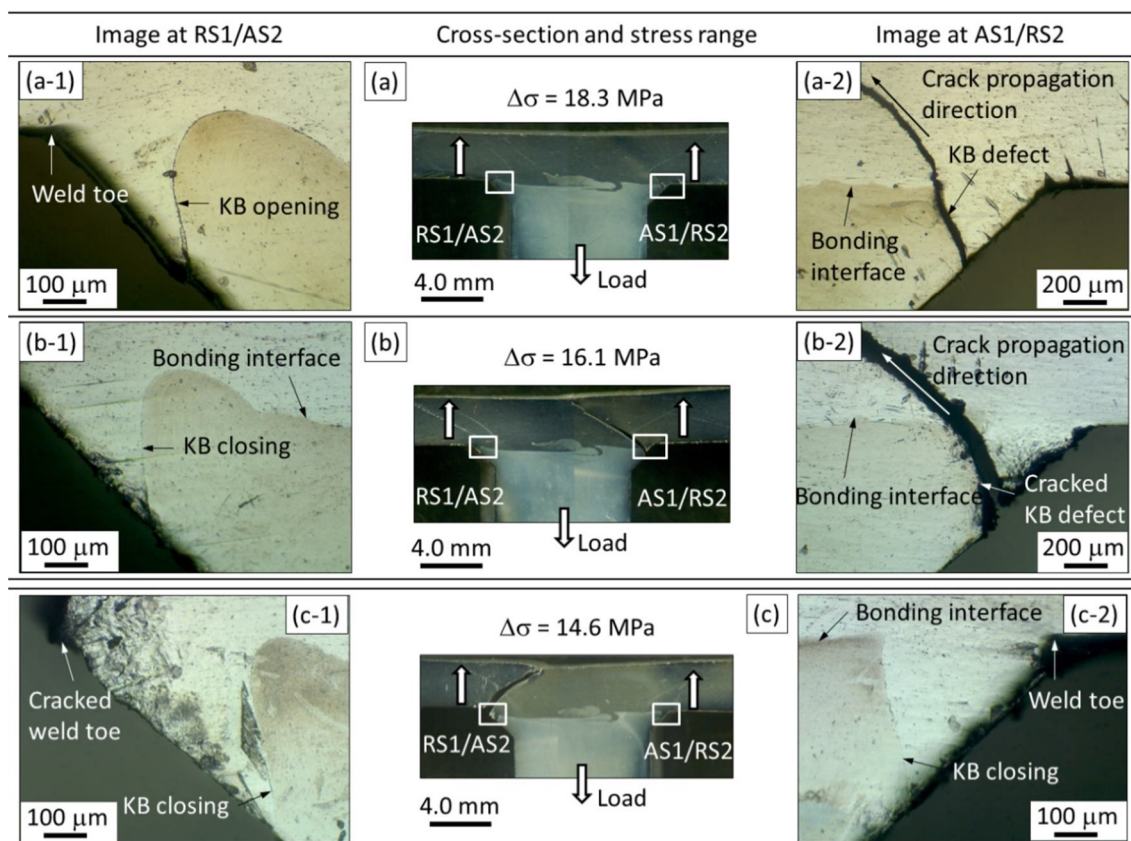


Figure 4-10 Images of specimens failed under stringer fatigue loading at (a) $\Delta\sigma = 18.3$ MPa, (b) $\Delta\sigma = 16.1$ MPa, and (c) $\Delta\sigma = 14.6$ MPa.

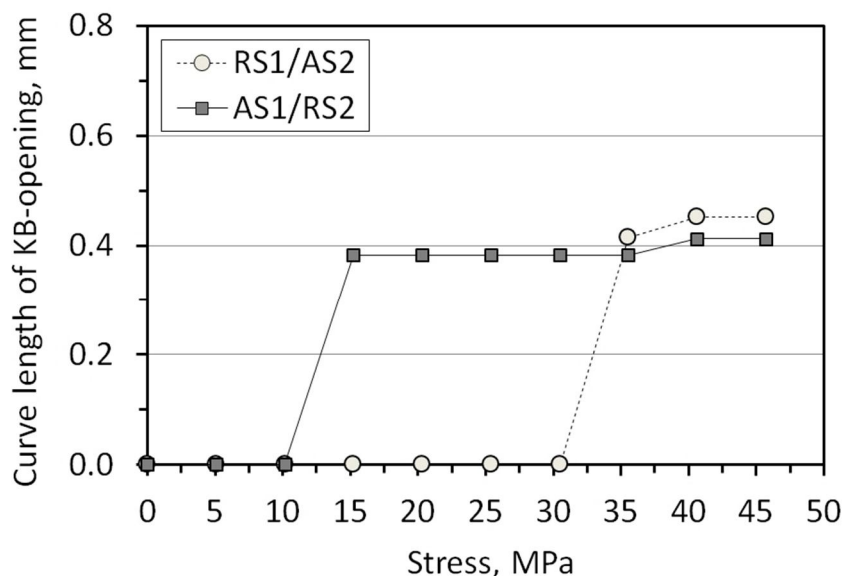


Figure 4-11 Effect of stress on KB-opening.

4.3.3.4 Fracture morphology

In order to more understand the failure of the T-lap joints under cyclic loading, the fracture surface of the specimens was analyzed by the SEM, and the results are shown in Figures 4-12,13 for the skin fatigue test and Figure 4-14 for the stringer fatigue test. Here, the KBs and weld toe sites were found in the bottom surface of the skin where originated a crack initiation, as shown in Figures 4-12(a), 4-13(a), and 4-14(a), respectively. The direction of crack propagation was marked by arrows (Figures 4-12(a), 4-13(a), and 4-14(a)). While the fracture surface of the KBs was observed as smooth facet that presented a weak adherence (Figures 4-12(b) and 4-14(d)), the rough fracture was found in the region of slow crack propagation (Figures 4-12(c), 4-13(b) and 14-14(c)). The region of fast crack propagation was characterized by a large number of dimples that indicated a ductile failure behavior (Figure 4-12(e) and 14-13(d)). The striation waves were also found on fracture surface (Figures 4-13(c) and 4-14(e)).

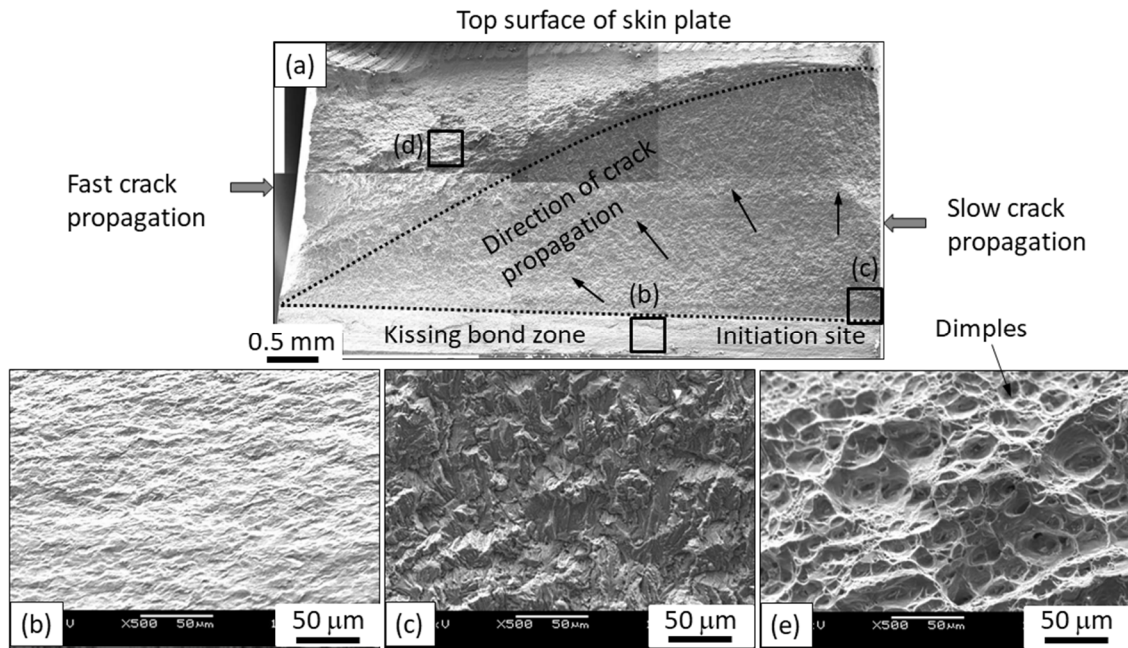


Figure 4-12 Fracture morphology of specimen cracked at KB-RS2 under skin fatigue test.

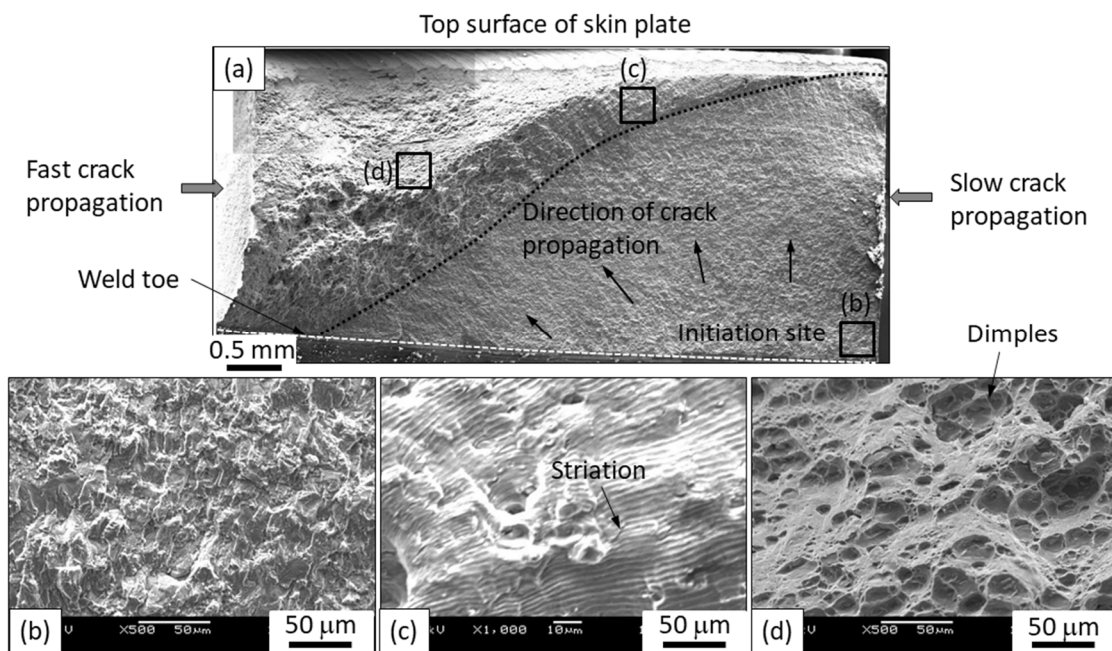


Figure 4-13 Fracture morphology of specimen cracked at weld toe under skin fatigue test.

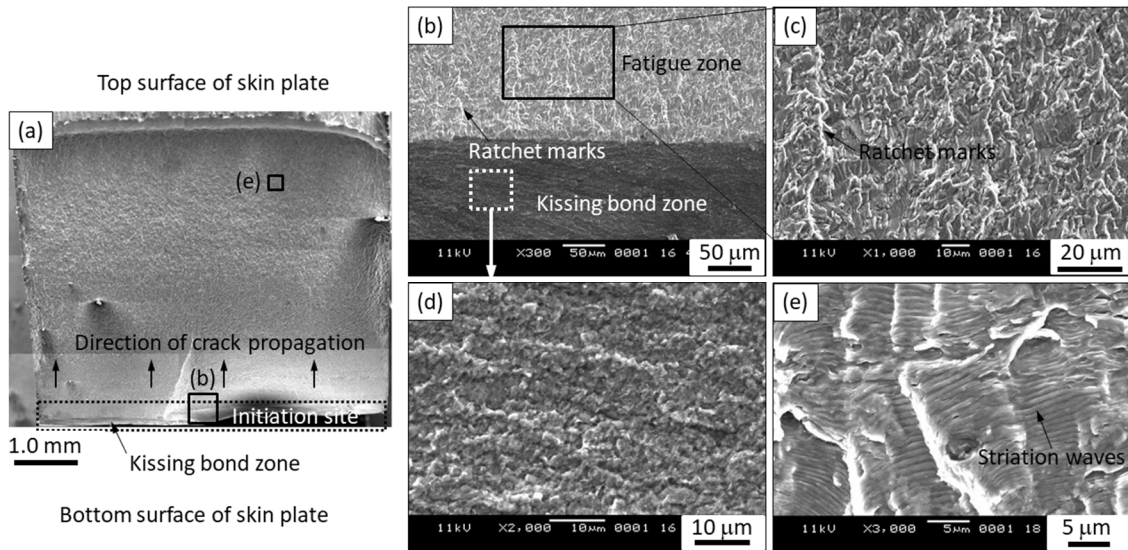


Figure 4-14 Fracture morphology of specimen S16 cracked at KB-RS2 under stringer fatigue test.

4.4 Chapter Summary

In this work, the failure behavior of the dissimilar T-lap joints between AA7075 and AA5083 under the skin and stringer fatigue tests was investigated. The following conclusions were derived:

- (4-1) The fatigue life of the joints under the skin and stringer loading tests was lower than that of two base alloys. The kissing bond defects that were improved by double-pass FSW significantly influenced the failure behavior of the joints.
- (4-2) In the skin fatigue test, the crack initiation was predominantly nucleated at the weld toe at the RS1/AS2 where the value of the hardness and effective skin thickness was lightly low in comparison with that at the AS1/RS2. This would lead to the higher stress concentration at the weld toe at the RS1/AS2.
- (4-3) Regarding the stringer fatigue test, the fatigue crack was predominantly initiated from the interface of the KBs at the AS1/RS2, and then propagated obliquely to the skin AA5083 under mixed mode failure. The interfaces of the KBs were comfortably delaminated under combining between tensile and bending loading, especially in the AS1/RS2. In these cases, the roles of the KB orientation in terms of crack tip angle significantly affected the fatigue crack initiation and the life of the T-lap joints.
- (4-4) The fracture surface of the KBs was detected as smooth facet with weak adherence. In contrast, the rough fracture was found in the region of slow crack propagation. The region of fast crack propagation was characterized by a large number of dimples that indicated a ductile failure behavior.

4.5 Chapter References

- [1] Oosterkamp, O., Oosterkamp, L.D. and Nordeide, A., 'Kissing bond' phenomena in solid-state welds of aluminum alloys, *Welding Journal*, Vol.83, (2004), pp.225-231.
- [2] Sato, Y.S., Takauchi, H., Park, S.H.C. and Kokawa, H., Characteristics of the kissing-bond in friction stir welded Al alloy 1050, *Materials Science and Engineering A*, Vol.405, (2005), pp.333-338.
- [3] Zhou, C., Yang, X., and Luan, G., Effect of kissing bond on fatigue behavior of friction stir welds on Al 5083 alloy, *Journal of Materials Science*, Vol.41(10), (2006), pp.2771-2777.
- [4] Kadlec, M., Růžek, R., Nováková, L., Mechanical behaviour of AA 7475 friction stir welds with the kissing bond defect, *International Journal of Fatigue*, Vol.74, (2015), pp.7-19.
- [5] Le Jolu, T., Morgeneyer, T.F., Denquin, A., and Gourgues-Lorenzon, A.F., Fatigue lifetime and tearing resistance of AA2198 Al–Cu–Li alloy friction stir welds: Effect of defects, *International Journal of Fatigue*, Vol. 70, (2015), pp.463-472.
- [6] Zhou, N., Song, D., Qi, W., Li, X., Zou, J., and Attallah, M.M, Influence of the kissing bond on the mechanical properties and fracture behaviour of AA5083-H112 friction stir welds, *Materials Science and Engineering: A*, Vol.719, (2018), pp.12-20.
- [7] Khan, N.Z., Siddiquee, A.N., Khan, Z.A., and Shihab, S.K, Investigations on tunneling and kissing bond defects in FSW joints for dissimilar aluminum alloys, *Journal of Alloys and Compounds*, Vol.648, (2015), pp.360-367.
- [8] Okamura, H., Aota, K., Sakamoto, M., Ezumi, M., and Ikeuchi, K., Behaviour of oxides during friction stir welding of aluminium alloy and their effect on its mechanical properties, *Welding International*, Vol.16(4), (2002), pp.266-275.
- [9] Delrue, S., Tabatabaeipour, M., Hettler, J., and Van Den Abeele, K., Applying a nonlinear, pitch-catch, ultrasonic technique for the detection of kissing bonds in friction stir welds, *Ultrasonics*, Vol.68, (2016), pp.71-79.
- [10] Dickerson, T., Fatigue of friction stir welds in aluminium alloys that contain root flaws. *International Journal of Fatigue*, Vol.25(12), (2003), pp.1399-1409.
- [11] Salari, E., Jahazi, M., Khodabandeh, A., and Ghasemi-Nanasa, H., Influence of tool geometry and rotational speed on mechanical properties and defect formation in friction stir lap welded 5456 aluminum alloy sheets, *Materials & Design*, 58, (2014), pp.381-389.
- [12] Dubourg, L., Merati, A., and Jahazi, M., Process optimisation and mechanical properties of friction stir lap welds of 7075-T6 stringers on 2024-T3 skin, *Materials & Design*, Vol.31(7), (2010), pp.3324-3330.
- [13] Moraes, J.F.C., Rodriguez, R.I., Jordon, J.B., and Su, X, Effect of overlap orientation on fatigue behavior in friction stir linear welds of magnesium alloy sheets, *International Journal of Fatigue*, Vol.100, (2017), pp.1-11.
- [14] Yadava, M.K., Mishra, R.S., Chen, Y.L., Carlson, B., and Grant, G.J., Study of

- friction stir joining of thin aluminium sheets in lap joint configuration, *Science and Technology of Welding and Joining*, Vol.15(1), (2010), pp.70-75.
- [15] Ericsson, M., Jin, L., and Sandstrom, R., Fatigue properties of friction stir overlap welds, *International Journal of Fatigue*, 29(1), (2007), pp.57-68.
- [16] Cui, L., Yang, X., Zhou, G., Xu, X. and Shen, Z., Characteristics of defects and tensile behaviors on friction stir welded AA6061-T4 T-joints, *Materials Science and Engineering A*, Vol.543, (2012), pp.58-68.
- [17] Zhao, Y., Zhou, L., Wang, Q., Yan, K. and Zou, J., Defects and tensile properties of 6013 aluminum alloy T-joints by friction stir welding, *Materials and Design*, Vol.57, (2014), pp.146-155.
- [18] Donati, L., Tomesani, L. and Morri, A., Structural T-joint produced by means of friction stir welding (FSW) with filling material, *International Journal of Material Forming* Vol.2, (2009), pp.295-298.
- [19] Said, M.T.S.M., Hamid, D.A., Ismail, A., Zainal, S.N.N., Awang, M., Rojan, M.A., Ikram, I.M. and Makhtar, M.F., Experimental Study on Effect of Welding Parameters of Friction Stir Welding (FSW) on Aluminium AA5083 T-joint, *Information Technology Journal*, Vol.15, (2016), pp.99-107.
- [20] Jesus, J.S., Costa, J.M., Loureiro, A. and Ferreira, J.M., Assessment of friction stir welding aluminium T-joints, *Journal of Materials Processing Technology*, Vol.255, (2018), pp.387-399.
- [21] Manuel, N., Silva, C., Costa, J.M.D., and Loureiro, A., Friction stir welding of T-joints in dissimilar materials: Influence of tool geometry and materials properties. *Materials Research Express*, Vol.6, (2019), pp.106528.
- [22] Buffa, G., Fratini, L., Micari, F. and Shivpuri, R., Material Flow in FSW of T-joints: Experimental and Numerical Analysis, *International Journal of Material Forming*, Vol.1(1), (2008), pp.1283-1286.
- [23] Fratini, L., Buffa, G., Micari, F. and Shivpuri, R., On the material flow in FSW of T-joints: Influence of geometrical and technological parameters, *International Journal of Advanced Manufacturing Technology*, Vol.44, (2009), pp.570-578.
- [24] Feistauer, E.E., Bergmann, L.A. and dos Santos, J.F., Effect of reverse material flow on the microstructure and performance of friction stir welded T-joints of an Al-Mg alloy, *Materials Science and Engineering A*, Vol.731, (2018), pp.454-464.
- [25] Hao, D.D., Okazaki, M., and Tra, H.T., Effect of tool offset and reversed metal flow on mechanical properties of dissimilar friction stir welding T-lap joints between AA7075 and AA5083, *JSME-Mechanical Engineering Journal*, Vol.7(1), (2020), pp.19-00490.
- [26] Annual Book of ASTM Standards, Standard Practice for Conducting Force Controlled Constant Amplitude Axial Fatigue Tests of Metallic Materials, E466, (2004), ASTM International.
- [27] Li, Z., Wang, Q., Luo, A.A., Fu, P., and Peng, L., Fatigue strength dependence on the ultimate tensile strength and hardness in magnesium alloys, *International Journal of Fatigue*, Vol.80, (2015), pp.468-476.
- [28] Lee, Y.L., Pan, J., Hathaway, R.B., Barkey, M.E., *Fatigue Testing and Analysis*

- (Theory and Practice), Elsevier Butter-worth Heinemann, Amsterdam, Boston, Heidelberg (2005).
- [29] Guerra, M., Schmidt, C., McClure, J.C., Murr, L.E., Nunes, A.C., Flow patterns during friction stir welding, *Materials Characterization*, Vol.49(2), (2002), pp.95-101.
- [30] Brennan, F.P., Peleties, P., Hellier, A.K., Predicting weld toe stress concentration factors for T and skewed T-joint plate connections, *International Journal of Fatigue*, Vol.22(7), 2000, Pages 573-584.
- [31] Peterson, R.E., Analytical approach to stress concentration effect in aircraft materials, U.S. air force-WADC symposium on fatigue of metals, Technical Report, (1959), 59–507:273.
- [32] Kuhn, P., The prediction of notch and crack strength under static or fatigue loading, SAE technical paper, (1964),640500;
- [33] Frank, D., Remes, H., and Romanoff, J., J-integral-based approach to fatigue assessment of laser stake-welded T-joints, *International Journal of Fatigue*, Vol.47, (2013), pp.340-350.
- [34] Gallo, P., Guglielmo, M., Romanoff, J., Remes, H., Influence of crack tip plasticity on fatigue behaviour of laser stake-welded T-joints made of thin plates, *International Journal of Mechanical Sciences*, Vol.136, (2018), pp.112-123.

Chapter 5

Numerical Model on Effect of Interface Morphology on Fracture Behavior of Friction Stir Welded T-lap Joints

In this chapter, the influence of interface geometry on the fracture behavior of FSWed T-lap joints under the skin and stringer loading tests is explored. At first, the roles of the interface characteristics in terms of the size and orientation of the defects on the stress intensity factor (SIF) are addressed based on the fracture mechanics. Here, in order to more understand the present experimental results, a simplified fracture mechanics model is proposed via introducing a new parameter; “geometrical resistance factor of defects (GRFD)”. The Maximum Tangential Stress (MTS) criterion is employed to estimate crack direction, since the fracture of the specimens is associated with mixed mode. The Finite Element Analysis (FEA) is also applied to elucidate the failure behavior of the T-lap joints for more quantitative discussion.

5.1 Introduction

As shown in the previous chapter, the fracture strength of the T-lap joints was significantly influenced by the defects which had been introduced during the FSW process. It is true that the fracture location of the specimens was almost taken place at the hook, kissing bond, and bonding line defects. It is worthy to note that these defects were formed along the interface between the skin and stringer parts. In the other words, the interface morphology of the FSWed T-lap joints seems to play the intrinsic role in the mechanical properties of the joints.

The aim of this chapter is to clarify the effect of interface morphology on the fracture behavior of the FSWed T-lap joints. As the fracture behavior in general have been successful analyzed based on the fracture mechanics, such a new concept that the interface in the FSWed T-lap joints is modeled by the corresponding crack is introduced in this work. A simplified fracture mechanics model is proposed via introducing a new parameter; “geometrical resistance factor of defects (GRFD)”. Finite Element Analysis (FEA) is also applied to understand more quantitatively the failure behavior of the T-lap joints.

5.2 Fracture Mechanic Concepts

5.2.1 Stress intensity factor (SIF)

It is well known that in linear elastic fracture mechanics (LEFM) principles, the stress intensity factor (SIF, K) keeps the most important role in the valuation of the reliability of a structural component that contains a crack [1]. The calculation of the SIFs depends on the type of mode failure of structures.

Figure 5-1 illustrates three types of failure modes which a crack can experience in the fracture mechanics. For mode I loading, where the principal load is employed normal to the crack plane, tends to open the crack. Mode II corresponds to in-plane shear loading and tends to slide one crack face with respect to the other. Mode III refers to out-of-plane shear. The SIFs for each mode can be defined as following [1,2]:

$$K_I = \lim_{r \rightarrow 0} \sqrt{2\pi r} \sigma_{yy}(r, 0) \quad (5-1)$$

$$K_{II} = \lim_{r \rightarrow 0} \sqrt{2\pi r} \sigma_{yx}(r, 0) \quad (5-2)$$

$$K_{III} = \lim_{r \rightarrow 0} \sqrt{2\pi r} \sigma_{yz}(r, 0) \quad (5-3)$$

A cracked body can be loaded in any one of these modes, or a combination between two or three modes that is called as mixed mode failure [3]. The equivalent SIF, K_{eq} in two dimensional mixed mode failures might be determined by Equation (5-4) [4].

$$K_{eq} = \sqrt{K_I^2 + K_{II}^2} \quad (5-4)$$

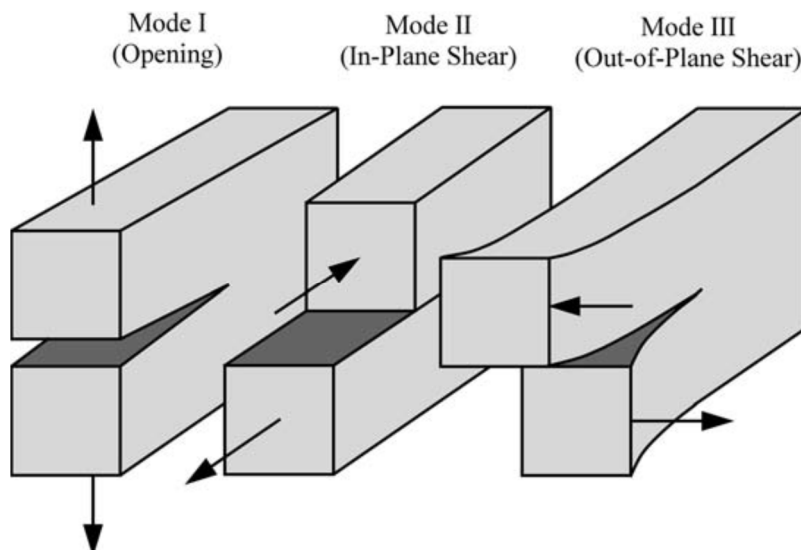


Figure 5-1 Three types of failure modes in fracture mechanics [3].

5.2.2 A simplified model to describe the interface, or defect morphology

5.2.2.1 Kinked edge crack in a semi-infinity plane

Taking account of the defect geometry presented in Chapter 2 to Chapter 4, the skin test can be modeled by Figure 5-2 simply, but not explicitly. Here, the SIFs at the crack tip of kinked edge crack in a semi-infinity plane for mode I and mode II can be determined and approximated as Equation (5-5) and (5-6), respectively following [5]:

$$K_I = F \times [(\sin\theta_2)^2 \times \sigma] \times (1.12)^2 \times \frac{\sqrt{\pi b_2}}{\sqrt{\sin\theta_2}} \quad (5-5)$$

$$K_{II} = F \times (\sin\theta_2 \cos\theta_2 \times \sigma) \times \frac{1}{1.12^2} \times \frac{\sqrt{\pi b_2}}{\sqrt[4]{\sin 2\theta_2}} \quad (5-6)$$

where factor F are determined as Equation (5-7) following [5]:

$$F = \frac{1}{\sqrt{\pi}} (1.99 - 0.41\lambda + 18.7\lambda^2 - 38.5\lambda^3 + 54\lambda^4) \quad (5-7)$$

with $\lambda = b_2/w$.

It is important to note that the K_I and K_{II} are sensitively changed by the crack length “ b_2 ” and little by “ b_1 ”, when the length c_2 is longer than $\geq 1.2c_1$, following the reference [5].

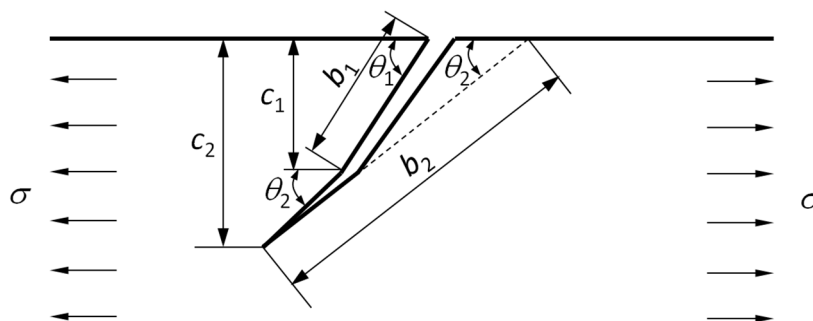


Figure 5-2 Kinked edge crack in a semi-infinity plane under uniform tension, a simplified model of the skin test.

5.2.2.2 Single inclined edge crack plate loaded in tension

The SIFs at the crack tip of single oblique crack (Figure 5-3) for mode I and mode II can be determined as Equation (5-8) and (5-9), respectively [5]. It might be considered as reasonable model for the stringer test.

$$K_I = F \times [(\sin\theta)^2 \times \sigma] \times (1.12)^2 \times \frac{\sqrt{\pi a}}{\sqrt{\sin\theta}} \quad (5-8)$$

$$K_{II} = F \times (\sin\theta \cos\theta \times \sigma) \times \frac{1}{1.12^2} \times \frac{\sqrt{\pi a}}{\sqrt[4]{\sin 2\theta}} \quad (5-9)$$

where factor F are determined as Equation (5-7) following [5]:

$$F = \frac{1}{\sqrt{\pi}} (1.99 - 0.41\lambda + 18.7\lambda^2 - 38.5\lambda^3 + 54\lambda^4) \quad (5-10)$$

with $\lambda = a/w$.

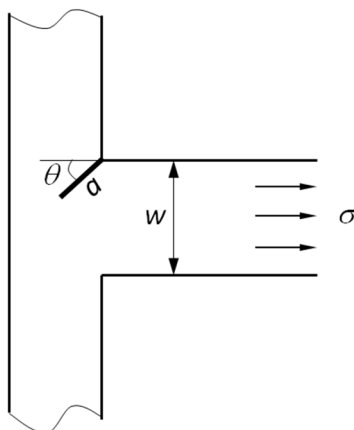


Figure 5-3 Single inclined edge crack plate loaded in tension, a simplified model of the stringer test.

5.2.2.3 Double inclined edge crack plate loaded in tension

As shown in Chapter 3, the application of double-pass FSW made the defect geometry from a single type to a doubly distributed type. This type of change can be modeled by Figure 5-3 and 5-4. The SIFs at crack tip of double crack (Figure 5-4) for mode I and mode II can be determined as Equation (5-8) and (5-9), respectively [5]. Factor F are determined as Equation (5-11) following [6,7]:

$$F = \left[1 + 0.122 \left(\cos \frac{\pi\xi}{2} \right)^4 \right] \times \sqrt{\frac{2}{\pi\xi} \tan \frac{\pi\xi}{2}} \quad (5-11)$$

with $\xi = 2a/w$.

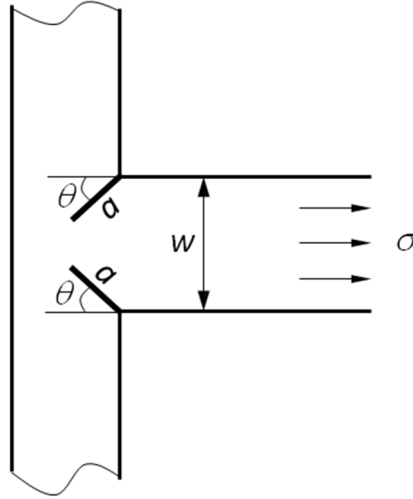


Figure 5-4 Double inclined edge cracks plate loaded in tension, a simplified model of the stringer test.

5.2.3 Stress components around a crack tip

The stress components at a crack tip in Cartesian co-ordinates (Figure 5-5(a)) are defined as followings [3]:

$$\sigma_x = \frac{1}{\sqrt{2\pi r}} \left\{ \left[K_I \cos \frac{\theta}{2} \left(1 - \sin \frac{\theta}{2} \sin \frac{3\theta}{2} \right) \right] - \left[K_{II} \sin \frac{\theta}{2} \left(2 + \cos \frac{\theta}{2} \cos \frac{3\theta}{2} \right) \right] \right\} \quad (5-12)$$

$$\sigma_y = \frac{1}{\sqrt{2\pi r}} \left\{ \left[K_I \cos \frac{\theta}{2} \left(1 + \sin \frac{\theta}{2} \sin \frac{3\theta}{2} \right) \right] + \left[K_{II} \sin \frac{\theta}{2} \cos \frac{\theta}{2} \cos \frac{3\theta}{2} \right] \right\} \quad (5-13)$$

$$\tau_{xy} = \frac{1}{\sqrt{2\pi r}} \left\{ \left[K_I \cos \frac{\theta}{2} \sin \frac{\theta}{2} \cos \frac{3\theta}{2} \right] + \left[K_{II} \cos \frac{\theta}{2} \left(1 - \sin \frac{\theta}{2} \sin \frac{3\theta}{2} \right) \right] \right\} \quad (5-14)$$

$\sigma_z = \nu(\sigma_x + \sigma_y)$ for plane strain, where ν is Poisson's ratio.

$\sigma_z = 0$ for plane stress.

The stress components at the crack tip in polar co-ordinates (Figure 5-5(b)) are defined as following [8,9]:

$$\sigma_{\theta} = \frac{1}{\sqrt{2\pi r}} \left\{ \left[\frac{K_I}{2} \cos \frac{\theta}{2} (1 + \cos \theta) \right] - \left[\frac{3K_{II}}{2} \sin \frac{\theta}{2} (1 + \cos \theta) \right] \right\} \quad (5-15)$$

$$\sigma_r = \frac{1}{\sqrt{2\pi r}} \left\{ \left[\frac{K_I}{2} \cos \frac{\theta}{2} (3 - \cos \theta) \right] - \left[\frac{K_{II}}{2} \sin \frac{\theta}{2} (1 - 3\cos \theta) \right] \right\} \quad (5-16)$$

$$\tau_{r\theta} = \frac{1}{\sqrt{2\pi r}} \left\{ \left[\frac{K_I}{2} \sin \frac{\theta}{2} (1 + \cos \theta) \right] - \left[\frac{K_{II}}{2} \cos \frac{\theta}{2} (1 - 3\cos \theta) \right] \right\} \quad (5-17)$$

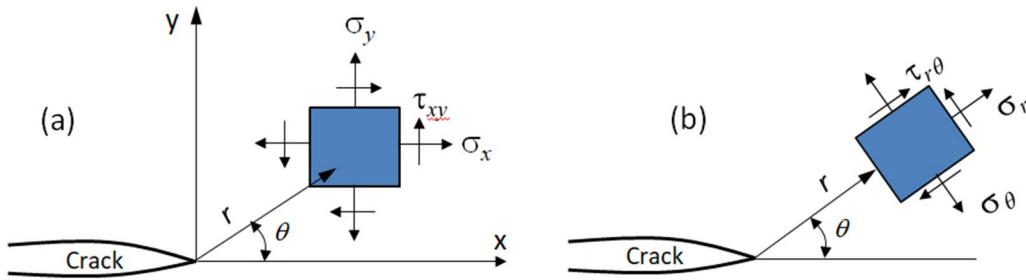


Figure 5-5 Stress components in (a) Cartesian co-ordinate and (b) polar co-ordinate systems.

5.2.4 Crack propagation direction criteria in mixed mode failure

Crack propagation criteria are applied to predict a crack direction under external load. It is well known that the crack will be moved in the crack plane in mode I failure. However, the crack propagation direction is difficult to predict exactly in mixed mode loading [10]. Two crack propagation direction criteria are introduced as following:

5.2.4.1 Maximum tangential stress (MTS) criterion

This method is hypothesised that a crack tip will move in the direction of the point where the highest value of the tangential stress component is found [11]. It can be expressed mathematically as follows:

$$\frac{\partial \sigma_{\theta}}{\partial \theta} = 0, \quad \frac{\partial^2 \sigma_{\theta}}{\partial \theta^2} < 0. \quad (5-18)$$

Applying the condition of Equation (5-18) into Equation (5-15) we have [8]:

$$\tan^2 \frac{\theta}{2} - \frac{\mu}{2} \tan \frac{\theta}{2} - \frac{1}{2} = 0, \quad (5-19)$$

$$-\frac{3}{2} \left[\left(\frac{1}{2} \cos^3 \frac{\theta}{2} - \cos \frac{\theta}{2} \sin^2 \frac{\theta}{2} \right) + \frac{1}{\mu} \left(\sin^3 \frac{\theta}{2} - \frac{7}{2} \sin \frac{\theta}{2} \cos^3 \frac{\theta}{2} \right) \right] < 0 \quad (5-20)$$

where μ is defined as: $\mu = \frac{K_I}{K_{II}}$

5.2.4.2 Strain energy density (SED) criterion

The SED criterion is suggested and issued by Sih in 1973 [12]. It is hypothesised that the crack tip will move to position where is minimum strain energy density S . In mathematical form, SED criterion can be expressed as:

$$\frac{\partial S}{\partial \theta} = 0, \quad \frac{\partial^2 S}{\partial \theta^2} < 0 \quad (5-21)$$

where S is defined as: $S = r_0 \frac{dW}{dV}$

where $dW = dV$ is the strain energy density function per unit volume, and r_0 is finite distance from the point of failure initiation [9]. The strain energy density function can be written as following [12]:

$$S = a_{11}K_I^2 + 2a_{12}K_I K_{II} + a_{22}K_{II}^2 \quad (5-22)$$

where the factors a_{ij} are functions of the angle θ , and are defined as following:

$$a_{11} = \frac{1}{16G\pi} [(1 + \cos\theta)(\kappa - \cos\theta)] \quad (5-23)$$

$$a_{12} = \frac{1}{16G\pi} \sin\theta [(2\cos\theta) - (\kappa - 1)] \quad (5-24)$$

$$a_{22} = \frac{1}{16G\pi} [(\kappa + 1)(1 - \cos\theta) + (1 + \cos\theta)(3\cos\theta - 1)] \quad (5-25)$$

where G is the modulus, and κ is a constant depended on stress state, and is defined as following:

$$\kappa = \frac{3-\nu}{1+\nu} \quad (5-26)$$

$$\kappa = 3 - 4\nu \quad (5-27)$$

From Equation (5-21), (5-22), (5-23), (5-24), and (5-25) we have [9]:

$$2\mu \tan^4 \frac{\theta}{2} (1 + \kappa) + \tan^3 \frac{\theta}{2} [2\kappa(1 - \mu^2) - 2\mu^2 + 10] - 24\mu \tan^2 \frac{\theta}{2} + \tan \frac{\theta}{2} [2\kappa(1 - \mu^2) + 6\mu^2 - 14] + 2\mu(3 - \kappa) = 0 \quad (5-28)$$

$$2\mu \sin\theta(\kappa - 1) - 8\mu \sin 2\theta + \cos\theta(\kappa - 1)(1 - \mu^2) + 2\cos 2\theta(\mu^2 - 3) > 0 \quad (5-29)$$

It is worthy to remind that the MTS and SED criteria can predict the fracture behavior almost comparable, as least for a two-dimensional crack [12].

5.3 Semi-Quantitative Discussion on Effect of Interface Morphology on Fracture Behavior of FSWed T-lap Joints

5.3.1 Effect of interface morphology in single-pass FSW

Figure 5-6 shows the crack size and geometry of defects at the AS and RS affected by the welding parameters in single-pass FSW. It is clear that the change in the welding speed or probe length would lead to the various formation of defect size. Noting that in all cases, the defect size at the RS seems to be bigger than that at the AS, especially in low welding speed or long probe. In addition, the higher value of h at the RS reduced the effective skin thickness that was discussed in previous chapter. This means that the failure of the joints is mainly affected by the defect size at the RS where the fracture location of the joints was found. So, the fracture mechanic parameter at the RS is considered and calculated to control the strength of the joints.

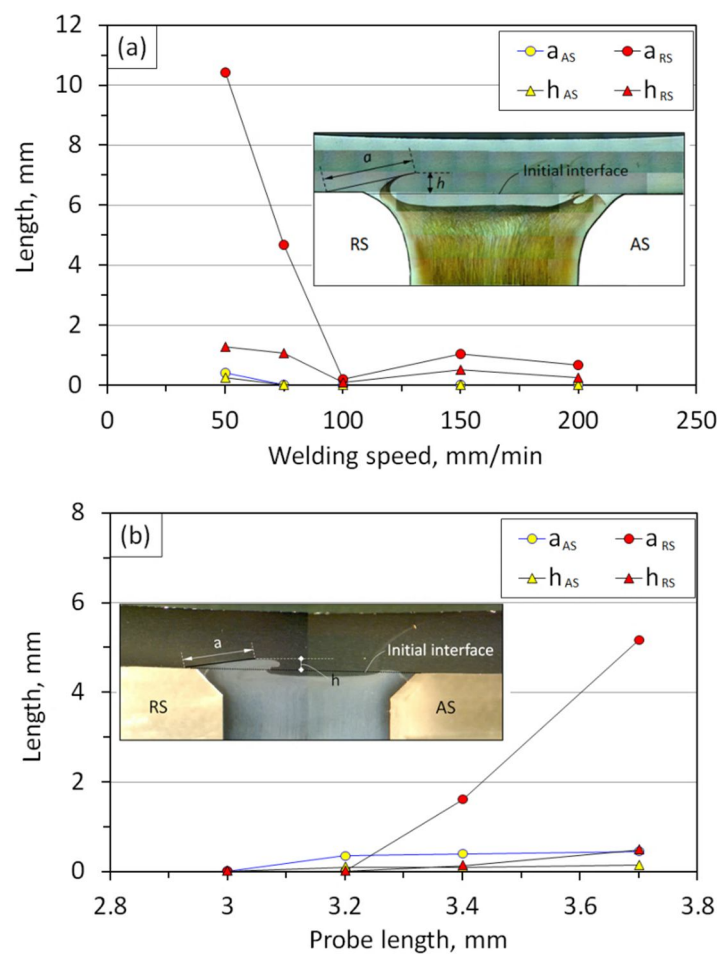


Figure 5-6 Comparison crack size between RS and AS affected by (a) welding speed and (b) probe length.

The SIFs at the crack tip at the RS can be calculated by Equation (5-30) and (5-31), as following:

$$K_I = F \times Y_I \times \sqrt{\pi a} \times \sigma \quad (5-30)$$

$$K_{II} = F \times Y_{II} \times \sqrt{\pi a} \times \sigma \quad (5-31)$$

where factor F is calculated by Equation (5-7), a is crack size, as presented in Figure 5-6. Geometry factor Y is expressed by Equation (5-32,33,34):

$$Y_I = 1.12^2 (\sin \theta)^2 / \sqrt{\sin \theta} \quad (5-32)$$

$$Y_{II} = \frac{1}{1.12^2} \sin \theta \cos \theta / \sqrt[4]{\sin 2 \theta} \quad (5-33)$$

$$Y_{eq} = \sqrt{(Y_I)^2 + (Y_{II})^2} \quad (5-34)$$

where θ is crack angle, as shown in Figure 2-38 and 2-39 in Chapter 2. Hereinafter, the parameters, $1/(F \times Y_I \sqrt{a})$ and $1/(F \times Y_{II} \sqrt{a})$ are called by “Geometrical resistance factor of defects (GRFD)”. The effects of welding speed and probe length on the GRFD under skin test are shown in Figure 5-7(a) and Figure 5-7(b), respectively. Note that the GRFD was reached the best value at the welding speed of 100 mm/min. Meanwhile, this value decreases with increasing the probe length. Figure 5-8 displays the influence of the welding speed on the GRFD under the stringer test. Similar to the skin test, the GRFD is small value at low welding speed. These results seem to have closed relation to defect size that was controlled by the welding parameters.

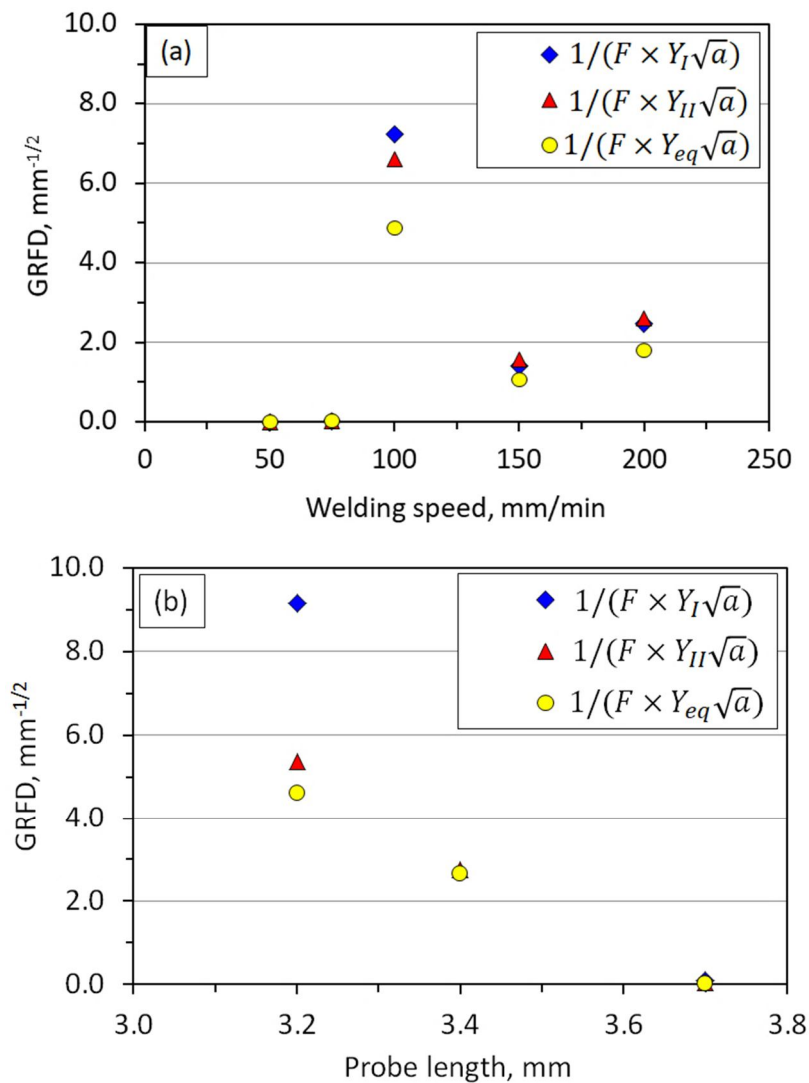


Figure 5-7 Effect of (a) welding speed and (b) probe length on GRFD under skin test.

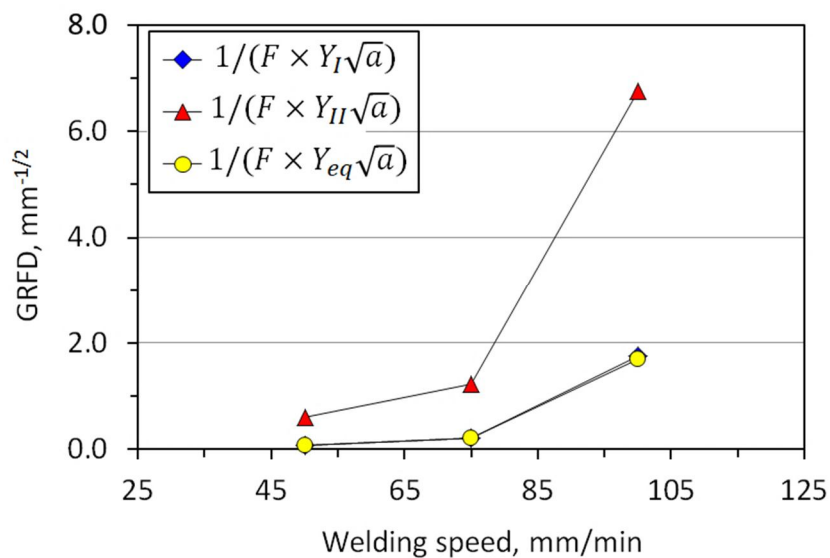


Figure 5-8 Effect of welding speed on GRFD under stringer test.

5.3.2 Effect of interface morphology in double-pass FSW

Figure 5-9 shows the crack size and geometry of defects at the RS1/AS2 and AS1/RS2 affected by tool offset in double-pass FSW. It is clear that the increase in the distance of tool offset toward the AS would lead to reduction in defect size. It is dissimilar to the single-pass, the double-pass FSW produced two cracks with the size is nearly same. This means that the strength of the joints can be affected by both cracks.

In order to more easily understand the influence of the various welding conditions on the interface geometry and the fracture of the T-lap joints, a simple mechanical model under the stringer test is shown in Figure 5-10. The application of various welding conditions might be obtained the different interface geometries, as shown in Figure 5-10(a). Here, the defect size was significantly decreased by employing double-pass and tool offset. Note that using single-pass FSW can produce two cracks those were significantly different size, as seen Figure 5-10(b). In contrast, the application of double-pass FSW was obtained the same crack size at the AS and RS. In the other words, the application of double FSW with offset makes change in crack geometry from a single crack to a double crack and reduction in crack length with tool offset.

From above overviews, three mechanical models were considered as correspondence with the interface geometry of each joint, as shown in Figure 5-10(c). In this case, the effect of crack length ratio on normalized SIFs in three mechanical modes shows Figure 5-11. It is clear that the normalized SIFs F at single crack is higher than that at double crack. This means that with same crack size, a single crack is easier failure than double crack.

The SIFs at the crack tip can be calculated by Equations (5-30) and (5-31). Here, factor F was calculated by Equation (5-11). Geometry factor Y is expressed by Equation (5-32,33,34). The effect of tool offset on the GRFD under the skin test is shown in Figure 5-12. Here, the GRFD increased with increasing the distance of tool offset that tended to decrease defect size (Figure 5-9). In the other words, this value significantly depended on the crack angle and size of defects. Note that the GRFD at mode I was higher than that at mode II. This result might be contributed by low crack angle that obtained from 16-22°, as shown in Chapter 3 (Figure 3-16).

Figure 5-13 displays the effect of tool offset on the GRFD under the stringer test. Similar to the skin test, increase in the distance of tool offset raised the GRFD in both

mode I and II. Note that the GRFD at mode I is significantly lower than that at mode II. In the other words, the influence of the geometry of defect on failure at mode I is more significant than that at mode II. As a result, the kissing bond, or interface is easy to be delaminated under the stringer test.

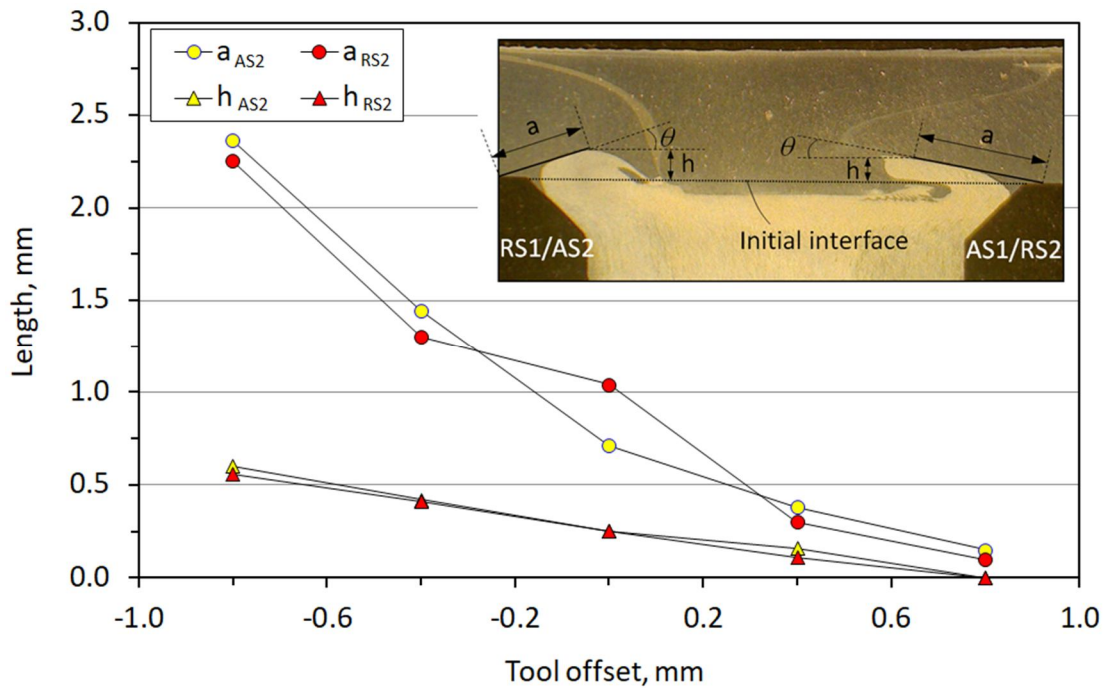


Figure 5-9 Comparison crack size between AS1/RS2 and RS1/AS2 affected by tool offset.

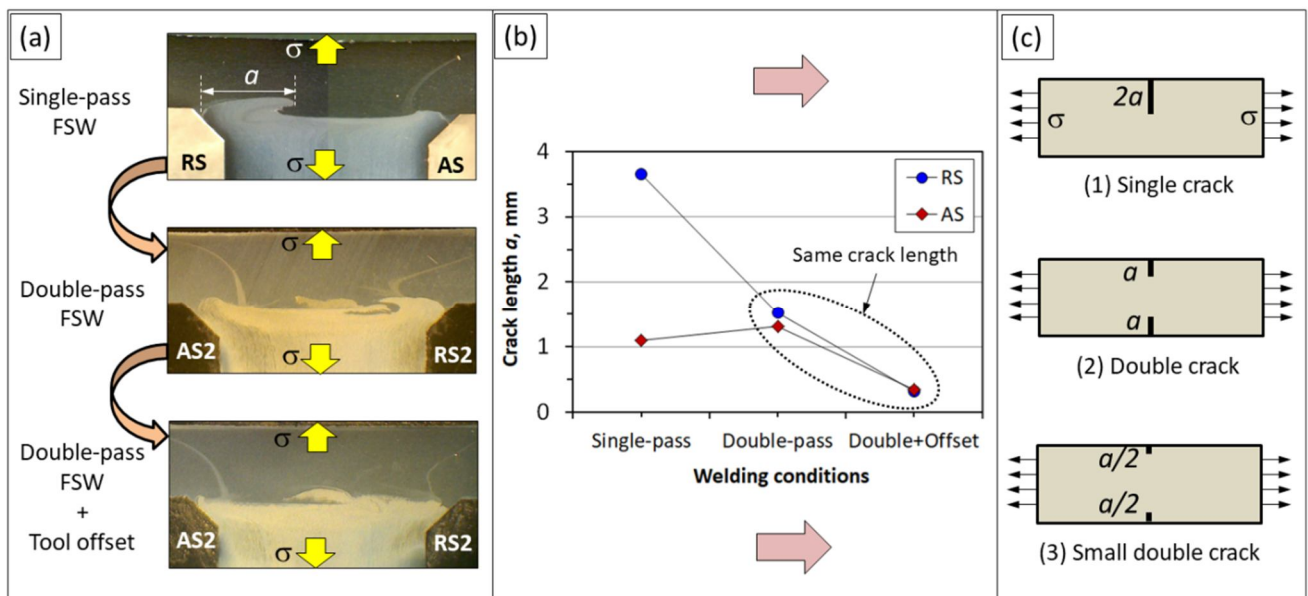


Figure 5-10 Effect of various welding conditions on (a) cross-section, (b) crack length, and (c) simple mechanical model in fracture of FSWed T-lap joints.

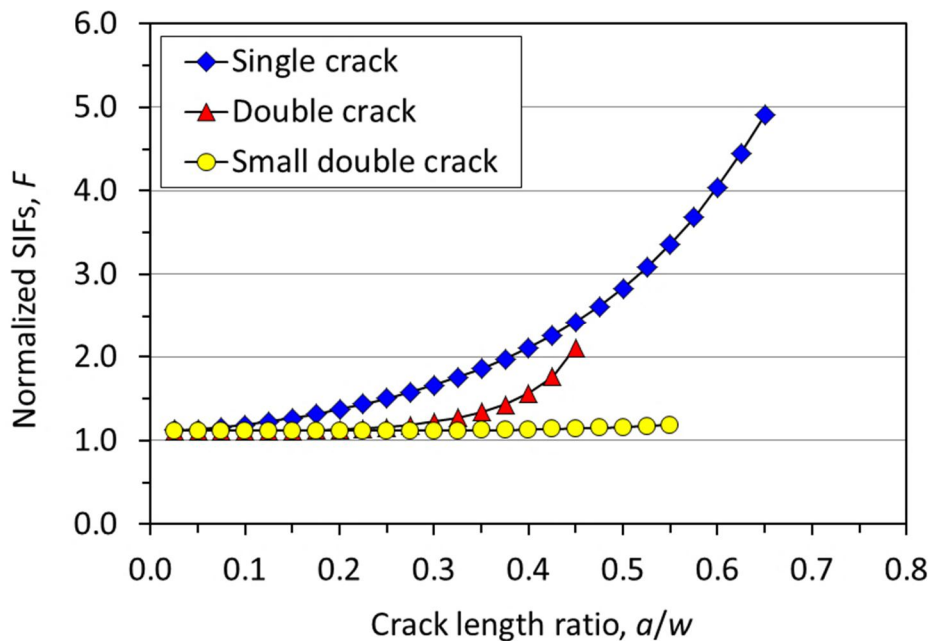


Figure 5-11 Normalized SIFs, F in three mechanical modes.

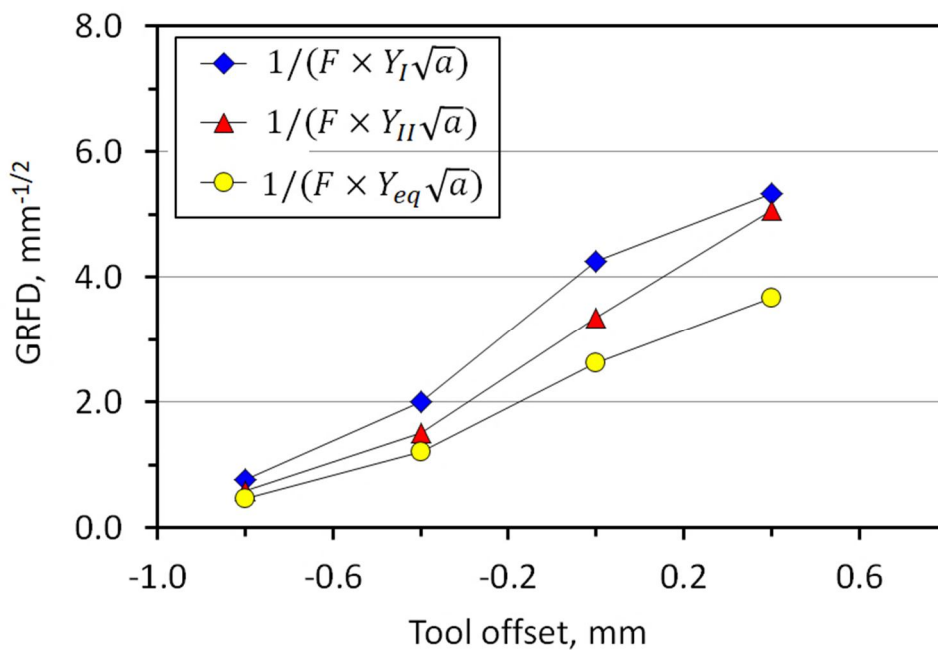


Figure 5-12 Effect of tool offset on GRFD under skin test.

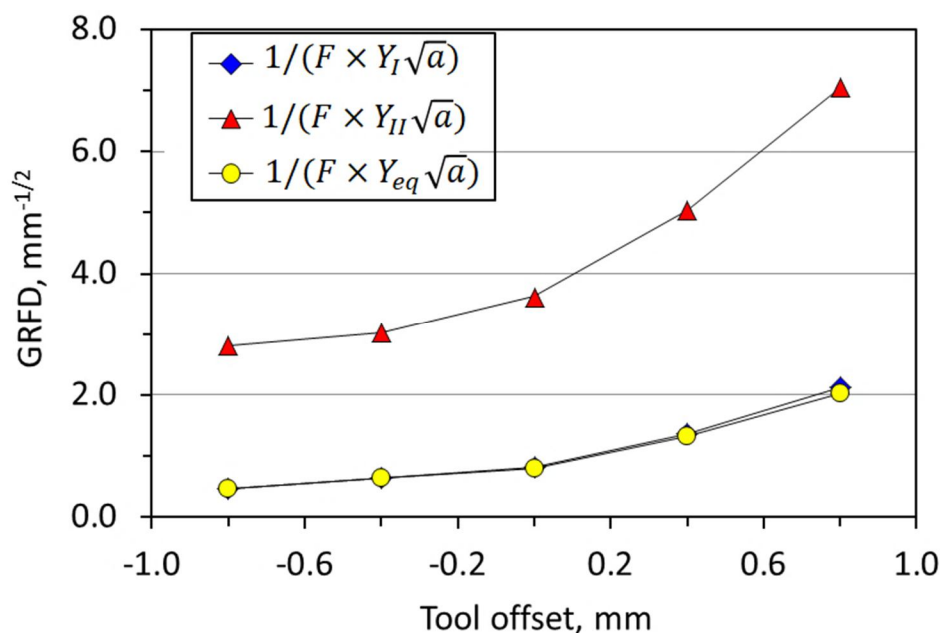


Figure 5-13 Effect of tool offset on GRFD under stringer test.

5.4 Finite Element Analysis (FEA)

5.4.1 Model and material description

In order to more quantitatively understand the influence of the geometry and size of defects on the failure of the FSWed T-lap joints and to rationalize the discussions in the Section 5.3, a Finite Element Analysis (FEA) is applied. Figure 5-14, as an example, illustrates a FEA model of specimen S12 produced by double-pass FSW, as presented in Chapter 4. The model had about 4306 elements that mainly located close to two cracks and long interface (Figure 5-15). The gap between the weld toe and the gripping part is set up by 1.0 mm. The curve length of two cracks inside the joints are introduced base on the real specimen so that the crack tip makes an angle, (α) as illustrated in Figure 5-14. The value of crack size at two sides is nearly same. The value of α is changed as calculation variable in this work. The uniform nominal stress (σ_{nom}) was applied along the stringer part.

For purpose of brevity, it is assumed that two materials have equal elastic properties with 71 GPa in Young's modulus, and 0.33 in Poisson's ratio, respectively. The interface of the joints was modeled by bonding between two materials. The FEA was carried out by means of the ANSYS v.15 software using bilinear isotropic hardening models with the mechanical properties of two alloys are given in Table 5-1.

To evaluate the failure behavior of the T-lap joints, the fracture mechanics parameters in terms of the SIFs, K is calculated for the various cases. Here, the equivalent SIF, K_{eq} was determined by Equation (5-4) [4].

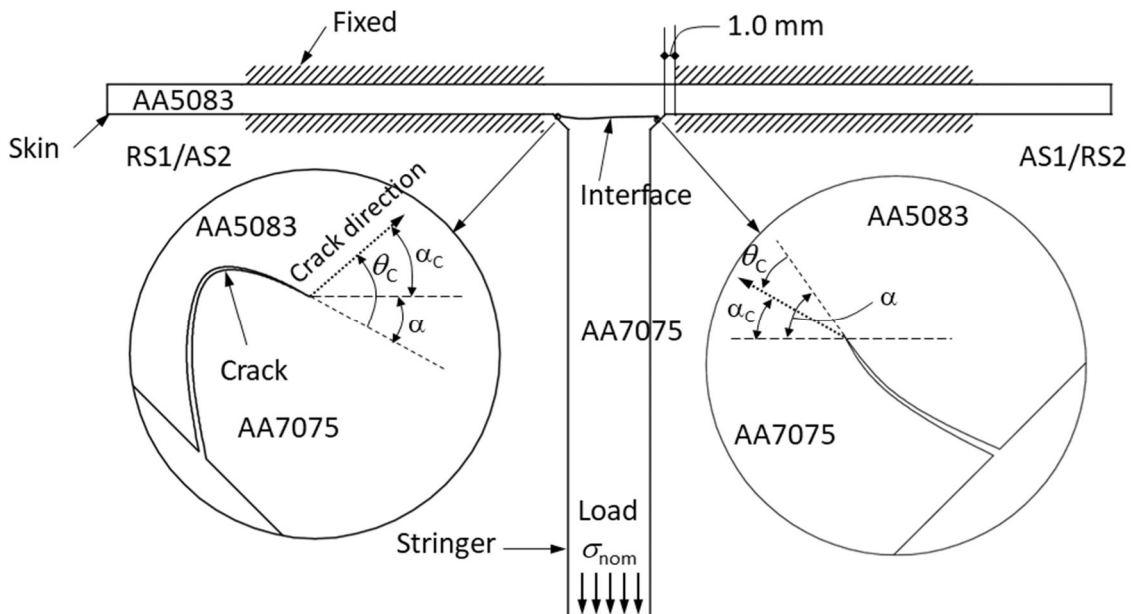


Figure 5-14 Model of specimen for FEA.

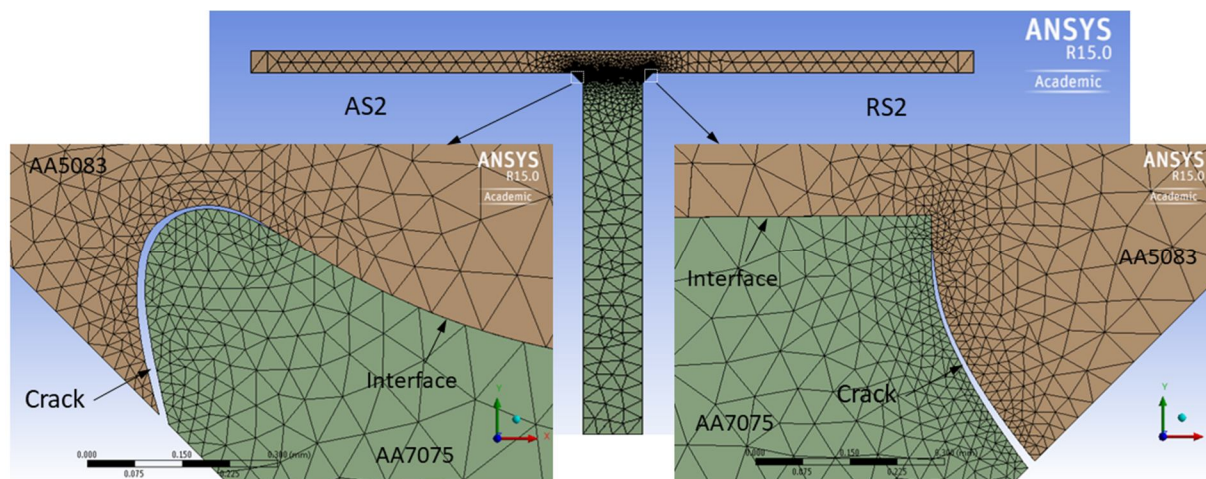


Figure 5-15 Image of meshing model of specimen S12.

Table 5-1 Mechanical properties of AA5083 and AA7075 for FEA model.

| Mechanical properties | Yield strength (MPa) | Tangent modulus (GPa) | Young modulus (GPa) | Poisson's ratio | Density (g/cm ³) |
|-----------------------|----------------------|-----------------------|---------------------|-----------------|------------------------------|
| AA5083 | 260 | 1.6 | 71 | 0.33 | 2.66 |
| AA7075 | 520 | 2.3 | 71 | 0.33 | 2.81 |

5.4.2 FEA results

The FEA results are presented in Figures 5-16 and 5-17. Here, equivalent (Von-Mises) stress and normal stress around two cracks at the RS1/AS2 and AS1/RS2 are shown in Figures 5-16(a,b) and 5-16(c,d), respectively. Note that the stress distribution was more highly concentrated in the AS1/RS2 than the RS1/AS2 side. An important fracture mechanic parameter in terms of the SIFs, K is presented in Table 5-2. According to that, although the size of crack was same, the value of the SIF at the RS1/AS2 was much lower than that at the AS1/RS2. These results mean that the role of the orientation of the crack tip might be key factor in this case. This postulation is more clearly shown in Figure 5-17 that indicated the effect of the crack tip angle at the AS1/RS2 on the SIFs. Here, the equivalent SIF, K_{eq} was obtained at a high value corresponded to crack tip angle of 45° - 60° . Especially, the highest value of the SIFs of K_I and K_{eq} at the crack tip angle of 50° was found.

As results indicated in Chapter 4, two main factors might be reason for the predominant crack at the AS1/RS2 compared to the RS1/AS2. Firstly, the bonding strength of the interface of the KBs at the AS1/RS2 is lower than that at the RS1/AS2, resulting in the easier delamination of interface at the AS1/RS2. Secondly, the geometry of the crack at the AS1/RS2 was more convenient for crack propagation than that at the RS1/AS2. The higher values of stress and SIFs at crack tip at the AS1/RS2 were considered as the evidences for this conclusion. In other words, the role of the orientation of the KBs plays key factor in the mechanical properties of the joints, as presented in literature for other junctions [13-15].

From above the obtained results, it seems that the fatigue life of the FSWed T-lap joints may be enhanced by changing the bonding angle of the interface at two corner fillets, which is believed to play vital role in the fatigue failure and the life of the T-lap joints in the present work. An evidence for this postulation is shown in Figure 5-18 that described the influence of crack tip angle on the fatigue life of the joints. Here, two main groups of crack tip angle were found inside of the joints; one is 45° - 60° (denoted as low crack tip angle), other is 80° - 110° (denoted as high crack tip angle) (Figure 5-18(a)). The change in the crack tip angle of the joint might be affected by the instability of the FSW process, especially in T-lap joint. It is worthy to note from Figure 5-18(b), the specimens with low crack tip angle had the shorter fatigue life compared to that with

high crack tip angle. This result had good correlation with the SIFs as seen in Figure 5-17. Thus, it can be concluded that the application of double pass FSW and the tool offset may change the bonding angle which made big contribution to advance the strength of the T-lap joints.

Table 5-2 Stress intensity factor at two crack tips.

| Stress intensity factor, SIFs at RS1/AS2, (MPa√m) | | | | Stress intensity factor, SIFs at AS1/RS2, (MPa√m) | | | |
|---|----------|----------|--------------|---|----------|----------|--------------|
| K_I | K_{II} | K_{eq} | K_I/K_{II} | K_I | K_{II} | K_{eq} | K_I/K_{II} |
| 0.245 | -0.282 | 0.374 | -0.869 | 0.896 | -0.642 | 1.102 | -1.396 |

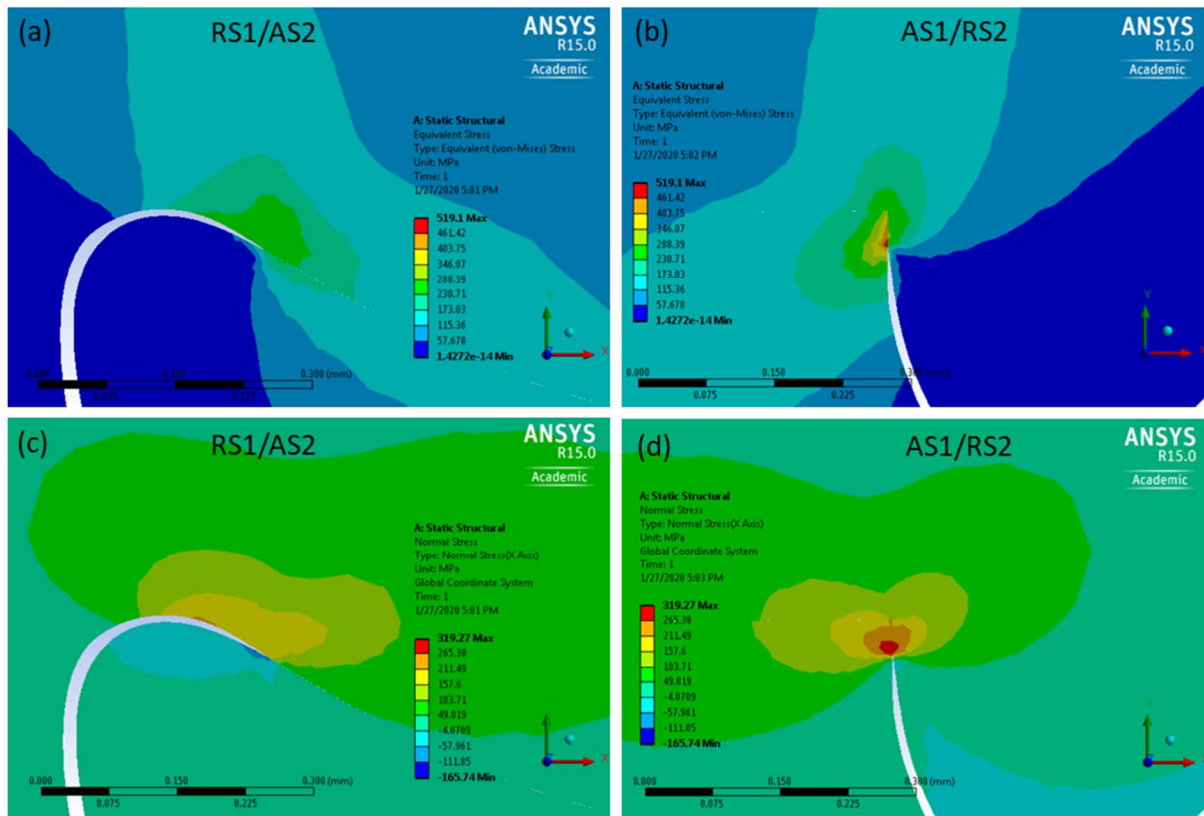


Figure 5-16 (a,b) Von-Mises equivalent stress distribution and (c,d) normal stress (X axis) around two crack tips at RS1/AS2 and AS1/RS2.

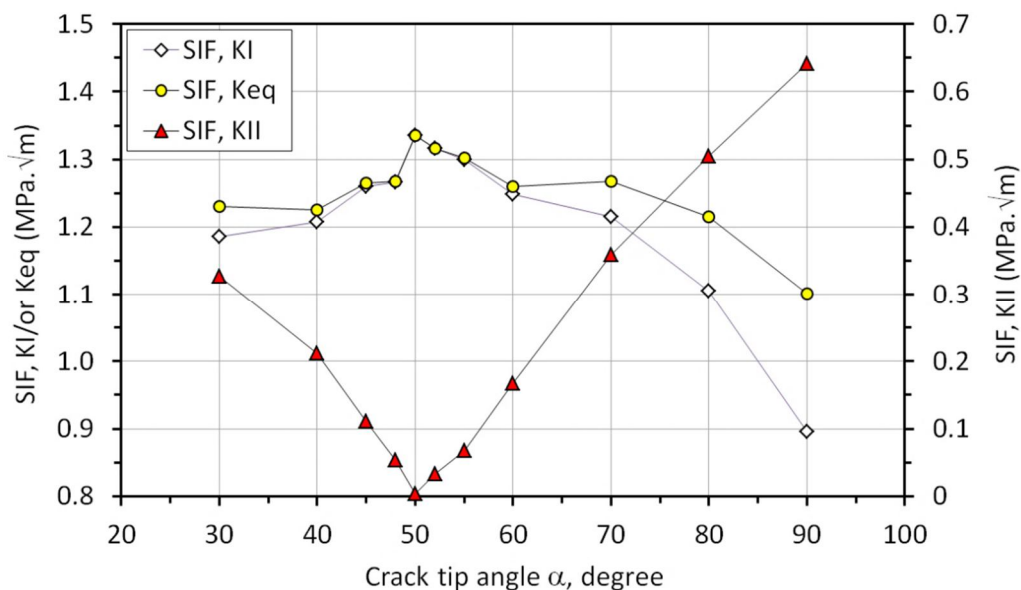


Figure 5-17 Effect of crack tip angle at AS1/RS2 on the SIFs.

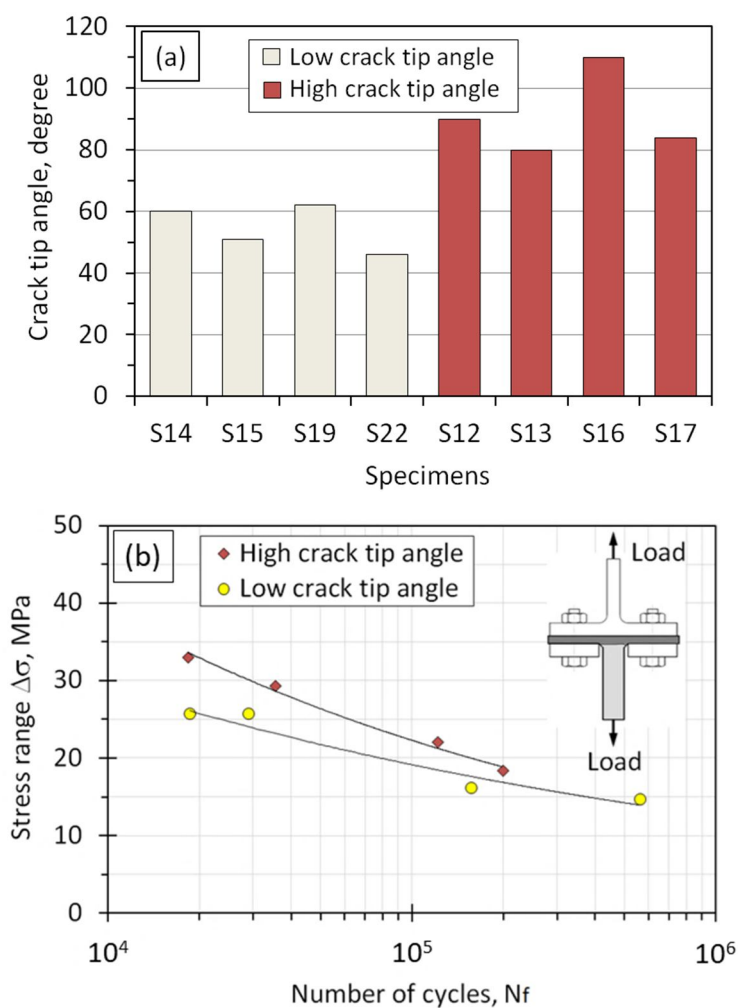


Figure 5-18 (a) Crack tip angle at AS1/RS2 measured on specimens and (b) effect of crack tip angle on the fatigue life of T-lap joints.

5.4.3 Prediction of crack growth angle under stringer test

In order to estimate the crack initiation angle under mixed mode loading, some available criteria such as Maximum Tangential Stress (MTS) [16-19], Strain Energy Density (SED) [20], maximum energy release rate [21], and Maximum Shear Stress (MSS) criterions [22] are applied in the literature. In this work, the crack direction was predicted by Maximum Tangential Stress (MTS) criterion. From Equation (5-19) and (5-20) with replacing (θ) by crack extension direction (θ_c) we have:

$$\theta_c = 2 \tan^{-1} \left[\frac{1}{4} \frac{K_I}{K_{II}} - \frac{1}{4} \sqrt{\left(\frac{K_I}{K_{II}} \right)^2 + 8} \right] \quad \text{for } K_{II} > 0 \quad (5-35)$$

$$\theta_c = 2 \tan^{-1} \left[\frac{1}{4} \frac{K_I}{K_{II}} - \frac{1}{4} \sqrt{\left(\frac{K_I}{K_{II}} \right)^2 + 8} \right] \quad \text{for } K_{II} < 0 \quad (5-36)$$

Table 5-3 shows the calculated results for the SIFs and crack initiation angles at the AS1/RS2, where θ_c and α_c are the crack initiation angle defined as Figure 5-14. Note that the value of K_{II} calculated in specimen S15 was nearly zero at the crack tip angle of $\alpha = 51^\circ$. Moreover, the crack initiation angle was predicted about 51.49° . This means that the crack direction propagates is the same crack tip angle. It is worthy to note from Figure 5-19 that a good agreement in the crack growth angles between estimation and experiment. This result indicates that the fracture angle of the T-lap joints under the stringer test can be predicted well via the MTS criterion that was widely applied by many researchers for aluminium alloys under mixed mode failure [17,23-25].

Table 5-3 Stress intensity factor and crack initiation angle at AS1/RS2.

| Spec. | Max. stress (MPa) | α ($^\circ$) | Stress intensity factor, SIF (MPa. \sqrt{m}) | | | K_I/K_{II} | θ_c ($^\circ$) | α_c ($^\circ$) |
|-------|-------------------|-----------------------|---|----------|-------|--------------|-------------------------|-------------------------|
| | | | K_I | K_{II} | K_e | | | |
| S12 | 36.6 | 90 | 0.9866 | -0.6599 | 1.187 | -1.4951 | 46.18 | 43.82 |
| S13 | 32.5 | 80 | 1.0055 | -0.4415 | 1.098 | -2.2775 | 37.42 | 42.58 |
| S14 | 28.5 | 61 | 1.0220 | -0.1390 | 1.031 | -7.3525 | 14.97 | 46.03 |
| S15 | 28.5 | 51 | 1.0457 | 0.0045 | 1.046 | 232.378 | -0.49 | 51.49 |
| S16 | 24.5 | 110 | 0.4152 | -0.4757 | 0.631 | -0.8728 | 55.14 | 54.86 |
| S17 | 20.3 | 84 | 0.6262 | -0.2935 | 0.692 | -2.1336 | 38.84 | 45.16 |
| S19 | 17.9 | 62 | 0.6612 | -0.0979 | 0.668 | -6.7538 | 16.18 | 45.82 |
| S22 | 16.3 | 46 | 0.5647 | 0.0520 | 0.567 | 10.8596 | -10.36 | 56.36 |

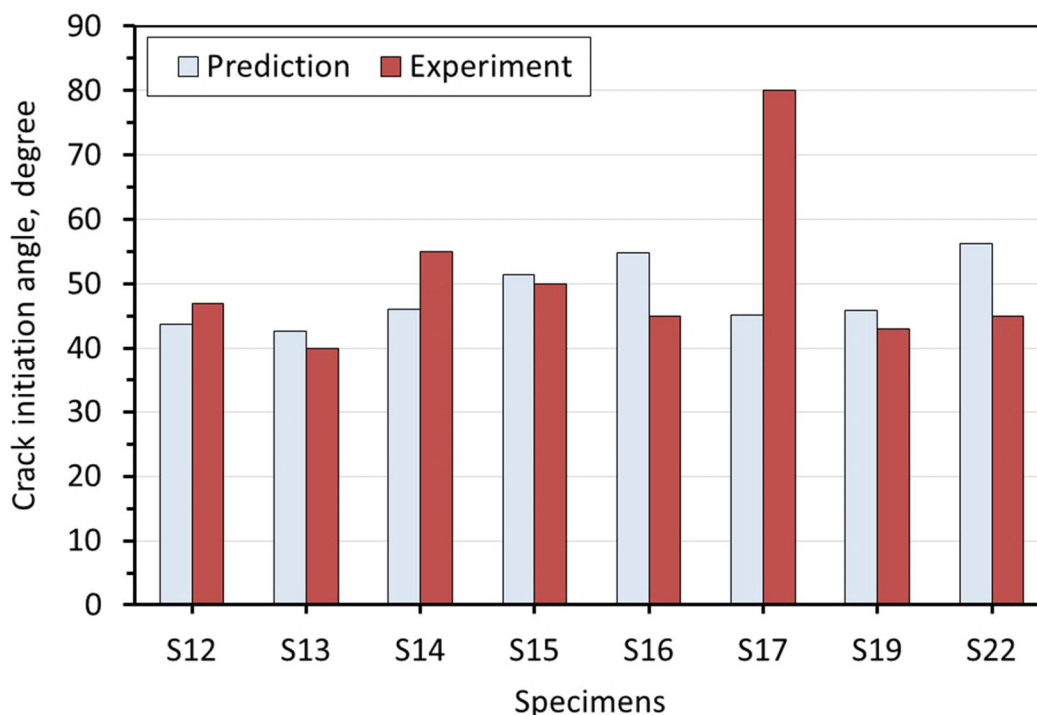


Figure 5-19 Comparison in crack initiation angle between prediction and experiment.

5.5 Brief Summary

As shown from Section 5.2 to Sec. 5.4, a simplified model which deals with the interface morphology in the FSW by approximating by the equivalent crack provided reasonable explanation to the strength of the dissimilar FSWed T-lap joints. Note that the magnitude of K is given by Equation (5-37):

$$K = Y\sqrt{\pi a} \times \sigma \quad (5-37)$$

Thus allowable stress is dominated by Equation (5-38):

$$\sigma_{allow} \simeq \frac{K_C}{Y\sqrt{\pi a}} \quad (5-38)$$

where K_C is interface strength which depends on bonding conditions. In the other words, when the K_C is given, the optimization of the FSW can be reached by;

- 1) Controlling the defect size, a
- 2) Decrease in the geometrical factor, Y
- 3) Increase in K_C

The FSW conditions can change all these factors.

5.6 Chapter Summary

The influence of the interface geometry on the fracture behavior of the FSWed T-lap joints was clarified in both single- and double-pass. Here, a new concept that the interface is modeled by an equivalent complicated crack has been proposed to make the analysis of the dissimilar FSWed T-lap joints, via introducing the “GRFD” parameter. This simplification could provide reasonable explanations to the experimental works in Chapter 2 to Chapter 4. The details are as follow:

- (5-1) The SIFs significantly depended on the interface geometry that was controlled by the welding parameters. Increasing defect size at low welding speed would lead to decreasing the GRFD that reduced applied load.
- (5-2) The application of the double-pass FSW that made the change in crack geometry from a single crack to a double crack and reduction in crack length with tool offset increased the GRFD in both the skin and stringer tests. The effect of defect geometry on the stringer test is more significant than that on the skin test.
- (5-3) In double-pass FSW, the FEA suggested that the geometry of the crack at the AS1/RS2 was more convenient for the crack propagation than that at the RS1/AS2. It is true that the values of stress and the SIFs at the crack tip of the AS1/RS2 were higher than that of the RS1/AS2. The fatigue life of the T-lap joints under the stringer fatigue test was low at the crack tip angle from 45°-60° those caused the high values of the equivalent SIFs.
- (5-4) The application of the MTS criterion might predict well the crack initiation angle that predominantly propagated at the KBs of the AS1/RS2 under the stringer fatigue test.
- (5-5) The analyzed results show that the optimization of the FSW can be reached by minimizing the defect size, by decreasing the geometrical factor, and by increasing the interface strength those can be attained by the change in the welding conditions via the control of the metal flow in the FSW process.

5.7 Chapter References

- [1] Maiti, S.K., Determination of Stress Intensity Factors, *Fracture Mechanics*, (2016), pp.102-151, doi.org/10.1017/CBO9781316156438.006.
- [2] Rooke, D.P. and Cartwright, D.J., *Compendium of stress intensity factors*, HMSO Ministry of Defence, Procurement Executive, (1976).
- [3] Anderson, T.L., *Fracture Mechanics: Fundamentals and Applications*, CRC Press, Boca Raton, FL (2005).
- [4] Irwin, G., Analysis of Stresses and Strains near the End of a Crack Traversing a Plate, *Journal of Applied Mechanics*, Vol.24, (1957), pp.361-364.
- [5] Nisitani, H., Stress Intensity Factor for the Tension of a Semi-Infinite Plate Having an Oblique or a Bent Edge Crack, *JSME*, Vol.41(344), (1975), pp.1103-1111.
- [6] Murakami, Y., *Stress Intensity Factors Handbook*, Vol.1, (1987).
- [7] Benthem, J.P., and Koiter, W.T., Asymptotic approximations to crack problems, *Methods of Analysis and Solutions of Crack Problems*, (1973), pp.131-178.
- [8] Williams, J.G, *Fracture Mechanics of Polymers*, New York, Wiley, (1984).
- [9] Khan, S.M.A., and Khraisheh, M.K., Analysis of mixed mode crack initiation angles under various loading conditions, *Engineering Fracture Mechanics*, Vol.67(5), (2000), pp.397-419.
- [10] Schreurs, P.J.G., *Fracture Mechanics: Lecture Notes*, Technische Universiteit Eindhoven, (2014).
- [11] Erdogan, F., and Sih, G.C., On the Crack Extension in Plates Under Plane Loading and Transverse Shear, *Journal of Basic Engineering*, Vol.85(4), (1963), pp.519-527.
- [12] Sih, G.C., Strain energy density factor applied to mixed mode crack problems, *International Journal of Fracture*, Vol.10 (3), (1974), pp.305-321.
- [13] Le Jolu, T., Morgeneyer, T.F., Denquin, A., and Gourgues-Lorenzon, A.F., Fatigue lifetime and tearing resistance of AA2198 Al–Cu–Li alloy friction stir welds: Effect of defects, *International Journal of Fatigue*, Vol. 70, (2015), pp.463-472.
- [14] Dickerson, T., Fatigue of friction stir welds in aluminium alloys that contain root flaws. *International Journal of Fatigue*, Vol.25(12), (2003), pp.1399-1409.
- [15] Zhou, C., Yang, X., and Luan, G., Effect of root flaws on the fatigue property of friction stir welds in 2024-T3 aluminum alloys, *Materials Science and Engineering: A*, Vol.418(1-2), (2006), pp.155-160.
- [16] Kim, T.-Y., and Kim, H.-K., Mixed-mode fatigue crack growth behavior of fully lower bainite steel, *Materials Science and Engineering: A*, Vol.580, (2013), pp.322-329.
- [17] Plank, R., and Kuhn, G., Fatigue crack propagation under non-proportional mixed mode loading, *Engineering Fracture Mechanics*, Vol.62(2-3), (1999), pp.203-229.
- [18] Selcuk, S., Hurd, D.S., Crouch, S.L., and Gerberich, W.W., Prediction of

interfacial crack path: a direct boundary integral approach and experimental study, *International Journal of Fracture*, Vol.67(1), (1994), pp.1-20.

- [19] Erdogan, F., and Sih, G.C., On the Crack Extension in Plates Under Plane Loading and Transverse Shear, *Journal of Basic Engineering*, Vol.85(4), (1963), pp.519-527.
- [20] Kipp, M.E., and Sih, G.C., The strain energy density failure criterion applied to notched elastic solids, *International Journal of Solids and Structures*, Vol.11(2), (1975), pp.153-173.
- [21] Palaniswamy, K., and Knauss, W. G., Propagation of a crack under general, in-plane tension, *International Journal of Fracture Mechanics*, Vol.8(1), (1972), pp.114-117.
- [22] Otsuka, A., Mori, K., and Miyata, T., The condition of fatigue crack growth in mixed mode condition, *Engineering Fracture Mechanics*, Vol.7(3), (1975), pp.429-439.
- [23] Mageed, A.M.A., and Pandey, R.K., Fatigue crack closure in kinked cracks and path of crack propagation, *International Journal of Fracture*, Vol.44, (1990), pp.39-42.
- [24] Mageed, A.M.A., and Pandey, R.K., Mixed mode crack growth under static and cyclic loading in Al-alloy sheets, *Engineering Fracture Mechanics*, Vol.40(2), (1991), pp.371-385.
- [25] Qian, J., and Fatemi, A., Fatigue crack growth under mixed-mode I and II loading, *Fatigue & Fracture of Engineering Materials and Structures*, Vol.19(10), (1996), pp. 1277-1284.

This page has been intentionally left blank

Chapter 6

Conclusions and Future Work

6.1 Conclusions

The Friction Stir Welding (FSW) technology is known as one of excellent methods for welding metal joints. However, its applicability to fabricate the T-lap joints has not been still satisfied in literature. The aim of this study was to improve the interface morphology and the mechanical properties of the FSWed dissimilar metal T-lap joints between AA7075 and AA5083. The fracture behavior of the joints was explored to make platform for the advance of the strength of the T-lap joints. The main results were derived as follows:

In **Chapter 2**: The fundamental formation of welding interface between skin and stringer parts was clearly observed in the FSWed dissimilar T-lap joints. Some undesirable defects, e.g. hook, kissing bond, and bonding line defects under various welding conditions were found along the interface. Here, increasing the welding rate or decreasing probe length might eliminate the hook defects that significantly degraded the strength of the joints, however, the bonding line defects were found in these cases. The low stirring efficiency along interface might be reason for forming this type of defect that reduced the bonding strength of interface. Among defects, the kissing bonds at the two corner fillets were formed under all the welding conditions. This means that they were independent on the welding parameters. These experimental findings indicated that the welding interface, where the fracture was found, played a vital role in the mechanical properties of the T-lap joints. As a result, the welding interface with smaller defect size might upgrade the mechanical properties of the joints that were obtained at the welding speed of 100 mm/min or the probe length of 3.4 mm. In spite of these, the interface morphology seems to be too difficult to be improved by employing only the traditional single-pass FSW, resulting in low joint efficiency.

In **Chapter 3**: The application of a double-pass FSW induced by tool offset and reversed metal flow successfully improved the interface morphology of the T-lap joints. Here, the KBs size was significantly reduced at both the advancing side (AS) and the retreating side (RS) by offsetting the tool probe toward the AS with the distance of 0.8 mm. As a result, the joint efficiency was reached approximately 90% in comparison with the strength of AA5083 base metal for both the skin and stringer tensile tests. Digital image correlation (DIC) analyses showed that the strain of the joints concentrated at the heat affected zone (HAZ) instead of the kissing bonds, where the

fracture location was found under skin tensile test. The above results were suitably interpreted by the tool position and asymmetric material flow during the double-pass FSW process. It was also found that the gap distance between probe and die kept a key role in the welding interface formation. These findings derived such as a postulation that the control of interface morphology is a key point in order to upgrade the strength of the FSWed T-lap joints.

In **Chapter 4**: The failure behaviour of the optimized dissimilar T-lap joints was largely investigated under cyclic loading. Here, the fatigue crack dominantly initiated at the weld toe under the skin loading tests. The optical observation showed that most of the interface of the KBs was not delaminated during testing process. This would be attributed the high stress concentration at weld toe, resulting in the acceleration of crack initiation. Regarding the stringer fatigue tests, however, the crack initiations were nucleated in the interface of the KBs. Then, the crack obliquely propagated to the skin AA5083 under mix-mode failure. It was found that the KBs interfaces were comfortably delaminated to form two cracks at corner fillets. In these cases, the crack initiation was strongly influenced by the crack geometry.

In **Chapter 5**: In order to consider the unified treatment for the present experimental results, a simplified fracture mechanics model was proposed via introducing the “Geometrical resistance factor of defects (GRFD)”. Here, the AA7075/AA5083 interface is presented by an equivalent defect or crack which is subjected to the corresponding equivalent stress intensity factor (SIF). It has been shown by the numerical model that the equivalent SIF significantly depended on the interface geometry that was controlled by the defects. Here, increasing defect size at low welding speed would lead to decreasing the GRFD. With the improvement of interface geometry by applying the double-pass FSW and tool offset, the GRFD increased in both the skin and stringer tests. In addition, the effect of defect geometry in the stringer test is more significant than that in the skin test. The Finite Element Analysis suggested that in the double-pass FSW, the crack shape produced at the retreating side of second-pass (AS1/RS2) caused a higher equivalent SIF, compared to that at the advancing side of second-pass (RS1/AS2). The crack propagation direction was predicted well by the application of the maximum tangential stress (MTS) criterion. These analysis show that the optimization of the FSW can be reached by minimizing the defect size, by decreasing in the geometrical factor, and by increasing the interface

strength those can be attained by the change in the welding conditions via the metal flow in the FSW process.

6.2 Future Work

The findings in this study demonstrated that the mechanical properties of the T-lap joints were significantly affected by the welding interface in which some undesirable defects are often unavoidable. So far, the absolute elimination of the KBs from the T-lap joints seems to be impossible in the FSW process. However, it is sure that the mechanical properties of the joints might be improved well due to controlling the interface morphology related to the KBs geometry. Nonetheless, it is prudent to advance the fatigue life of the T-lap joints to upgrade the quality of the joints that is able to apply widely in automotive, shipbuilding, railway, and aviation industries. In order to approach this goal, some issues are recommended as follows:

- The application of double-pass induced by tool offset may allow us to fabricate the FSWed T-lap joints with tool probe has smaller diameter than the thickness of the stringer part. This is useful for structure that has the big thickness of the stringer. The selection of the suitable diameter of tool probe may advance the weldability of the FSWed T-lap joints.
- It is well known that the microstructure of the joints is one of the key factors in crack propagation. So, the fatigue crack propagation of the T-lap joints needs to be investigated to clarify this effect, especially in the stringer fatigue test.
- In the dissimilar T-lap joints, the interface of the bonded mismatch of materials that is significant differences in Young's modulus and Poisson ratio may take stress singularity. Some possibilities to reduce it are also a future work.
- Some of candidate methods were tried to control the interface morphologies by changing the process parameters in the FSW in this work, however, more sophisticated methods should be requested to control the defect geometry and the size in future.